# Mechanisms of Iron Oxidation in the Ferroxidase Centre of *Escherichia coli* Bacterioferritin: A Comparison to Other Ferritins

Jacob Alexander Samuel Pullin

A thesis submitted for the degree of Doctor of Philosophy

School of Biology

University of Essex

October 2019

# Abstract

Ferritins are iron storage proteins that are both widespread and abundant in nature, being an essential means of solubilising and storing iron in a non-toxic manner for most organisms. While ferritins have been known and studied since the mid-20$^{th}$ century, it has become increasingly clear that despite their outward spherical appearances and ferroxidase activity, ferritins have intimate differences in their structures which lead to differing mechanisms of iron storage and an additional role in oxidative stress prevention.

Ferritins have been studied rigorously since 1937 (Wang *et al.*, 2010), yet even the mechanisms of the most extensively studied mammalian ferritins, are the subject of debate within the academic community; it is hotly debated whether ferritins operate via a single 'unifying' mechanism or through a diverse range of different mechanisms (Hagen, Hagedoorn and Honarmand Ebrahimi, 2017). New ferritins are still discovered; the unprecedented observation of a mixed-valent ferroxidase centre forming in the cyanobacterial ferritin *Syn*Ftn directly upon reaction with $O_2$ was incompatible with any reaction scheme currently published in the literature. This unprecedented reactivity was detected again in human mitochondrial ferritin and another newly discovered ferritin, *n* ferr, in quick succession. The detection of $H_2O_2$ as the product of $O_2$ reduction suggested that ferroxidase centres operate in pairs, transferring electrons over long distances. Thus, the experimental results in Chapter 3 may be the early identifiers of a new class of oxidative-stress-protectant ferritins that has as of now gone undescribed. *Syn*Ftn (a recently discovered cyanobacterial ferritin) variant proteins where residues in the three-fold channels have been substituted are also discussed here, showing subtle differences in the way iron enters and exits the diiron sites.

Unlike many ferritin studies, this thesis has primarily focused on the reactivity of the ferroxidase centre, rather than the ferritin's mineralisation activity. Characterization of the ferroxidase centres provides information that gives major clues about the functional role of the ferritin *in vivo*.

The kinetics of $Fe^{2+}$ oxidation at the diiron centres in *E. coli* bacterioferritin have expanded upon the evidence that the protein exists to prevent oxidative stress. This was performed in novel anaerobic setups by directly measuring the protein's reactivity with $H_2O_2$. UV/ vis spectroscopy highlighted that $H_2O_2$ is a preferential oxidant for bacterioferritin, and that there are several optically distinct phases of iron oxidation. Through a collaboration with the Blondin Group, Mössbauer spectroscopy allowed for the assignment of these phases. Chapter 4 details these findings and proposes an updated mechanism that expands upon the existing models. Electron paramagnetic resonance spectroscopy revealed that at supra-stoichiometric concentrations of $H_2O_2$, large protein-based free radical signals are observed.

Each of the ferritins studied in this thesis form free radicals upon the aerobic addition of $Fe^{2+}$, and these have been simulated and assigned to a universally conserved tyrosine at the ferroxidase centre. Chapter 5 focuses on electron paramagnetic resonance, depicting microwave power saturation and temperature dependence studies which reveal several free radicals that form in the $H_2O_2$-driven $Fe^{2+}$ oxidation by *E. coli* bacterioferritin. This is given consideration with respect to the protein's native role, which may be to prevent uncontrolled Fenton chemistry occurring elsewhere within the bacterium.

The experiments and results described in this thesis should be of broad interest to those who study ferritins and iron biochemistry in general.

# Acknowledgements

I would like to thank the University of Essex for accepting me as a PhD student, and to their wonderful staff and students: Hannah, Louise and Tadeo, all of whom worked in the Protein Structure and Function Laboratory, who each took time to teach me how to use various pieces of equipment. I would also like to highlight Nick, Justin and Geoff at UEA for providing both expertise and reagents. Justin has always been responsive to my queries about the literature and contributed significantly to my understanding of ferritins. Perdi and Jack were highly accommodating of me at the University of Manchester, teaching me how to perform native mass spectrometry experiments on ferritins. Mössbauer spectroscopy experiments were carried out and simulated in Grenoble by the Blondin group, which helped us crack the mechanism through which BFR operates.

Lastly and most importantly, I owe a huge debt of gratitude to Dima and Mike Wilson, who have gone out of their way to help me in my work. Mike, who was not an official supervisor of my PhD, taught me how to do stopped flow experiments, and allocated his free time to help me with data analysis and determining the mechanism of BFR action. Mike also helped me outside of university, giving a presentation on hemoglobin at one of my events for the Pint of Science Festival.

I owe most gratitude to Dima, who chose to take me on as a PhD student and has shown me how to design and perform EPR-based experiments. I have been given ample space to carry out work independently and develop as a researcher but help has always been readily available whenever I asked for it.

# Disclaimer

Some passages of text in Chapters 2 and 3 of this thesis, of which I am an author, have been quoted from the following source issued from the research presented in this work (or the electronic supporting information thereof):

Bradley, J. M., Svistunenko, D. A., Pullin, J., Hill, N., Stuart, S. K., Palenik, B., Wilson, M. T., Hemmings, A. M., Moore, G. R. and Le Brun, N. E. (2019) 'Reaction of $O_2$ with a diiron protein generates a mixed valent $Fe^{2+}/Fe^{3+}$ center and peroxide', *Proceedings of the National Academy of Sciences*, 116(6), pp. 2058-2067. doi: 10.1073/pnas.1809913116.

Bradley, J.M., Pullin, J., Moore, G. R., Svistunenko, D. A., Hemmings, A. M. and Le Brun, N. E. (2019) 'Routes of iron entry into, and exit from, the catalytic ferroxidase sites of the prokaryotic ferritin *Syn*Ftn', *Dalton Transactions*, (in press)

# Table of Contents

## Contents

# Table of Figures

# List of Tables

# Abbreviations

$\delta$- isomer shift in Mössbauer spectroscopy

Δ9-FtMt- truncated FtMt variant missing the first 9 N-terminal amino acids

$\Delta E_Q$- quadrupole splitting in Mössbauer spectroscopy

ABTS- 2,2-azinobis (3- ethylbenthiazoline-6-sulfonic acid)

ACP- acyl carrier protein

AD- Alzheimer's disease

ARC- ATPase forming ring-shaped complexes

BFR- bacterioferritin

BFR: $Fe^{2+}$- a solution of BFR anaerobically incubated with enough ferrous iron to fill all the ferroxidase centres

CpI- compound I

CpII- compound II

Da- Daltons

DFP- diferric-peroxo

DMPO- 5,5-dimethyl-1-pyrroline N-oxide

Dps- DNA-binding protein from starved cells (a mini-ferritin)

DtpA- dye-type peroxidase A

EDTA- ethylenediaminetetraacetic acid

EPR- electron paramagnetic resonance

FC- ferroxidase centre

FbpA- ferric binding protein

Fe-S- iron sulfur cluster (often used in reference to iron-sulfur cluster proteins)

FtMt- human mitochondrial ferritin

Ftn- Ftn-type ferritins (formerly known as prokaryotic ferritins)

FtnA- The primary Ftn protein in *E.coli*

FtnB- ferritin-like protein in *E.coli* that lacks active ferroxidase centres

*h*- Hill coefficient

HEPES- (4-(2-hydroxyethyl)1-piperazineethanesulfonic acid)

Hr- hemerythrin

HuHF- human H-chain ferritin

HuLF- human L-chain ferritin

IPTG- isopropyl β-D-1-thiogalactopyranoside

IRE- iron regulatory element

IRP- iron regulatory protein

$K_4[Fe(CN)_6]$- potassium ferricyanide

$K_D$- dissociation constant

$k_{obs}$- apparent rate constant

MES- 2-(*N*-morpholino)ethanesulfonic acid

MIOX- *myo*-inositol oxygenase

MMOH- methane monooxygenase

MVFC- mixed valent ferroxidase centre

*n*-ferr- Ftn-type ferritin from the archaeon *Natronolimnobius innermongolicus*

PDA- photodiode array

PDB- Protein Data Bank

PmFtn- *Pseudo-nitzschia multiseries* ferritin

Pup- Prokaryotic ubiquitin-like protein

RA- rheumatoid arthritis

RFQ- rapid freeze quench

ROS- reactive oxygen species

RNR- ribonucleotide reductase

SDS PAGE- sodium dodecyl sulfate polyacrylamide gel electrophoresis

SVD- single value decomposition

*Syn*Ftn- cyanobacterial ferritin sync_1539 from *Synechococcus* strain CC9311

Tf- transferrin

ToMOH- toluene/ *o*-xylene monooxygenase hydroxylase

TRSSA-W- tryptophanyl radical spectra simulation algorithm

TRSSA-Y- tyrosyl radical spectra simulation algorithm

UEA- University of East Anglia

WT- wild type

# Chapter 1

# An Introduction to the Structure and Function of Ferritins

**Iron in biological systems**

The evolution of organisms has taken place with a continuous dependence on iron, the fourth most abundant element in the earth's crust (Briat, 1992), even after dioxygen became readily available in the atmosphere due to photosynthesis (Theil, 1987). In the presence of water at physiological pH, dioxygen oxidizes iron and causes insoluble deposits of hydrous ferric oxide to form as rust (Yang, Chiancone, *et al.*, 2000) The hydrolytic mechanism of ferric iron precipitation is detailed in Fig. 1.1.

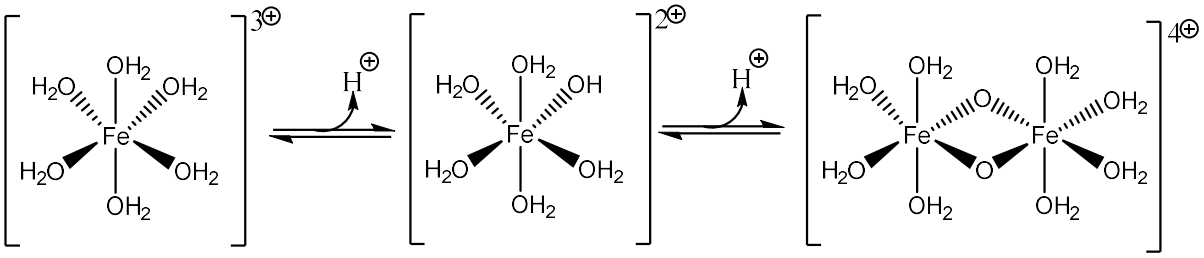

**Fig. 1.1.** The mechanism of iron (III) oxide-hydroxide polymers revolves around the loss of a proton to form a hydroxyl group, which upon loss of a second proton is able to react with an adjacent octahedral complex to form a dimer via an oxo bridge (Bottero *et al.*, 1994). This is the basis for the formation of larger polymers which become increasingly less soluble in water.

The widespread evolution of organisms with a complex transport and storage system for iron despite its insolubility and toxicity is a testament to its invaluable biochemical properties. Iron is of utmost importance to biological processes such as photosynthesis, $N_2$ fixation, methanogenesis, $H_2$ production and utilisation, respiration, the citric acid cycle, oxygen transport and DNA biosynthesis (Dexter *et al.*, 1991). This is due to iron's key role as a single electron acceptor and donor in redox reactions. The toxicity of iron arises from the ferric metal's reaction with superoxide to generate $Fe^{2+}$, Eq. (1.1), which in turn can heterolytically cleave hydrogen peroxide via the Fenton reaction (Eq. 1.2) to form hydroxyl radicals (Biemond *et al.*, 1984) (Albretsen, 2006). The overall reaction is an iron-catalysed Haber Weiss reaction (Eq. 1.3) (Harrison and Arosio, 1996).

$$Fe^{3+} + {}^{\cdot}O_2^{-} \rightarrow Fe^{2+} + O_2 \qquad (1.1)$$

$$Fe^{2+} + H_2O_2 \rightarrow Fe^{3+} + OH^{-} + OH^{\cdot} \qquad (1.2)$$

$${}^{\cdot}O^{2-} + H_2O_2 \rightarrow O_2 + OH^{-} + OH^{\cdot} \qquad (1.3)$$

Hydroxyl radicals are capable of damaging all major types of organic macromolecule, which when coupled with their high reactivity, make them incredibly harmful to an organism (Smith, 2004). Oxidative damage to proteins, for example, is hypothesised to be a significant factor in the development of neurodegenerative diseases (Baraibar *et al.*, 2012). However, it has also been hypothesised that free iron, amongst other metals, contribute to neurological disease by causing the aggregation of proteins, such as β-amyloid which progressively builds up in Alzheimer's disease (AD) patients (Carmona *et al.*, 2013). The evolutionary response to iron's toxicity and solubility was ferritin-like proteins. These are ubiquitous across nearly all species of organism, with a highly conserved protein structure (Torti and Torti, 2002). Yeasts are notable organisms in that they do not rely on ferritins to buffer cytosolic iron concentrations (Levi *et al.*, 2001). Ferritins are typically some of the more complex proteins in any organism's iron regulatory systems; in addition to iron, they can also interact with anions, such as phosphate and citrate, role-specific chelators known as siderophores, and advanced iron transport proteins, such as transferrins (Tf) in higher organisms and ferric binding proteins in bacteria (Parker Siburt, Mietzner and Crumbliss, 2012). Further to managing the solubility and toxicity issues previously mentioned, the tight iron regulation systems act as an antibacterial system in eukaryotes as the vital metal is rendered inaccessible to pathogens when bound by host proteins (Weinberg and Miklossy, 2008). Despite the toxicity of iron, there is no known regulated mechanism to excrete excess iron (De Domenico, McVey Ward and Kaplan, 2008).

**Ferritins: soluble but safe iron storage**

Ferritins and ferritin-like proteins give organisms the ability to exploit iron in an $O_2$-rich environment by removing $Fe^{2+}$ from the cytoplasm, and sequestering the iron in a non-toxic

form (Smith, 2004). An example of a mineralisation reaction driven by ferritins is shown below, as determined for *E. coli* bacterioferritin (BFR) in Eq. 1.4 (Yang, Le Brun, *et al.*, 2000).

$$4\ Fe^{2+} + O_2 + 6\ H_2O = 4\ FeO(OH) + 8\ H^+ \quad (1.4)$$

It is thus not unsurprising to find that the expression of most ferritins is controlled through the use of iron regulatory elements (IREs). These are short stem-loops found in untranslated regions of mRNA upstream of the coding region that act as post-transcriptional controls on the level of expression. Iron regulatory proteins (IRPs) have been shown to act in several ways. In some cases, they bind to these stem loops and prevent the binding of ribosomes to the mRNA. IRPs have a higher affinity for free iron than the stem loop, and detach from the stem loop to allow a ribosomal complex to form and translation to occur (Thomson, Rogers and Leedman, 1999). Alternatively, IRP binding can prevent the degradation of the mRNA, thus increasing expression (Muckenthaler, Galy and Hentze, 2008). The general trend is that ferritins are regulated through the former mechanism, and iron chaperones like transferrin, are controlled by the latter.

Equal or highly similar subunits form dimers (Fig. 1.2A) that in turn assemble into a large spherical structure surrounding a cavity within which iron will form an insoluble mineral core (Andrews, 2010). While the mass and oligomeric state of ferritins can vary, a 24mer of around 450 kDa is typical (Bauminger *et al.*, 1994). These 24meric ferritins are known as macroferritins, while ferritins made up of 12 subunits are referred to as microferritins. Microferritins have distinct catalytic sites and structures compared to their 24meric equivalents, and thus will not be considered further here. Macroferritins are very stable, being highly tolerant to pH and temperature in comparison to other proteins found in non-extremophile species. The denaturation temperatures, while varying between different ferritins, tends to be around 70˚C, while the protein is stable at pH values between 3 and 10 (Stefanini

*et al.*, 1996). This physical property is often exploited in the purification process of ferritins. Sequentially, macroferritins can share as little as 15 % sequence similarity, but their structure is conserved to an incredible degree across a wide range of species, despite their differing origins (Langlois d'Estaintot *et al.*, 2004). The oligomers form spontaneously; salt bridges between a subunit's two glutamate residues with an arginine and the terminal amine on a neighbouring subunit have been demonstrated to be key to the assembly of *R. capsulatus* and *E. coli* BFR (Fig. 1.2B) (Kilic, Spiro and Moore, 2003) (Malone *et al.*, 2004).

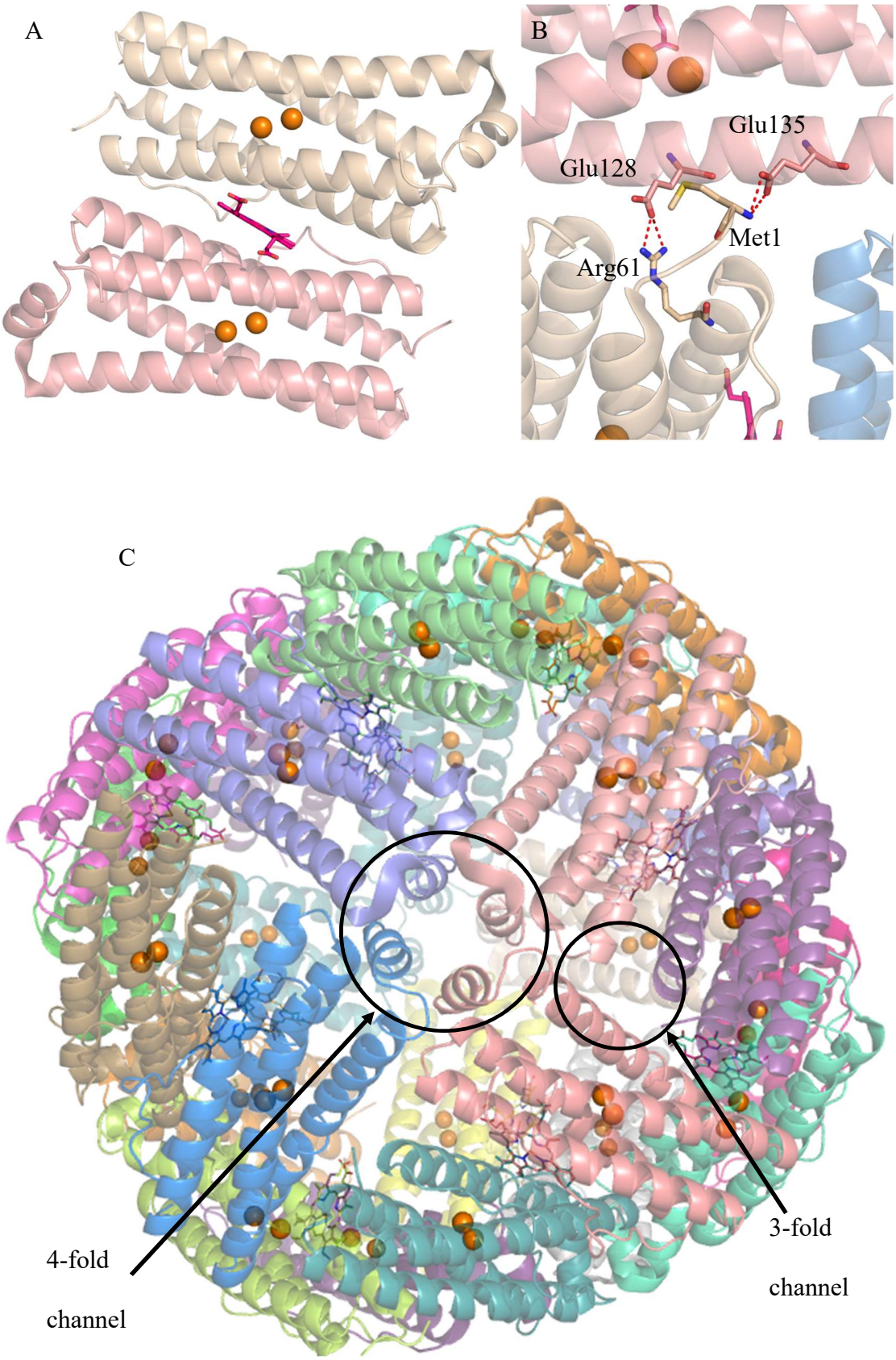


**Fig. 1.2.** Crystal structures of *E. coli* BFR showing: A. the dimeric unit, showing heme in the 2-fold channel. B. Salt bridges shown to be necessary for twelve dimers to come together in

formation of the 24mer. C. The 24meric structure, with each monomer coloured individually. The 3- and 4-fold channels are both labelled. Figures adapted from PDB 2VXI (Willies *et al.*, 2009).

The general function of ferritins is to catalyse the oxidation of $Fe^{2+}$ and reversibly store the resultant $Fe^{3+}$ as an oxy-hydroxide mineral in the core of the protein structure (Pfaffen *et al.*, 2015). The amount of phosphate present in these minerals varies depending on the organism, and, in the case of multicellular organisms, the tissue; bacterial ferritins tend to contain greater ratios of iron to phosphate (1.1:1), and mammalian ferritin cores tend to be more crystalline in nature, with the iron: phosphate ratio typically being lower than 10:1 (Aitken-Rogers *et al.*, 2004). The capacity of this biomineralization process is impressive, being able to accommodate up to 4500 iron atoms in the central cavity in this manner (Harrison, 1979). It should be noted that this iron capacity is rarely reached *in vivo* (Tatur *et al.*, 2006) As such, ferritins act as a buffer against the toxicity of free iron, and provide a source of available iron for anabolic processes (Aitken-Rogers *et al.*, 2004). The large cavity space within ferritins and their stability has made them a point of interest for medical researchers utilising them as protein nanocages for the delivery of drug molecules; for example, the poor stability and solubility of cisplatin can be improved using ferritin encapsulation (Falvo *et al.*, 2013).

The nature of the mineral inside the ferritin shells has been found to be polyphasic; the ratio of ferrihydrite, magnetite and hematite has been demonstrated to very depending on the iron loading. Healthy horse spleen, human liver and brain ferritins showed the cores are made up predominantly of singular nanocrystals containing hexagonal ferrihydrite and some hematite, with a small amount of cubic magnetite and maghemite. Human brain ferritins taken from patients diagnosed with progressive supranuclear palsy (PSP) and AD have a face-centred

cubic structure that is highly disordered like wustite, and a cubic magnetite phase (Quintana, Cowley and Marhic, 2004). Ferrihydrite is a ferric oxide, whilst magnetite is a mixed ferric-ferrous oxide; this suggests incomplete oxidation of the iron at the ferroxidase centre, and a dysfunctionality in the protein. It was proven however, that raised levels of free ferrous iron in the brain is not caused by magnetite in ferritin (Galvez *et al.*, 2008). Fig. 1.3 shows how a fully formed ferritin core is structured.

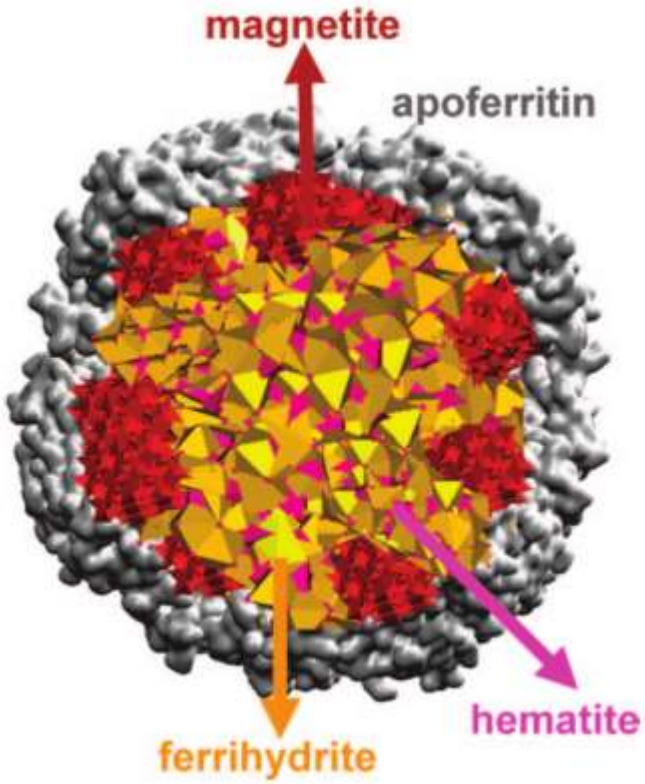


**Fig. 1.3.** The polyphasic arrangement of the mineral core of ferritin. At high iron loadings, ferrihydrite dominates while the surface is primarily magnetite. Diagram from (Galvez *et al.*, 2008).

The 24 subunits are arranged with 4,3,2 symmetry, assembled from 12 dimers, with channels running through the protein shell at the symmetry axes (Bradley, Moore and Le Brun, 2014). These channels are named corresponding to the number of subunits in contact with the channel.

Eight 3-fold channels are lined with hydrophilic residues leading into the interior of the shell, while six 4-fold channels are predominantly hydrophobic (Lee *et al.*, 1994). An example of each channel has been highlighted in Fig. 1.2C. The 3-fold channels have been established as the route through which $Fe^{2+}$ enters the shell in frog M ferritin (Tosha *et al.*, 2010). There are a number of conserved residues; a leucine, an arginine, and an aspartate, that act as a gate over the 3-fold channel, preventing $Fe^{2+}$ from leaving the ferritin. These pores are likely controlled by biological regulators, and protect the core from cellular reductants (like reduced flavin) until iron is required (Theil, Liu and Tosha, 2008). The 4-fold channels have been suggested to be involved in the diffusion of $O_2$ and $H_2O_2$ (Liu and Theil, 2005). Experiments on human H-chain ferritin (HuHF) replaced Asp131 and Glu134, key residues at the narrowest point in these channels, causing a 50% decrease in both iron uptake from ferrous solution and ferroxidase activity, and resulting in a loss of at least two metal binding sites in the cavity (Levi *et al.*, 1996).

**Ferroxidase centres**

Ferritins contain a dinuclear metal binding site called a ferroxidase centre (FC) which can be necessary for nucleation of the iron mineral in some ferritins, and rapidly increases the rate of iron uptake in the early stages (Baaghil *et al.*, 2003). This centre has been accepted to be unstable in most ferritins, but this claim has been challenged in recent years (Hagen, Hagedoorn and Honarmand Ebrahimi, 2017). FCs are fundamental to the action of most ferritins and have structural differences that can easily be sorted into three different types, which will be discussed below. Where the FC does not act as its own nucleation site, a number of cavity-exposed

carboxyl residues aid the hydrolysis of ferric iron complexes to form an insoluble mineral (Finazzi and Arosio, 2014).

Typically, there are three observable phases associated with $Fe^{2+}$ oxidation in ferritins: the first is the binding of $Fe^{2+}$ to the protein; this has been observed spectrophotometrically in *E. coli* BFR by monitoring the perturbation of the heme group (Le Brun, Wilson, *et al.*, 1993). The second phase is a rapid $Fe^{2+}$ oxidation phase, which occurs at the FC. The third, slowest phase is mineralisation, where iron is stored in the central cavity.

All known FCs can be classified as one of three different types: (H)eavy-chain-type, Ftn-type, or BFR-type. H-chain-type ferritins are generally found in higher order organisms like plants and animals, while prokaryotes contain Ftn-type and BFR-type ferritins (Le Brun *et al.*, 2010).

**Mammalian ferritins**

Vertebrate ferritins are the most widely studied of all ferritins (Bradley, Moore and Le Brun, 2014). *In vivo* mammalian ferritins tend to be heterooligomeric, with the proportion of 'H-chain-type' and 'Light-chain-type'' subunits varying based on the iron status of the cell, and between organs and species (Balla *et al.*, 1992). L-chain-type subunits do not contain FCs, but possess carboxylate-rich regions ideal for nucleation of the mineral core. These nucleation sites are important for ferritins, with it being demonstrated that they are sufficient to drive iron mineralisation following spontaneous iron hydrolysis; H-chain ferritins were less efficient than L-chain homopolymers at building up large iron cores at neutral or alkaline pH, where FC-independent iron oxidation can occur (Levi *et al.*, 1994). In acidic conditions, however, competition assays where equimolar concentrations of H-chain and L-chain ferritin are mixed

with iron, L-chain's nucleation efficiency is sufficiently high enough to build a core using some of the iron that is oxidized by the H-chain homopolymers (Levi *et al.*, 1992).

In plants there are also two subunit types, but these are both relatable to mammalian H-chain-type FCs, with one having an FC identical to mammalian H-chain-type and the centre of the other differing by a single residue (Li, Hu and Zhao, 2009). There is also an M-chain subunit that is only found in frogs, which also contains an active FC. The structure of the ferroxidase centre of human H-chain ferritin (HuHF) has long been established and is shown below in Fig. 1.4.

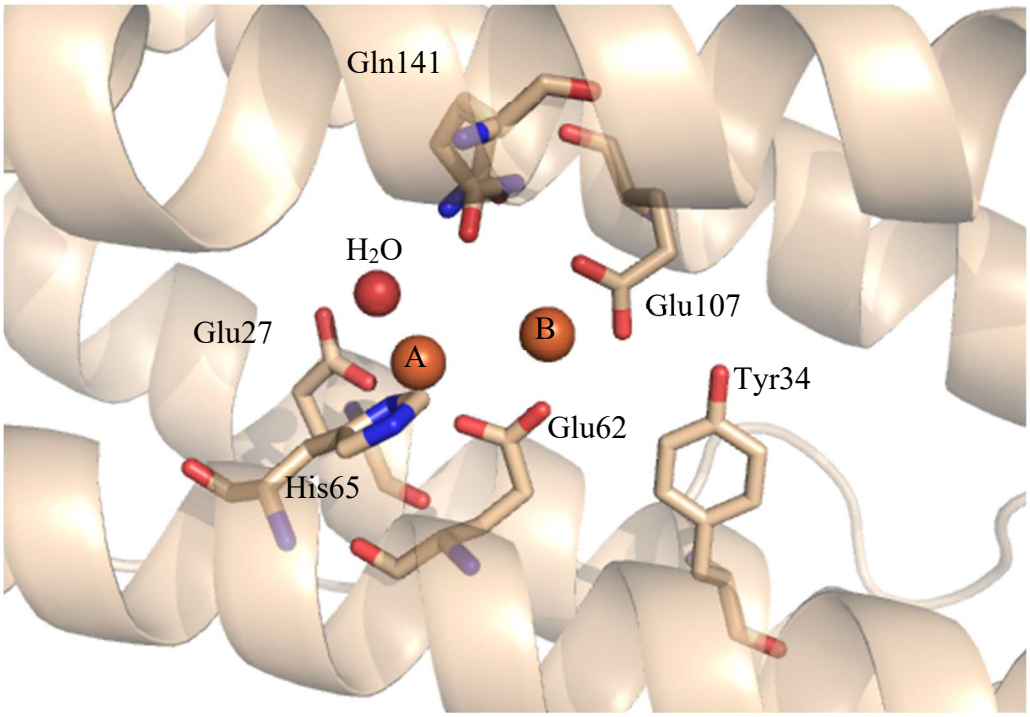


**Fig. 1.4.** The ferroxidase centre of HuHF, highlighting the iron binding sites and key coordinating/ adjacent residues. A water molecule stabilized by Glu27 is shown. Adapted from PDB 4ZJK (Pozzi *et al.*, 2015).

$Fe_A$ is singularly coordinated by Glu27 and His65. Glu62 acts as a bridging ligand between the two metal centres. The $Fe_B$ site is bound by the bidentate ligand Glu107. This site has a lower

occupancy than the $Fe_A$ site. A water molecule is stabilized by the $Fe_A$ site and hydrogen bonding with the Glu27 and Gln141 residues. The two iron atoms are separated by a distance of 3.48 Å (Pozzi *et al.*, 2015).

The FC's role in mineralisation was determined through the study of homopolymers of HuHF, rather than the heteropolymeric 24mers that incorporate L-chain-type (HuLF) ferritin subunits. As mentioned above, the entry of $Fe^{2+}$ occurs through three-fold channels. These are gated by Arg72 and Asp122, two residues that are conserved among H-chain ferritins (Theil, Liu and Tosha, 2008). These residues adopt different conformations under different conditions and may possibly be controlled by molecular regulators *in vivo*. Two $Fe^{2+}$ ions bind at the FCs; the $Fe_A$ site has a higher affinity than the $Fe_B$ site (Ebrahimi *et al.*, 2016). The ions are each oxidized by $O_2$, which forms $H_2O_2$ as shown in Eq. 1.6 (Jameson *et al.*, 2002):

$$2Fe^{2+} + O_2 + 2H^+ \rightarrow 2Fe^{3+} + H_2O_2 \qquad (1.6)$$

A blue diferric-peroxo (DFP) species is formed which has an absorption peak at 650 nm (Treffry *et al.*, 1995). This has been found in many ferritins, and it can be speculated to be transiently formed in all H-chain ferritins, even in those where it is not observed. This has been universally accepted since 1995 to be a μ-1,2-peroxo species, but a recent hypothesis has become popular which suggests that this blue species is actually a η2-peroxo species instead (Ebrahimi *et al.*, 2016). In any case, this breaks down to form a μ-1,2-oxodiferric species, which is observed in most, if not all diferric crystal structures (Fig. 1.5).

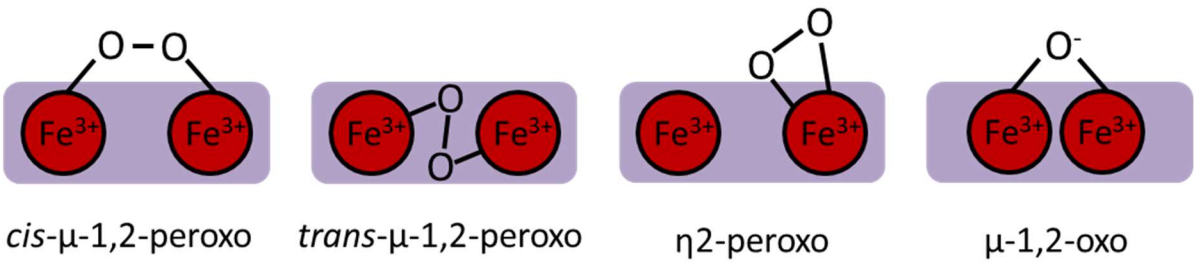


**Fig. 1.5.** Peroxo-diferric intermediates hypothesised to form in the oxidation of $Fe^{2+}$ by iron in ferritins, and their resultant oxo-product. The μ-1, 2-peroxo species (Treffry *et al.*, 1995) has long been accepted, but with the emergence of the unified mechanism theory, the η2-peroxo is becoming more established.

The next step is generally regarded to be that the bridged metal ion pair move into the central cavity, where the iron is hydrolysed and added to the mineral core, as shown in Eq. 1.7 (Yang *et al.*, 1998):

$$4Fe^{3+} + 8H_2O \rightarrow 4FeOOH_{(core)} + 12H^+ \quad (1.7)$$

Equations 1.6 and 1.7 combine to give the overall reaction described in Eq. 1.8:

$$4Fe^{2+} + O_2 + 6H_2O \rightarrow 4FeOOH_{(core)} + 8H^+ \quad (1.8)$$

However, the alternative mechanism (utilising the η2-peroxo species) has been suggested where only one ferric iron atom leaves the FC; the lower affinity $Fe_B$ site releases its ligated $Fe^{3+}$ into a third iron binding site, and a new $Fe^{2+}$ atom replaces it (Appendix 1). This suggestion is supported by EPR studies, where anaerobically adding $Fe^{2+}$ to a diferric FC in HuHF yields a mixed-valent FC (MVFC) (Honarmand Ebrahimi *et al.*, 2012). Furthermore, a MVFC was observed in rapid freeze quench (RFQ, see Materials and Methods) experiments on horse spleen ferritin, reaching detectable concentrations within the first second of the reaction (Sun and Chasteen, 1994). The argument for the universal existence of a third iron binding site in

the FCs of all ferritin species is gaining widespread approval, but remains controversial (Ebrahimi *et al.*, 2016). Indeed, time-resolved X-ray crystallography indicates a third iron atom bound by Glu58 and Glu61 in such a way that this iron is situated directly over the aromatic ring of the Tyr34 residue. These residues lie at the end of the three-fold, 15 Å hydrophilic channel, which was shown to have several iron binding sites within it (Pozzi *et al.*, 2015). The existence of third iron binding site (in addition to a single tyrosine residue) would allow a single $O_2$ molecule to be oxidized to water at a single FC to avoid ROS. This would avoid the problems that arise when trying to thermodynamically justify how diiron clusters are released from the FC (Hagen, Hagedoorn and Honarmand Ebrahimi, 2017). However, this iron binding site cannot be compared to the $Fe_C$ shown in Fig. 1.7, and is likely just a conduit to the FC (Bradley, Moore and Le Brun, 2017). The latter hypothesis is supported by other crystal structures showing Glu61 in two conformations, either binding to $Fe_B$ or facing towards the channel (Lawson *et al.*, 1991).

After an initial reaction with $Fe^{2+}$, HuHF recovers ≈ 65 % of its rapid phase FC activity after 40 mins when mixed with successive iron additions (Bou-Abdallah *et al.*, 2005). This implies that the FC has a low affinity for ferric iron, which eventually leaves the site and moves into the central cavity. HuHF is also capable of performing a detoxification reaction at the mineral core to remove $H_2O_2$, and thus prevent oxidative stress. This reaction is shown in Eq. 1.9 below.

$$2Fe^{2+} + H_2O_2 + 2H_2O \rightarrow 2FeOOH_{(core)} + 4H^+ \qquad (1.9)$$

The native mechanism of iron release in eukaryotic ferritins has been subject to speculation. Early proposals suggested that reagents would directly interact with the crystalline core of the protein (Harrison *et al.*, 1974). Indeed, several means of iron release have been demonstrated, but most of these have been shown to be undesirable. Xanthine oxidase was one of the earliest methods found to remove iron from ferritin while keeping the 24meric shell intact (Mazur *et*

*al.*, 1958). Later work explained this; superoxide generated through free metal-catalysed oxidation could reduce ferritin iron, which was shown to cause oxidative damage (Reif, 1992). This has been hypothesised to play a role in the pathogenesis of rheumatoid arthritis (RA); superoxide is produced by polymorphonuclear leucocytes in synovial fluid which form hydroxyl radicals in the presence of free iron. As such superoxide is both able to increase the amount of ROS and its own toxicity by releasing iron from ferritins (Biemond *et al.*, 1988). Arsenic-containing-compounds are suggested to be toxic due to their ability to drive iron release and lead to the formation of ROS (Ahmad, Kitchin and Cullen, 2000). Nitric oxide generation can induce the release of iron from horse spleen ferritin (Reif and Simmons, 1990).

*Beneckea harveyi* NAD(P)H: flavin oxidoreductase was used to maintain a constant concentration of dihydroflavin which could rapidly release all iron from the core of horse ferritins. Iron release performed in this manner was approximately two times faster from the L-chain rich spleen ferritin than from ferritin isolated from the heart, which has a larger proportion of H-chain subunits (Boyer, Clark and LaRoche, 1988). Catecholamine analogues have also been associated with iron release; 6-hydroxydopamine is able to drive iron release from ferritins at a rate over 100 times faster than that which can be achieved by physiological reductants ascorbate or glutathione (Monteiro and Winterbourn, 1989).

**Mitochondrial ferritin and its function**

In addition to H-chain and L-chain ferritins, another type of mammalian ferritin was discovered relatively recently (Levi *et al.*, 2001). Unlike most ferritins, which are cytosolic proteins, this new protein was found within the matrices of human mitochondria. An analogue of this mitochondrial ferritin (FtMt) was found to be present in primate and rodent mitochondria

(Campanella *et al.*, 2004). This was the first example of a mammalian ferritin specifically targeted to an organelle. The mitochondria are notable for their high iron throughput (roughly 80 % of an organism's iron intake), being the production site of heme prosthetic groups (Horowitz and Greenamyre, 2010) and iron-sulfur clusters within the cell (Mena *et al.*, 2015). A 'kiss and run' fusion mechanism has been described in developing erythroid cells (Chen and Paw, 2012) (Ponka, 1997). This refers to the highly transient interaction between the membranes of the mitochondria and endosomes, where the endosome only partially binds for long enough for iron to exchange from vesicular transferrin to the mitochondria (Bonkovsky *et al.*, 1996). Thus, mitochondrial iron levels are in constant flux, and the high rate of iron usage means that FtMt would be expected to have different requirements in the mitochondria than in the cytosol. Increases in free mitochondrial iron has been associated with a range of conditions, particularly Friedrich's ataxia (Babcock, 1997) while the upregulation of FtMt has been observed in response to sideroblastic anaemia (Levi *et al.*, 2001). Excess iron is suggested to inhibit mitochondrial function in an supplementary mechanism separate to oxidative stress (Tan, 2001).

FtMt is not found in high concentrations in iron storage organs, like the liver (De Domenico, McVey Ward and Kaplan, 2008) which tend to have higher concentrations of cytosolic ferritins (Corsi *et al.*, 2002). Instead, it is expressed at high volumes in the testes, but not the brain (Levi *et al.*, 2001). This is interesting given that both of these tissues contain large numbers of mitochondria (Smirnova *et al.*, 1998).

FtMt expression levels increase with FtMt iron loading, but counter-intuitively, there is no IRE upstream of the coding region in the FtMt gene (Levi *et al.*, 2001). It has been shown that if heme synthesis is disrupted in HeLa cells, FtMt is upregulated, and accounts for all mitochondrial iron. (Corsi *et al.*, 2002). This same work showed that FtMt was found to incorporate iron more slowly in the cytoplasm than in the mitochondria, where in the latter it

oxidized iron more efficiently than HuHF. This is likely due to different iron chelators present in each environment. It was later shown that FtMt was regulated at the transcriptional level, being upregulated by transcription factors SP1, CREB and YY1, and inhibited by GATA2, FoxA1 and C/EBPβ. The authors indicated the activation of the FtMt gene in response to oxidative stress, and its repression in cells that were not metabolically active (Guaraldo *et al.*, 2016). This is likely because when FtMt is expressed, there are lower levels of cytosolic iron (Nie, 2005) and an increase in the number of transferrin receptors. High levels of FtMt was also linked with increased apoptosis and reduced heme synthesis (Santambrogio *et al.*, 2011). As such, FtMt has the potential to be disruptive to the cellular iron distribution, and can cause iron deprivation when expressed unnecessarily.

FtMt was found to be both sequentially and structurally similar to HuHF, with a higher occupation of the $Fe_A$ site than the $Fe_B$ site. The protein is 30 kDa in length as expressed with a mitochondrial targeting sequence which directs the protein to the mitochondrial matrices. This is cleaved *in vivo* to yield a 22 kDa subunit which forms the 24meric shells typical of ferritins (Levi *et al.*, 2001). The protein has a nine-amino acid N-terminal extension relative to HuHF; removal of this sequence gives 79 % sequence homology between HuHF and FtMt. Removal of this N-terminal extension (referred to in this thesis as the Δ9 FtMt variant) lowers protein stability due to these residues' involvement in intra- and interchain bonding interactions (Langlois d'Estaintot *et al.*, 2004).

The FCs of HuHF and FtMt are nearly identical except for Ser144, which binds to the $Fe_B$ site in FtMt. Crystal structures show this residue can be found in two conformations, with one facing away from the FC (Fig. 1.6). Metal binding sites analogous to those in HuHF were found in the three-fold channels, while an iron nucleation site similar to that found in HuLF was found on the inner site. Thus, FtMt is distinct from cytosolic mammalian ferritin in that it functions as a homopolymer which possesses both a FC and a nucleation site on a single subunit. If

denatured and renatured in the presence of equimolar concentrations of HuHF or HuLF, FtMt readily forms hybrid ferritin 24mers (Langlois d'Estaintot *et al.*, 2004).

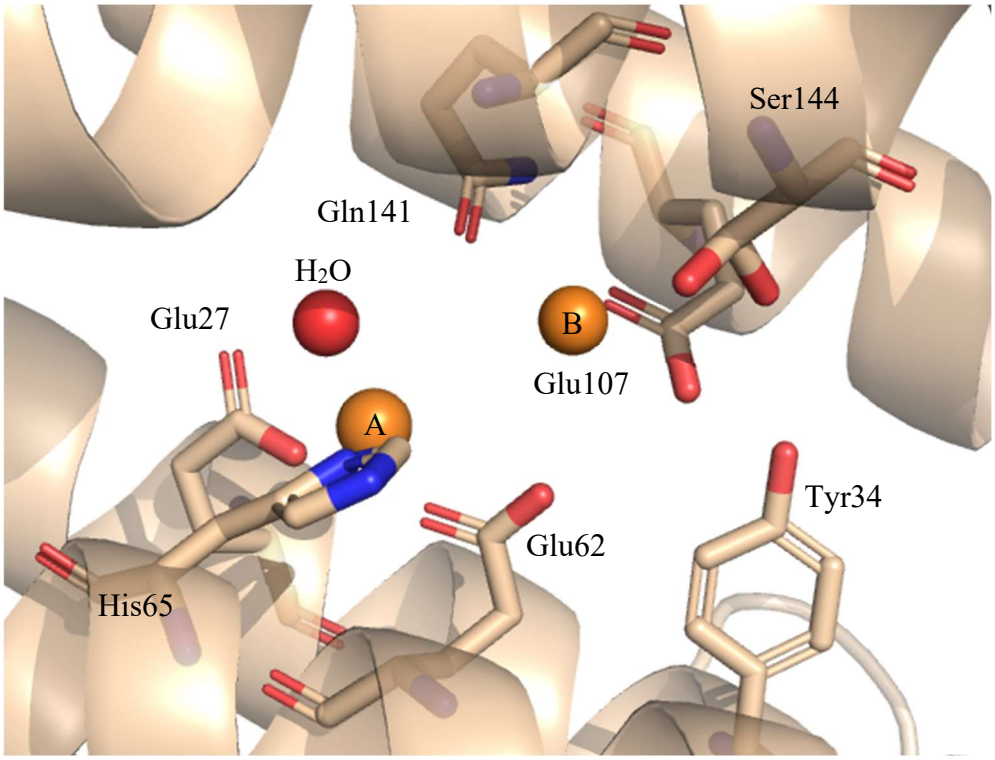


**Fig. 1.6.** The ferroxidase centre of FtMt, highlighting the iron binding sites and key coordinating/ adjacent residues. A water molecule stabilized by Glu27 is shown. Adapted from PDB 1R03 (Langlois d'Estaintot *et al.*, 2004).

Despite the remarkable resemblance of FtMt's FC to that of HuHF, the rates of iron oxidation are much slower; the ferroxidase activity was only 41 % of that observed in HuHF (Langlois d'Estaintot *et al.*, 2004), and does not appear to regenerate its rapid $Fe^{2+}$ oxidation phase at all with subsequent additions of $Fe^{2+}$. Furthermore, unlike HuHF, which can bind up to 48 $Fe^{2+}$/24mer (i.e. two $Fe^{2+}$ at each FC), FtMt is only able to bind 24 $Fe^{2+}$/24mer. This may imply that only half of the FCs in FtMt bind $Fe^{2+}$ which is indicated to be due either to ferrous iron's low affinity for the FC or to a negative cooperativity effect. This cannot be explained by each

FC only binding a single iron, as there is not a large EPR signal attributable to $Fe^{3+}$ at g =4.3 following iron oxidation (Bou-Abdallah *et al.*, 2005). Faster rates of FC activity, and the ability to regenerate 30 % of the FC's rapid phase could be restored in subsequent iron additions through an S144A substitution (alanine is the corresponding residue in HuHF). Furthermore, the S144A variant is able to concurrently form 24 DFP species per 24mer, as opposed to just 12 (Bou-Abdallah *et al.*, 2005). This is probably because the S144A variant has a higher occupancy of the $Fe_B$ site (Langlois d'Estaintot *et al.*, 2004).

When incubated with equimolar concentrations of apo-HuHF at pH 7.0 in the presence of free $Fe^{2+}$, FtMt was found to incorporate similar amounts of iron (Levi *et al.*, 2001). It is not clear why this is the case; it could possibly be that the FC in HuHF has a much faster rate of $Fe^{2+}$ oxidation, but no nucleation site. Ferric iron may leave the HuHF shell and bind to FtMt's nucleation site, forming a mineral core. FtMt has a sigmoidal mineralisation curve that is indicative of an autocatalytic mineral core (Bou-Abdallah *et al.*, 2005). As such, it may be that FtMt can act like an L-chain type ferritin when in the presence of HuHF.

To understand the specialised function of FtMt, several key points are important. Upregulation of FtMt in mammalian cells caused a shift of iron from cytosol to the mitochondria. (Campanella *et al.*, 2009). The truncated Δ9 FtMt variant has an unaltered FC relative to the WT FtMt, and incorporates iron similarly to HuHF (Levi *et al.*, 2001). The only difference between Δ9 FtMt and HuHF's coordination sphere is S144 in FtMt, where in the latter the residue is an alanine and thus does not bind to the $Fe_B$ site. S144 is thus proposed to keep iron in the FC, where it is more accessible to iron chelators; iron that is bound in the mineral core is inaccessible to biological iron chelators, like transferrin (Honarmand Ebrahimi *et al.*, 2012). This makes sense given the large fluctuations in iron levels that will occur in the mitochondria.

FtMt can be compared to frataxin, a mitochondrion-localised, 60meric iron-chaperone protein where reduced expression causes Friedrich's ataxia in humans. Frataxin does not self-assemble, but forms the multimeric structure in the presence of $Fe^{2+}$ (Adamec *et al.*, 2000). Cells deficient in frataxin show reduced iron-sulfur cluster (Fe-S) protein activity; interactions between frataxin and the Fe-S protein aconitase show that frataxin donates an iron atom to the inactive $[3Fe\text{-}4S]^{1+}$ aconitase cluster to reactivate it (Bulteau *et al.*, 2004). In frataxin-deficient HeLa cells, there was a severe inhibition of growth, aconitase and superoxide dismutase-2 activity which were all restored to WT levels when the expression of FtMt was induced (Zanella *et al.*, 2008). The upregulation of FtMt could therefore be a possible therapeutic approach for Friedrich's Ataxia; indeed, there has already been some promising results in the fibroblasts of afflicted patients (Campanella *et al.*, 2009).

Unlike ferritins, a frataxin homologue is also found in yeasts; when frataxin is genetically inactivated in these microorganisms, mitochondrial iron accumulates and the cells become hypersensitive to oxidative stress (Adamec *et al.*, 2000). Expressing FtMt in these cells restored WT functionality, preventing mitochondrial iron overload and restoring cell resistance to $H_2O_2$ (Campanella *et al.*, 2004). The extent to which FtMt was effective in replacing frataxin in yeasts, which do not have any ferritin in their genome is outstanding. It is unclear if other ferritins would be able to replace frataxin's role in a similar fashion.

In HeLa cells which were incubated with $H_2O_2$ and Antimycin A (an uncoupling inhibitor of the respiration chain in the mitochondria which produces ROS), upregulation of FtMt reduced oxidative stress while increasing the activity of mitochondrial Fe-S enzymes and the level of ATP found within the cell (Campanella *et al.*, 2009).

The replaceability of frataxin with FtMt is notable, but they are not interchangeable- mice that lack HuHF or frataxin are not viable, but those that lack FtMt show no significant defects and

have normal lifespans (Bartnikas *et al.*, 2010). However, when exposed to doxorubicin, an anthracycline that catalytically produces ROS when exposed to free iron (Minotti *et al.*, 2004), severe mitochondrial damage was observed, and every mouse died (Maccarinelli *et al.*, 2014). Other work has shown that FtMt is upregulated in rat heart cells to protect against doxorubicin treatment (Ichikawa *et al.*, 2014). The reduced ability for cells to mobilise iron due to doxorubicin treatment had previously been attributed to the lysosomal degradation of cytosolic ferritins (Xu, Persson and Richardson, 2005), but in the same year, published work showed that FtMt upregulation alone can account for the observed reduction in iron mobilisation (Nie, 2005).

Thus, the evidence for FtMt's role as an oxidative stress protectant is overwhelmingly clear, but the increased activity of Fe-S proteins as a result of FtMt expression in frataxin-deficient cells shows that the protein can also substitute for frataxin's ability to keep iron readily accessible to mitochondrial proteins. This is made possible by the S144 residue which increases the occupancy of iron at the $Fe_B$ site, ensuring a greater amount of accessible iron within the mitochondria.

The high similarity between HuHF and FtMt has led to the assumption that their structure and mechanism would be the same; there have been very few structural and mechanistic studies of the protein since its discovery, most or possibly all of which have been discussed so far. None of the iron-bound structures currently published show the route of entry into the protein. The molecular basis of FtMt function is an important aspect of potentially developing therapies based on FtMt upregulation in mitochondrial disease sufferers.

**Bacterial ferritins**

While Ftns have been referred to as 'bacterial' or 'prokaryotic' ferritins in the past, the discovery of an Ftn in archaea (Le Brun *et al.*, 2010) and a planktonic diatom showed that this distinction was inaccurate (Pfaffen *et al.*, 2013). As such, they are often simply referred to as Ftn-type ferritins, or Ftns.

Ftns bear semblance to H chain ferritin subunits, but differ at the $Fe_B$ site, where an additional glutamate ligand (Glu130) is bound in addition to the two found in mammalian ferritins. This additional glutamate bridges the $Fe_B$ and $Fe_C$ sites. A third iron binding site $Fe_c$ has been clearly identified in Ftns (Hempstead *et al.*, 1994). This $Fe_C$ site has long been thought to be the key distinguishing feature of Ftns, with their absence in mammalian ferritins not being controversial until recently. The $Fe_C$ site is proposed to be for keeping a small amount of iron more rapidly accessible to the cell than that mineralised in the core (see Fig. 1.7), however its purpose is a point of conjecture (Bradley, Moore and Le Brun, 2014). The $Fe_C$ site has been noted in some proteins to increase the $Fe:O_2$ ratio from 2:1 to 4:1. It has also been hypothesised that this site has functionally distinct roles between species; there are reports that suggest that the $Fe_C$ in *E. coli* FtnA participates in FC $Fe^{2+}$ oxidation (yielding a higher $Fe:O_2$ ratio) and prevents the egress of iron from the FC. Given that the rates of iron oxidation and mineralisation are not substantially affected by the removal of the $Fe_C$ site, it appears that site C exists here to influence the oxidation intermediates and keep iron accessible by retaining it in the FC (Treffry *et al.*, 1998). In the hyperthermophilic, archaeal *Pyrococcus furiosus* Ftn the $Fe_C$ site and the adjacent Tyr24 allow for the simultaneous oxidation of three iron atoms. Removal of the $Fe_C$ site in this Ftn showed that site C is essential for mineralisation (Ebrahimi, Hagedoorn and Hagen, 2013). It is not immediately clear if the different $Fe:O_2$ stoichiometries

of Ftn species is relevant to their function; *E. coli* FtnA has a stoichiometry of ≈ 3-4: 1 (Bou-Abdallah *et al.*, 2014), *P. furiosus* ≈ 2-3: 1 (Honarmand Ebrahimi *et al.*, 2009) and *P. multiseries* ≈ 2: 1 (Marchetti *et al.*, 2009).

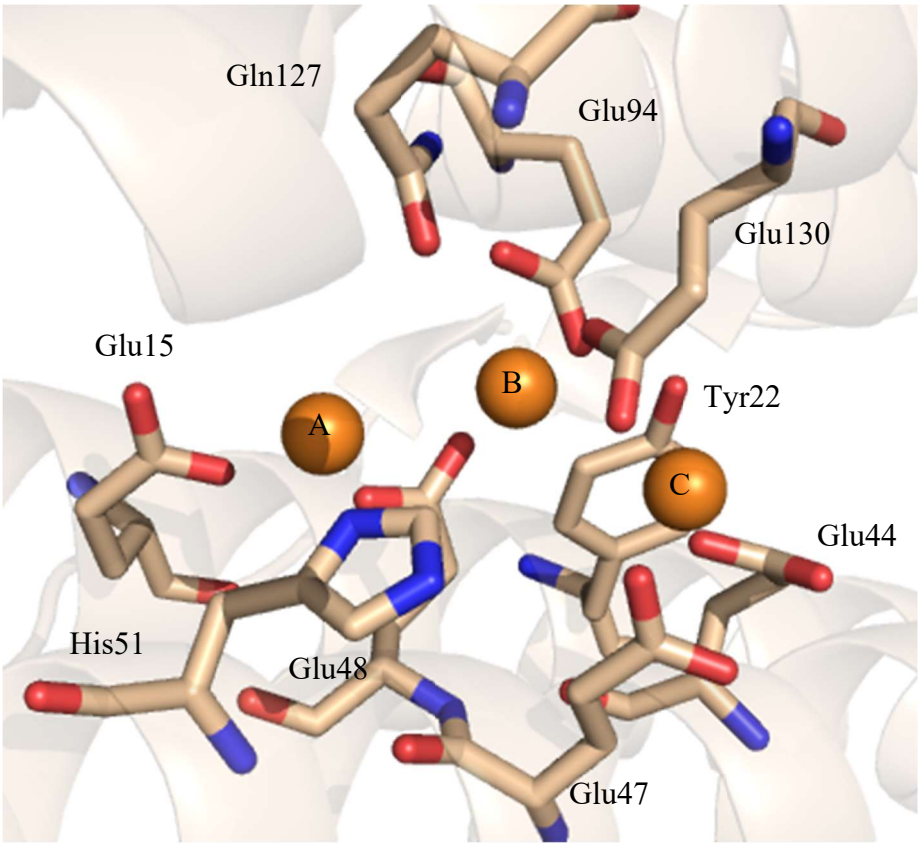


**Fig. 1.7.** The ferroxidase centre of *Pseudo-nitzschia multiseries* Ftn, highlighting the iron binding sites and key adjacent residues. Adapted from PDB 4IWK (Pfaffen *et al.*, 2013).

Each binding site has a different affinity for iron; $Fe_A$ is preferentially occupied to $Fe_B$ or $Fe_C$, with $Fe_B$ having the lowest occupancy (Tatur, Hagen and Matias, 2007). Mixed valence diiron signals have also been reported in Ftn from *P. furiosus*, with EPR-mediated redox titrations suggesting three redox states for the ferroxidase centre (Tatur and Hagen, 2005). These ferritins also proceed via a DFP intermediate similar to that detected in H-chain ferritins (Zhao *et al.*,

1997) (Pereira *et al.*, 1998). In *E. coli* FtnA, this decays to form a μ-oxo-bridged $Fe^{3+}$ dimer which is more stable than that in mammalian ferritins (Treffry *et al.*, 1998).

Iron release from Ftns is not well studied. However, it has been shown to be strongly associated with pupylation, a post-translational modification discovered in *Mycobacterium tuberculosis*. The covalent addition of prokaryotic ubiquitin-like protein (Pup) to lysine residues on proteins signals to the organism that the protein is to be degraded, typically through activation of the proteasome (Pearce *et al.*, 2008). This is analogous to ubiquitination in eukaryotes (Poulsen *et al.*, 2010). Pupylation of ferritin molecules induces ATPases that form ring-shaped complexes (ARCs) to dissemble the 24meric structure without the use of a hydrolytic protease (Küberl, Polen and Bott, 2016). This would likely expose the mineral core to large reductants that would otherwise be unable to access the iron, and allow the organism to utilise it.

Of the ferritin families discussed in this review, Ftns are probably the most diverse in terms of their chemistry. A ferritin has been discovered in cyanobacteria which sequentially appears to have a FC more similar to FtMt than any other Ftns, and more importantly, lacks the $Fe_C$ site which is deemed to be an essential feature of this class of ferritins. This protein has since been called *Syn*Ftn and may prove to be a catalyst for the re-evaluation of how three main classes of ferritins are defined.

**Bacterioferritins**

The FCs of BFRs are the most unique of the three ferritin families. $Fe^{2+}$ is stable enough within the FC that crystal structures have been solved with a diferrous FC (Bradley, Moore and Le Brun, 2014). Evidence exists to support the presence of nucleation centres for biomineralization in BFRs (Malone *et al.*, 2004), suggesting that each subunit contains all

necessary functional features, unlike the more specific H and L chains of mammalian ferritins. While these proteins share extensive similarities in structure, there appears to be key differences that lead to more specialised functions. These do not necessarily align between different organisms; for example, in *E. coli*, an Ftn functions as the primary iron storage protein, whereas in *S. enterica*, a BFR fulfils this role (Velayudhan *et al.*, 2007) (Abdul-Tehrani *et al.*, 1999).

Unlike in other ferritins, in BFRs the FC does not move these two iron atoms into the core, but cycles their oxidation states like a true catalytic centre to drive free $Fe^{3+}$ into the core. The diferric centre is unstable in most ferritins, yet in BFR the diiron centre's 'resting' state appears to be the occupied diferric form (Macedo *et al.*, 2003). These ferric iron ions are closely associated, with the observation of an iron dimer under certain spectroscopic conditions (Le Brun, Cheesman, *et al.*, 1993). The iron binding sites are highly symmetrical, each being ligated with a histidine and a glutamate, with two bridging glutamates between them. In this way, the coordination sphere is closer to that of ribonucleotide reductase than other ferritins (Minnihan, Nocera and Stubbe, 2013). There is no $Fe_C$ site, but an iron binding site coordinated by three water molecules, an aspartate and a histidine lies around 9 Å from the ferroxidase centre (see Fig. 1.8). This is called the inner surface site ($Fe_{IS}$) and has been shown to be important for the transfer of electrons from oxidizing iron in the mineral core to the ferroxidase centre (Crow *et al.*, 2009).

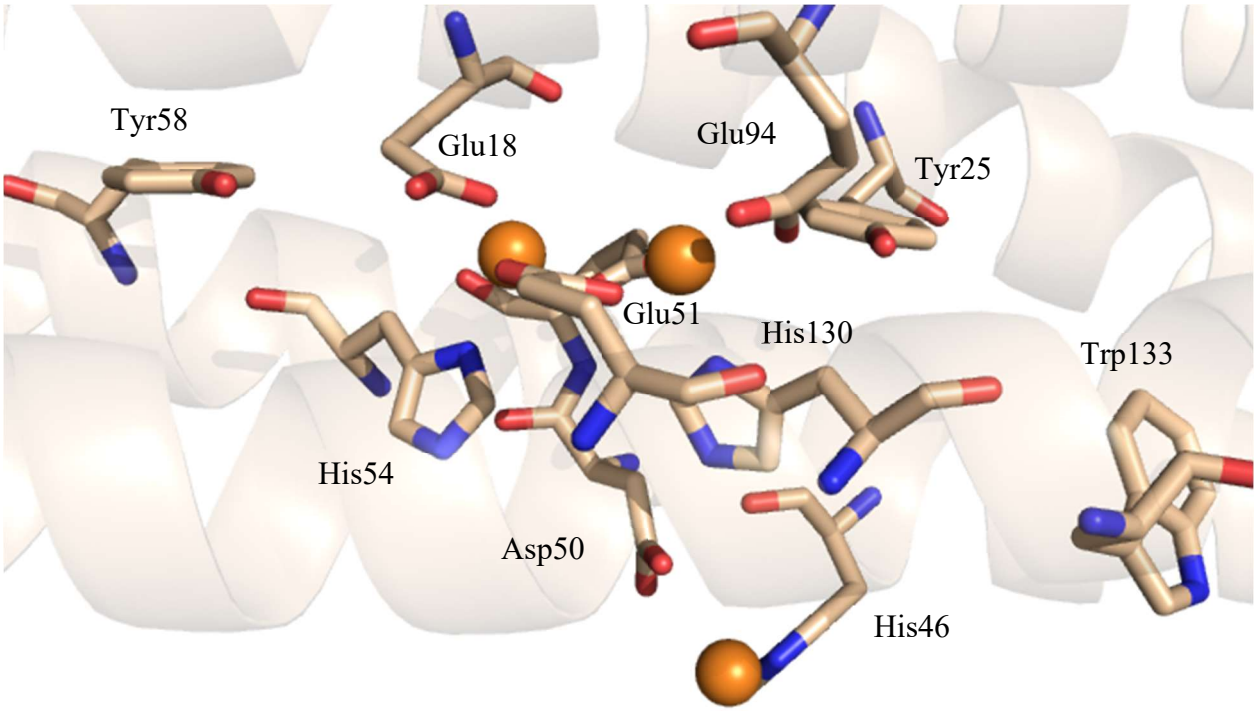


**Fig. 1.8.** The diferrous ferroxidase centre of *E. coli* BFR, highlighting the iron binding sites and key adjacent residues. Glu127 is also coordinating the FC in this diagram in a similar bridging fashion to Glu51, from the opposing side. Adapted from PDB 3E1M (Crow *et al.*, 2009).

In some structures where $Fe^{2+}$ is bound, His130 (the ligand bound to Fe-B) is found in some crystal structures to dissociate from the ferrous iron (Swartz *et al.*, 2006); whether this is significant to the mechanism is not yet clear. In Fig. 1.9, the structure of *E. coli* BFR bound with $Fe^{3+}$ at the FC is shown from above, with a small sphere indicating electron density where there is likely to be an oxygen-containing bridging species, which is unsurprising since the other ferritin classes are accepted to have μ-oxo-bridged diferric products before release from the FC. This is further confirmed by the change in inter-iron distance, with 3.6 Å in the ferric form connected with a μ-oxo/hydroxo bridge, and 4 Å in the ferrous form where the electron density was absent (Bradley, Moore and Le Brun, 2014).

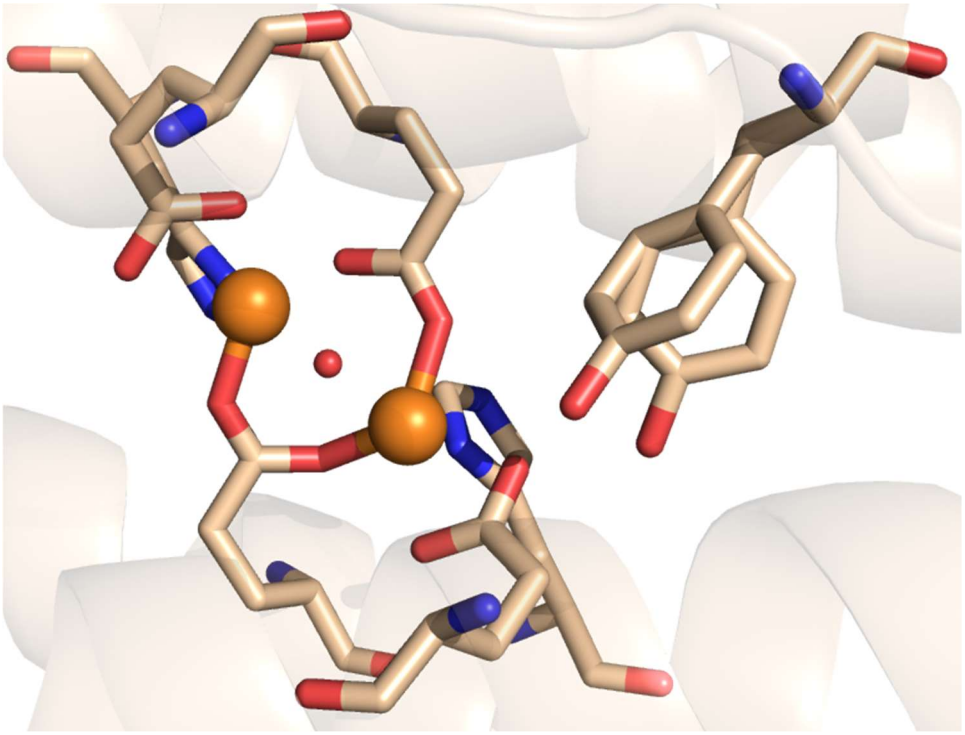

**Fig. 1.9.** The diferric FC of *E. coli* BFR, viewed from a different angle to Fig. 1.8 in order to view the location of the oxo/ hydroxo bridge, denoted here by a red sphere. In this structure, Tyr25 was found in two conformations. Adapted from PDB 3E1N (Crow *et al.*, 2009).

The key distinguishing feature of BFRs is that they contain heme *b* groups between subunit pairs, a characteristic unique to this type of ferritin (Le Brun, Wilson, *et al.*, 1993). These are ligated axially by a single methionine from each subunit (Macedo *et al.*, 2003). The purpose of these heme groups has been unclear until recently; they do not appear to be essential to the aerobic uptake of iron (Baaghil *et al.*, 2003), but it was demonstrated that without heme, BFR was capable of accumulating over four times the amount of iron *in vivo* than when bound with heme (Andrews *et al.*, 1995). Other evidence has shown that heme in BFR decreases the rate of iron oxidation at the ferroxidase centres, but increases the rate of core formation *in vitro* (Wong *et al.*, 2012). This implies that the heme groups increase the bioavailability of iron within BFR to the organism.

These heme groups have been shown to have low reduction potentials (-475 mV) but are significantly more positive before the iron core is present (-225 mV) (Watt *et al.*, 1986). The presence of heme in BFR was indeed shown to increase the rate of iron extraction from the mineral core, independent of the ferroxidase centre (Yasmin *et al.*, 2011). This evidence suggests that the heme could be an intermediate reduction target, allowing electrons to be transported to the core rather than requiring the entrance of the reductants to the interior of the ferritin. This was supported by the finding that in *P. aeruginosa*, BFR-associated ferredoxin shuttles electrons from NADPH to the heme in BFR, which subsequently releases iron (Weeratunga *et al.*, 2009). A crystal structure was published showing that these proteins form a complex, with ferredoxin binding over the two-fold channel within which the heme lies (Rivera, 2017). This is the first and currently only known structure of a ferritin molecule in complex with a physiological protein partner.

The heme group can also be used as a spectroscopic tool to identify iron binding; a small perturbation of the heme group's spectrum occurs when $Fe^{2+}$ binds at the FC (Le Brun, Wilson, *et al.*, 1993). This perturbation supports the notion of a conformational change upon occupation of the FC by iron, rather than the view that ferritin is simply a semipermeable membrane (as put forward by Hagen et. al. (Hagen, Hagedoorn and Honarmand Ebrahimi, 2017)), but does not exclude the possibility that this change is due to an electrostatic effect.

BFR prefers $H_2O_2$ as an oxidant as opposed to $O_2$, forming water as a final product (Bou-Abdallah *et al.*, 2002). The ability to utilise both molecules results in the Fe: $O_2$ stoichiometry strictly being 4:1, rather than the typical 2:1. *D. vulgaris* BFR has been shown to be able to bind DNA and protect it against hydroxyl radical and DNase damage (Timóteo *et al.*, 2012). This is reminiscent of the Dps (DNA-binding protein from starved cells) mini-ferritin, which in several bacterial species has been established to protect DNA from ROS-induced damage through binding DNA (Zhao *et al.*, 2002). These proteins are vital to bacterial pathogens that

lack catalase, such as *Porphyromonas gingivalis*, where Dps protein fulfils the role as a rapid $H_2O_2$ detoxifier (Chiancone *et al.*, 2004).

Although the FC of BFR is more comparable to other diiron proteins than H-chain ferritins, the three kinetic phases associated with mineralisation by ferritins are observable by absorbance spectroscopy (Le Brun, Wilson, *et al.*, 1993). In addition to the iron binding sites having a high and equal level of occupancy, there is evidence to suggest that iron binding to the FC is cooperative (Keech *et al.*, 1997).

The first phase is the reversible binding of $Fe^{2+}$ at the FCs. The second phase is the rapid oxidation of $Fe^{2+}$, leading to a μ-oxo-bridged diferric species in the ferroxidase centre. The third phase is the mineralization of the iron, with iron binding to the inside of the shell and hydrolysis of iron causing the core to grow inwards. Where the iron initially binds within the cavity is unclear, although the $Fe_{IS}$ is a viable and likely candidate. While ferritins have numerous nucleation sites within each 24mer, during the early stages of biomineralization a single centre will tend to dominate, with the majority of the iron centralised around a single site. In addition, depending on how much iron each 24mer reacts with, there can be erratic differences in the amount of iron found within ferritins found in a single sample (Harrison and Arosio, 1996). This makes determining the mechanism of formation and the structural characterization of the core a technically problematic task (Malone *et al.*, 2004).

EPR has already been used to characterise iron metabolism by ferritins; high spin ferric iron in a rhombic coordination has been identified in BFRs from *E. coli* and *R. capsulatus*. In *R. capsulatus* this mononuclear iron was found in two chemically distinct environments (Malone *et al.*, 2004). A similar result was observed in mammalian ferritins (Hanna, Chen and Chasteen, 1991). In *R. capsulatus* BFR the first isoform grew larger with iron loading, but at greater iron loads the second isoform became dominant. Much of the iron added in these BFR experiments

was EPR silent yet could be detected by the addition of desferrioxamine (DFO, an iron chelator) and/ or HCl to break up the polynuclear clusters formed on the protein's nucleation sites. This suggests antiferromagnetic coupling of the iron core. It is not clear where these g=4.3 isoforms arise from; isoform I could be associated with soluble BFR, while isoform II may be bound within precipitated protein. It is also speculated that isoform II could be $Fe^{3+}$ on the edge of polynuclear clusters, where they are unable to magnetically couple to other $Fe^{3+}$ (Malone *et al.*, 2004). Other groups propose that the g = 4.3 signal represents iron that has not been aggregated yet, and that the mineral core can be attributed to a broad signal with a maximum intensity at ≈ g = 6, which disappears for temperatures below 14 K. This suggests that this temperature is the Néel point, and that the core is superparamagnetic (Wajnberg *et al.*, 2001). Superparamagnetism describes the phenomenon where a particle's magnetism can randomly flip direction depending on changes in temperature. This effect has been described in other iron oxides, such as magnetite, ferric green rusts and ferrihydrite (Wajnberg *et al.*, 2001)(Wencka *et al.*, 2009). These iron compounds make up the composition of horse spleen ferritin core, as shown previously in Fig. 1.3.

**Free radicals and their interaction with the ferroxidase centre**

It has already been addressed that tyrosine is found adjacent to the FC; its position is universally conserved among all maxi-ferritins (Ebrahimi, Hagedoorn and Hagen, 2013). In BFRs, a second tyrosine is conserved on the opposite side of the FC (Macedo *et al.*, 2003) (Bradley, Moore and Le Brun, 2014).

The fastest rate observed in ferritins had been attributed to the formation of a $Fe^{3+}$-tyrosinate complex in bullfrog H-chain-type ferritin (Waldo and Theil, 1993), but this was later attributed

to the DFP species discussed and displayed in Fig. 1.5 (Jameson *et al.*, 2002). In any case, a low concentration of tyrosyl radical was found in human and horse spleen ferritin. They were formed as a result of the FC reaction, but radicals could also be found on light-chain type subunits. These non-tyrosyl radicals had a different lineshape and were attributed to hydroxyl radical-damaged histidine (Chen-Barrett *et al.*, 1995). In the early stages of the reaction with H-chain ferritin, an axially symmetric radical forms within the first second which decays quickly. This was not formed through hydroxyl radical damage as neither catalase nor superoxide dismutase prevented its formation (Sun and Chasteen, 1994). The tyrosyl radical seen in HuHF was assigned to the universally conserved Y34, next to the FC, through variant studies. However, there is currently no evidence that the formation of this radical was essential for function (Chen-Barrett *et al.*, 1995).

In Ftns, a free radical was found on the homologous Y24 residue of both E. coli (Bou-Abdallah *et al.*, 2014) and P. furiosus (Honarmand Ebrahimi *et al.*, 2012). The decay of the free radical in E. coli FtnA was slow, decaying over approximately 15 mins. It has been proposed that with the additional electron provided by $Fe^{2+}$ at the $Fe_C$ site, the formation of the tyrosyl radical would allow for the four-electron reduction by the FC of $O_2$ directly to water.

The diiron centres of BFRs have already been highlighted for their similarities to the B2 RNR subunit. RNR is notable for the large tyrosyl radical that forms on Y122, which is remarkably stable at room temperature ($t^{1/2} \approx 3$ days, Atkin *et al.*, 1973). This radical forms after activation of molecular $O_2$ at the diiron centre, the binding of which is stabilized within a hydrophobic pocket in the vicinity of the metallocentres (Ormö *et al.*, 1995). This radical is then transferred over a significant distance ($\approx 35$ Å) to continually generate a cysteine thiyl radical, which is essential for the catalytic reduction of nucleotides to deoxynucleotides (Greene *et al.*, 2017). Despite the similarities of the residues surrounding the metallocentres in BFR and RNR, there

is currently no evidence to suggest that there are long-distance electron transport mechanisms in ferritins.

Unlike in mammalian and Ftn-type ferritins, mineralisation in *E. coli* BFR was found to be dependent on Y25, which was clearly established to be the site of radical formation (Bradley *et al.*, 2015). Mineralisation rates were also hindered by Y58F and W133F substitutions. These redox-active aromatic residues are also in the immediate vicinity of the FC. The rapid phase of $Fe^{2+}$ oxidation (i.e. direct oxidation at the FCs) was not affected in any of these three variants. Free radicals have not been detected on Y58 or W133. It is believed that these three residues act together in an as of yet unknown mechanism to promote mineralisation by ensuring the simultaneous delivery of two electrons from oxidation of iron in the core to the FC (Bradley *et al.*, 2017). It is possible these residues reduce the diferric form of the FC and restore it for further use. The formation and decay of the Y25 radical were noted to both be slower in Y58F and W133F variants relative to the WT (Bradley *et al.*, 2017).

**Research aims**

For several decades, three sub-families of ferritins have been sufficient to accurately characterise and appropriately sort the known ferritins. However, studies of a marine-blooming diatom revealed the first observation of a eukaryotic ferritin to contain an $Fe_C$ site (Pfaffen *et al.*, 2013). FtMt and *Syn*Ftn are both iron storage proteins whose upregulation does not appear to be controlled by IREs. As newer ferritins are discovered which do not adhere to the defined classifications, further work must be carried out to establish how these groupings must be adjusted. This thesis will describe several protocols that were employed to do this.

There is a large body of work describing the mechanisms by which ferritins oxidize iron. But despite this, the process is still not fully understood. Many of the following results will be discussed in the context of the 'unity vs diversity' debate that at the time of writing, is highly topical. As such, a primary goal of this research will be to try and determine the mechanisms of different ferritins and determine whether they are comparable. This can be tested by investigating whether ferritins operate via the same intermediates. Many transient chemical species observed in ferritins, such as DFP species or MVFCs have already been discussed in this chapter, and can be observed optically or using EPR spectroscopy. Also, while research indicates that *E. coli* BFR preferentially utilises $H_2O_2$ as an oxidant, no experiments have ever directly measured the concentration dependence of either oxidant's reactivity at the FC. This thesis describes experimental protocols used to study BFR that could in turn be applied to other ferritins in order to compare their rates and mechanisms in a more comprehensive manner.

# Chapter 2

# Materials and Methods

**Plasmids and proteins from the University of East Anglia**

All bacterioferritin (BFR) plasmids (WT and variants) were generously provided by the Le Brun group at the University of East Anglia. In addition to this, Y25F and Y58F BFR protein stocks were also supplied, along with all *Syn*Ftn, FtMt, HuHF and n-ferritin proteins.

**Transformation of bacteria with plasmid DNA**

Two microcentrifuge tubes containing competent cells of the same strain were thawed on ice before adding 1 µL of the plasmid to one of them and leaving on ice for 20 mins. The cells were then heat-shocked in a water bath at 42˚C for 45 s and stored on ice again for 10 mins. A 1 mL aliquot of preheated LB was added to each sample and incubated for 45 mins at 37˚C while being shaken. A small 25 µL amount of each bacterial culture was plated on Petri dishes containing 25 mL of LB-agar prepared with ampicillin at a concentration of 100 µg/mL.

Success of transformation is confirmed by presence of colonies on the plate containing the transformed bacteria whilst the control plate has no colonies growing on it.

**Expression and purification of bacterioferritin**

*E. coli* strain BL21 (DE3) was used to overexpress BFR, being grown at 37 ˚C in LB. Ampicillin was used in all cell media, at a concentration of 100 μg/mL. An overnight 10 mL starter culture was scaled up to 100 mL for another overnight growth; 5 mL aliquots of this culture were added to 10 x 2 L flasks containing 500 mL media. This was grown to an $OD_{600}$ of 0.6-0.8 before being induced with 25 μM IPTG. After three hours the cells were harvested by centrifuging at 7000 x g, 4 ˚C for 15 min. Cells were lysed using an Emulsiflex, then centrifuged at 35000 x g for 45 mins. The soluble fraction was heated to 65 ˚C for 15 mins, then centrifuged as before. An ammonium sulfate cut of 0.55 g/mL was used to precipitate the BFR, and this was once again centrifuged as above. The protein was re-dissolved in 'BFR Buffer' (20 mM HEPES, 100 mM KCl, 0.1 mM EDTA, pH 7.8) and purified using a Hi Prep 26/60 Sephacryl S-300 HR column. The protein-containing fractions were combined and loaded onto a Hi Trap FF Q Sepharose ion exchange column, then eluted using a gradient with 'Buffer B' (20 mM HEPES, 100 mM KCl, 0.1 mM EDTA, 1 M NaCl, pH 7.8). Iron was removed from this protein by sparging 500 mL MES buffer (100 mM, pH 6.2) with nitrogen gas for 2 hr then adding 3 % w/v sodium dithionite and 1 mg 2, 2' dipyridyl (Bauminger *et al.*, 1991). The protein was dialysed against this solution four times then into 500 mL of 100 mM MES/ 500 μM NaCl (pH 6.2) overnight. Once this protein was dialysed into 100 mM MES (pH 6.5) the protein was ready for spectroscopic measurements.

Protein purity was assessed using 15 % SDS PAGE gels (Fig. 2.1) and by observing the $A_{280}/A_{260}$ ratio. The heme concentration per 24mer could also be identified using an $\varepsilon_{418}$ of 107,000 $M^{-1}$ $cm^{-1}$(Cheesman *et al.*, 1993). Extinction coefficients at 280 nm for a set of BFR variants are reported in Table 2.1.

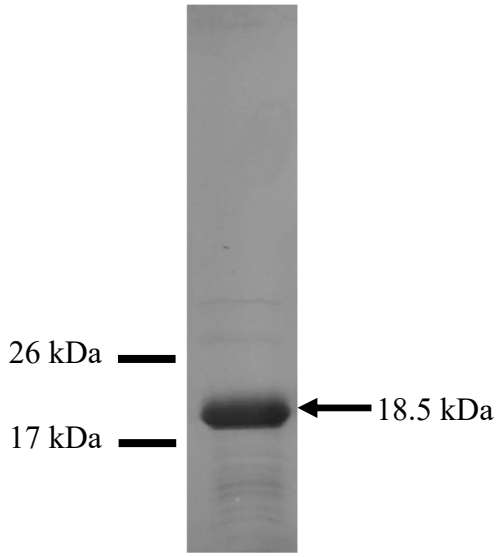


**Fig. 2.1.** An SDS PAGE gel showing the band for BFR. A MW protein ladder (not shown) was used to confirm that the protein was the expected molecular weight.

**Table 2.1**. A summary of the BFR variant proteins expressed at Essex, and the extinction coefficients used to determine their concentration as determined by Bradley *et al.*, 2017.

| Variant | $\varepsilon_{280}$ ($M^{-1}$ $cm^{-1}$) |
|---|---|
| WT | 33,000 |
| Y25F | 25,585 |
| Y58F | 24,600 |
| W35F | 22,300 |
| W133F | 23,375 |
| H46A | 33,000 |
| W35F/ W133F | 18,665 |

Activity of the proteins was tested using an iron mineralisation assay by observing the $A_{340}$ as a function of time when 0.5 μM BFR is mixed with 200 μM $Fe^{2+}$ (Fig. 2.2). The activity of each variant has been reported previously (Bradley *et al.*, 2015).

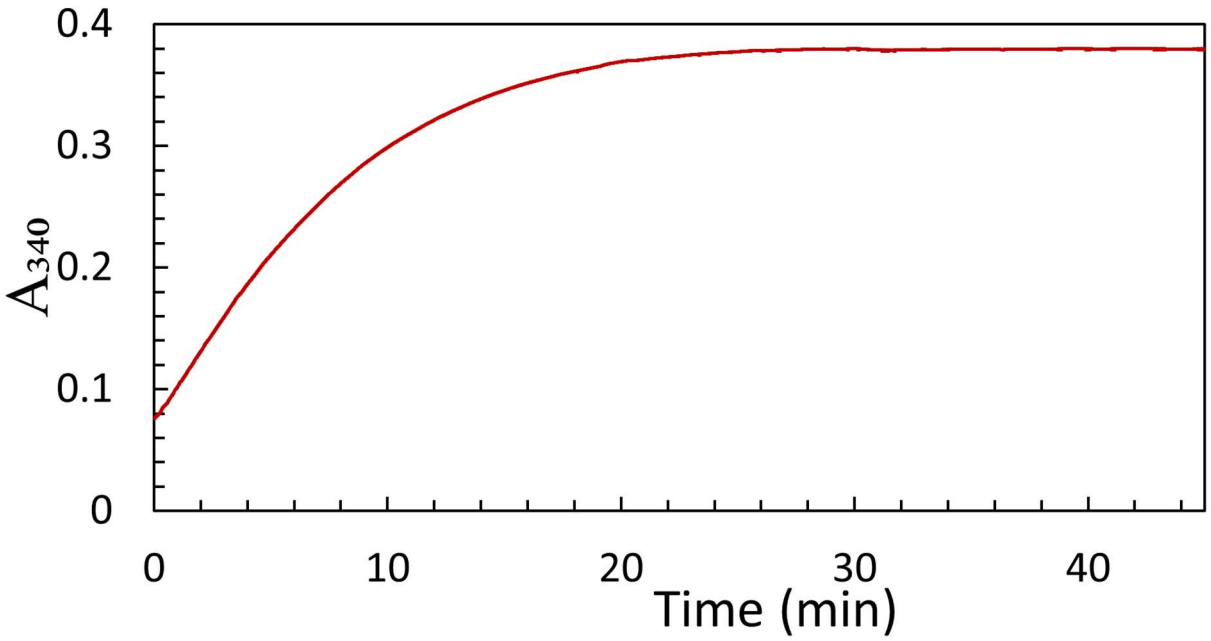


**Fig. 2.2.** An example of the $\Delta A_{340}$ increase showing the oxidation of 200 µM $Fe^{2+}$ by 0.5 µM WT BFR in the presence of $O_2$.

**Preparation of spectroscopy buffer**

Unless stated otherwise, all references to buffer refer to 100 mM 2-(*N*-morpholino)ethanesulfonic acid (MES) that has been adjusted to pH 6.5 using NaOH. The buffer was filtered through a slurry of Chelex beads to remove metal ions prior to use.

**Preparation of anaerobic protein and buffer solutions**

To prepare anaerobic buffer for stopped flow spectroscopy, 100 mM MES (pH 6.5) was added to a tonometer (Fig. 2.3). This was attached to a Schlenk line and cycled several times between a vacuum (to remove gases from solution) and ≈ 10 mm Hg argon. To remove the buffer a

glass syringe is fitted to the outlet and then filled with buffer. The additional outlet is then opened, allowing this buffer to be expelled from the syringe. This is repeated several times to rinse the syringe with anaerobic buffer, reducing $O_2$ contamination. Glass syringes filled with anaerobic buffer were fitted with needles and sealed using a rubber bung.


**Fig. 2.3.** A tonometer used for removing $O_2$ from buffer solutions for stopped flow experiments. The air is first pumped out of the device to a pressure of ≈-60 mm Hg, then the inlet is opened inside a buffer solution, drawing it into the glassware. The blue arrow shows the flow of Ar into/ air out of the tonometer, while the red arrow shows the flow of buffer to wash and fill syringes.

For stopped flow experiments, protein was diluted in a volumetric flask and stoppered with a Suba Seal septum. The solution was made anaerobic on a Schlenk line by cycling between a

vacuum and Ar five times. $Fe^{2+}$ was added under argon. The anaerobic BFR: $Fe^{2+}$ complex was transferred by placing a positive pressure on the volumetric flask with Ar, and slowly drawing the protein solution out into a syringe washed with anaerobic buffer. This syringe was sealed with a rubber bung until it could be fitted to the stopped flow instrument.

$H_2O_2$ was added in small aliquots to anaerobic buffer. In experiments where [$O_2$] was controlled, an $O_2$-saturated solution (typically around 1.2 mM) was made and then diluted with anaerobic buffer as appropriate. The concentration of this $O_2$ solution was determined by using temperature and local atmospheric pressure readings to calculate the solubility of $O_2$ on a given day (Gundersen, Ramsing and Glud, 1998).

For EPR experiments, protein was added to a glass bulb (Fig. 2.4) under flowing argon. This was left for 10-20 mins while occasionally shaking the bulb to remove $O_2$ from the solution. Ferrous ammonium sulfate was added using a plastic cannula through the top of the system. This can then be mixed with $H_2O_2$ or $O_2$-saturated buffer solutions for slow-freeze experiments.


**Fig. 2.4.** A glass bulb used for preparing anaerobic protein solutions for EPR spectroscopy. Protein is placed in the glass bulb, while the orange balloon has a hole in it to act as a valve for gas flow around the system.

**Titrations of protein solutions with $O_2$ or $H_2O_2$ in UV-vis experiments**

A spectrophotometer quartz cuvette sealed with a Suba Seal septum was filled with Ar and weighed. A glass syringe was used to add ≈1 mL degassed protein. The mass of the protein was used to determine the volume of 50 mM $Fe^{2+}$ (dissolved in 50 mM HCl) to add. Aliquots of saturated $O_2$ or degassed $H_2O_2$ solutions in buffer were added using a Hamilton syringe. Spectra were recorded using a Cary Series UV-Vis-NIR Spectrophotometer (Agilent Technologies).

**Stopped flow absorbance spectroscopy**

Degassed protein and $O_2$/ $H_2O_2$ loaded buffer solutions were loaded onto the stopped flow apparatus using gas-tight syringes prepared as described above. An Applied Photophysics DX17MV stopped flow spectrophotometer, capable of being equipped with both photomultiplier and photodiode array (PDA) detectors was used to optical absorbance changes. Photomultiplier experiments were performed at 340 nm and 25˚C unless expressly stated otherwise; this wavelength reports on the oxidation of iron from $Fe^{2+}$ to $Fe^{3+}$ (Bradley *et al.*, 2015).

**Stopped flow experiments in the presence of dye-decolourising peroxidase DtpA**

A mixture of protein and a dye-decolourising peroxidase, DtpA (Chaplin, Wilson and Worrall, 2017) was prepared in 100 mM MES (pH 6.5) and drawn into a glass syringe. This was affixed on the stopped flow instrument alongside a syringe containing $Fe^{2+}$ solutions at selected concentrations. A photodiode array was used to track the oxidation of the ferric resting state of DtpA to compound I (Cp I).

**Isolation of bacterioferritin oligomeric units by size exclusion chromatography**

A concentrated BFR solution (118 μM by 24mer) was loaded onto a Sephadex G-75 size exclusion column, and the fractions were collected and each prepared as described in 'Preparation of anaerobic protein and buffer solutions.'

**Electron paramagnetic resonance spectroscopy**

All spectra were recorded on a Bruker EMX (X-Band) EPR spectrometer. For low-temperature experiments, the machine was equipped with an Oxford Instruments liquid helium system and a spherical high-quality ER 4122 SP 9703 Bruker resonator.

Broad scans between 600 and 4400 G had the following uniform parameters: modulation frequency νM = 100 kHz; modulation amplitude AM = 3 G; scan rate v = 22.6 G/s; time constant τ = 81.92 ms; conversion time, at a 2048 data point scan range, tconv = 81.92 ms. Scans between 3315-3415 G (to attain resolved spectra of the free radical signal) instead had a scan rate v = 0.60 G/s. To measure the mixed-valence ferroxidase centre in addition to the free radical, spectra were measured between 3150-4150 G at a scan rate of 6.0 G/s.

An AquaX (Bruker) capillary system was used with a 4103TM Bruker resonator for room temperature experiments. Spectra were measured between 3477-3547 G with modulation frequency νM = 100 kHz; modulation amplitude AM = 1 G; scan rate v = 3.3 G/s; time constant τ = 10.24 ms; conversion time, at a 2048 data point scan range, tconv = 10.24 ms.

**Preparation of electron paramagnetic resonance samples using 'slow freeze' methodology**

A 250 µL aliquot of protein solution was prepared in an Eppendorf (for anaerobic experiments, 500 µL of protein was placed in a glass bulb instead) at room temperature. A Hamilton syringe was used to line the inner walls of a plastic cannula with a small aliquot of ferrous ammonium sulfate (in anaerobic experiments, the cannula was first flushed with Ar and lined with an aliquot of $H_2O_2$, given that the $Fe^{2+}$ was already anaerobically incubated with the protein). The reaction was started by drawing the protein mixture into the syringe, then dispensing the mixture into an X-band EPR tube. At the desired reaction time, the tube was dropped into methanol cooled by dry ice. Once frozen, the EPR tube was transferred into liquid nitrogen.

**Measuring protein kinetics by slow freezing samples for EPR spectroscopy**

A large volume (1.5- 3 mL) of protein was prepared. $Fe^{2+}$ was added to begin the reaction, then 250 µL aliquots were taken and added to multiple EPR tubes. These were slow-frozen as described above at the desired time intervals to give a complete kinetic series.

**Spin trap experiments with 5,5-dimethyl-1-pyrroline N-oxide**

A homemade mixing device was used to mix equal volumes of two liquid components and fill the AquaX capillary bundle. The dead volume of the mixing device was 130 µL and the minimal volume to be taken by each syringe was 180 µL. The dead time of the mixing device

was 2 s. 5,5-dimethyl-1-pyrroline N-oxide (DMPO, Sigma) was used to spin-trap short-lived radicals in the room temperature experiments. A 228 mM solution of DMPO in water was prepared and filtered over activated charcoal. EPR spectra were recorded before and after this filtration step to measure the removal of paramagnetic impurities. In a typical experiment, a solution of protein with DMPO was mixed with an equal volume of $Fe^{2+}$ so that the final concentrations were as follows: 5.4 μM protein, 40 mM DMPO, 375 μM $Fe^{2+}$- in 100 mM MES buffer, pH 6.5. The reference spectra of the superoxide radical DMPO adduct and hydroxyl radical DMPO adduct were obtained in a xanthine oxidase/xanthine system (0.16 units of xanthine oxidase (Sigma), 0.4 mM xanthine, 100 mM DMPO in 50 mM sodium phosphate buffer, pH 7.7) and in a Fenton reagent system (1 mM $Fe^{2+}$,1mM $H_2O_2$, 40 mM DMPO), respectively. Instrumental parameters were as follows: microwave frequency νMW = 9.799 GHz, microwave power = 12.57 mW, modulation frequency νM = 100 kHz, modulation amplitude AM = 1 G, time constant μ = 40.96 ms, and scan rate v = 0.83 G $s^{-1}$.

**Rapid freeze quench methodology**

EPR tubes were cut into two pieces and the bottom sections were attached to glass funnels using heat-shrink tubing.

Protein (16.6 μM) was diluted in 100 mM MES was prepared alongside a separate solution of ferrous ammonium sulfate (800 μM) dissolved in 2 mM HCl. Each of these solutions were drawn concurrently into apparatus syringes in a rapid freeze quench (RFQ) tower (Fig. 2.5). These were then fitted with a mixing chamber and rapidly mixed before being ‘shot’ onto a metal disc cooled with liquid $N_2$.

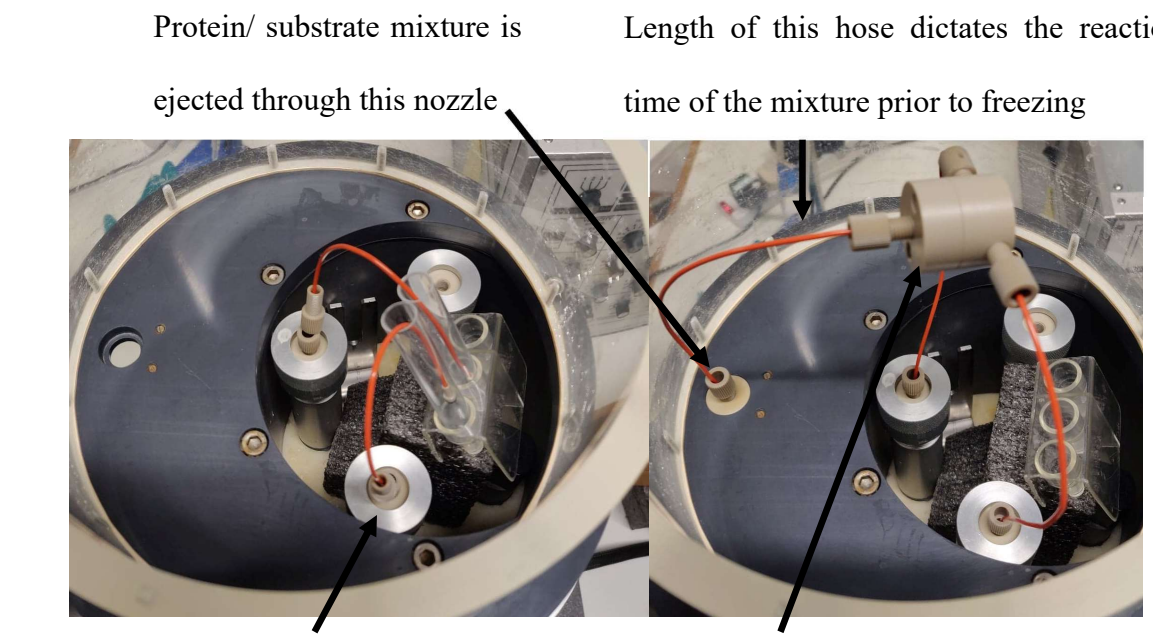


**Fig. 2.5.** Photos showing the internal setup of the RFQ tower. The loading syringes are filled with the reagent solutions in the leftmost image, then the rightmost figure shows the setup for 'shooting' the reaction mixture.

This left a ring of protein snow (Fig. 2.6) which could be poured into the funnel, packed into the bottom half of the EPR tube, then while the protein remained in liquid $N_2$, the funnel was removed and the top half of the EPR tube was reattached.

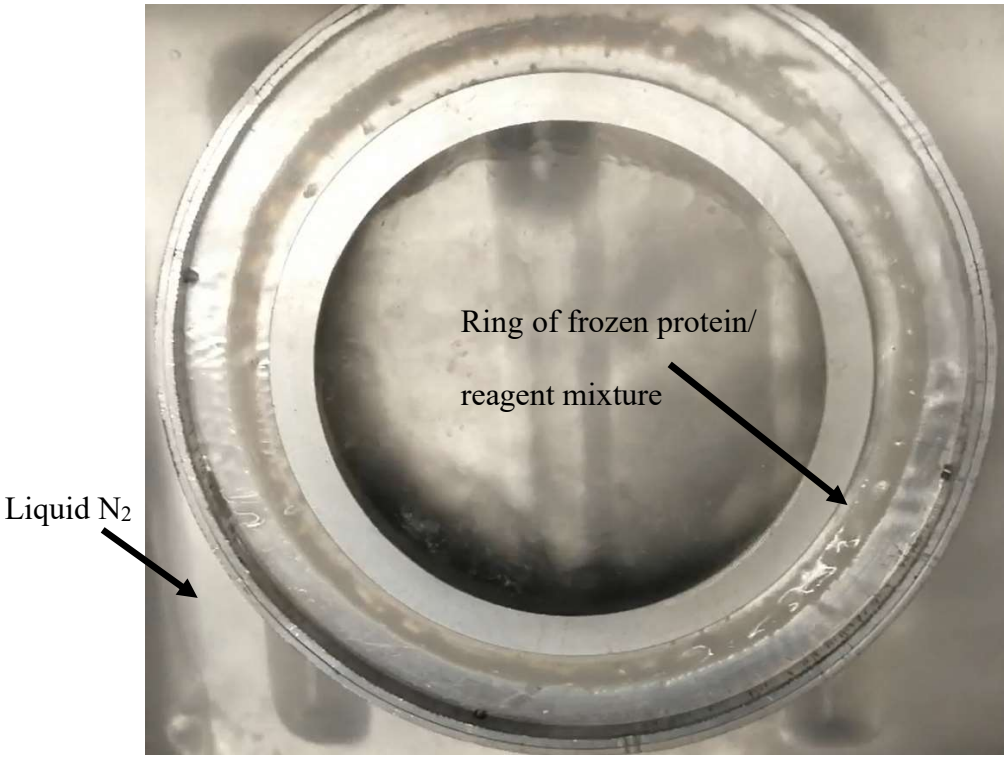


**Fig. 2.6.** The result of a single RFQ shot on a metal disc, removed from the liquid $N_2$ bath on the RFQ machine.

**Preparing anaerobic rapid freeze quench samples**

$O_2$ was removed from the protein by placing it in a glass bulb under Ar. Meanwhile an anaerobic glove bag was fitted over the RFQ syringe tower (Fig. 2.7), filled with Ar and allowed to remain under a positive pressure for 30 mins. The syringes were flushed with Ar. Protein was transferred from the bulb to the glove bag using a syringe with a sealed needle, and then allowed further time to equilibrate with the Ar environment within the bag. In this time, a $H_2O_2$ solution (and water for control and t=0 samples) were left in wide beakers to increase the surface area exposed to Ar.

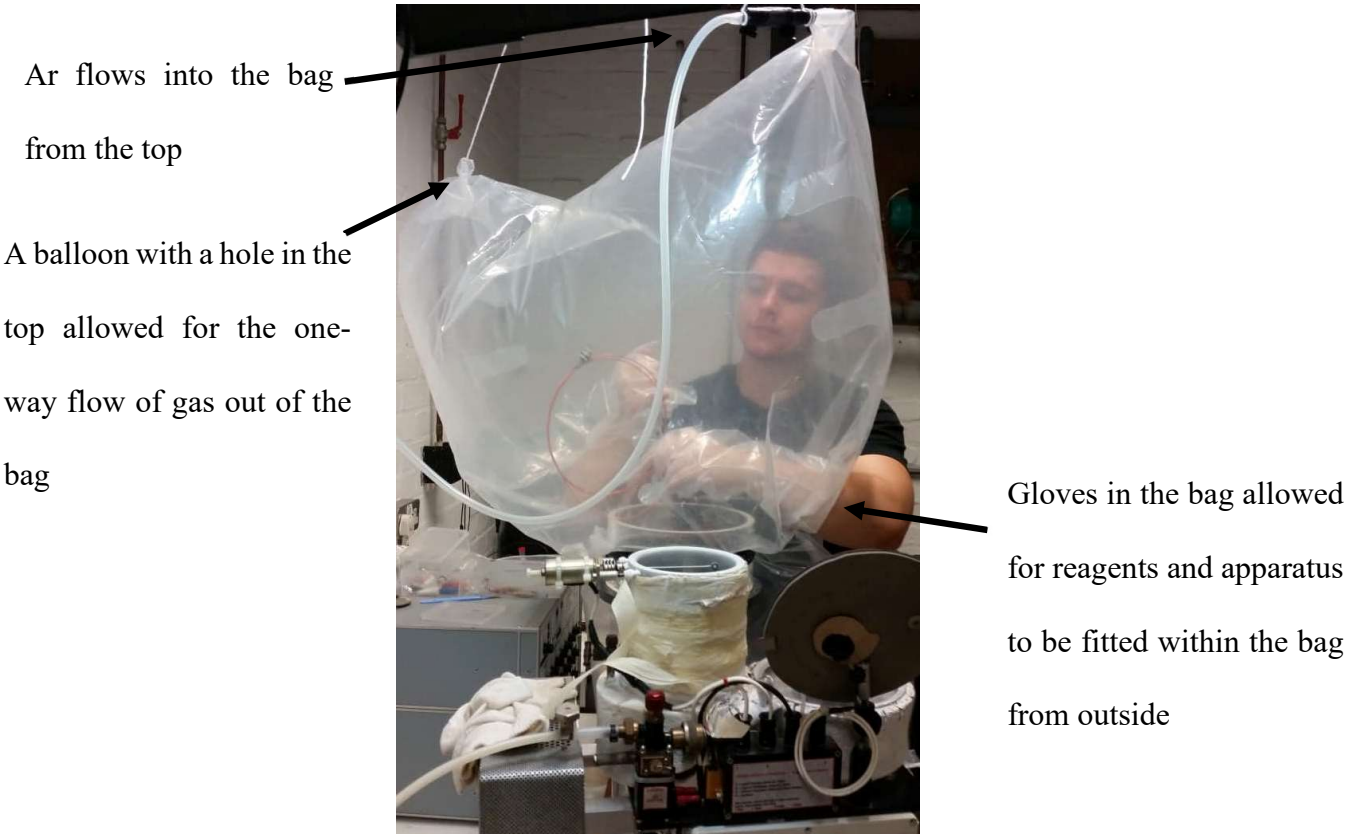


**Fig. 2.7.** The glove bag fitted to the RFQ tower. The bag is filled with Ar, and a used mixing chamber is being replaced with a clean one inside the anaerobic environment without exposing to air.

These solutions were loaded and shot as in 2.11. Mixing chambers could be replaced without opening the bag, allowing for continuous sample preparation without $O_2$ contamination.

**Mössbauer Spectroscopy**

A stock $^{57}$Fe ferrous ammonium sulfate powder was kindly provided by UEA. Anaerobic RFQ was performed as before, but instead three shots were stored in a single funnel of liquid $N_2$, a

small amount of snow was packed into the EPR tube attachment then the rest was poured into a new funnel attachment custom made to fill Mössbauer cups (Fig. 2.8). The funnel was removed once the snow was packed and the lid (cooled in advance by liquid $N_2$) was screwed on to tightly pack the sample.

As a form of quality control, a small portion of the protein snow was packed into an EPR tube for measurement. The ratios of mononuclear $Fe^{3+}$ and free radical were compared to previously measured samples under similar conditions.

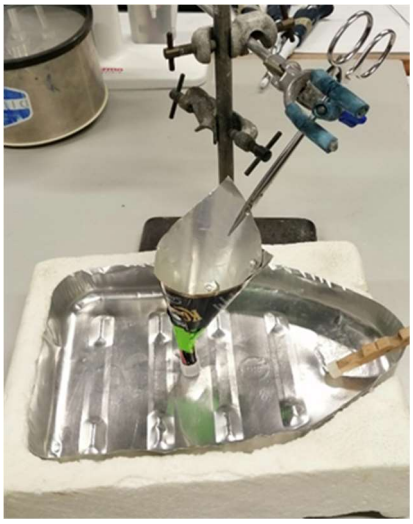

**Fig. 2.8.** The setup used to pack Mössbauer cups with RFQ-produced snow. The metal dish is filled with liquid $N_2$. A metal funnel is fitted with holes that allow liquid $N_2$ to filter out of the funnel but allows the protein snow to drift downwards into the cup.

Spectra were recorded at 4.2 K with a small external magnetic field (60 mT) applied parallel to the γ-beam.

**Approximating the concentration of paramagnetic species**

The protein-based free radical concentrations in proteins were estimated by comparing the double integrals of their spectra to a $Cu^{2+}$[EDTA] standard (Fig. 2.9) where the concentration (1 mM) was known. $Cu^{2+}$ is paramagnetic and has a characteristic EPR spectrum that covers the $g \approx 2$ region where protein-based free radicals are detected. By measuring the free radical in question and $Cu^{2+}$ standard at 0.8 μW (where the intensities of both the free radical and $Cu^{2+}$ increase linearly with microwave power), 10 K and with the same field width, the double integral of each spectrum is expected to be linearly correlated with the concentration of paramagnetic species.

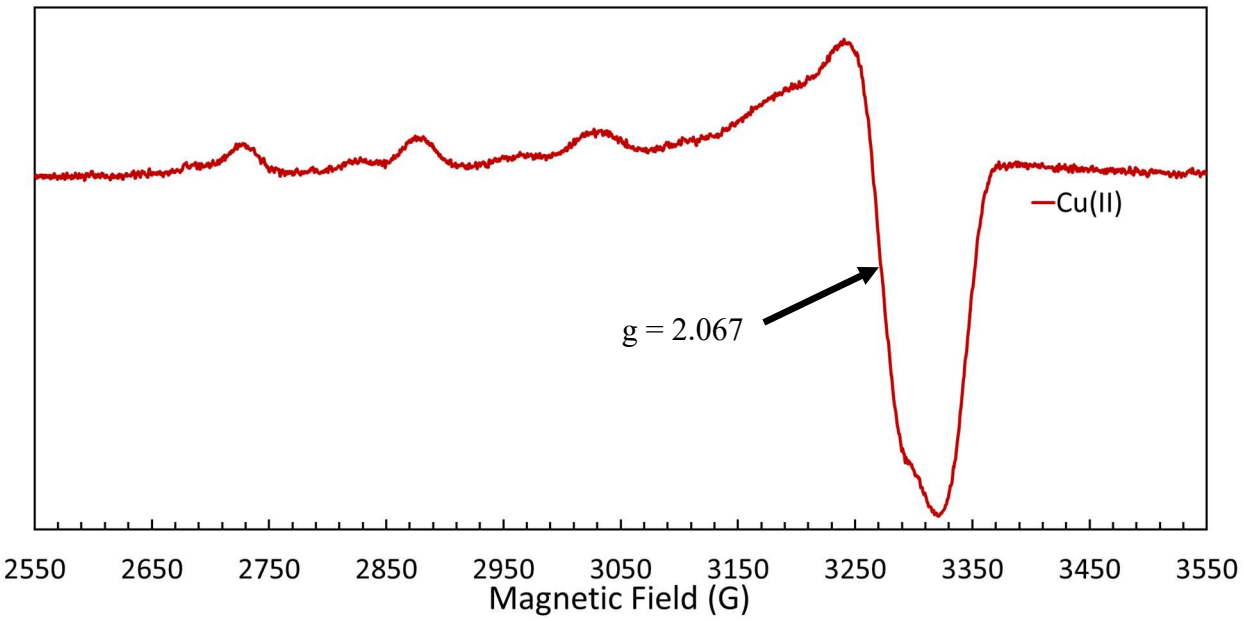


**Fig. 2.9.** The EPR spectrum of the 1 mM $Cu^{2+}$ standard used to determine the free radical concentration. Measurements were taken at the following instrumental conditions: microwave frequency $\nu_{MW}$ = 9.4655 GHz; modulation frequency $\nu_M$ = 100 kHz; modulation amplitude $A_M$ = 3 G; scan rate v = 0. 60 G/s; time constant $\tau$ = 81.92 ms; conversion time, at a 2048 data point scan range, $t_{conv}$ = 163.84 ms.

A similar method was used to estimate the concentration of rhombically coordinated, mononuclear $Fe^{3+}$. This high-spin iron species has a characteristic EPR signal at g = 4.3. Here, the standard was 35 µM ferric binding protein (Fbpa) from *Neisseria gonorrhoeae*. FbpA is a bacterial transferrin (Parker Siburt, Mietzner and Crumbliss, 2012) (Dhungana *et al.*, 2005) where each protein molecule tightly binds a single $Fe^{3+}$, making it an accurate measure of magnetically uncoupled $Fe^{3+}$ in the sample. In this instance, all spectra were recorded at 3.157 mW at 10 K.

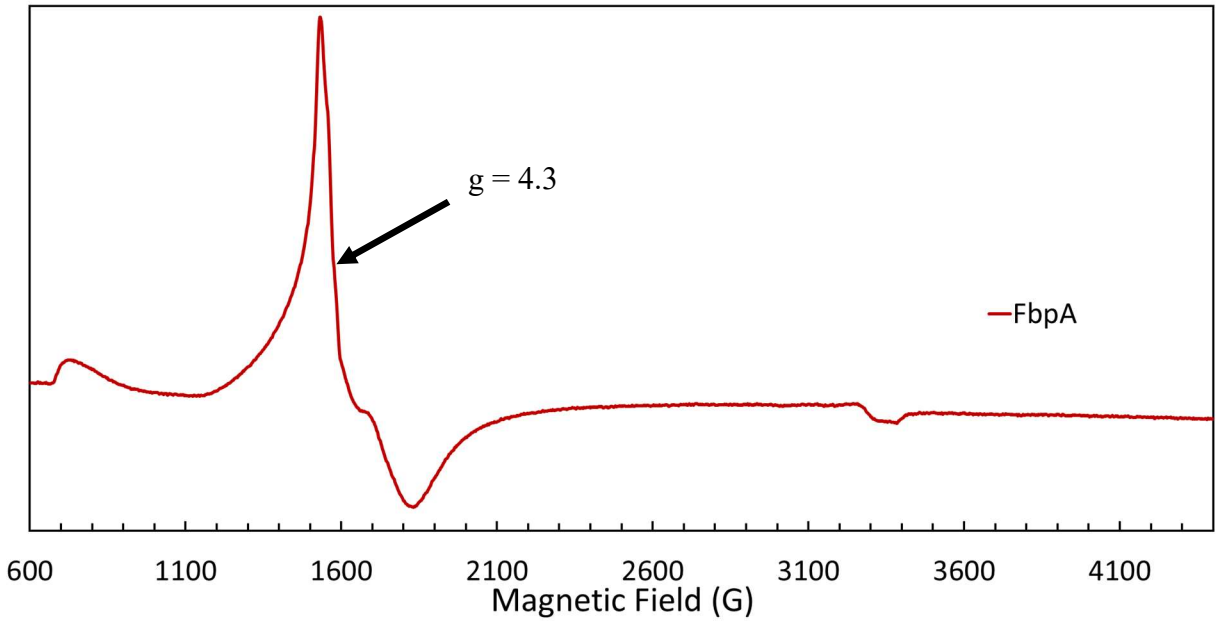


**Fig. 2.10.** The EPR spectrum of 35 µM FbpA used to determine the g = 4.3 concentration. Measurements were taken at the following instrumental conditions: microwave frequency $\nu_{MW}$ = 9.4662 GHz; modulation frequency $\nu_M$ = 100 kHz; modulation amplitude $A_M$ = 3 G; scan rate v = 0. 60 G/s; time constant $\tau$ = 81.92 ms; conversion time, at a 2048 data point scan range, $t_{conv}$ = 81.92 ms.

# Chapter 3

# Mixed-valent ferritins: the diversity of mechanisms in ferritins

## Introduction

Organisms can have numerous ferritins encoded within their genome that have been evolutionarily driven to fulfil particular purposes; new ferritins continue to be discovered. This chapter concerns four ferritins; human H-chain ferritin (HuHF), a well-studied 'classical' ferritin, and three which are relatively new, with little or no scientific literature currently describing their properties.

The first is the ferritin sync_1539 (henceforth referred to as *Syn*Ftn) is one of five bacterial ferritins recently found in the genome of *Synechococcus* strain CC9311. It is notable that most cyanobacterial genomes only contain one ferritin sequence (Palenik *et al.*, 2006). It was observed that coastal *Synechococcus* strain CC9311 was more tolerant to copper shock than strains that grow in open-ocean waters, and that this could be attributed to specialised genes that are upregulated in the presence of copper. Copper shock is the term for a range of toxic effects attributed to the metal, such as blocking essential metal binding sites and inhibiting electron transport in photosystem II (Stuart *et al.*, 2013). *Syn*Ftn is a protein coded for by one

of these genes and upregulated by high copper levels, likely to quickly sequester iron and prevent it from participating in Fenton chemistry (Stuart *et al.*, 2009). There is precedent for ferritins fulfilling roles beyond oxidative stress, however; it has been demonstrated that overexpression of alfalfa ferritin not only increases tolerance to oxidative stress, but to attack from necrotrophic pathogens (Dudits *et al.*, 1999).

Despite being a prokaryotic ferritin, *Syn*Ftn does not fit the well-defined criteria of the Ftn family; its ferroxidase centre (FC) has no site C, which before the discovery of *Syn*Ftn, was a universal feature of the bacterial ferritins. It also has no carboxylate rich patch on the inner surface of the protein, which is typically important for nucleation of the mineral core. In this sense, *Syn*Ftn is more similar to mammalian H-chain ferritins. Sequence alignments of ferritins from available cyanobacterial genomes showed that there were >100 homologues of *Syn*Ftn (with no site C and minimal, if any, carboxylate rich patches for nucleation). While the more 'conventional' types of bacterial ferritin are found in a more diverse range of cyanobacteria, *Syn*Ftn homologues are much more common overall. In *Synechococcus* or *Prochlorococcus* species, almost all organisms contain a *Syn*Ftn-like ferritin. Crystal structures of *Syn*Ftn show an unusually long Fe-Fe bond length (3.9 Å) which is uncharacteristic of ferritins or of a diferric diiron centre (Bradley *et al.*, 2019).

The second ferritin addressed here is human mitochondrial ferritin (FtMt). Unlike other mammalian ferritins, FtMt is a homopolymer, but the protein is structurally and sequentially similar to human H-chain ferritin (Langlois d'Estaintot *et al.*, 2004). Over 80% of fluctuation in the body's concentration of iron occurs in the mitochondria, so it is of particular importance that an efficient iron storage protein is present. The protein's similarity to HuHF was discussed in Chapter 1; the Δ9 variant where the N terminal chain of 9 residues were removed from the protein increased sequence homology to HuHF to ≈79 % (Levi *et al.*, 2001).

The final ferritin discussed in this chapter is *n* ferr, a prokaryotic ferritin isolated from the archaeon *Natronolimnobius innermongolicus*. The sequence of this protein was deposited in the UniProt database in 2013, and as of now, there are no publications on this protein. Data by J.M. Bradley have shown that *n* ferr has the fastest known $O_2$-driven rapid $Fe^{2+}$ oxidation phase of any ferritin, but in contrast, the slowest mineralisation phase (this data is not shown within the thesis).

In this chapter, HuHF will be used to demonstrate a new protocol for observing the release of $H_2O_2$ from metalloproteins. After that, an EPR-based approach will be taken to study the cyanobacterial protein *Syn*Ftn which, at least sequentially, bears some resemblance to HuHF. Rapid freeze quench (RFQ) studies were performed on FtMt and its Δ9 variant to observe the effect the N-terminal chain has on the formation of free radical and $Fe^{2+}$ oxidation. Finally, the *n* ferr protein's initial characterization by EPR will be discussed in relation to the other ferritins presented in this chapter.

## Results

### Human H-chain ferritin

#### Human H-chain ferritin is capable of forming a mixed valence ferroxidase centre directly upon $Fe^{2+}$ addition in the presence of $O_2$

HuHF was mixed with 48 $Fe^{2+}$/ 24mer (enough to fill all the FCs) in the presence of atmospheric and half-atmospheric concentrations of $O_2$. The results of this experiment are

displayed in Fig. 3.1 below. While the detection of a mixed-valence ferroxidase centre (MVFC) in HuHF is not unprecedented, (Honarmand Ebrahimi *et al.*, 2012), its detection directly upon addition of $Fe^{2+}$ has not been reported previously (Bauminger *et al.*, 1991)(Bauminger *et al.*, 1994). The MVFC formed here has comparable g-factors to those shown in this work. With MVFC-containing ferritins being more prominent in the literature now, it may be possible that the small MVFC seen in Fig. 3.1 simply went unnoticed in the past.

The g = 4.3 signal associated with mononuclear $Fe^{3+}$ appears to be identical between the two samples. Conversely, both the free radical and the MVFC appear to be 1.5- 2 x smaller under low-$O_2$ conditions. As the Fe:$O_2$ stoichiometry for the FC of HuHF is reported to be 2:1 (Xu and Chasteen, 1991), (Zhao *et al.*, 2003) with the FC having little or no reductive capabilities towards $H_2O_2$, the lower concentration of paramagnetic species is consistent with only 65 % of the FCs having been oxidized.

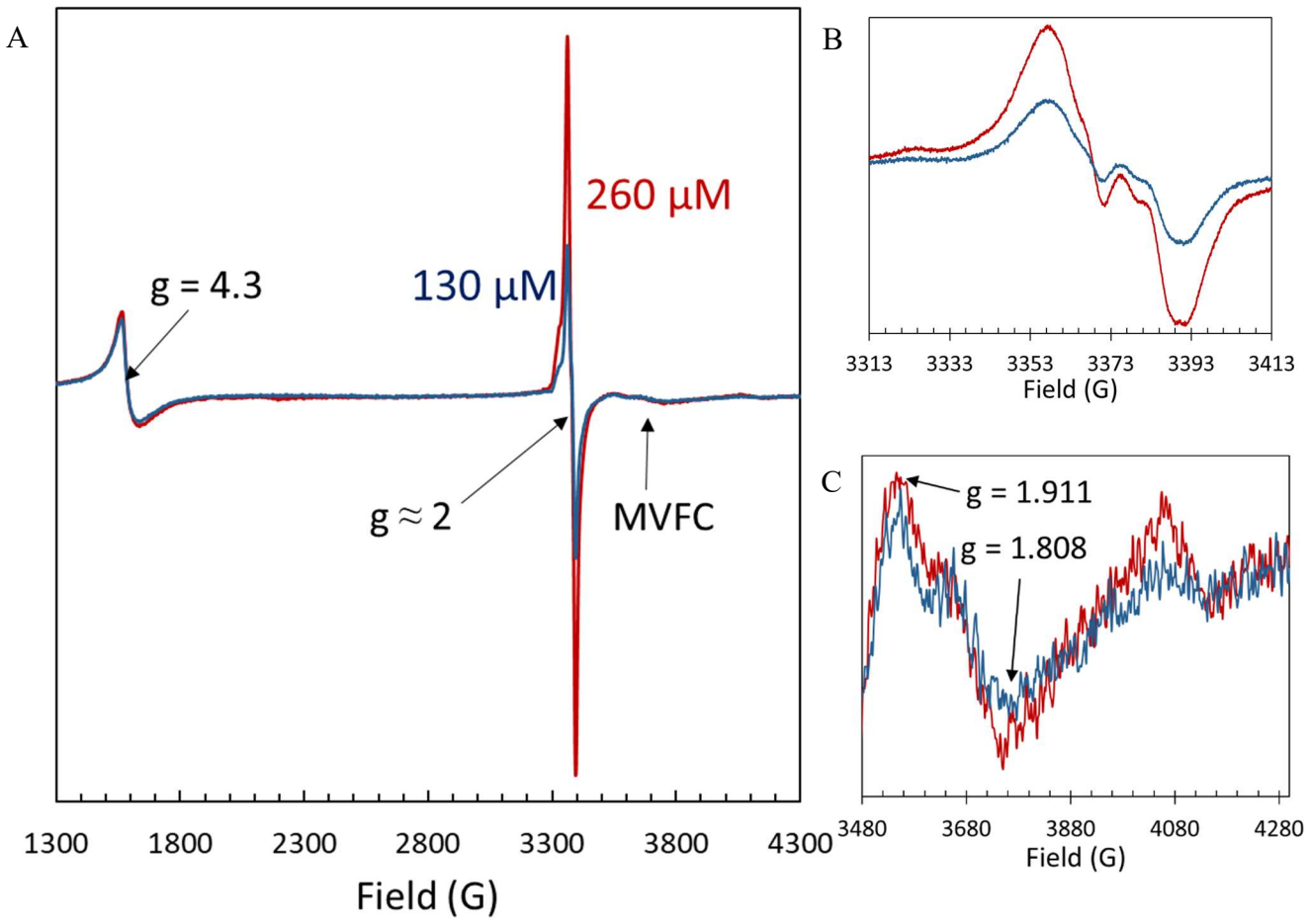


**Fig. 3.1.** A. EPR spectra of 8.3 µM HuHF mixed with 48 $Fe^{2+}$/24mer under atmospheric [$O_2$] (red) and half-atmospheric [$O_2$] (blue) and frozen 9 and 10 s after mixing, respectively. B. The spectra of the corresponding free radicals (recorded separately at microwave power $P_{MW}$ = 0.05 mW). C. The MVFC signal in both samples.

**The release of $H_2O_2$ from Human H-chain ferritin**

The release of $H_2O_2$ as a product of $O_2$ reduction is well documented in H-chain ferritins (Zhao *et al.*, 2001). This could be measured using a photodiode array in a novel manner by adding $Fe^{2+}$ to HuHF in the presence of the peroxidase DtpA.

DtpA is a dye-decolourising peroxidase with a ferric heme group that reacts very rapidly with $H_2O_2$ to form Compound I (CpI), a ferryl heme with a free radical localised on the porphyrin ring that has a distinctive optical spectrum. In DtpA this then spontaneously decays over a period of some minutes to another spectral form, Compound II (CpII). On mixing aerobic solutions of HuHF with ferrous ammonium sulfate in the presence of DtpA we observed the time-dependent spectra shown in Fig. 3.2.

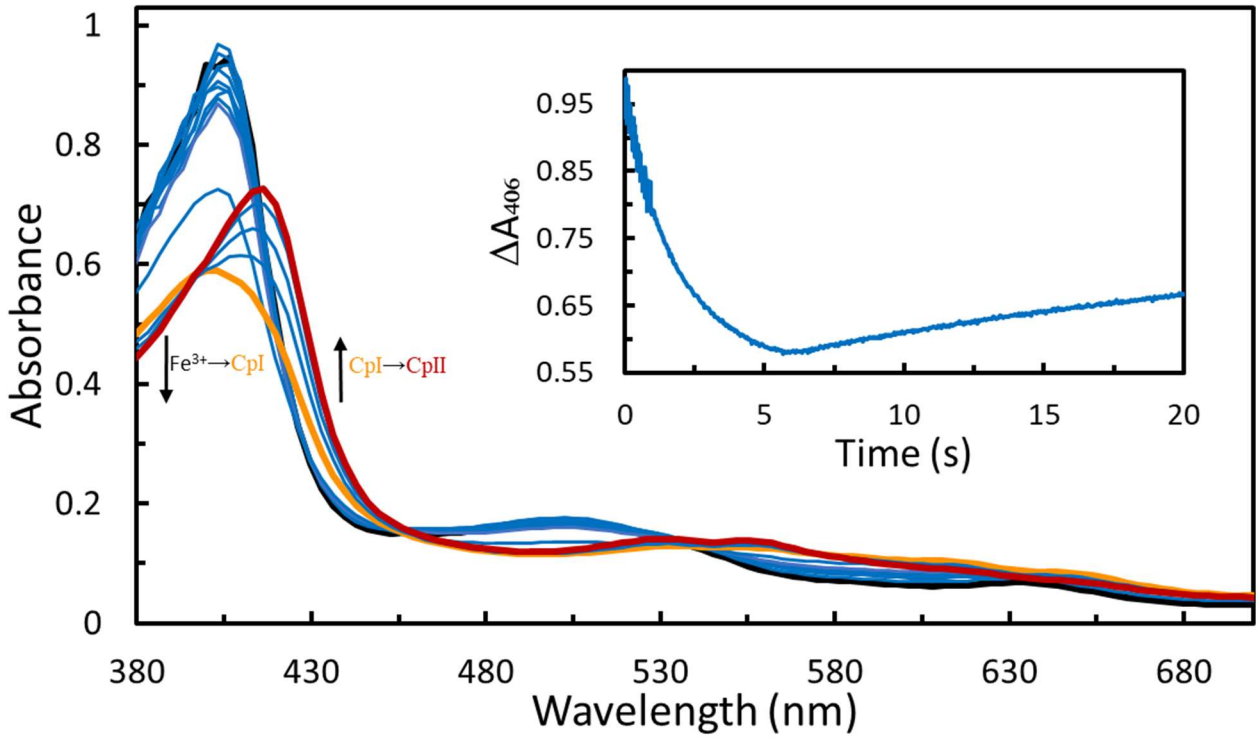


**Fig. 3.2.** A PDA spectrum of 18 µM DtpA in the presence of 1 µM HuHF as it is mixed with 96 $Fe^{2+}$/24mer in 263 µM $O_2$. The spectra shown are taken at the following times: t= 0.0024, 0.06, 0.1272, 0.1872, 0.252, 0.312, 0.372, 0.4368, 0.4992, 0.5616, 1.752, 5.91, 10.068, 13.9884, 18.186, and 20.76 s. The inset figure shows the $\Delta A_{406}$, associated with formation and decay of the intermediate CpI.

In this figure the dominant $Fe^{3+}$DtpA Soret band, centred at 406 nm bleaches over ~5 s. The time-dependent spectra collected were subjected to SVD analysis and then fitted globally to the model (Fig. 3.3):

$$Fe^{3+}DtpA > Fe^{3+}DtpA + BFR(DFP) > CpI > CpII$$

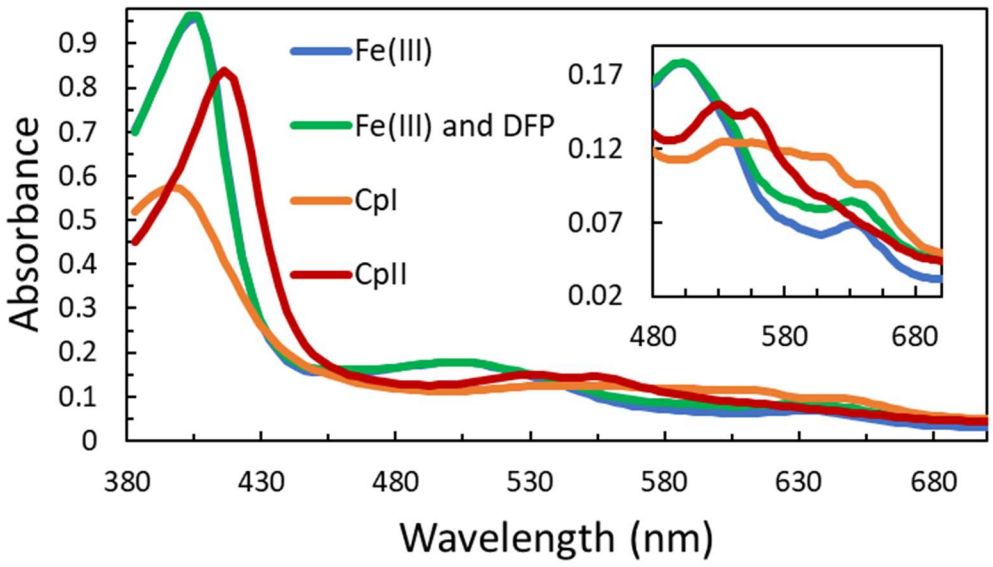


**Fig. 3.3.** A global fit of the data shown in Fig. 3.2, as derived by SVD analysis. This was fitted to a three-phase model, $Fe^{3+}$DtpA> Fe3+DtpA + BFR(DFP) > CpI > CpII. The decay of the DFP species at the BFR FCs coincided with the formation of CpI; this is reflected in the global fit. The rates associated with the formation of the species shown were 17.4, 5.5 and 0.07 $s^{-1}$ respectively. The inset shows the fitted spectra between 480 and 690 nm in greater detail.

The resulting spectrum shows that there is no change in the $Fe^{3+}$DtpA until the formation of a DFP species becomes detectable at the HuHF FC. As this species decays a proportion of $Fe^{3+}$DtpA has been converted to CpI (see for comparison the DtpA standard spectra by Chaplin, Wilson and Worrall, 2017 in Fig. 3.4). The ~5 s timescale is consistent with the decay of the DFP species which can be seen in the globally fitted spectra. Fig. 3.1 also shows the

spontaneous decay of CpI to CpII over the subsequent 10 s. Given that mineralisation has never been reported to proceed on such a short time scale, the formation of CpI was assumed to accurately represent all of the $H_2O_2$ released by HuHF. Indeed, the results suggest that $H_2O_2$ is produced in the reaction between HuHF: $Fe^{2+}$ and $O_2$ and that all of this is released into bulk solution where it reacts exclusively with DtpA.

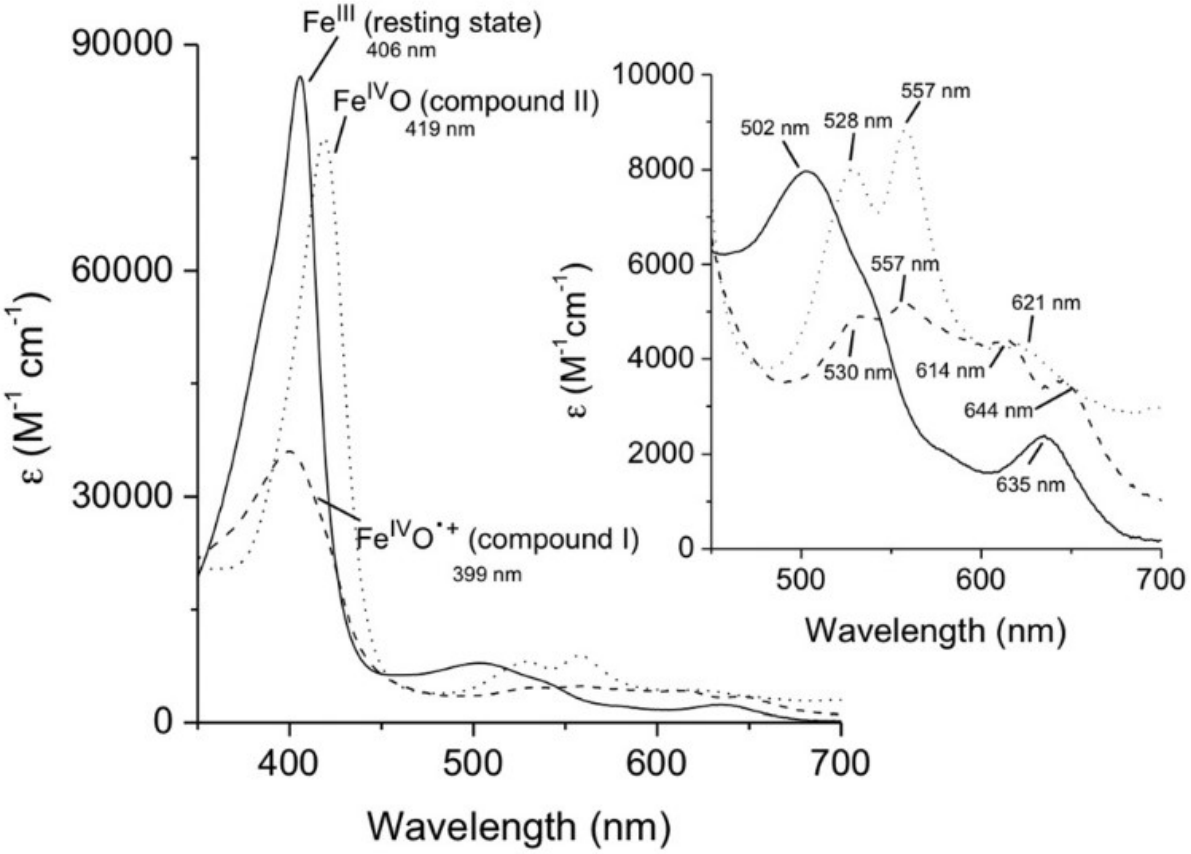


**Fig. 3.4.** UV-visible absorbance spectra of DtpA at pH 7.0. The different heme oxidation states of DtpA (8 μM) are indicated along with the wavelength of the absorbance maxima of the Soret band. Compound I was formed following addition of one equivalent of $H_2O_2$ to the resting ferric state enzyme with compound II formed from compound I by addition of one equivalent $K_4[Fe(CN)_6]$. Inset shows a close-up of the Q-bands with wavelengths indicated. These have been used here as standard spectra of DtpA, shown here as presented in (Chaplin, Wilson and Worrall, 2017).

To determine how much $H_2O_2$ is released the experiment was repeated varying the [$Fe^{2+}$] from sub- to supra- stoichiometric concentrations (Fig. 3.5).

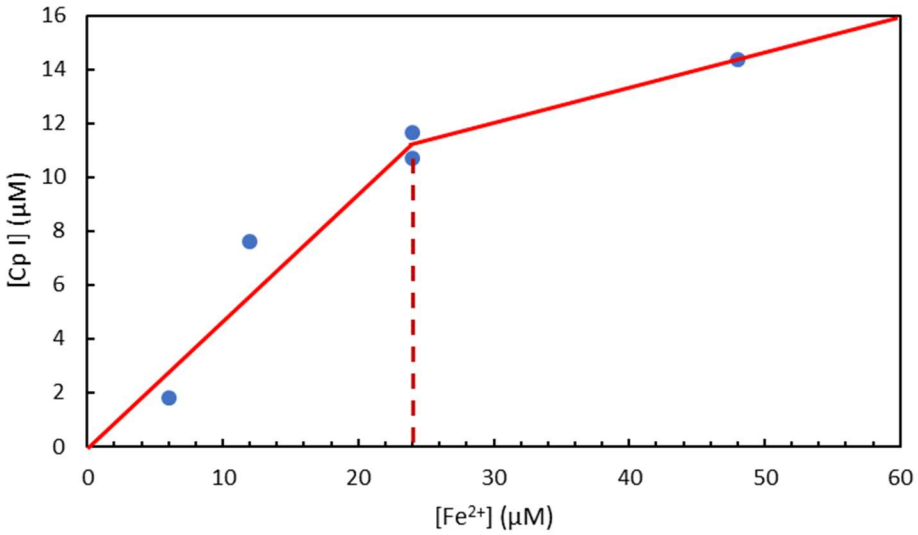


**Fig. 3.5.** A plot showing the concentration of compound I generated in each mixing experiment as a function of [$Fe^{2+}$]. The dashed red line shows the [$Fe^{2+}$] at which all the HuHF FCs would be expected to be fully occupied with iron (24 µM).

The concentration of CpI observed is equal to half of the concentration of $Fe^{2+}$ added at all points up to and including 24 µM $Fe^{2+}$ (the way the concentration was derived is reported in Appendix 2). This is consistent with a stoichiometry of 2 $Fe^{2+}$: 1 $O_2$ which has been previously observed. While adding more iron than necessary to saturate the FCs does not proportionally increase the amount of $H_2O_2$ produced over the timescale monitored, it influences the rate of $Fe^{2+}$ oxidation (Fig. 3.6)

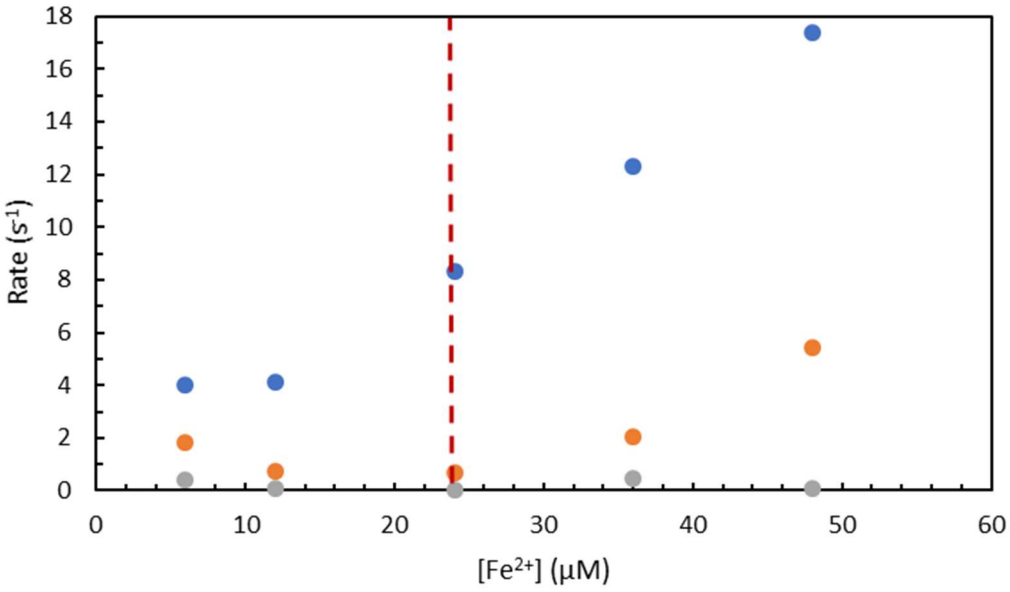


**Fig. 3.6.** The dependence of HuHF's rates of $Fe^{2+}$ oxidation in (blue), CpI formation (orange), and CpII formation (grey) in on [$Fe^{2+}$] when utilizing $O_2$ as an oxidant.

In isolated experiments where DtpA is mixed directly with $H_2O_2$, the rate of CpI formation is linearly dependent on [$H_2O_2$]. Here, CpI formation is rate-limited by the decay of the DFP species (see Fig. 1.5) that forms after the reduction of $O_2$. This also happens to have a linear dependence on [$Fe^{2+}$]. The decay of CpII is independent of [$H_2O_2$].

## Cyanobacterial ferritin (*Syn*Ftn)

### *Syn*Ftn has a mixed-valent ferroxidase centre

Fig. 3.7A shows the paramagnetic species observed at g = < 2 when *Syn*Ftn is aerobically mixed with 80 $Fe^{2+}$/24mer and frozen after 12 s. This could be simulated as the sum of two different forms of $Fe^{2+}/Fe^{3+}$ mixed-valent ferroxidase centres (MVFC). This suggests that an individual *Syn*Ftn FC only provides one electron when oxidized by $O_2$. This is unprecedented amongst previously studied ferritins; even where a MVFC has been observed previously, this has been generated through partial reduction of the FC using sodium dithionite rather than oxidation by $O_2$ (Tatur and Hagen, 2005). This is also distinct from the MVFC observed upon mixing apo-horse spleen ferritin with $Fe^{2+}$ under aerobic conditions (Sun and Chasteen, 1994). The kinetics of the MVFC formation observed in that work are incompatible with the oxidation of $Fe^{2+}$ by $O_2$; it is more likely a result of either $Fe^{2+}$ binding at an FC occupied by a single $Fe^{3+}$, or through displacement of $Fe^{3+}$ at the $Fe_B$ site by incoming $Fe^{2+}$, the latter of which has also already been demonstrated to occur (Honarmand Ebrahimi *et al.*, 2012). Even when compared to the MVFC in HuHF that is displayed above in Fig. 3.1 above, a significantly higher concentration of the MVFC is observed, which is too high to be explained by residual iron in the FCs. Adding 12-80 $Fe^{2+}$/24mer showed that the MVFC forms even at sub-stoichiometric $Fe^{2+}$ loadings, where a rapid phase of iron oxidation was not detected (Bradley *et al.*, 2019). However, at loadings ≥24 $Fe^{2+}$/24mer the MVFC signal was much more intense (Fig. 3.7B). This is likely because both iron binding sites must be occupied, but it may be indicative of a cooperative mechanism between two FCs; $O_2$ is a two-electron acceptor and thus would need electrons from two FCs to become fully oxidized.

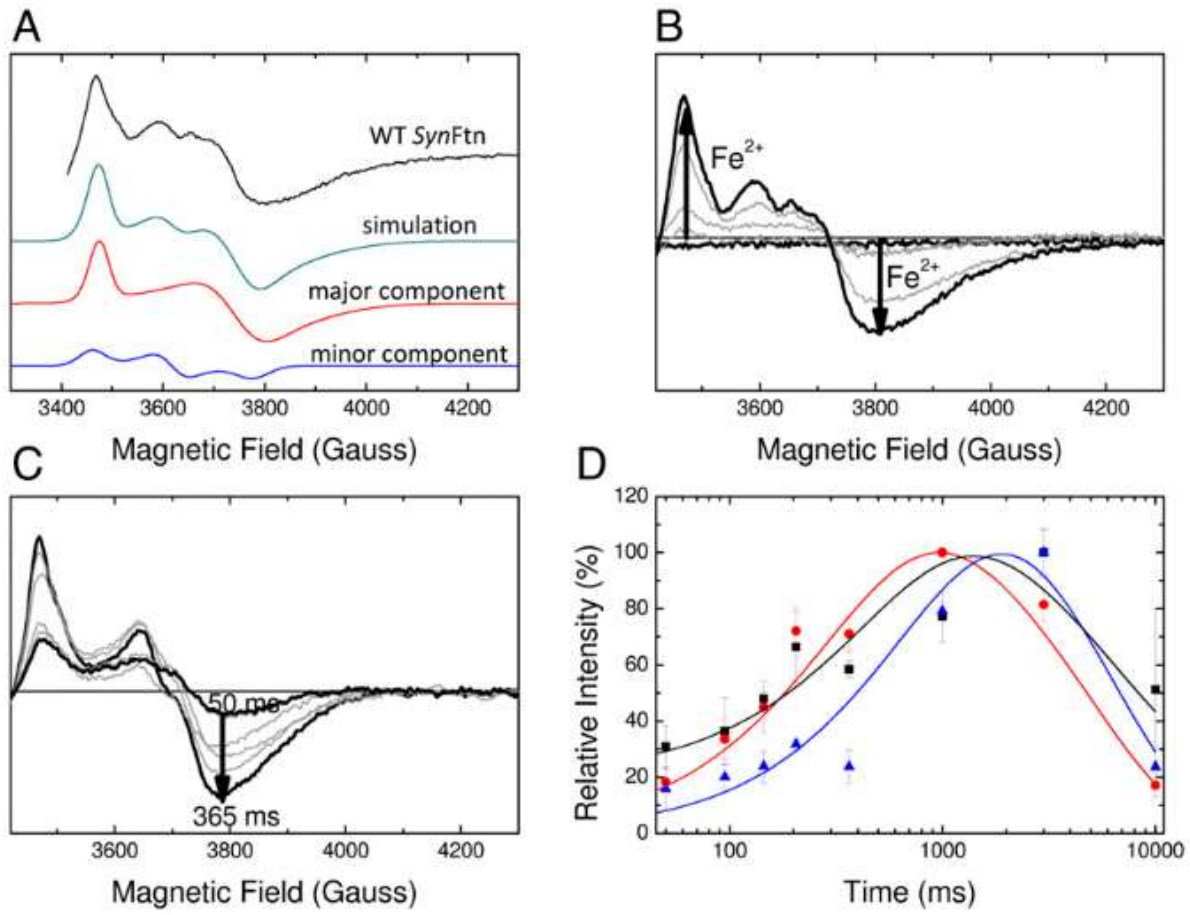


**Fig. 3.7.** EPR monitored iron-$O_2$ reactivity of *Syn*Ftn. A. The EPR signal attributed to an MVFC in *Syn*Ftn frozen 12 s after initiating iron oxidation (iron added at 80 $Fe^{2+}$/24mer) and its modelling as a sum of two signals simulated with the parameters listed in Table 3.1. Experimental data are truncated to omit the region of overlap with the tyrosyl radical (Fig. 3.10). B. Intensity of the MVFC signal at increasing iron loading in samples of 4.17 µM *Syn*Ftn frozen 10 s after mixing. Response from the apo-protein and protein loaded with 80 $Fe^{2+}$/24mer are shown in black; intermediate iron loadings (12, 24 and 48 equivalents of $Fe^{2+}$) are shown in grey. C. Increase in signal intensity in the high-field region ($g < 2$) assigned to the MVFC in samples of 4.17 µM *Syn*Ftn frozen 50-365 ms after mixing with 72 equivalents of $Fe^{2+}$. Thick traces are the shortest (50 ms) and longest (365 ms) aging times shown, the latter corresponding to maximum signal intensity. Traces at intermediate freezing times are shown in grey. The EPR signal minimum at ≈ 3,800 G shifts in both sets of spectra, for iron load (B) and reaction time

(C), due to increasing relative input of the 'minor' MVFC component (A), which has a greater $g_z$ value than the 'major' one. D. Intensity plots showing the formation and decay of the MVFC (red circles), mononuclear $Fe^{3+}$ (black squares), and tyrosyl radical (blue triangles) detected by low-temperature EPR spectroscopy over the first 10 s of iron oxidation (72 $Fe^{2+}$/24mer) by *Syn*Ftn. Solid lines represent fits of the data, yielding apparent first-order rate constants of 3.0 $s^{-1}$ (MVFC), 2.0 $s^{-1}$ ($Fe^{3+}$), and 1.2 $s^{-1}$ (free radical) for the formation phase, and 0.2 $s^{-1}$ (MVFC), 0.15 $s^{-1}$ ($Fe^{3+}$), and 0.17 $s^{-1}$ (free radical) for the decay phase. Figure taken as published from (Bradley *et al.*, 2019).

Rapid freeze quench (RFQ) EPR was used to observe the formation of the MVFC at 72 $Fe^{2+}$/24mer (Fig. 3.7C). The formation and decay kinetics of the MVFC are shown alongside those of the free radical and detectable mononuclear $Fe^{3+}$ in Fig. 3.7D. The MVFC intensity reaches a maximum at approximately 1 s after addition of $Fe^{2+}$. Using a 1 mM Cu[EDTA] solution, the MVFC concentration was determined to account for ≈70 % of all FCs in the protein (i.e. 17 MVFCs per 24mer). This decayed slowly over the next 10 s.

The MVFC (Fig. 3.7A) was simulated as a sum of two overlapping species which were referred to as the major and minor species based on their intensities (80 % and 20 % of the signal, respectively). Their g values are reported in Table 3.1. These values are comparable to those reported for the two MVFC species observed in the one-electron reduction of *P. furiosus* (1.946, 1.838, 1.80 for component I, 1.923, 1.838 and 1.77 for component II, Tatur and Hagen, 2005). The formation of the MVFC signal was consistent with the rate of the rapid phase of $Fe^{2+}$ oxidation observed in stopped flow absorbance experiments, and the decay was comparable to that of the slow phase (Bradley *et al.*, 2019).

**Table 3.1.** Principal g values and individual linewidths used in simulation (S = ½) of the two components of the EPR signal assigned to MVFC in *Syn*Ftn.

| Component | $g_x$ | $g_y$ | $g_z$ | $\Delta H_x$, G | $\Delta H_y$, G | $\Delta H_z$, G | Contribution, % |
|---|---|---|---|---|---|---|---|
| Wild-type MVFC major component | 1.943 | 1.800 | 1.760 | 35 | 95 | 230 | 80 |
| Wild-type MVFC minor component | 1.955 | 1.870 | 1.790 | 50 | 56 | 63 | 20 |
| Y40F MVFC major component | 1.943 | 1.798 | 1.765 | 40 | 100 | 320 | 83 |
| Y40F MVFC minor component | 1.955 | 1.840 | 1.770 | 40 | 40 | 80 | 17 |

The observation of a MVFC helps to explain the crystallographic evidence that the Fe-Fe bond is unusually long (3.9 Å, see Fig. 3.8) and that only 50 % of the iron is observed to be oxidized in UV/ vis stopped flow experiments.

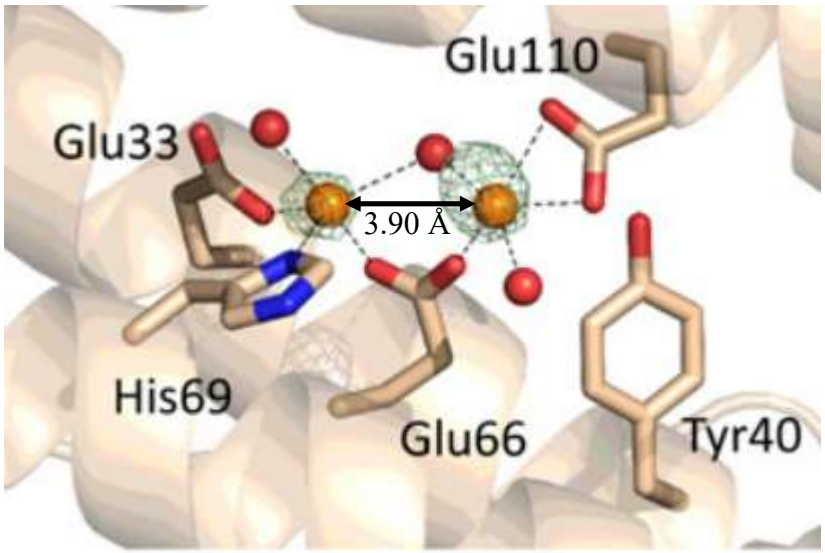


**Fig. 3.8.** The FC of *Syn*Ftn following a 2-min soak in a solution containing 5 mM $Fe^{2+}$ at pH 6.5 with the anomalous difference map of the iron atoms shown in green (PDB entry 6GCK). The coordinating residues of the FC, and Tyr40, are labelled. The Fe-Fe bond is also labelled on the diagram. Figure taken as published from (Bradley *et al.*, 2019).

The MVFC is continually formed throughout turnover; at high iron loadings, MVFC intensity remains high after the first oxidation of $Fe^{2+}$ by $O_2$ (Fig. 3.9). This indicates that the FC remains

a functional catalytic centre throughout mineralisation. It was also shown that *Syn*Ftn's FC almost completely recovered its rapid oxidation activity after 1 hour, showing that the diferric FC is unstable, and is translocated into the mineral core to regenerate the apo-FC.

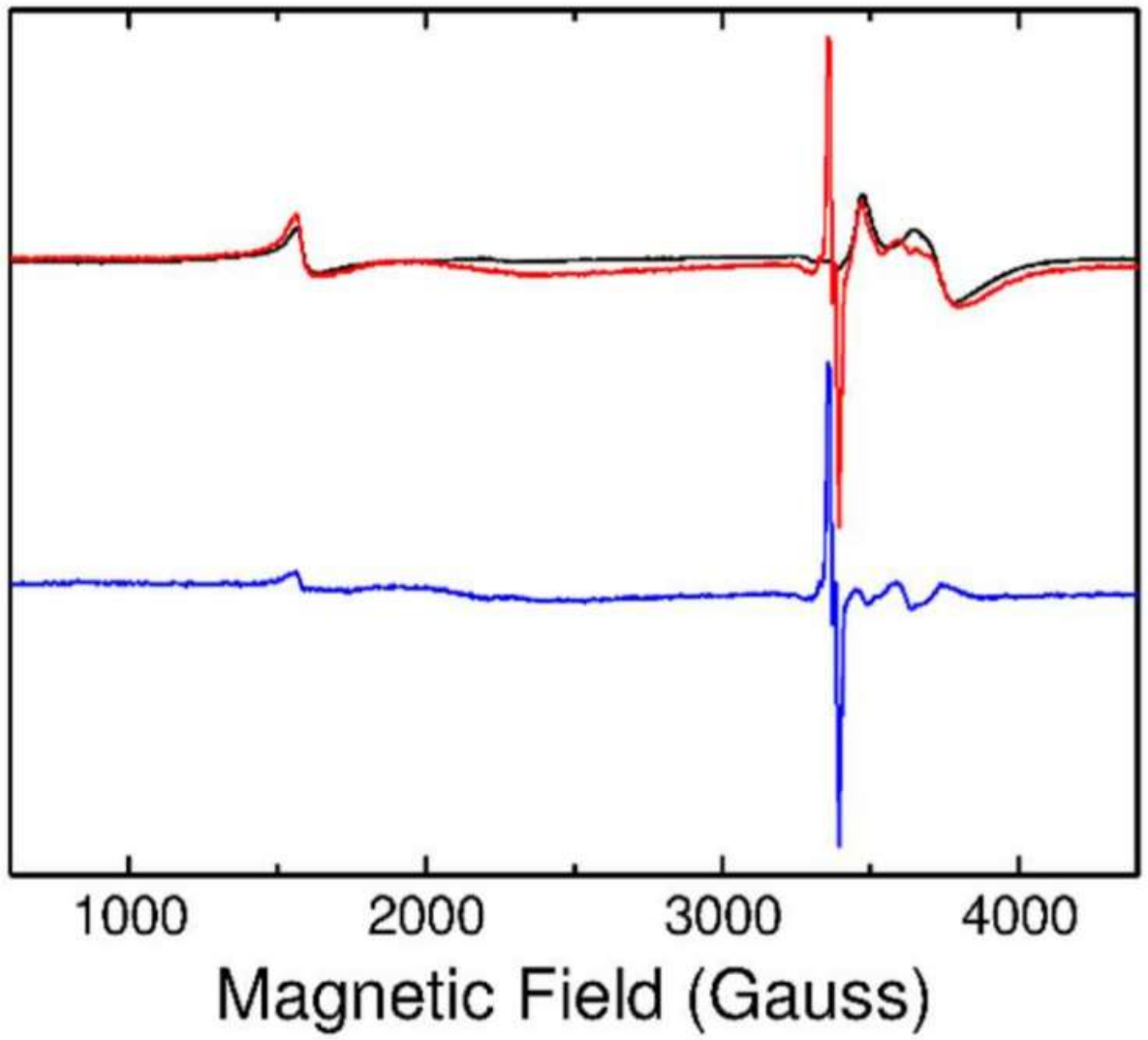


**Fig. 3.9.** EPR spectra showing 4.17 µM *Syn*Ftn frozen 10 s after the addition of 72 $Fe^{2+}$/24mer (red trace) and 20 s after the addition of 200 $Fe^{2+}$ (black trace). The blue trace is a difference spectrum, showing the termination of the free radical while the MVFC remains consistent throughout turnover. The spectra were measured at 10 K at microwave frequency $\nu_{MW}$ = 9.4659 GHz. Figure taken as published from (Bradley *et al.*, 2019).

Tyr40 is a universally conserved tyrosine among all ferritins with a catalytic diiron centre. Given the unique reactivity of *Syn*Ftn a Y40F variant was expressed to understand the role of this residue. Fig. 3.10 shows the time dependence of this Y40F variant. No rapid phase of $Fe^{2+}$ oxidation was observed in stopped flow experiments (Bradley *et al.*, 2019) which was concurrent with a significantly reduced rate of MVFC formation. Two species were once again required to simulate the MVFC (the parameters can be found in Table 3.1). Maximum intensity of the MVFC was reached 3 s after the addition of $Fe^{2+}$, and only corresponded to 60 % of the FCs (as opposed to 70 % in WT). Furthermore, the intensity of the free radical in the Y40F variant is almost entirely eliminated in this variant, strongly suggesting the possibility that the free radical is located on this residue. It is important to highlight that the rate of mineralisation was not affected in the Y40F variant (Bradley *et al.*, 2019). In the Y40F mineralisation experiments, it was shown that $Fe^{2+}$ oxidation proceeded at the rate observed for the slow oxidation of the MVFC to the diferric form. This suggests that MVFC decay is the rate-limiting step for core formation under the experimental conditions used in this work.

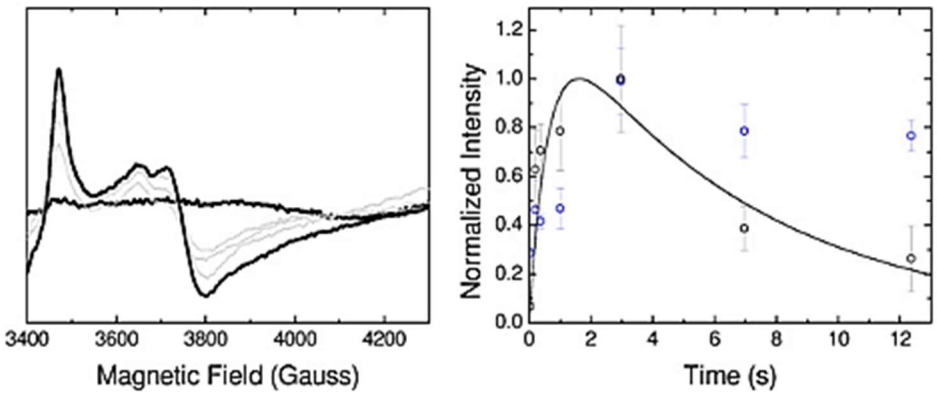


**Fig. 3.10.** Time dependence of Y40F *Syn*Ftn EPR. Left. Increase in signal intensity in the high field region ($g < 2$) assigned to the MVFC in solutions frozen 50-2965 ms after mixing with 72 equivalents of $Fe^{2+}$. The thick traces are the shortest (50 ms) and the longest aging times shown, the latter corresponding to maximum signal intensity. Traces at intermediate freezing times are shown in grey. Right. Normalized intensity of observed EPR signals as a function of time after the mixing of Y40F *Syn*Ftn and 72 $Fe^{2+}$/24mer. MVFC intensity is shown as black circles, and mononuclear $Fe^{3+}$ as blue. The black trace shows the predicted kinetics of a species formed and decaying in a first-order reaction at the rates observed in stopped-flow experiments performed by J. M. Bradley. Figure taken as published from (Bradley *et al.*, 2019).

Because mineralisation is not dependent on Y40, and the radical does not show steady state kinetics during mineralisation (while the MVFC remains at a high intensity) it is clear that the rapid phase of $Fe^{2+}$ oxidation in *Syn*Ftn produces a species that is capable of oxidizing a tyrosine residue, but the oxidation of the MVFC does not.

To understand iron entry into the FC of *Syn*Ftn, two protein variants were measured using EPR. One variant, D137A, replaces an aspartate residue that lines the three-fold channel. The other, E62A, replaces a glutamate that is hypothesised to coordinate $Fe^{2+}$ in a transient complex

between the three-fold channels and the FC. Fig. 3.11 shows EPR spectra of WT *Syn*Ftn and the E62A and D137A protein variants, which report the intensity of the MVFC between 10 and 60 s.

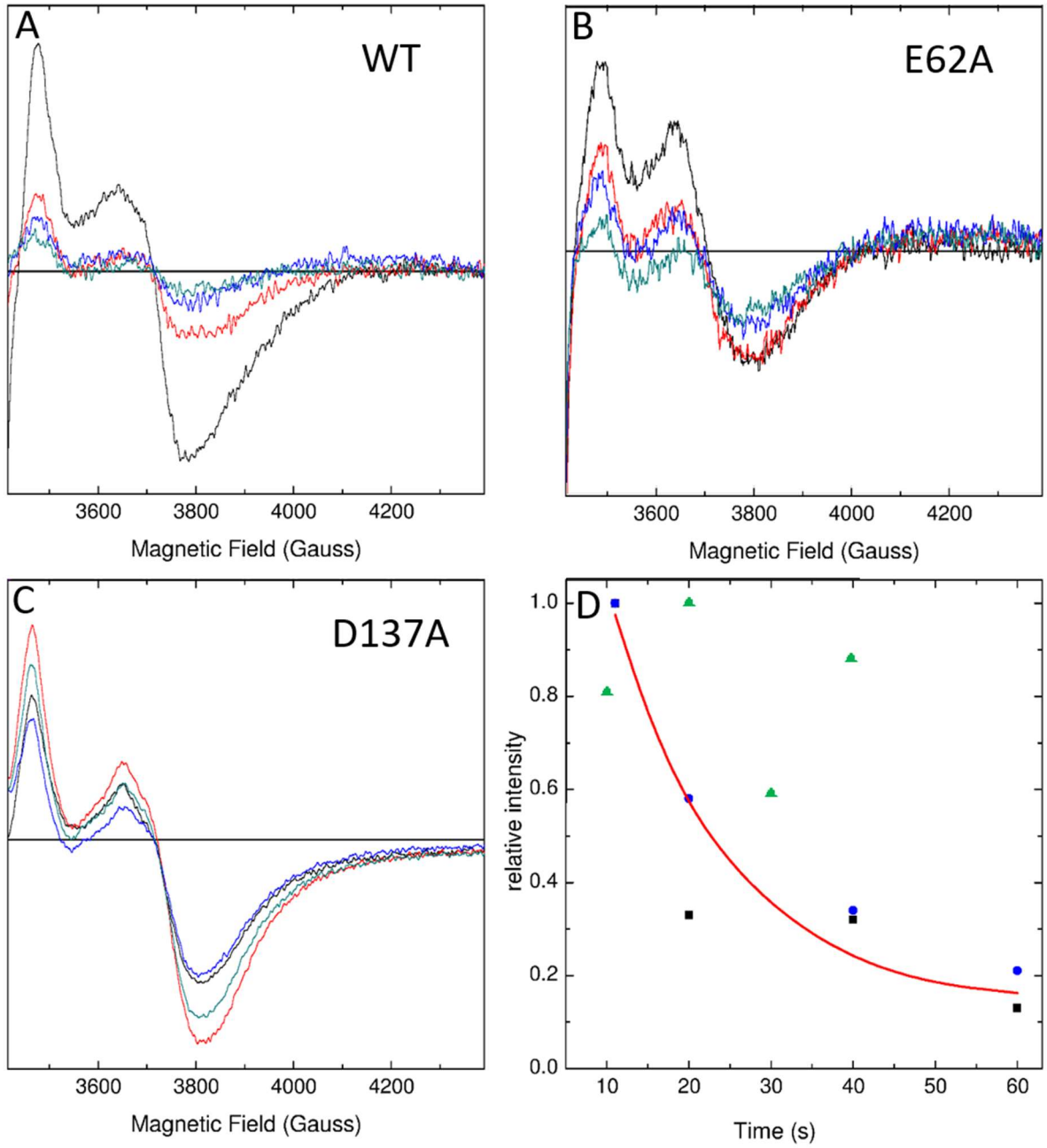


**Fig. 3.11.** Stability of the MVFC in WT, E62A and D137A *Syn*Ftn. The EPR signal due to the MVFC of A. WT, B. E62A and C. D137A *Syn*Ftn frozen 10 s (black trace), 20 s (red trace), 40 s (blue trace) and 60 s (cyan trace) after the addition of 200 μM $Fe^{2+}$ to a 4.17 μM (100 μM monomer) protein solution in 100 mM MES pH 6.5. Panel D shows the percentage maximal observed intensity remaining as a function of freezing time for wild type (black squares), E62A (blue circles) and D137A (green triangles) *Syn*Ftn.

The MVFC decays at comparable rates in the WT and E62A proteins (Fig. 3.11D). This data suggests that the rate of the second oxidative step ($Fe^{3+}Fe^{2+}$ to $Fe^{3+}Fe^{3+}$) is not affected by the mutation of E62. The D137A variant, however, reaches peak intensity 20 s after mixing, compared to 1 s for WT *Syn*Ftn (Fig. 3.7D). This data is consistent with the hypothesis that the D137A variant contains an active FC but has an impaired ability to acquire $Fe^{2+}$ from solution.

**Power/ temperature dependence of the *Syn*Ftn radical**

The microwave power and temperature dependence of the *Syn*Ftn free radical is mapped below in Fig. 3.12. While there is broadening in the spectra associated with an increase in microwave power, there is no indication that there is more than one species present (or that any species present have similar saturation behaviour).

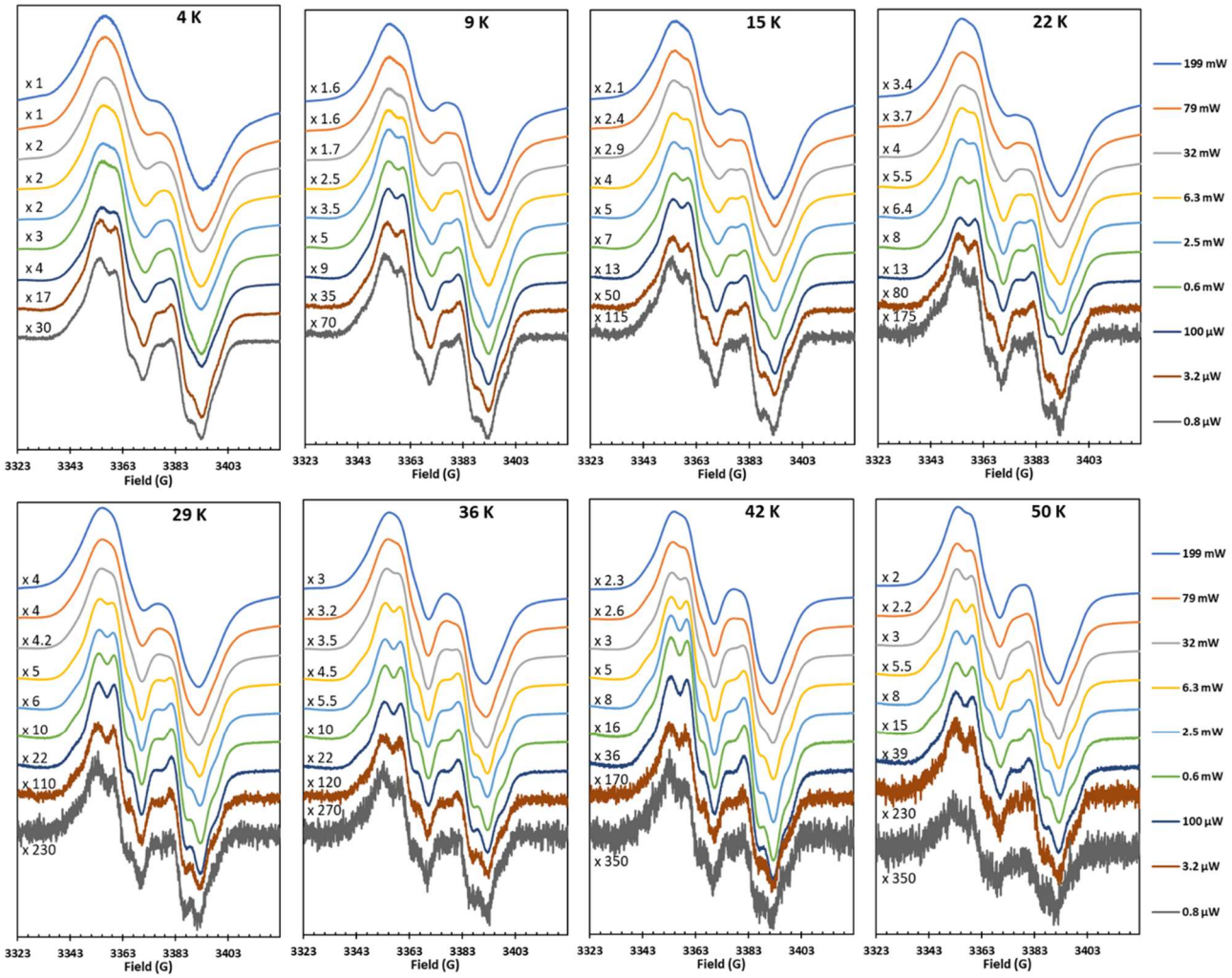


**Fig. 3.12.** The EPR signal of WT *Syn*Ftn free radical measured at eight values of temperature (4 K-50 K) and twelve values of microwave power (0.8 µW – 199 mW). Protein, $Fe^{2+}$ and $O_2$ concentrations are 4.17 µM, 200 µM and 263 µM respectively, slow frozen after 15 s. The instrumental conditions used to record the spectra were as follows: microwave frequency $\nu_{MW}$ = 9.466411 GHz; modulation frequency $\nu_M$ = 100 kHz; modulation amplitude $A_M$ = 3 G; scan rate v = 0. 60 G/s; time constant $\tau$ = 81.92 ms; conversion time, at a 2048 data point scan range, $t_{conv}$ = 81.92 ms.

The free radical appears to saturate at all temperatures; this is more clearly seen in Fig. 3.13. The line broadens non-homogenously at higher microwave powers, explaining the loss of

spectral features in the lineshape which can be seen in all spectra measured at 0.8 μW, but never at 199 mW.

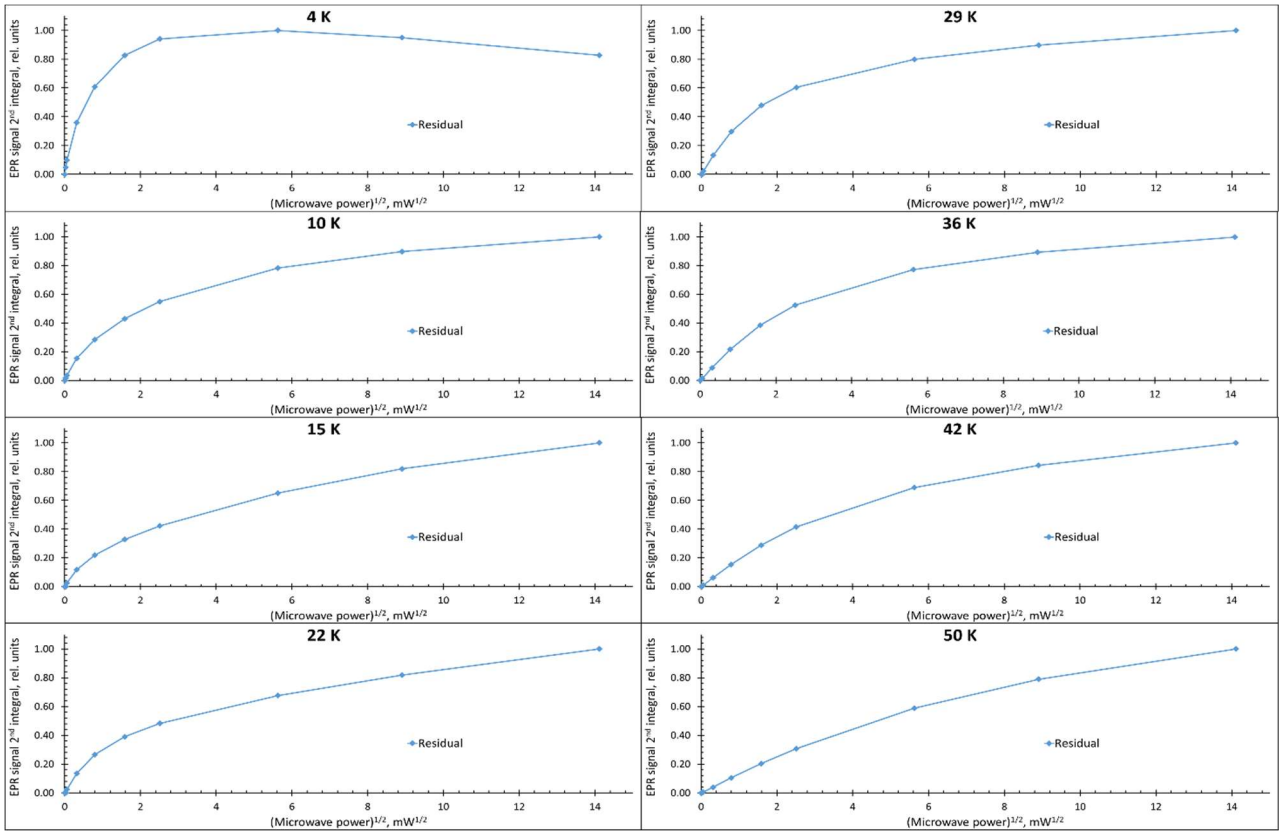


**Fig. 3.13.** The microwave power dependences of the free radical EPR signal at different temperatures in the WT *Syn*Ftn spectra shown in Fig. 3.12. The highest value of intensity is normalised to 1.0 in each panel.

The saturation behaviour can be more clearly seen as a function of temperature as shown in Fig. 3.14. The red traces in these plots show the 1/T dependence which is known as Curie's Law (this is described in more detail in Chapter 5). The free radical spectral intensity closely matches the 1/T curve at low powers, showing that the radical does not saturate under these

conditions. At microwave powers of 0.63 mW or higher, the free radical begins to saturate at lower temperatures.

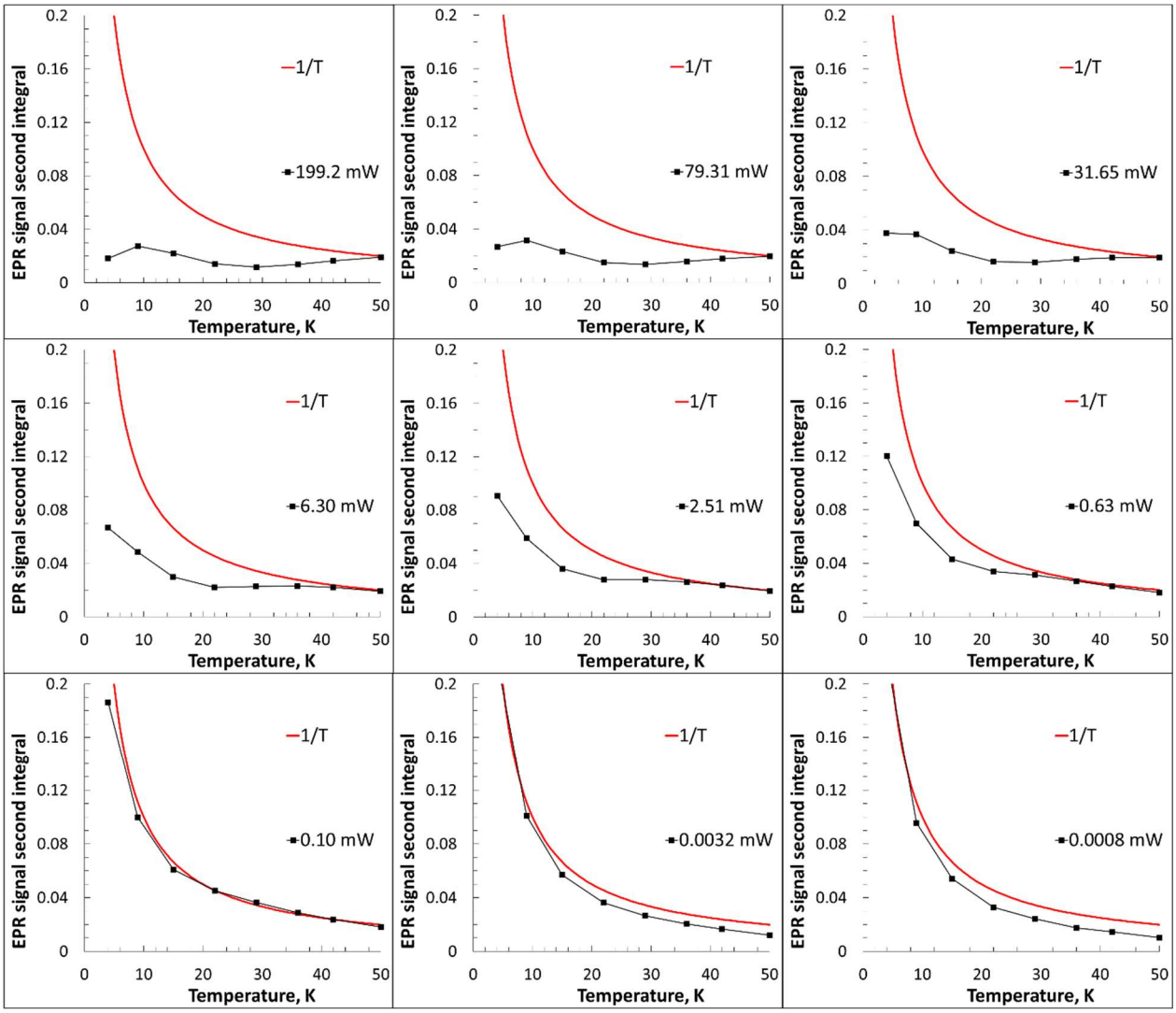


**Fig. 3.14.** Temperature dependences of the EPR signal in the WT *Syn*Ftn spectra (Fig. 3.11) at nine values of microwave power. The red line in each panel is the 1/T dependence. The EPR signal intensities are those reported in Fig. 3.12 multiplied by a factor, individual for each panel, to make the curve touch the 1/T line from beneath.

**Assignment and kinetics of the *Syn*Ftn free radical**

*Syn*Ftn's free radical was simulated as a single tyrosyl radical (Fig. 3.15A) using the tyrosyl radical spectra simulation algorithm (TRSSA) parameters shown in Table 3.2 (Svistunenko and Cooper, 2004). These parameters align well with those predicted from the conformation of Y40 in *Syn*Ftn crystal structures (Bradley *et al.*, 2019).

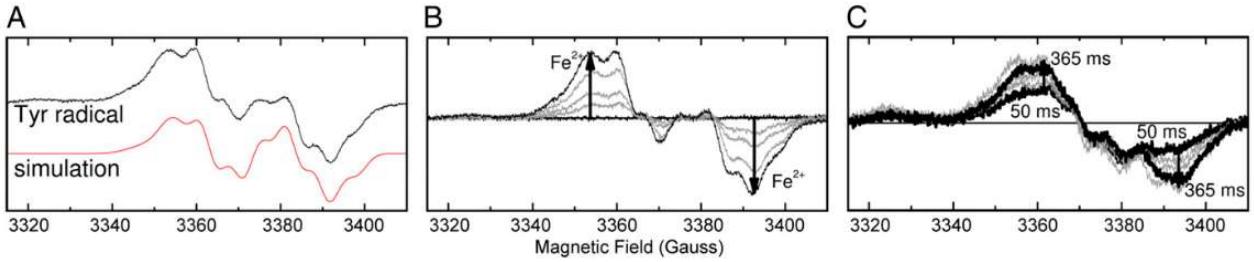


**Fig. 3.15.** The transient tyrosyl radical of *Syn*Ftn. A. EPR signal due to a tyrosyl radical in *Syn*Ftn frozen 12 s after initiating iron oxidation (iron added at 80 $Fe^{2+}$/24mer). The simulation parameters are reported in Table 3.2 below. B. Intensity of the tyrosyl radical signal at increasing iron loading in samples of 4.17 µM *Syn*Ftn in 100 mM MES, pH 6.5, frozen 10 s after mixing. Response from the apo-protein and protein loaded with 80 $Fe^{2+}$/24mer are shown in black, and intermediate loadings (12, 24, and 48 equivalents of $Fe^{2+}$) are shown in grey. C. Increase in signal intensity due to the radical at g ≈ 2 in samples of 4.17 µM *Syn*Ftn frozen 50-365 ms after mixing with 72 equivalents of $Fe^{2+}$. Thick traces are the shortest (50 ms) and longest (365 ms) aging times shown. Traces at intermediate freezing times are shown in grey. Figure taken as published from (Bradley *et al.*, 2019).

The lineshape of the WT *Syn*Ftn free radical which has its time dependence plotted in Fig. 3.7D does not change over time, or with different iron loadings (Figs. 3.15B and C). The intensity of the observed tyrosyl radical increases linearly with added $Fe^{2+}$ up to 80 $Fe^{2+}$/24mer. The maximum concentration of free radical was seen at 3 s and coincides with the point at which the MVFC decay is faster than the rate of MVFC formation. This radical is likely involved in an electron transfer pathway between FCs, allowing for a $O_2$ binding at a single FC to take two electrons and form two MVFCs.

**Table 3.2.** The simulation parameters for the Tyr radical EPR spectrum of *Syn*Ftn during iron oxidation (Fig. 3.15A) as determined by TRSSA with an input of $\theta = -4^{\circ}$ and $\rho c_1 = 0.395$. The *inset* shows the neutral tyrosyl radical structure with atom nomenclature. Table shown as published from (Bradley *et al.*, 2019).

| $g_x$ | $g_y$ | $g_z$ |
|---|---|---|
| 2.00743 | 2.00427 | 2.00220 |

| $\Delta H_x$, Gauss | $\Delta H_y$, Gauss | $\Delta H_z$, Gauss |
|---|---|---|
| 6.23 | 4.66 | 4.52 |

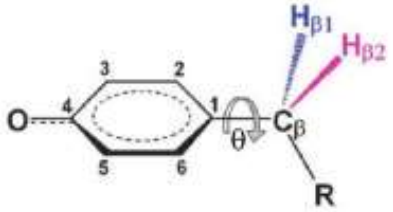


| Protons hyperfine coupling matrix principal values[a] | | | Euler angle[b] $\Phi_1$ | Euler angle $\Phi_2$ | Euler angle $\Phi_3$ |
|---|---|---|---|---|---|
| $A^{\beta1}_{cc}$, MHz | $A^{\beta1}_{bb}$, MHz | $A^{\beta1}_{aa}$, MHz | $-\Phi_1^{\beta1}$, degree | $-\Phi_2^{\beta1}$, degree | $-\Phi_3^{\beta1}$, degree |
| 63.06 | 56.35 | 56.35 | -10.2 | -34.8 | -82.6 |
| $A^{\beta2}_{cc}$, MHz | $A^{\beta2}_{bb}$, MHz | $A^{\beta2}_{aa}$, MHz | $-\Phi_1^{\beta2}$, degree | $-\Phi_2^{\beta2}$, degree | $-\Phi_3^{\beta1}$, degree |
| 18.89 | 15.35 | 15.35 | 29.5 | 4.1 | 50.4 |
| $A^{C3}_{cc}$, MHz | $A^{C3}_{bb}$, MHz | $A^{C3}_{aa}$, MHz | $-\Phi_1^{C3}$, degree | $-\Phi_2^{C3}$, degree | $-\Phi_3^{C3}$, degree |
| -25.9 | -8.1 | -20.5 | 23.0 | 0.0 | 0.0 |
| $A^{C5}_{cc}$, MHz | $A^{C5}_{bb}$, MHz | $A^{C5}_{aa}$, MHz | $-\Phi_1^{C5}$, degree | $-\Phi_2^{C5}$, degree | $-\Phi_3^{C5}$, degree |
| -25.9 | -8.1 | -20.5 | -23.0 | 0.0 | 0.0 |
| $A^{C2}_{cc}$, MHz | $A^{C2}_{bb}$, MHz | $A^{C2}_{aa}$, MHz | $-\Phi_1^{C2}$, degree | $-\Phi_2^{C2}$, degree | $-\Phi_3^{C2}$, degree |
| 7.5 | 5.0 | 1.5 | 40.0 | 0.0 | 0.0 |
| $A^{C6}_{cc}$, MHz | $A^{C6}_{bb}$, MHz | $A^{C6}_{aa}$, MHz | $-\Phi_1^{C6}$, degree | $-\Phi_2^{C6}$, degree | $-\Phi_3^{C6}$, degree |
| 7.5 | 5.0 | 1.5 | -40.0 | 0.0 | 0.0 |

[a] The three principal components of A tensors are $A_{aa}$, $A_{bb}$ and $A_{cc}$.

[b] Three Euler angles are the three rotations of tensor A, $\Phi_1$ - around Z-axis , $\Phi_2$ - around Y and $\Phi_3$ - around X, required to bring aa direction of A with X, bb with Y and cc with Z axes.

**Spin trapping protocols with *Syn*Ftn**

The reduction of $O_2$ by a single electron (a scenario hypothesised to occur in the Y40F variant) in *Syn*Ftn would yield the superoxide radical anion. To investigate this, the spin trap 5,5-

dimethyl-1-pyrroline-*N*-oxide (DMPO) was used to detect short-lived ROS. Fig. 3.16 shows the four DMPO-free radical adduct spectra pertinent to the work on *Syn*Ftn.

Superoxide control spectra were formed by mixing xanthine and xanthine oxidase in the presence of DMPO and $O_2$ (Mottley, Connor and Mason, 1986), while the hydroxyl radical adduct spectra were formed by reacting a DMPO/$Fe^{2+}$ mixture with $H_2O_2$ to perform Fenton chemistry (see Materials and Methods). Adding 1 % ethanol to the xanthine oxidase system yields the same superoxide radical adduct, but adding ethanol to the Fenton system forms an α-hydroxyethyl radical which subsequently reacts with DMPO (Finkelstein, Rosen and Rauckman, 1982).

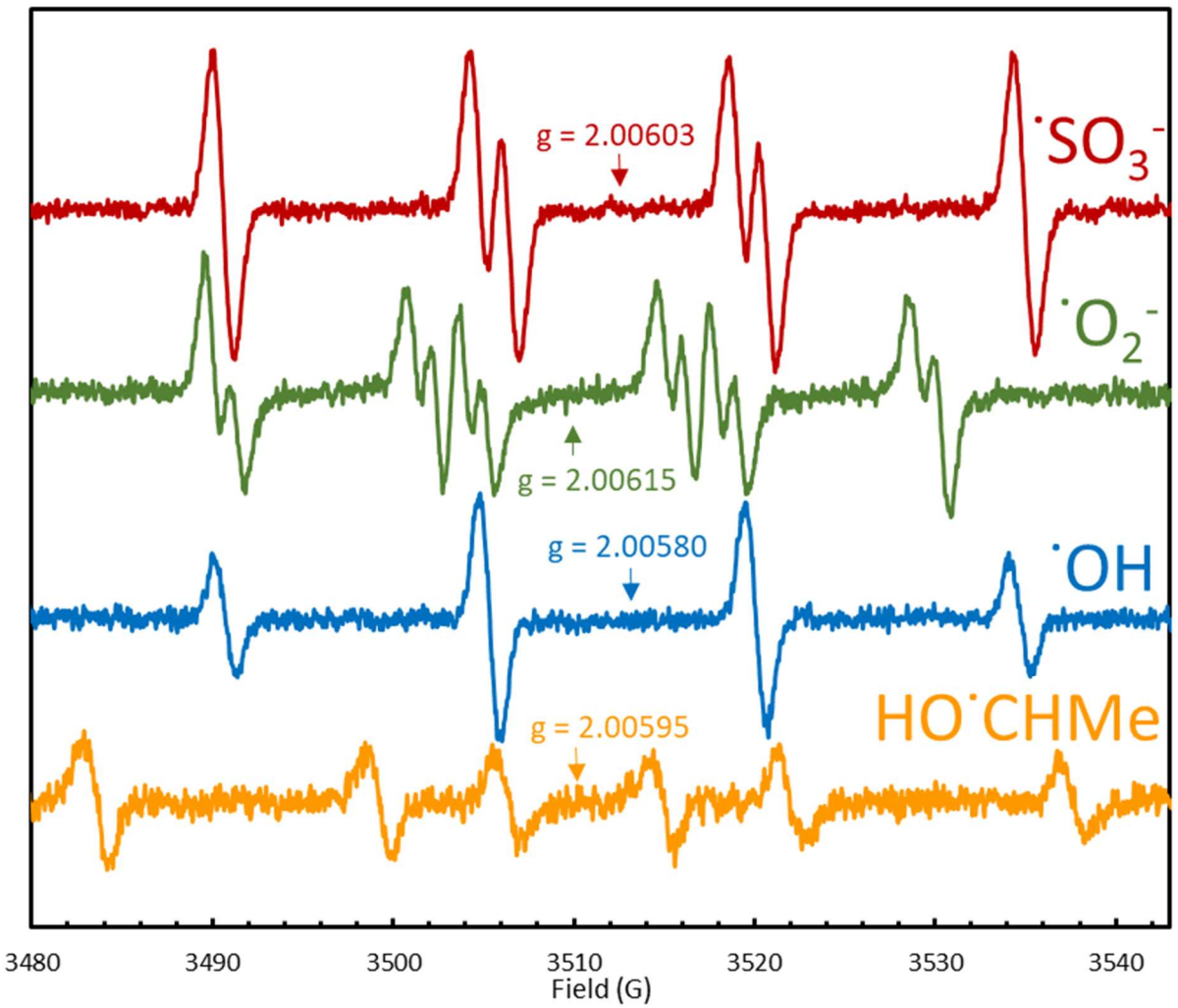

**Fig. 3.16.** Standard spectra of the DMPO-free radical adducts that were prepared in the *Syn*Ftn spin trapping experiments. The superoxide radical adduct was generated using a standard xanthine oxidase system, while the hydroxyl and carbon radical adducts were formed using a $Fe^{2+}$-based Fenton system. The sulfite radical arose from the *Syn*Ftn experiments (Fig. 3.16) and is not a standard spectrum; it is shown here for comparison.

It can be seen from Fig. 3.17 that the Y40F variant produces a different radical to the WT or E62A *Syn*Ftn proteins. The superoxide-DMPO adduct is capable of breaking down to form the hydroxyl-DMPO adduct, but even with identical spectra, these can be distinguished by repeating the experiment in the presence of 1 % ethanol: hydroxyl radicals are capable of removing a hydrogen atom from ethanol, while superoxide radicals cannot (Kuppusamy and Zweier, 1989). Thus, observation of the α-hydroxyethyl radical adduct spectrum confirmed that the Y40F variant formed hydroxyl radicals, not superoxide. Superoxide may still be formed during the initial reaction of $Fe^{2+}$ at the FCs and $O_2$, but the high concentration of MVFC in the Y40F variant's EPR spectra (Fig. 3.9) shows that superoxide must be released and consumed before the slow oxidative formation of the diferric FC. This suggests that the mechanism of MVFC formation is more complex than a simple one-electron reduction of $O_2$. The presence of hydroxyl radicals is easily explained by the abolishment of the rapid phase of $Fe^{2+}$ oxidation in the Y40F variant; because $Fe^{2+}$ is oxidized slowly, it is susceptible to oxidation by $H_2O_2$ released from the FCs.

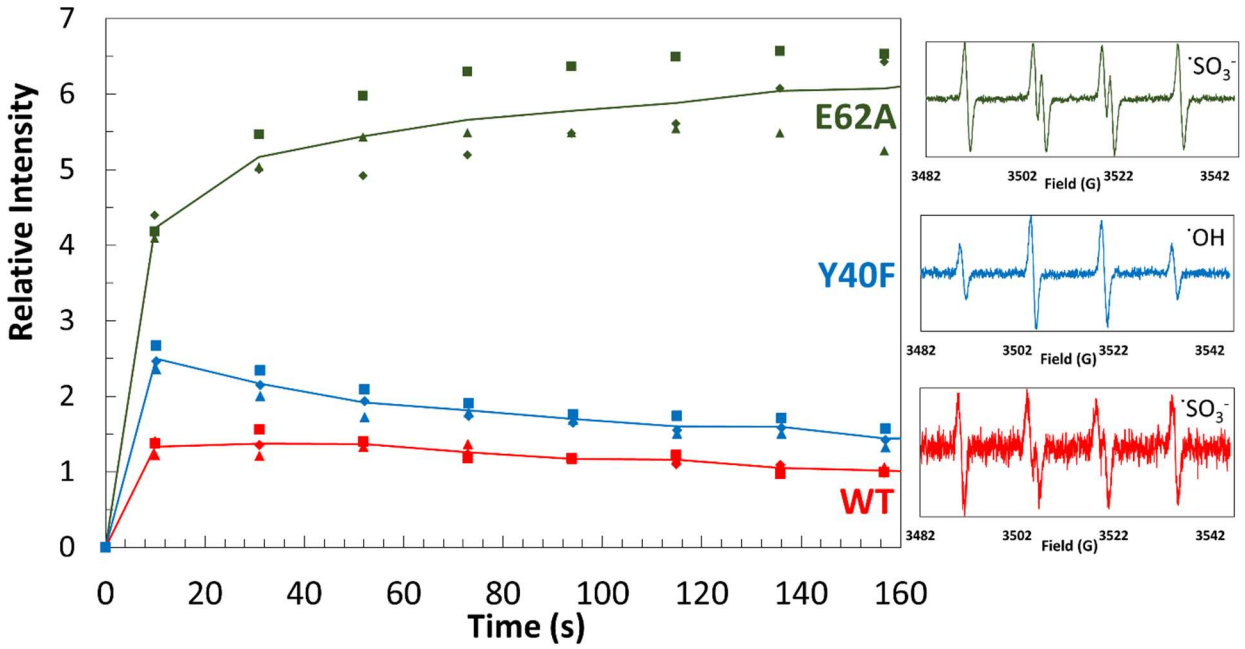


**Fig. 3.17.** A plot of the DMPO free radical adduct intensities of WT *Syn*Ftn and two variants, Y40F and E62A, attained using room temperature cw-EPR. The corresponding spectra for each DMPO radical adduct are also shown, with the nature of the adducts assigned. Protein, $Fe^{2+}$ and DMPO concentrations were 5.4 µM, 375 µM (approx. 70 $Fe^{2+}$/24mer) and 40 mM respectively.

The detection of sulfite radicals in the WT protein and E62A variant was unexpected, and the timescale within which the sulfite radical adduct intensity kept increasing in the E62A variant was not in agreement with the rates of decay for either the MVFC or the Tyr radical. It has been suggested that DMPO is able to react with sulfurous compounds to form sulfite radical adducts through a radical-free, Forrester-Hepburn pathway via nucleophilic addition (Zamora and Villamena, 2012). It is not clear why sulfite radicals are not observed in the Y40F variant, or why the relative intensity of sulfite radical adducts is so much higher in the E62A variant than in the WT protein. To determine the true intermediate oxygen species, the experiment

could be repeated in sulfur-free buffers (MES was used in these experiments) using a different iron salt to ferrous ammonium sulfate.

## Mitochondrial ferritin

### Rapid freeze quench electron paramagnetic resonance spectroscopy of full-length mitochondrial ferritin

Rapid freeze quench (RFQ) was used to mix full-length FtMt with $Fe^{2+}$ aerobically and prepare samples with short reaction times for EPR spectroscopy. Example RFQ EPR spectra for FtMt is shown in Fig. 3.18A. Despite the large artefactual oxygen line present in the sample's spectra, the key features attributable to the FtMt reaction can be discerned and are labelled. The free radical appears to be a sum of at least two radicals, one of which could possibly a peroxyl radical formed on tryptophan residues within the protein; the g value at 2.0366 is characteristic of these species (Svistunenko, 2001). The g factors for a peroxyl species do not align perfectly with those shown in Fig. 3.18B, likely due to the presence of a tyrosyl radical detected within the same field. It is worth highlighting that the radical bears some resemblance to the radical reported in HuHF (Ebrahimi, Hagedoorn and Hagen, 2013) which was assigned to a protein-based radical intermediate.

Unlike other ferritins discussed in this work, FtMt expressions had a significantly lower yield. As an organelle-specific ferritin from humans, it is possible that the classical ferritin protocol utilising an *E. coli* expression system protocol can be refined.

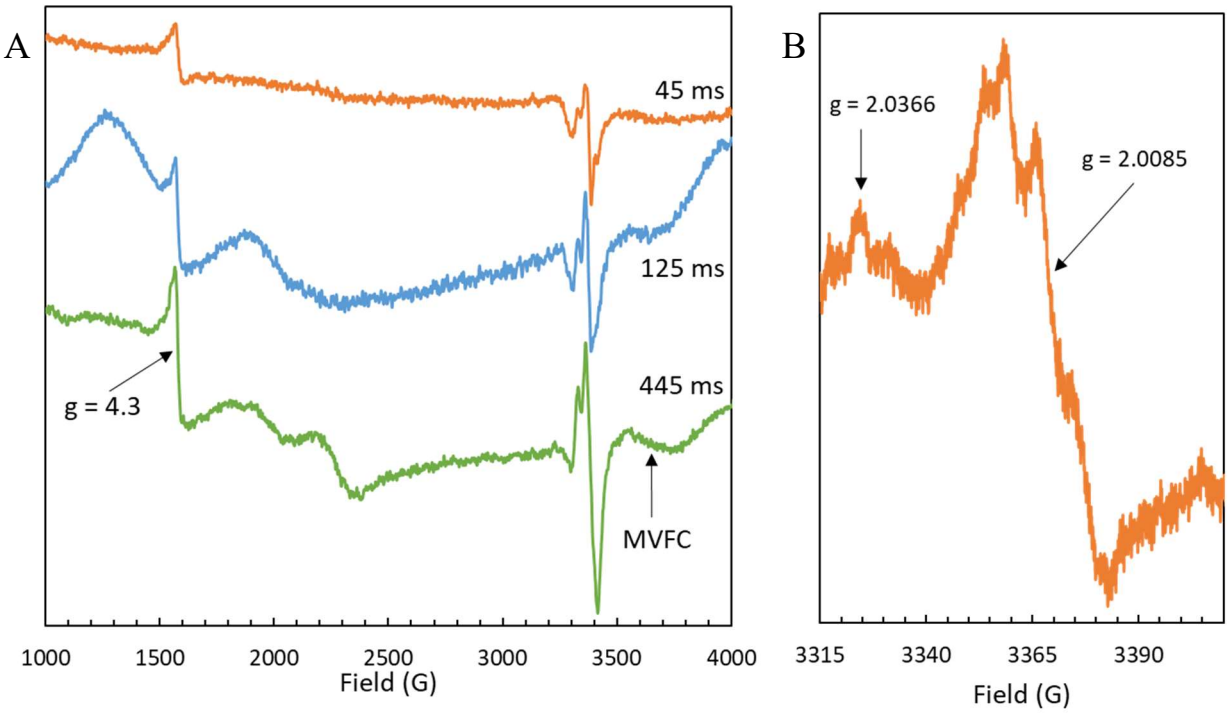


**Fig. 3.18.** A. Selected RFQ EPR spectra of 4.17 μM full-length FtMt mixed with 72 $Fe^{2+}$/24mer, frozen at 45, 125, and 445 ms. B. The spectrum of the free radical in the sample with a 45 ms freezing time, recorded at a slower scan rate. The spectra were measured at 10 K using a microwave frequency $\nu_{MW}$ = 9.4693 GHz.

As a result of the poor-quality protein (and lower yield) most experiments were performed on the Δ9 variant described below, which had an improved yield over the full-length variant.

**Characterisation of the Δ9 mitochondrial ferritin variant**

FtMt has been indicated to reduce the level of reactive oxygen species (ROS) in mitochondria (Campanella *et al.*, 2009). A truncated FtMt variant where the N-terminal chain is shortened by nine residues has 79 % sequence homology with HuHF and has been studied in other work

(Langlois d'Estaintot *et al.*, 2004), (Bou-Abdallah *et al.*, 2005). An EPR investigation into the properties of the Δ9 FtMt variant was carried out, simultaneously comparing the protein to HuHF and full-length FtMt. Fig. 3.19 shows the EPR spectra of HuHF and the Δ9 FtMt variant.

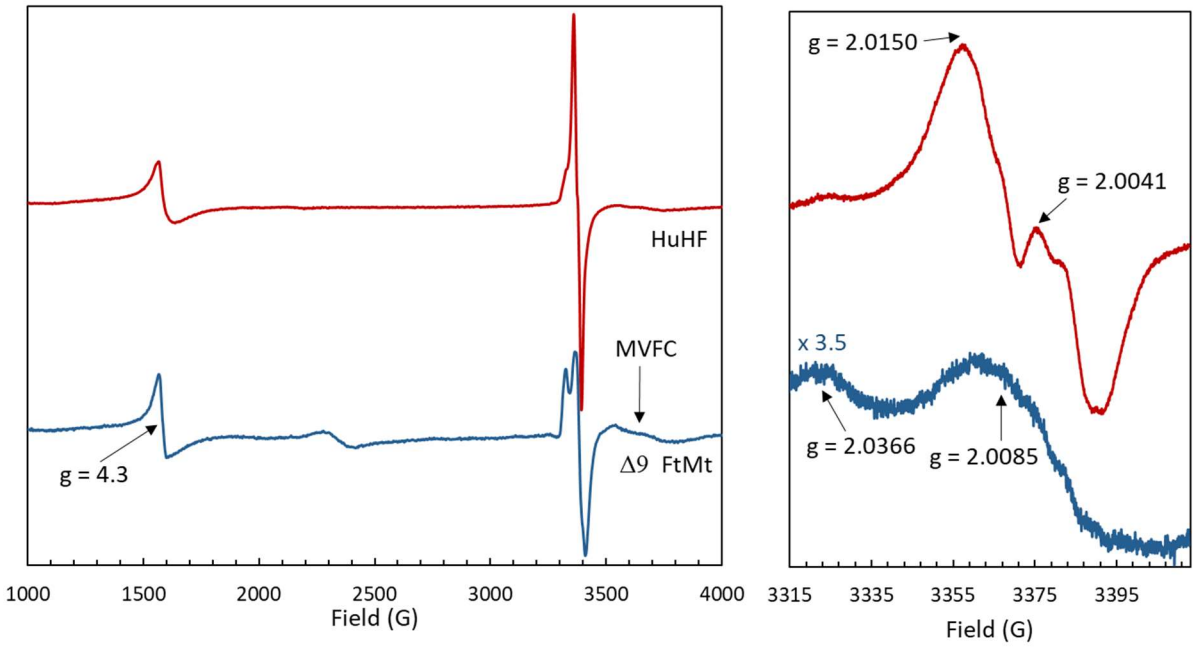


**Fig. 3.19.** EPR spectra of 8.3 μM HuHF (red) at microwave powers $P_{MW}$ = 3.16 mW (left) and 0.05 mW (right) compared to those of FtMt (blue). Each protein was mixed with 48 $Fe^{2+}$/ 24mer aerobically and frozen 10 s after mixing.

As demonstrated in Fig. 3.1 a MVFC signal was detected in HuHF. The lineshape of the g = 4.3 signal is of comparable intensity in both variants, but with a different lineshape, which is consistent with the idea that the diiron complex formed at each FC is not equivalent (Bou-Abdallah *et al.*, 2005). HuHF appears to primarily form a tyrosyl radical. FtMt's free radical appears to be similar to that shown in the full-length variant but remains different to the FtMt free radical spectrum that was displayed in a grant submission in 2017 (see Appendix 3).

FtMt has been reported to be incapable of detoxifying $H_2O_2$ (Bou-Abdallah, 2010). The Δ9 FtMt variant's reactivity with $H_2O_2$ was examined by EPR spectroscopy; the results of these experiments are shown in Fig. 3.20.

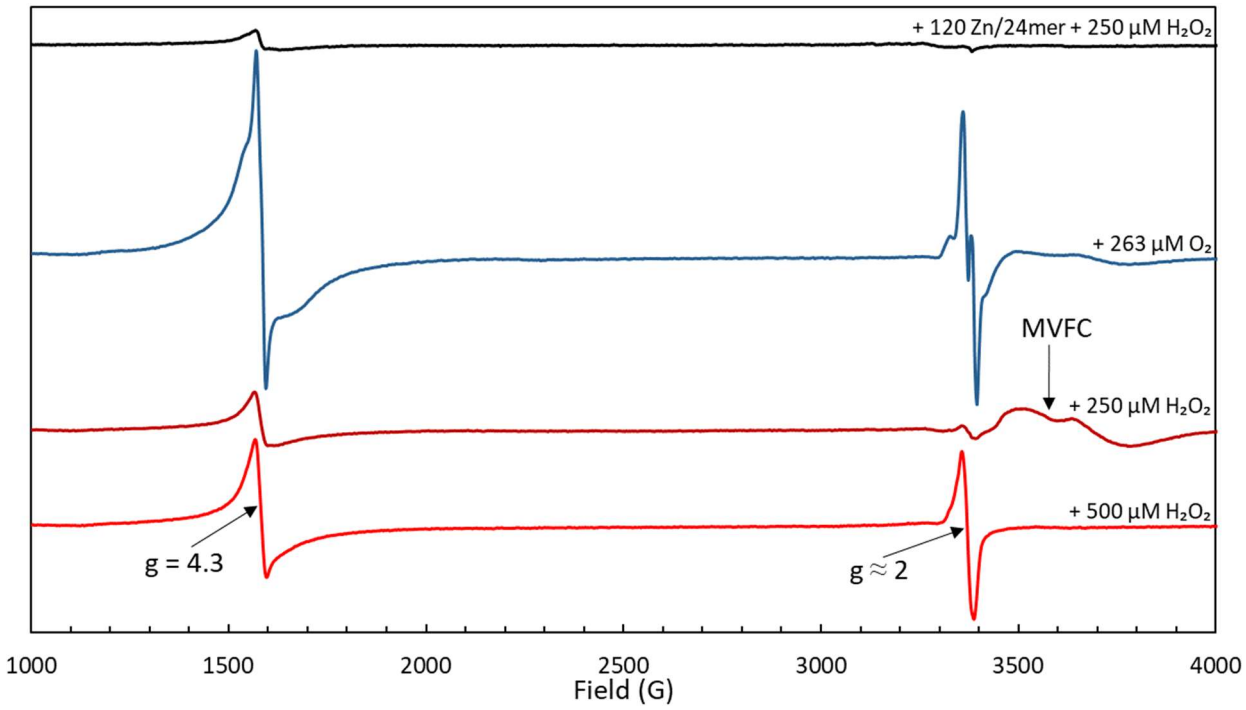


**Fig. 3.20.** EPR spectra of the Δ9 FtMt (8.3 µM) variant incubated anaerobically with 72 $Fe^{2+}$/24mer, and then mixed with 250 (dark red) or 500 µM (bright red) $H_2O_2$, and frozen 12 s thereafter. The black spectrum was recorded for the same conditions, but 120 $Zn^{2+}$/24mer was added anaerobically prior to incubation with $Fe^{2+}$. The blue spectrum shows a control where the Δ9 FtMt is mixed with 72 $Fe^{2+}$ under atmospheric $O_2$ and frozen at 12 s.

The spectra show that when mixed with 250 µM [$H_2O_2$], a larger MVFC signal is seen than in the $O_2$ reaction. This effect is not seen at 500 µM [$H_2O_2$]; instead a large free radical is observed (Fig. 3.21 shows the lineshapes of the free radical in greater detail). A much smaller g = 4.3 signal is observed in the reactions where $H_2O_2$ was used as an oxidant, suggesting that less $Fe^{3+}$

has been oxidized in the 12 s timescale in which the samples were prepared. Overall, the spectra support the hypothesis that $H_2O_2$ is a less effective oxidant than $O_2$.

The larger free radical observed at 500 μM [$H_2O_2$] is reminiscent of a peroxyl radical, while the free radical formed by oxidation by $O_2$ in Fig. 3.19 is likely to be tyrosine-based (see Fig. 3.21 below). There was variability in the intensity of peroxyl radical observed between protein batches for both the full-length and the Δ9 FtMt when oxidizing $Fe^{2+}$ with $O_2$; the reason for this was not clear. The low yields of the FtMt proteins lead to the speculation that the proteins' purities were lower than that of *Syn*Ftn, or *E. coli* BFR (see Chapters 4 and 5).

It is important to highlight that the formation of the MVFC and the free radical are dependent on the FC; when $Zn^{2+}$ is added to obstruct the FC prior to $Fe^{2+}$ addition, no chemistry is observed. This suggests that the peroxyl radical detected at high [$H_2O_2$] cannot form as the result of Fenton chemistry.

The results in Fig. 3.20 should be considered in the context of other work where FtMt's reactivity with $H_2O_2$ was studied (Bou-Abdallah *et al.*, 2005). Here, it is suggested that $H_2O_2$ is eliminated through two one-electron transfers at the surface of the core, and that the FC of FtMt cannot reduce $H_2O_2$. In the timescale of the reactions shown in Fig. 3.20, there will be little to no mineral core formed, and the formation of the MVFC under anaerobic conditions by $H_2O_2$ suggests that the FC can indeed utilise peroxide as an oxidant.

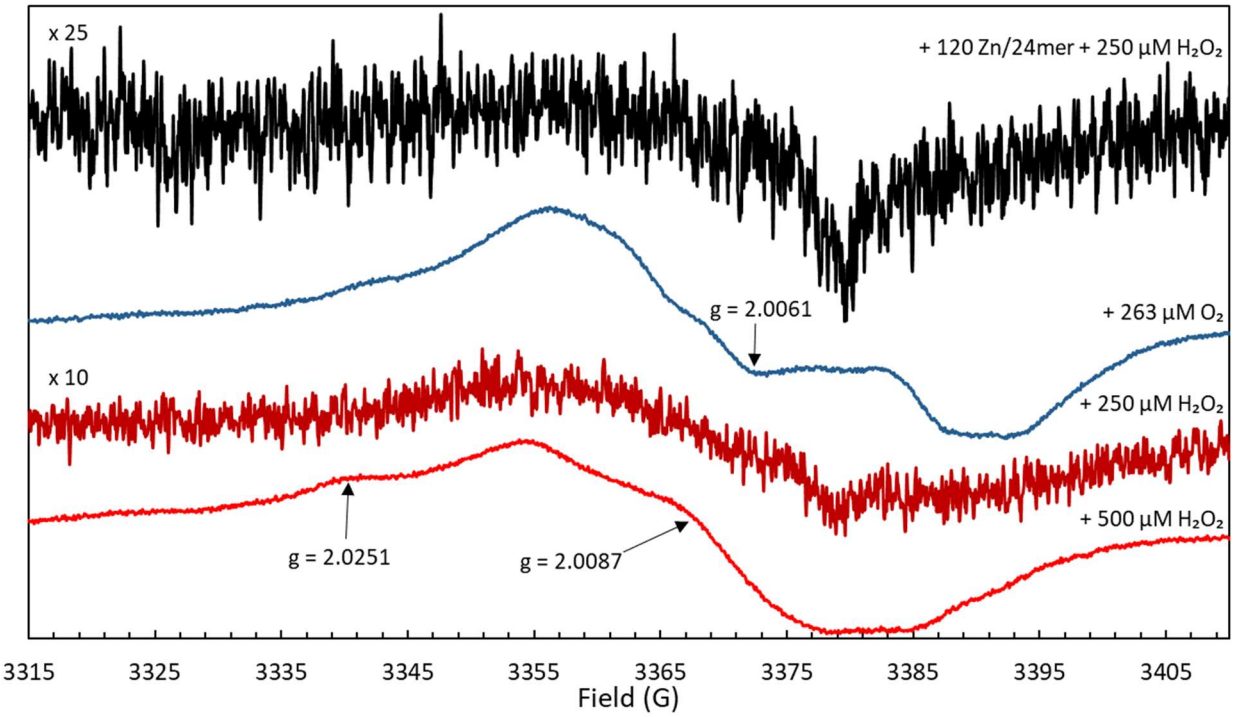


**Fig. 3.21.** The free radical EPR spectra shown in Fig. 3.19, recorded at a slower scan rate at microwave power $P_{MW}$ = 3.16 mW.

To simulate the radical formed when Δ9 FtMt oxidizes $Fe^{2+}$ with $O_2$, the lineshape of the peroxyl free radical (the spectrum of the 500 µM $H_2O_2$ sample) was subtracted from the experimental spectrum using a variable coefficient. This resulted in the blue difference spectrum shown in Fig. 3.22.

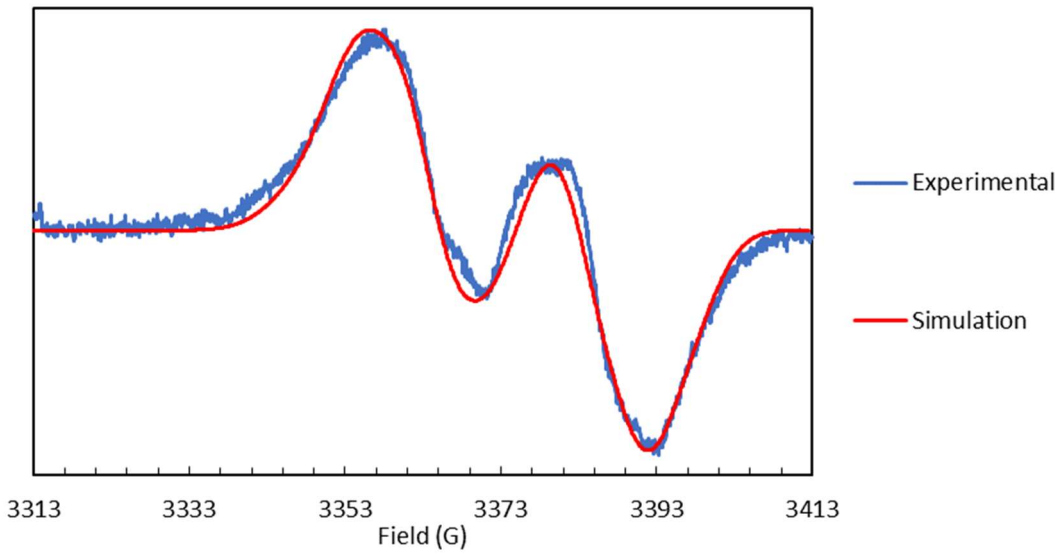


**Fig. 3.22.** Simulation (orange trace) of the free radical found on FtMt (blue trace). The TRSSA simulation parameters are shown below in Table 3.3.

The difference spectrum could be simulated as a single tyrosyl radical using the tyrosyl radical spectra simulation algorithm (TRSSA), the parameters of which are reported in Table 3.3.

**Table 3.3.** TRSSA-Y generated parameters used to simulate the FtMt free radical signal.

| Microwave frequency, GHz |
|---|
| 9.46674 |

| $H_1$, G | $H_2$, G |
|---|---|
| 3312.7 | 3412.5 |

| Data points |
|---|
| 2048.0 |

| $g_x$ | $g_y$ | $g_z$ |
|---|---|---|
| 2.00842 | 2.00434 | 2.00216 |

| Hyperfine coupling matrix principal values | | | Euler angle α | Euler angle β | Euler angle γ |
|---|---|---|---|---|---|
| $A^{\beta1}_{cc}$, MHz | $A^{\beta1}_{bb}$, MHz | $A^{\beta1}_{aa}$, MHz | $-\Phi_1^{\beta1}$, degree | $-\Phi_2^{\beta1}$, degree | $-\Phi_3^{\beta1}$, degree |
| 58.45 | 52.24 | 52.24 | -10.0 | -35.2 | -83.4 |
| $A^{\beta2}_{cc}$, MHz | $A^{\beta2}_{bb}$, MHz | $A^{\beta2}_{aa}$, MHz | $-\Phi_1^{\beta2}$, degree | $-\Phi_2^{\beta2}$, degree | $-\Phi_3^{\beta1}$, degree |
| 18.48 | 15.24 | 15.24 | 29.6 | 4.3 | 52.1 |
| $A^{C3}_{cc}$, MHz | $A^{C3}_{bb}$, MHz | $A^{C3}_{aa}$, MHz | $-\Phi_1^{C3}$, degree | $-\Phi_2^{C3}$, degree | $-\Phi_3^{C3}$, degree |
| -25.9 | -8.1 | -20.5 | 23.0 | 0.0 | 0.0 |
| $A^{C5}_{cc}$, MHz | $A^{C5}_{bb}$, MHz | $A^{C5}_{aa}$, MHz | $-\Phi_1^{C5}$, degree | $-\Phi_2^{C5}$, degree | $-\Phi_3^{C5}$, degree |
| -25.9 | -8.1 | -20.5 | -23.0 | 0.0 | 0.0 |
| $A^{C2}_{cc}$, MHz | $A^{C2}_{bb}$, MHz | $A^{C2}_{aa}$, MHz | $-\Phi_1^{C2}$, degree | $-\Phi_2^{C2}$, degree | $-\Phi_3^{C2}$, degree |
| 7.5 | 5.0 | 1.5 | 40.0 | 0.0 | 0.0 |
| $A^{C6}_{cc}$, MHz | $A^{C6}_{bb}$, MHz | $A^{C6}_{aa}$, MHz | $-\Phi_1^{C6}$, degree | $-\Phi_2^{C6}$, degree | $-\Phi_3^{C6}$, degree |
| 7.5 | 5.0 | 1.5 | -40.0 | 0.0 | 0.0 |

| $\Delta H_x$, G | $\Delta H_y$, G | $\Delta H_z$, G |
|---|---|---|
| 6.51 | 5.11 | 5.06 |

The kinetics of the Δ9 FtMt variant were also ascertained using RFQ EPR spectroscopy. Examples of the spectra are shown in Fig. 3.23 below. These show that the MVFC is of much lower intensity in this variant than in the full-length protein, and the free radical is of a higher concentration (≈ 1.42 μM at 445 ms). A greater proportion of the free radical appears to be a peroxyl-species than in full-length FtMt.

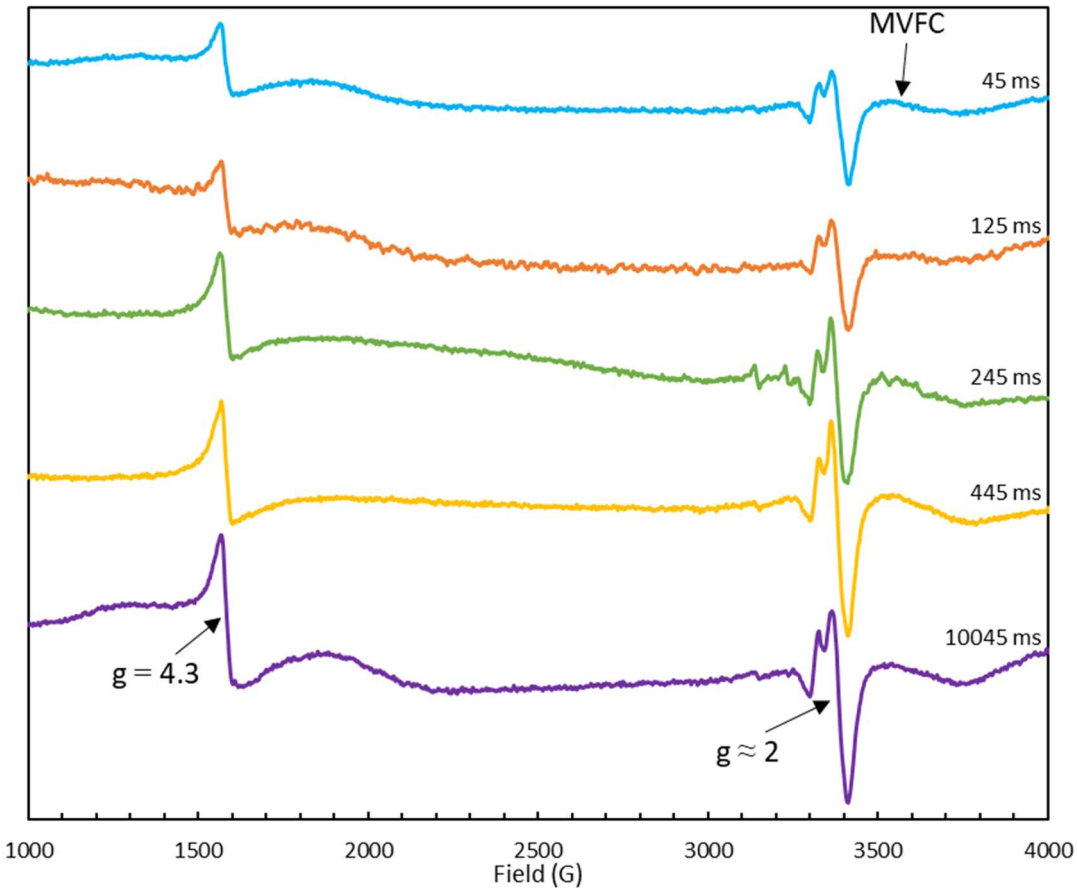


**Fig. 3.23.** EPR spectra of 4.17 μM Δ9 FtMt + 72 $Fe^{2+}$ prepared by RFQ, frozen at selected timepoints after mixing.

Kinetic plots for the g = 4.3 (rhombically coordinated, mononuclear $Fe^{3+}$), the MVFC, and the free radical are each reported in Fig. 3.24. The relative intensities were plotted through subtraction of a variable coefficient (Svistunenko *et al.*, 2000). Due to changes in the lineshape of all three components as the reaction progressed, relative intensities were determined within three groups of samples within which it was believed the lineshape was comparatively consistent. Double integration was then performed on a sample in each set with the smallest oxygen line, which would allow for the expression of all samples with common units. Finally, the sample length within each tube was taken into account. The results of this analysis are shown below in Fig. 3.24.

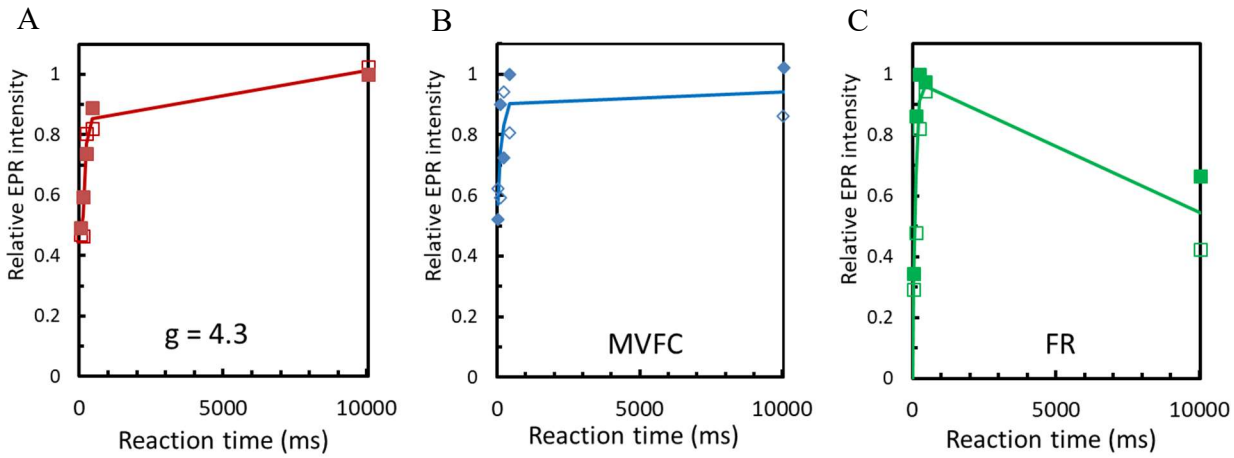


**Fig. 3.24.** EPR monitored iron-$O_2$ reactivity of Δ9 FtMt + 72 $Fe^{2+}$; intensity plots showing the formation of mononuclear $Fe^{3+}$ (A), MVFC (B), and free radical (C) detected by low-temperature EPR spectroscopy over the first 10 s of iron oxidation. Samples were prepared in two batches over two days, with the filled and unfilled shapes showing the timepoints for each series.

As seen in other ferritins, the mononuclear $Fe^{3+}$ concentration increases with time, but does not reflect the concentration of iron present in the samples due to antiferromagnetic coupling (Malone *et al.*, 2004). All the reagents reach a maximal concentration at ≈ 445 ms, but only the free radical showed decay within the timescale monitored. It could be speculated that the MVFC may reach a maximal concentration between 445 ms and 10 s, but due to limitations associated with the protein yield (which was only marginally improved in the Δ9 variant) it was not possible to prepare any further timepoints within the time available.

Unlike in *Syn*Ftn, replacing Y25 in the truncated FtMt protein did not prevent free radical formation in the Y25F variant of Δ9 FtMt. RFQ EPR spectra of this variant are shown in Fig. 3.25A. The free radical (highlighted in Fig. 3.25B) has g values that perfectly match the properties of a peroxyl-species. The concentration of this free radical was approximately 1.09

μM at 445 ms. This is 77 % of the free radical intensity observed in the unsubstituted Δ9 FtMt variant and supports the hypothesis that the Δ9 FtMt variant produces proportionally more peroxyl-radical species than tyrosine-based free radicals when compared to the full-length FtMt.

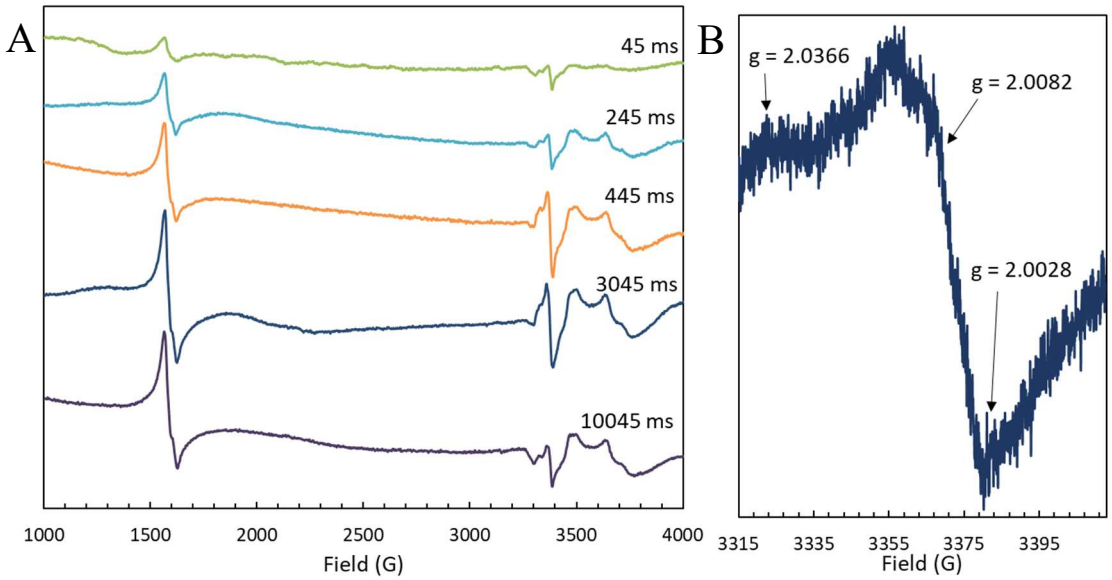


**Fig. 3.25.** A. Selected RFQ EPR spectra showing Y25F Δ9 FtMt frozen at selected timepoints after mixing aerobically with $Fe^{2+}$. B. EPR spectrum of the free radical frozen 3045 ms after mixing, showing the g values reminiscent of a peroxyl-free radical. The spectrum was recorded at 10 K at microwave frequency $\nu_{MW}$ = 9.4695 GHz.

The EPR kinetics of the Y25F Δ9 FtMt variant are displayed in Fig. 3.26 below. Stopped flow experiments by J.M. Bradley suggest that the Y25F substitution in Δ9 FtMt causes the rapid phase of $Fe^{2+}$ oxidation to be three times slower, but with limited timepoints, it is not possible to comment on the agreement of the RFQ data with this statement. Removal of Y25 does not

seem to slow the formation of the MVFC, but it appears to begin decaying within the observed timescale. Furthermore, the MVFC is notably more intense.

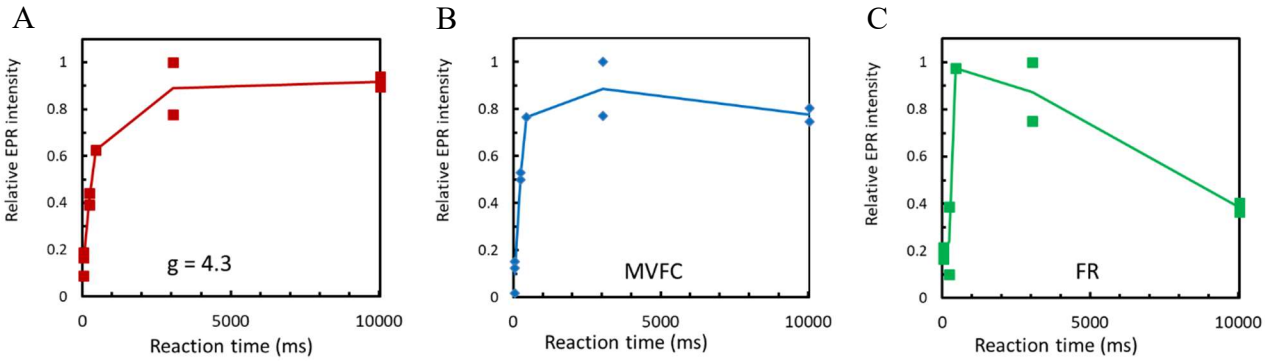


**Fig. 3.26.** EPR monitored iron-$O_2$ reactivity of Y25F Δ9 FtMt + 72 $Fe^{2+}$; intensity plots showing the formation of mononuclear $Fe^{3+}$ (A), MVFC (B), and free radical (C) detected by low-temperature EPR spectroscopy over the first 10 s of iron oxidation.

***n* ferr**

The EPR spectra of *n* ferr and its Y24F variant (this removes the universally conserved tyrosine analogous to Y25 in HuHF, Y40F in *Syn*Ftn and Y34 in FtMt) were recorded. Like *Syn*Ftn and FtMt, both form a MVFC after the oxidation of the FC by $O_2$ (Fig. 3.26). The MVFC is of a higher intensity than in FtMt, but lower than in *Syn*Ftn. Like in FtMt, the Y24F variant increases the observable concentration of MVFC.

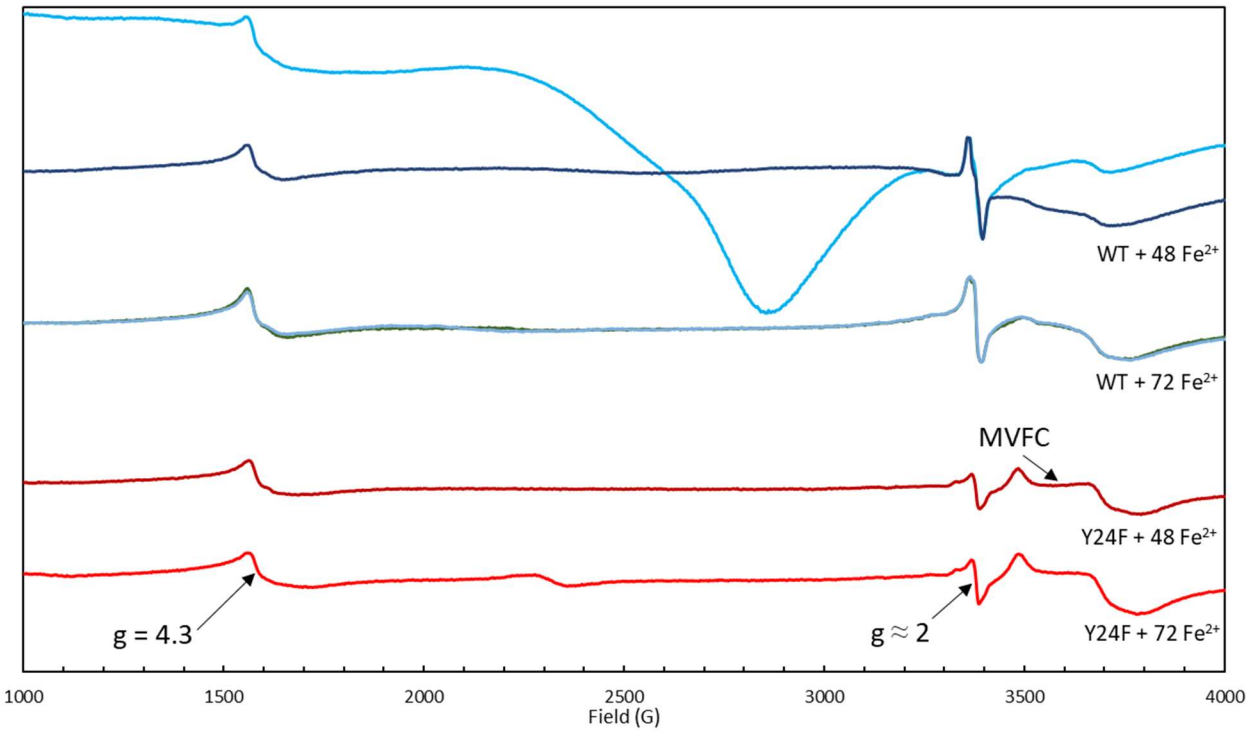


**Fig. 3.27.** Stacked plot showing low-temperature EPR spectra of 4.16 μM *n*-ferr after being mixed with 48 or 72 $Fe^{2+}$/24mer under aerobic conditions and frozen 12 s after mixing. The blue traces show the WT protein, where there are two repeats per iron loading, while the red traces report the Y24F variant All spectra were recorded using microwave power $P_{MW}$ = 3.16 mW.

Like in FtMt, it appears that *n* ferr is capable of forming peroxyl radicals. However, there is little, if any, peroxyl radical present in the WT spectra where only 48 $Fe^{2+}$/24mer is added. The free radical in the Y24F is exclusively peroxyl radical at both 48 and 72 $Fe^{2+}$/24mer. While the peroxyl radical in Δ9 FtMt did not decrease in intensity when Y25 was substituted, in *Syn*Ftn, the Y40F variant only had a small intensity associated with peroxyl radical. *n* ferr appears to appear to have a drop in intensity associated with the Y24F substitution, but it is not as extreme as that in *Syn*Ftn.

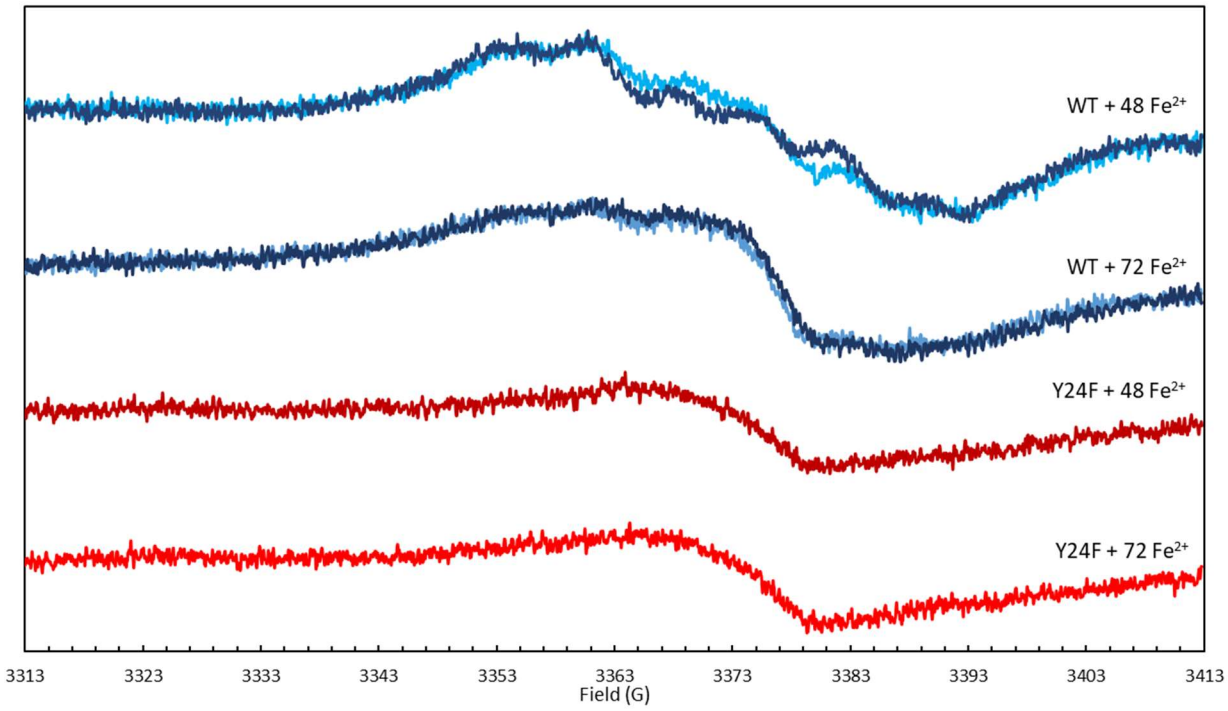


**Fig. 3.28.** The *n* ferr free radicals formed by oxidation of $Fe^{2+}$ by $O_2$ in Fig. 3.27, recorded at a slower scan rate and lower microwave power $P_{MW}$ = 0.05 mW.

Several attempts to simulate the radical as a single tyrosyl radical were performed. This was ineffective, suggesting the radical is a mixture of several radical species. This was supported by the similarity of this lineshape to that of *E. coli* bacterioferritin's free radical signal when $H_2O_2$ is used as an oxidant (See Fig. 5.8). The lineshape in this protein was hypothesised to be the sum of several tyrosyl and tryptophanyl radicals. However, these free radicals could not be separated based on their microwave power saturation properties over the range of powers measured. Instead, a 'pure' radical lineshape was attained by subtracting a high iron-loaded *n* ferr sample spectrum (72 $Fe^{2+}$/24mer) from a low loaded sample spectrum (48 $Fe^{2+}$/24mer). This yielded the lineshape shown and simulated in Fig. 3.29.

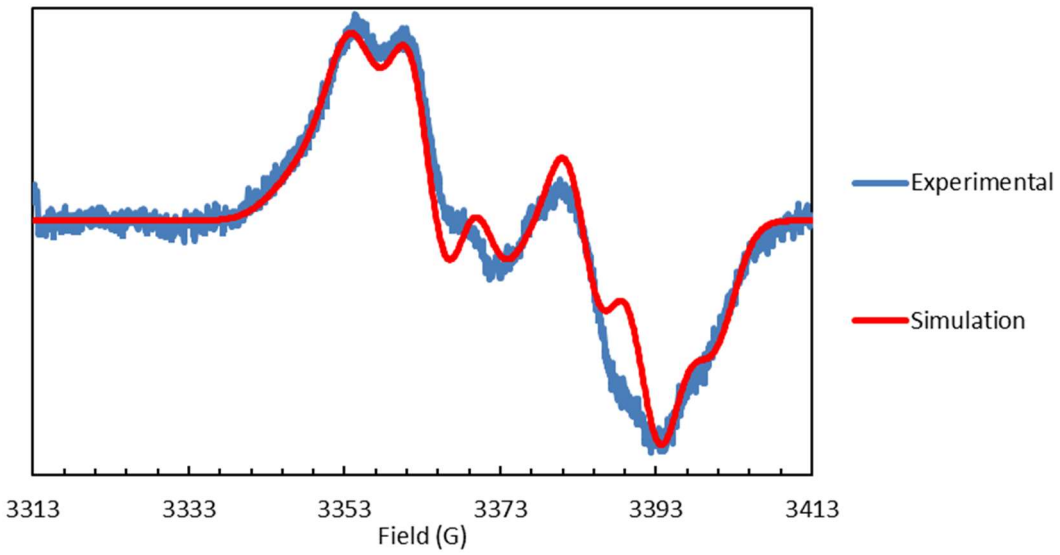


**Fig. 3.29.** Simulation (red trace) of the free radical found on *n* ferr (blue trace). The simulation parameters are shown below in Table 3.4.

The parameters of the following simulation match those of a single tyrosyl radical. As there are currently no published crystal structures of *n* ferr, the conformational angle cannot be compared to the protein.

**Table 3.4.** TRSSA-Y generated parameters used to simulate the *n* ferr free radical signal in Fig. 3.29 above.

| Microwave frequency, GHz |
|---|
| 9.46856 |

| $H_1$, G | $H_2$, G |
|---|---|
| 3312.7 | 3412.5 |

| Data points |
|---|
| 2048.0 |

| $g_x$ | $g_y$ | $g_z$ |
|---|---|---|
| 2.00730 | 2.00425 | 2.00220 |

| Hyperfine coupling matrix principal values | | | Euler angle α | Euler angle β | Euler angle γ |
|---|---|---|---|---|---|
| $A^{\beta1}_{cc}$, MHz | $A^{\beta1}_{bb}$, MHz | $A^{\beta1}_{aa}$, MHz | $-\Phi_1^{\beta1}$, degree | $-\Phi_2^{\beta1}$, degree | $-\Phi_3^{\beta1}$, degree |
| 60.69 | 54.23 | 54.23 | -8.2 | -38.5 | -89.4 |
| $A^{\beta2}_{cc}$, MHz | $A^{\beta2}_{bb}$, MHz | $A^{\beta2}_{aa}$, MHz | $-\Phi_1^{\beta2}$, degree | $-\Phi_2^{\beta2}$, degree | $-\Phi_3^{\beta1}$, degree |
| 27.99 | 24.45 | 24.45 | 30.2 | 5.8 | 65.0 |
| $A^{C3}_{cc}$, MHz | $A^{C3}_{bb}$, MHz | $A^{C3}_{aa}$, MHz | $-\Phi_1^{C3}$, degree | $-\Phi_2^{C3}$, degree | $-\Phi_3^{C3}$, degree |
| -25.9 | -8.1 | -20.5 | 23.0 | 0.0 | 0.0 |
| $A^{C5}_{cc}$, MHz | $A^{C5}_{bb}$, MHz | $A^{C5}_{aa}$, MHz | $-\Phi_1^{C5}$, degree | $-\Phi_2^{C5}$, degree | $-\Phi_3^{C5}$, degree |
| -25.9 | -8.1 | -20.5 | -23.0 | 0.0 | 0.0 |
| $A^{C2}_{cc}$, MHz | $A^{C2}_{bb}$, MHz | $A^{C2}_{aa}$, MHz | $-\Phi_1^{C2}$, degree | $-\Phi_2^{C2}$, degree | $-\Phi_3^{C2}$, degree |
| 7.5 | 5.0 | 1.5 | 40.0 | 0.0 | 0.0 |
| $A^{C6}_{cc}$, MHz | $A^{C6}_{bb}$, MHz | $A^{C6}_{aa}$, MHz | $-\Phi_1^{C6}$, degree | $-\Phi_2^{C6}$, degree | $-\Phi_3^{C6}$, degree |
| 7.5 | 5.0 | 1.5 | -40.0 | 0.0 | 0.0 |

| $\Delta H_x$, G | $\Delta H_y$, G | $\Delta H_z$, G |
|---|---|---|
| 7.98 | 6.36 | 6.17 |

## Discussion

### The detection of a mixed-valence ferroxidase centre in human H-chain ferritin

HuHF was selected for control experiments as a ferritin which did not form a MVFC. The observation of a MVFC in HuHF directly upon aerobic addition of $Fe^{2+}$ was an unexpected result and would need to be repeated with subsequent batches of protein to be considered significant; this has never been observed in any previous work performed through EPR or Mössbauer studies (Chen-Barrett *et al.*, 1995), (Ebrahimi, Hagedoorn and Hagen, 2013). The existence of iron in the FCs before the addition of $Fe^{2+}$ is unlikely, as iron removal procedures were followed and there was no indication of $Fe^{3+}$ present in UV/vis spectra. The EPR spectrum of the apo-protein is shown in Appendix 4. While incompatible with the diferric cluster mechanism typically associated with mammalian ferritins, it is also marginally problematic for the $Fe^{II}/Fe^{III}$ displacement mechanism, which does not elaborate upon how a MVFC would form from apo-ferritin oxidizing two $Fe^{2+}$ with $O_2$.

$Fe^{3+}Fe^{2+}$ centres are not unprecedented; they have been found in hemerythrins (Pearce *et al.*, 1987), rubrerythrins (Smoukov *et al.*, 2003), purple acid phosphatases (Lauffer *et al.*, 1983), RNR (Davydov *et al.*, 1997), soluble methane monooxygenase (Davydov *et al.*, 1999), and HD-domain protein superfamily members *myo*-inositol oxygenase (MIOX) (Xing, Diao, *et al.*, 2006) and PhnZ (Wörsdörfer, Lingaraju, *et al.*, 2013). With the exception of MIOX, however, the mixed-valent diiron centre is formed by reduction of the diferric form, and not by oxidation by $O_2$ of the diferrous form. While there is a relatively low sequence homology between *n* ferr and HuHF, it is also notable for forming the MVFC from a diferrous FC after reacting with $O_2$.

There are numerous examples of carboxylate-bridged diiron proteins that have a four α-helical bundle motif which coordinates the diiron centre with a large number of carboxylate ligands. This is seen in some ferritins and BFRs (Sazinsky and Lippard, 2006), RNRs, plant fatty acyl-ACP desaturase, methane monooxygenase, and toluene 4-monooxygenase (Trehoux, Mahy and Avenier, 2016) (Jasniewski and Que, 2018). All of these (except *E. coli* BFR, see Fig. 4.7) activate $O_2$ to form a diferric-peroxo intermediate. The HD-domain of MIOX is exceptional in that the diiron centre is coordinated instead by histidines. This protein uses $O_2$ to form an $Fe^{3+}Fe^{2+}$ species that reacts with an additional $O_2$ molecule to form a diferric-superoxo complex which is oxidizing enough to cleave a C-H bond. As such, the mixed-valent form of MIOX is only observed when reacted with sub-stoichiometric [$O_2$], or in the presence of a mild reductant (Xing, Hoffart, *et al.*, 2006). At supra-stoichiometric [$O_2$], the diferric species is formed, just as in the carboxylate-coordinated diiron proteins. Thus, the observation of a MVFC in the carboxylate-bridged ferritins HuHF, *Syn*Ftn, FtMt and *n* ferr following oxidation by $O_2$ is an interesting outcome. This forms in the absence of a reductant, and it has been proven in *Syn*Ftn to appear regardless of the $O_2$ excess (Bradley *et al.*, 2019). It is not immediately clear why these MVFC species form in ferritins, given there is no apparent need for highly oxidative intermediates during mineralisation. The $Fe_A$ and $Fe_B$ sites in *Syn*Ftn and FtMt have highly comparable ligands to HuHF, yet a DFP intermediate has not been detected in *Syn*Ftn.

**Detecting peroxide release in human H-chain ferritin with a novel assay**

It is standard for those measuring $H_2O_2$ release to use the Amplex® Red Assay which uses horseradish peroxidase to oxidize the Amplex® Red reagent and produce spectroscopically observable changes. However, this assay is only sensitive between a pH range of 7-8, and

involves the addition of numerous non-native reagents. A superior assay when using a PDA is to use the DyP-type peroxidase DtpA. This allows for the direct detection of $H_2O_2$ reacting with the peroxidase by observing the change in oxidation state of the heme group with the simple addition of a single reagent.

### *Syn*Ftn operates through a novel mechanism

Despite being a prokaryotic ferritin, *Syn*Ftn contains an FC that more closely resembles those of eukaryotic H-chain ferritins than those isolated from other prokaryotes. FtMt also shares a high sequence homology with HuHF, which was increased further through removal of the N-terminal chain. As such, an H-chain-type mechanism of $Fe^{2+}$ oxidation was expected, but instead a large MVFC was observed upon reaction with $Fe^{2+}$ and $O_2$.

*Syn*Ftn is unique among HuHF and FtMt in that the protein has no reactivity with $H_2O_2$. This is a point of contention within the scientific community with respect to both FtMt (Bou-Abdallah, 2010) and HuHF (Ebrahimi, Hagedoorn and Hagen, 2013). The former discrepancy will be discussed later. It was claimed that both apo- and loaded HuHF could react with $H_2O_2$, but the data is more likely to suggest that the inverse is true; the authors show the decomposition of $H_2O_2$ in MOPS buffer, with apo-HuHF, and loaded HuHF. As it is not possible to completely remove iron from ferritins, and it is already established that the core is able to detoxify $H_2O_2$ when mineralising $Fe^{2+}$ (Zhao *et al.*, 2003). As $H_2O_2$ is able to access the core, it is more than likely to perform Fenton chemistry at its surface. Furthermore, if this is the case, then it would support the hypothesis that iron is moved from the FC to the core after oxidation, rather than remaining in the FC. The timescale for the 'regeneration' of the FC- i.e. release of iron at the FCs- is complete within 10 mins (Yang *et al.*, 1998); the definition of

'loaded' HuHF as described by Ebrahimi et. al. is ferritin that has had 48 $Fe^{2+}$/ 24mer added to it aerobically and allowed to incubate for at least 5 hours.

It was predicted that the one-electron oxidation of a diferrous FC to $Fe^{3+}Fe^{2+}$ by $O_2$ would form superoxide in *Syn*Ftn, but this was not detectable by spin trap experiments (Fig. 3.16). An almost stoichiometric quantity of $H_2O_2$ was instead observed (Bradley *et al.*, 2019).

The formation of the MVFC, tyrosyl radical and $Fe^{3+}$ all occurred on a timescale that was closely associated with the rapid phase of $Fe^{2+}$ oxidation seen in stopped flow absorbance experiments. The mechanism by which the MVFC forms can be speculated. It is unlikely to be formed through reduction of a diferric FC, because it is unclear how a diferric species would be oxidizing enough to generate a tyrosyl radical, and there was no evidence for two phases in the rapid oxidative phase in the stopped flow experiments. Furthermore, in crystallographic experiments where incubation of *apo-Syn*Ftn crystals in aerobic $Fe^{2+}$ for increasing time periods was performed, crystal structures of MVFCs in *Syn*Ftn were formed at lower soaking times, with the diferric centres arising afterwards. The substitution of Y40 also eliminated rapid oxidation, suggesting that it is necessary for rapid oxidation, and not a result of it (Figs. 3.7D and 3.9). Replacement of Y40 with a redox-inactive phenylalanine would prevent formation of the MVFC if it was generated through oxidation of a tyrosine; however, the data suggests the opposite.

Assuming the hypothesis that the MVFC forms through direct oxidation by $O_2$, a mechanism is proposed in Fig. 3.30. Iron binds in pairs at the FC (3.30A). Oxidation of a single $Fe^{2+}$ at the FC following $O_2$ binding (3.30B) requires an additional electron which is provided by a paired FC (3.30C). This results in an $Fe^{2+}$: $O_2$ stoichiometry of 2:1, the formation of two MVFCs and the release of one $H_2O_2$ molecule (3.30D).

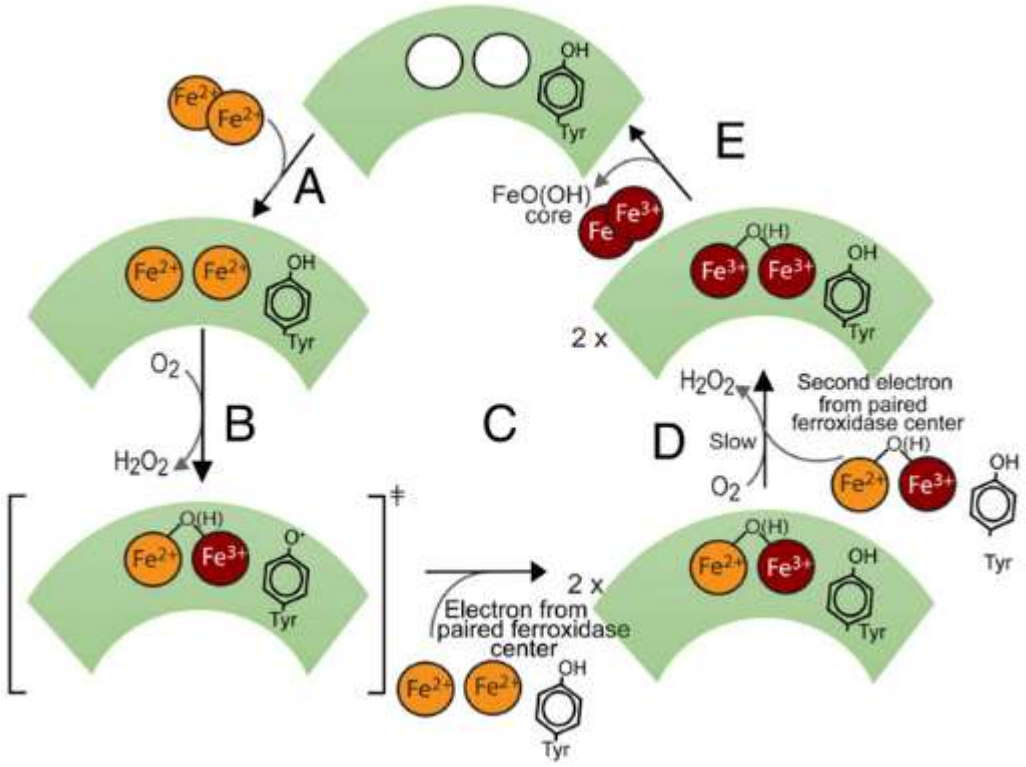


**Fig. 3.30.** Proposed catalytic cycle of *Syn*Ftn. A. Apo-FC binds two $Fe^{2+}$ ions from solution. B. Two-electron reduction of $O_2$ to $H_2O_2$ leads to oxidation of a single $Fe^{2+}$ ion, thus yielding the MVFC, and a radical on Y40. C. The Tyr radical is transient and only observed in the subset of subunits where the partner subunit's FC is unoccupied. In the remainder, rapid electron transfer from $Fe^{2+}/Fe^{2+}$ or monomeric $Fe^{2+}$ bound at a second FC results in quenching of the radical. D. Slow reaction of the MVFC with a second molecule of $O_2$, accompanied by transfer of a second electron from the paired FC, results in formation of the unstable bridged diferric centre observed in other ferritins and a second molecule of $H_2O_2$. The kinetics of this process was unaltered in a Y40F variant, suggesting that Y40 is not required for transfer of the second electron. E. Hydration and translocation of oxidized iron from the FC to the internal cavity results in formation of mineral core and regeneration of apo-FCs. Overall, four FC-bound $Fe^{2+}$ ions are oxidized, reducing two molecules of $O_2$ to $H_2O_2$, accounting for the observed 2:1 stoichiometry. Figure taken as published from (Bradley *et al.*, 2019).

For this mechanism to operate in *Syn*Ftn, an electron must pass approximately 24.5 Å between two FCs (Fig. 3.30A). This long-range electron transport is likely dependent on Y40, and the simultaneous formation of the MVFC and the tyrosyl radical is consistent with this. The tyrosyl radical is immediately quenched by oxidation of $Fe^{2+}$ at the partner FC; the radical is only observed if the partner binding site is unoccupied. An alternative electron transfer pathway is shown in Fig. 3.30B, which shows significantly reduced distances for electron transfer.

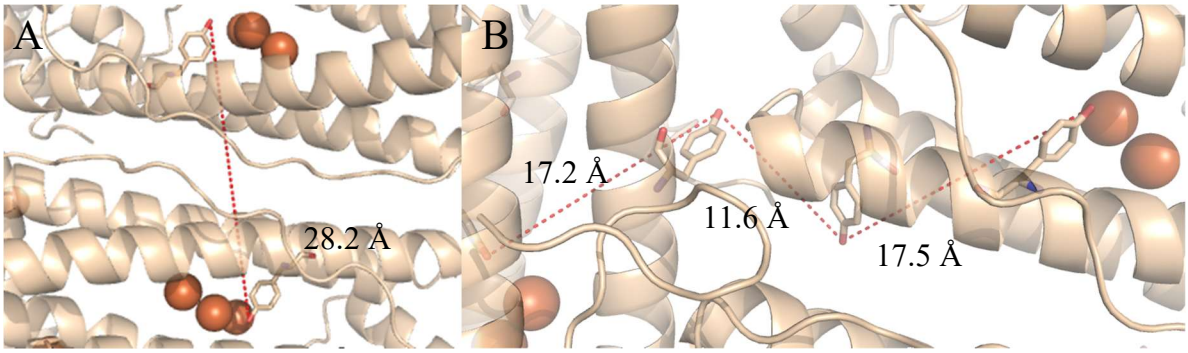


**Fig. 3.31.** A. The distance between the oxygen atoms on two Y40 residues in the FCs of a *Syn*Ftn dimer. B. Rather than intradimer electron transfer, a plausible electron transfer pathway utilises four tyrosine residues to connect a *Syn*Ftn monomer's FC with that of the monomer perpendicular to the dimer. Figures adapted from PDB 6GKC (Bradley *et al.*, 2019).

The MVFC is necessary for mineralisation, but Y40 allows for the rapid formation of this intermediate. It has been previously reported that a diferrous site can be oxidized to the $Fe^{3+}Fe^{2+}$ form, and that intersubunit electron transfer mediated by aromatic amino acids can occur, but the conjecture that both of these mechanisms occur simultaneously to reduce an $O_2$ molecule using two diiron centres has not been previously identified among any carboxylate-bridged diiron proteins.

The upregulation of *Syn*Ftn in response to high concentrations of copper may suggest a role for *Syn*Ftn. Copper is toxic due to its participation in Fenton chemistry, and because it displaces

native metals from active sites, for example, in iron-sulfur cluster proteins (Macomber and Imlay, 2009). Most ferritins are capable of rapidly removing free iron and detoxifying it to prevent its participation in Fenton chemistry. *Syn*Ftn has additional reactive utility over other ferritins due to the formation of a MVFC, which contains a single unpaired electron. This could react with ROS like superoxide radicals to form closed-shell molecules, reducing oxidative stress in a superior fashion to other ferritins. This suggests a reason why *Syn*Ftn is so widespread among *Prochlorococcus* species, which is noted for genome shrinkage to the point where only proteins which provide an environmental advantage remain (Dufresne, Garczarek and Partensky, 2005).

**The mixed-valence ferroxidase centre of mitochondrial ferritin and its role in oxidative stress protection**

It was not possible to trap any DMPO-free radical adducts in the presence of Δ9 FtMt. Spin trap experiments have been performed on the full-length FtMt before, but these experiments show the generation of hydroxyl radicals during the oxidative deposition of $Fe^{2+}$ in FtMt using $O_2$ as an oxidant (Bou-Abdallah *et al.*, 2005). However, the authors conclude that the detoxification reaction found in HuHF does not occur in FtMt, and that an $Fe^{2+}$: $H_2O_2$ stoichiometry of 2:1 arises through two one-electron transfers and the formation of hydroxyl radicals. Despite the Δ9 variant showing greater homology with HuHF, the results shown in Fig. 3.19 show that the FC is indeed capable of reacting with $H_2O_2$, but at a much slower rate than with $O_2$, thus being outcompeted under high [$O_2$] conditions (which would also lead to hydroxyl radical production when there is excess $Fe^{2+}$). This is an important distinction from *Syn*Ftn; there is no oxidation state of the FC that reacts with $H_2O_2$ in the cyanobacterial ferritin.

The other major difference between FtMt and *Syn*Ftn is the radical formed; even in WT FtMt, a large proportion of the free radical formed could be attributed to a peroxyl-species (Fig. 3.17). In *Syn*Ftn, this radical is only observed in the Y40F variant. This is likely the result of the missing rapid phase, which allows $Fe^{2+}$ to persist in solution. Fig. 3.16 shows that the production of hydroxyl radicals was detected in spin trapping experiments with the Y40F variant; these radicals probably go on to react indiscriminately with side chains in the protein. This effect is clearly seen in all the FtMt variants studied in this work, which react more quickly with $O_2$ than $H_2O_2$. Given that FtMt was presumed in the literature to play a protective role in mitochondria against oxidative stress, it seems counterintuitive to react slowly with $H_2O_2$. The role proposed above for *Syn*Ftn, where the MVFC within FtMt may serve as a one-electron donor/ acceptor for a range of ROS is less likely due to the lower concentration of the MVFC. Substituting Y25 for a phenylalanine in Δ9 FtMt only reduces the rate of the rapid phase of $Fe^{2+}$ oxidation rather than eliminating it as it does in *Syn*Ftn (Bradley *et al.*, 2019) and *E. coli* bacterioferritin (Bradley *et al.*, 2015). Given the protein's high sequence homology with HuHF, the consistent formation of a MVFC through $Fe^{2+}$ oxidation by $O_2$ might be present in both proteins, but is only observed in FtMt due to its low rate of reaction.

Like *Syn*Ftn, the free radical and MVFC form in parallel, but only the free radical decays over the timescale measured for FtMt. It is possible that FtMt and *Syn*Ftn operate via the same mechanism; in *Syn*Ftn, a stoichiometric quantity of MVFC is observed at a rate in line with that of rapid $Fe^{2+}$ oxidation, and its decay rate aligns well with that of the slow oxidation. In FtMt, the rapid phase of $Fe^{2+}$ oxidation is only associated with half of the FCs (Bou-Abdallah *et al.*, 2005). The decay of the MVFC in FtMt is in line with the slow phase of $Fe^{2+}$ oxidation in UV/vis stopped flow kinetics, and like *Syn*Ftn, the substitution of the conserved tyrosine adjacent to the FC does not impair the formation of the MVFC.

### *n* ferr also forms a mixed-valence ferroxidase centre and a peroxyl radical

The *n* ferr protein from *Natronolimnobius innermongolicus* was also shown to form a MVFC when oxidizing $Fe^{2+}$ using $O_2$ as a substrate. The WT protein formed a protein-based free radical at $Fe^{2+}$ loadings stoichiometric to the FC, but at supra-stoichiometric $Fe^{2+}$ loadings the protein formed peroxyl radicals (Fig. 3.27). Like each of the proteins shown in this work, Y24F also produced peroxyl radicals. Of the ferritins studied in this chapter, the hypothesis may be suggested that the formation of a MVFC in ferritins may be an indicator of a fast rate of reaction with $O_2$, with a much weaker preference for reacting with $H_2O_2$; *Syn*Ftn forms a large MVFC and cannot react with $H_2O_2$, and FtMt forms a smaller MVFC yet has a slow rate of reaction with $H_2O_2$. While the reactivity of *n* ferr has not yet been tested with $H_2O_2$ as a substrate, the protein's rapid phase is much faster than that observed in any other ferritin (82 $s^{-1}$). This could potentially lead to a study of non-binding FC-adjacent residues which may either facilitate formation of a DFP species or a MVFC species, which may have functionally important differences.

## Conclusion

Using DtpA to detect $H_2O_2$ is a novel use for the protein, similar in use to the Amplex Red assay which uses horseradish peroxidase. A PDA is the ideal experiment for DtpA as an alternative means of measurement; irreversibly reacting with $H_2O_2$ directly and quickly, with less pH sensitivity than the Amplex Red assay and no requirement for a calibration curve to determine the $H_2O_2$ concentration. While the results of the assay reported in Fig. 3.2 show unambiguously that $H_2O_2$ is released when $Fe^{2+}$ is oxidized by HuHF, this result cannot be

interpreted as support for the hypothesis that the FCs do not react with $H_2O_2$, or as conflicting evidence to the 'detoxification' reaction demonstrated previously in HuHF and HuLF (Zhao *et al.*, 2003). This is, first and foremost, because the detoxification reaction (which occurs on a similar timescale to mineralisation in HuHF) is several orders of magnitude slower than the reaction of $H_2O_2$ with DtpA (which is in excess).

The MVFC observed in *Syn*Ftn is the most conclusive proof so far that ferritins do not mineralise $Fe^{2+}$ via a common mechanism, and that the widespread prevalence and functionality of ferritins has resulted in divergent mechanistic functions. Work on FtMt remains challenging due to the protein's low yield and poor reproducibility of the free radical, but RFQ data achieved so far nonetheless indicate a similar set of properties, and maybe even a role, to that of *Syn*Ftn.

The discovery of *n* ferr has shown that MVFCs are more common than previously anticipated. With a sufficient number of MVFC-forming proteins to study, it will be significantly easier to identify functional roles for the proteins *in vivo*.

The discovery of a MVFC in HuHF through direct oxidation should be considered with caution. The simplest reason for this is simply because of the absence of its observation anywhere else in the literature; numerous Mössbauer and EPR studies have been carried out on the protein previously. Further work is required to understand this finding properly.

# Chapter 4

# Reactions of the *Escherichia coli* bacterioferritin ferroxidase centre with $O_2$ and $H_2O_2$

**Introduction**

*E. coli* bacterioferritin (BFR) is one of four ferritins coded for within the organism's genome. Two of the others are bacterial ferritins (FtnA and FtnB), the fourth is the mini-ferritin Dps that is expressed in starved cells (Cornell *et al.*, 2017). The expression of FtnA is negatively controlled by the *fur* regulatory protein. Mutants where the *fur* gene is knocked out are incapable of surviving under aerobic conditions, but can with the addition of an iron chelator or overexpression of FtnA (Touati *et al.*, 1995). FtnA accounts for ≈50 % of all cellular iron in *E.coli*, clearly showing that it is the primary iron storage protein in the organism (Nandal *et al.*, 2010). It has also been shown that iron stored in FtnA can be utilized under periods of iron scarcity, and that FtnA showed no protective effect against oxidative stress (Abdul-Tehrani *et al.*, 1999). FtnB, while the sequence is that of a ferritin-like protein, lacks active FCs.

Starved cells that have high levels of Dps are capable of surviving in the presence of 45 mM $H_2O_2$, three times the $H_2O_2$ concentration that rapidly killed cells that have not been starved. Starved cells that had the *dps* gene knocked out were incapable of surviving longer than 40 mins (Smith, 2004). *E coli* DNA is cleaved when exposed to $FeSO_4$ and $H_2O_2$, but this effect

is not observed in the presence of Dps. This is explained partly by Dps' non-specific ability to bind DNA and form highly stable structures (Almiron *et al.*, 1992). Another explanation is the FC activity of Dps, which preferentially reacts with $H_2O_2$ over $O_2$ in a 2 $Fe^{2+}$: 1$H_2O_2$ ratio, preventing the formation of hydroxyl radicals (Zhao *et al.*, 2002).

No phenotype has been identified for *bfr* deficient *E. coli* mutants, so its purpose is unclear. Iron storage appears to be unaffected in these variants, and the upregulation of Dps may compensate for any loss in redox stress resistance caused by the absence of BFR. Like Dps, BFR is capable of utilising $O_2$ or $H_2O_2$ as an oxidant for the FCs, with a mechanism eliminating the production of hydroxyl radicals through the simultaneous oxidation of a pair of ferrous iron atoms (Bou-Abdallah *et al.*, 2002). The $Fe^{2+}$: $O_2$ stoichiometry of BFR's ferroxidase centres (FCs) is 4:1, suggesting that $H_2O_2$ is a more rapid oxidant of the FC than $O_2$ (Yang, Le Brun, *et al.*, 2000).

Understanding the reactivity of the FC with $H_2O_2$, and how this differs from its reaction with $O_2$, is key to elucidating the mechanism by which the BFR FC operates, and hence its biological function. It could also be an important step in identifying why many other ferritins do not react with $H_2O_2$. This work investigates the kinetics of the iron oxidation in BFR by both $O_2$ and $H_2O_2$, providing further evidence that BFR is an important redox stress protectant in *E. coli*.

## Results

### Kinetics of bacterioferritin:$Fe^{2+}$ oxidation by $O_2$ for different [$Fe^{2+}$] loadings

The stoichiometry of $Fe^{2+}$ binding and kinetics of $Fe^{2+}$ oxidation by $O_2$ have been studied previously (Le Brun, Wilson, *et al.*, 1993) (Lawson *et al.*, 2009). However, these studies were

conducted by mixing ferrous ammonium sulfate with aerobic apoprotein. As the protocol employed in the majority of our investigations involves incubation of $Fe^{2+}$ anaerobically with the apoprotein and thereafter mixing with $O_2$ (see Materials and Methods: Preparation of anaerobic protein and buffer solutions) it is prudent to re-examine the stoichiometry under these specific anaerobic incubation conditions.

BFR apoprotein was incubated under anaerobic conditions with varying concentrations of $Fe^{2+}$ for approximately 10 min. This was then rapidly mixed with a buffer solution saturated with $O_2$. The time courses for the oxidation of the $Fe^{2+}$ seen in these experiments are given in Fig. 4.1A.

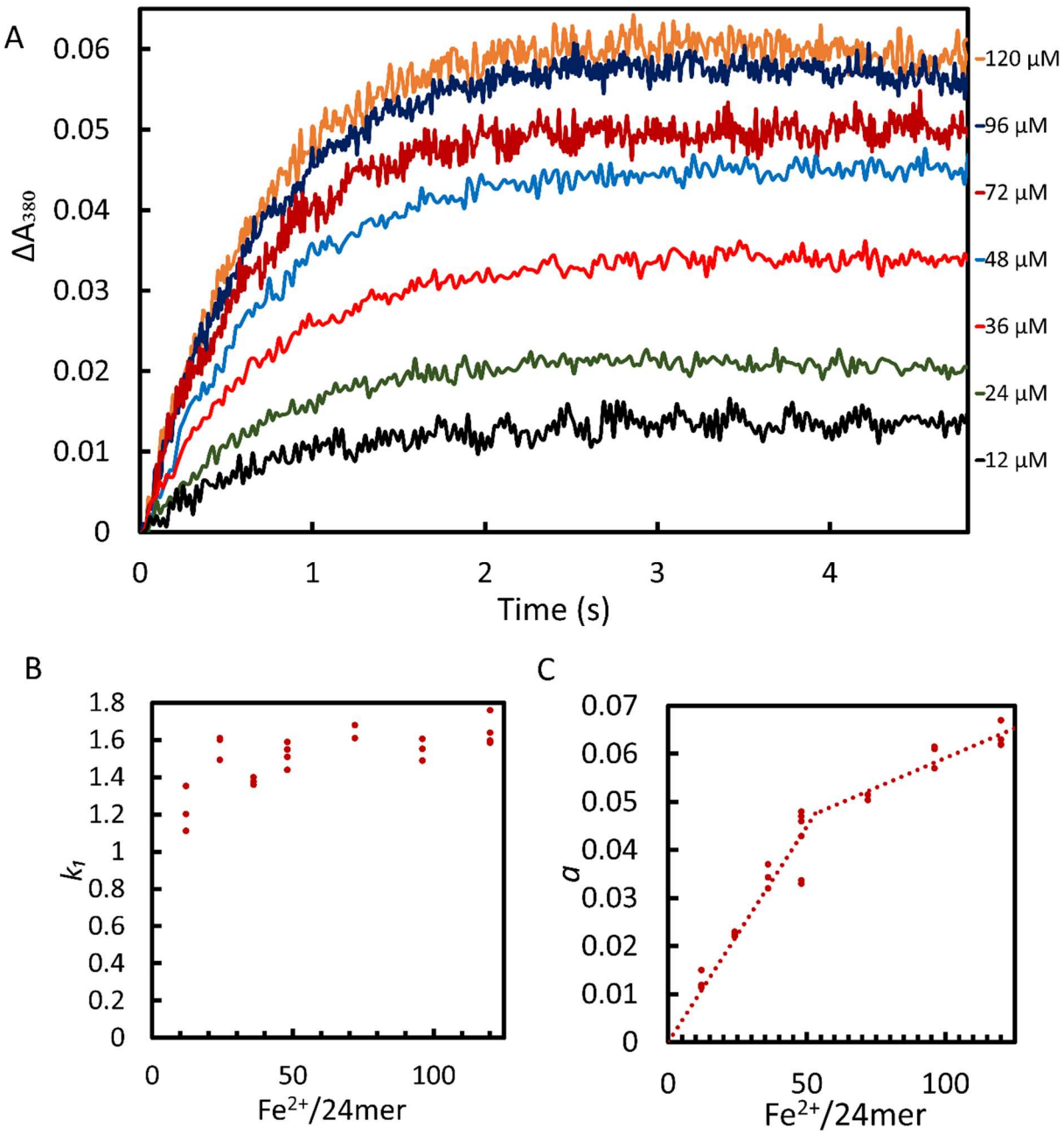


**Fig. 4.1.** Panel A shows kinetics of $Fe^{2+}$ oxidation to $Fe^{3+}$, as measured using a photodiode array (PDA) by the $\Delta A_{380nm}$ increase, in the WT BFR:$Fe^{2+}$ anaerobic system after addition of 600 μM $O_2$. The concentration of BFR was 1 μM and the $Fe^{2+}$ concentrations are indicated by the traces. All concentrations are final, i.e. after mixing. Each trace represents an average of nine mixing experiments. These averages were approximated by a single exponent function $\Delta \boldsymbol{A_{380}} = \boldsymbol{a}(\mathbf{1} - \boldsymbol{e}^{-\boldsymbol{k_1 t}})$ and the dependences of the $k_1$ and $a$ values obtained from the fits on iron excess over BFR are shown in panels B and C respectively.

The first-order rate constants are given in Fig. 4.1B and are essentially independent of [$Fe^{2+}$]. The amplitude, $\Delta A_1$, for this rapid phase of reaction does, in contrast, increase with [$Fe^{2+}$]. Fig. 4.1C shows these amplitudes taken at 380 nm plotted against the $Fe^{2+}$/ BFR ratio. These data show a linear dependence of amplitude on $Fe^{2+}$/ BFR up to approximately 53 $Fe^{2+}$/ BFR, after which the amplitude continues to increase, but with a shallower slope. This result is very similar to that reported previously (Le Brun, Wilson, *et al.*, 1993) and the break point in the titration is close to the expected value of 48 $Fe^{2+}$ per BFR 24mer for full saturation of the FC. One difference that may be noted between the data in Fig. 4.1C and the earlier reports is that in Fig. 4.1C, though a break point is clearly discernible, the amplitude continues to rise and does not plateau. We suggest this difference may be caused by the altered experimental protocol. Here, incubating supra-stoichiometric $Fe^{2+}$ (more than 48 $Fe^{2+}$/ 24mer) with the protein for 10 min allows the excess $Fe^{2+}$ to bind not only to the FC, but also to penetrate and equilibrate with other sites within the core. On adding $O_2$ not only can the FC be oxidized but also $Fe^{2+}$ bound at sites within the inner cavity, leading to enhanced absorption at 380 nm. In those experiments where $Fe^{2+}$ is added to aerobic apoprotein only oxidation of the FC may be monitored, but not the oxidation of iron in other binding sites which, in this timespan of observation, have not been filled. Furthermore, the linearity of the initial portion of the titration seen in Fig. 4.1C is consistent with cooperative binding of $Fe^{2+}$ to the FC. Were it otherwise, and assuming $O_2$ oxidizes pairs of $Fe^{2+}$ atoms, then at sub-stoichiometric $Fe^{2+}$ the fraction of centres with 2 $Fe^{2+}$ would follow a binomial distribution and would not be linear. Cooperative binding of $Co^{2+}$ to the FC has been reported and a Hill coefficient of $h$ = 1.6 found (Keech *et al.*, 1997). If the cognate metal, $Fe^{2+}$, binds with a larger value of $h$ this would ensure that the metal bound essentially in pairs as the maximum possible value of $h$ for the FC is 2.

**Bacterioferritin: $Fe^{2+}$ oxidation by $O_2$**

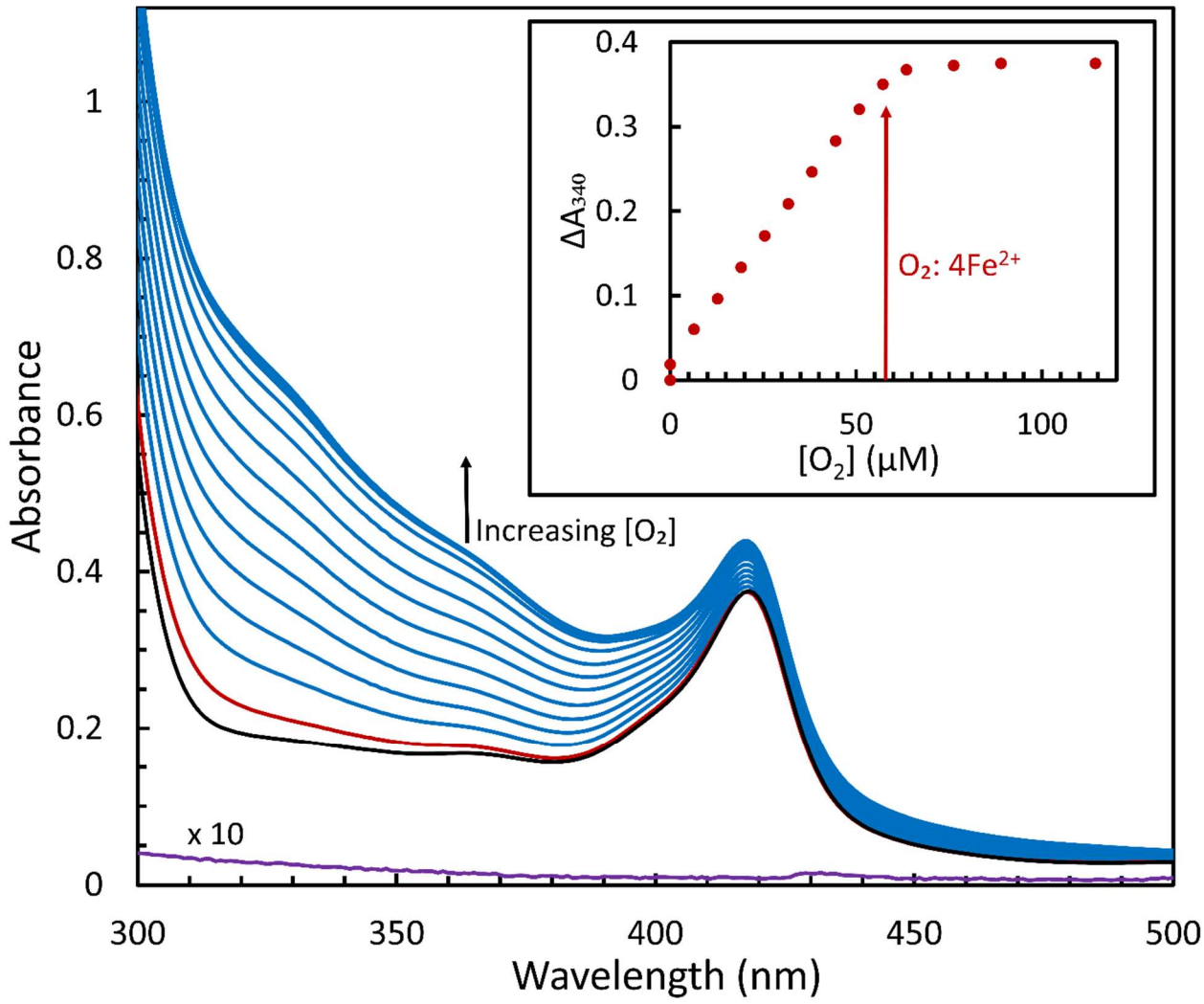


**Fig. 4.2.** Anaerobic apo-BFR (5.13 μM) was incubated with $Fe^{2+}$ (246 μM) and then MES buffer (100 mM, pH 6.5) saturated with $O_2$ (1.27 mM) was titrated into the mixture. The spectrum of the apo-protein is in black. After $Fe^{2+}$ was first added, 4.6 % was oxidized by residual $O_2$ (red spectrum). The blue spectra represent subsequent additions of $O_2$. A 200 μM $Fe^{2+}$ spectrum is shown in purple at the bottom of the figure, multiplied by a factor of 10, thus showing that unbound $Fe^{2+}$ does not contribute to the optical changes reported above. The inset displays the $\Delta A_{340}$ associated with the oxidation of iron, corrected for dilution of the protein throughout the titration. The red arrow indicates the expected $O_2$ concentration corresponding to the 4:1 stoichiometry of iron oxidation by oxygen ($Fe^{2+}$: $O_2$).

Having established that stoichiometric [$Fe^{2+}$] binds fully to BFR, we have adopted the conditions described in Fig. 4.1 to titrate the BFR: $Fe^{2+}$ complex with oxidants. Fig. 4.2 shows such a titration of anaerobic BFR: $Fe^{2+}$ complex with $O_2$. The initial spectrum of the apoprotein is shown in black and on addition of a stoichiometric concentration of $Fe^{2+}$ (i.e. 48 $Fe^{2+}$/ 24mer) a small increase in absorbance is observed in the 340 nm region (red spectrum) indicative of oxidation of some 4.6 % of the added $Fe^{2+}$ by residual $O_2$ in the system. This small increase cannot be accounted for by the spectrum of $Fe^{2+}$, as indicated by the control experiment in which the spectrum of 200 μM $Fe^{2+}$ is shown to be at least ten times smaller than the spectral change between the apoprotein and that of the iron-loaded protein. Additions of aliquots of $O_2$-saturated buffer led to progressive oxidation of the $Fe^{2+}$ as shown by the growth of the broad feature throughout the spectral region explored. The inset shows the $\Delta A_{340}$ corrected for protein dilution throughout the titration as a function of [$O_2$]. It may be observed that $\Delta A_{340}$ increases linearly with [$O_2$] until an equivalence point is reached and thereafter plateaus. The inset also shows the expected equivalence point on the assumption that each $O_2$ oxidises four $Fe^{2+}$. It can be concluded that this data strongly supports this assumption. The linearity of the titration shows that the reaction is essentially irreversible, and that the overall reaction may be written as described by Eq. 4.1:

$$4Fe^{2+} + O_2 + 4H^+ \rightarrow 2H_2O + 4Fe^{3+} \qquad (4.1)$$

On rapidly mixing iron-loaded BFR (prepared anaerobically) with $O_2$ saturated buffer (600 μM $O_2$ after mixing), spectral changes that may be assigned to oxidation of the $Fe^{2+}$ in the FC were observed as shown in Fig. 4.3, in which selected spectra at known times are given. The overall spectral transition is consistent with that shown in Fig. 4.2, which suggests that the reaction is completed within the timescale of the stopped flow experiments shown below. A time course of the reaction at 380 nm is given in the inset.

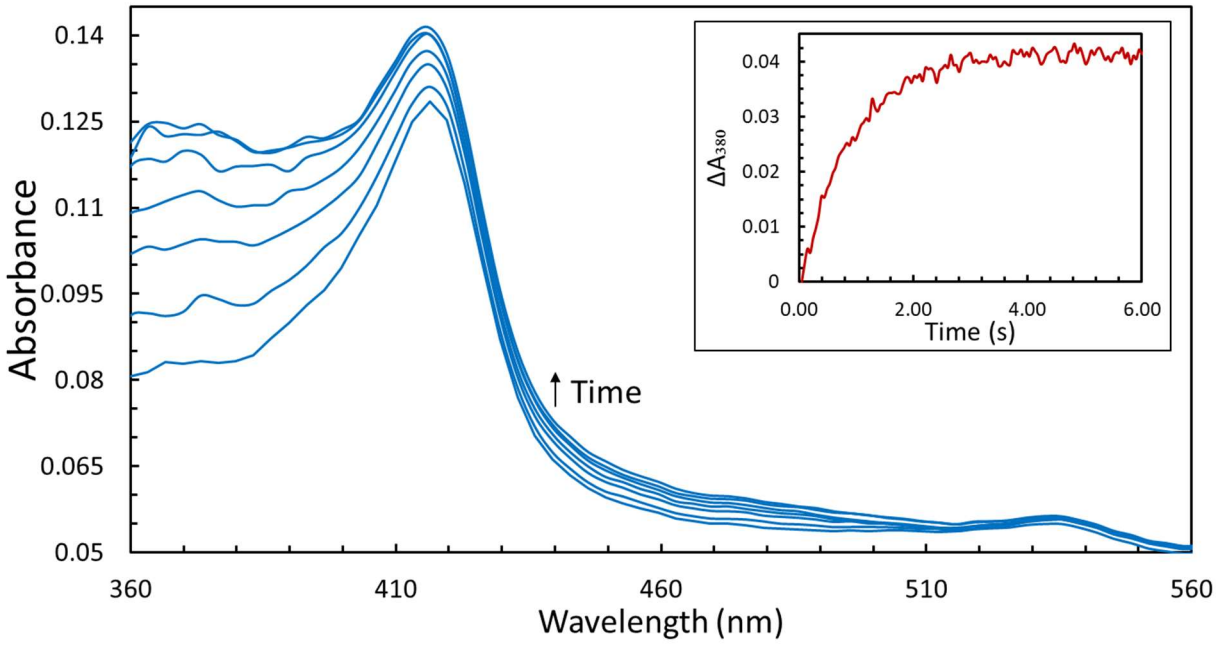


**Fig. 4.3.** A PDA spectrum associated with oxidation of the BFR: $Fe^{2+}$ complex by $O_2$ are shown. The $Fe^{2+}$ was added to apo-BFR anaerobically and subsequently mixed with 100 mM MES (pH 6.5), saturated with $O_2$ to a concentration of 600 µM. Protein 24mer and iron concentrations were 1 and 48 µM after mixing, respectively. The spectra shown are taken at the following times: t= 0.05, 0.30, 0.64, 1.03, 1.53, 2.46 and 19.68 s. The inset figure shows the time course of the reaction monitored at 380nm.

To obtain data at 340 nm, a wavelength used by others (Malone *et al.*, 2004) to characterise $Fe^{2+}$ oxidation by ferritins but not not accessible to the PDA employed here, a photomultiplier was used. Fig. 4.4 shows the $\Delta A_{340}$ at several $O_2$ concentrations. Each time course could be fitted well to a double exponential (Eq. 4.2), where a single exponential accounted for 90 % of the total absorbance change.

$$\Delta A_{340} = (A_1 + A_2) - A_1 e^{-k_1 t} - A_2 e^{-k_2 t} \qquad (4.2)$$

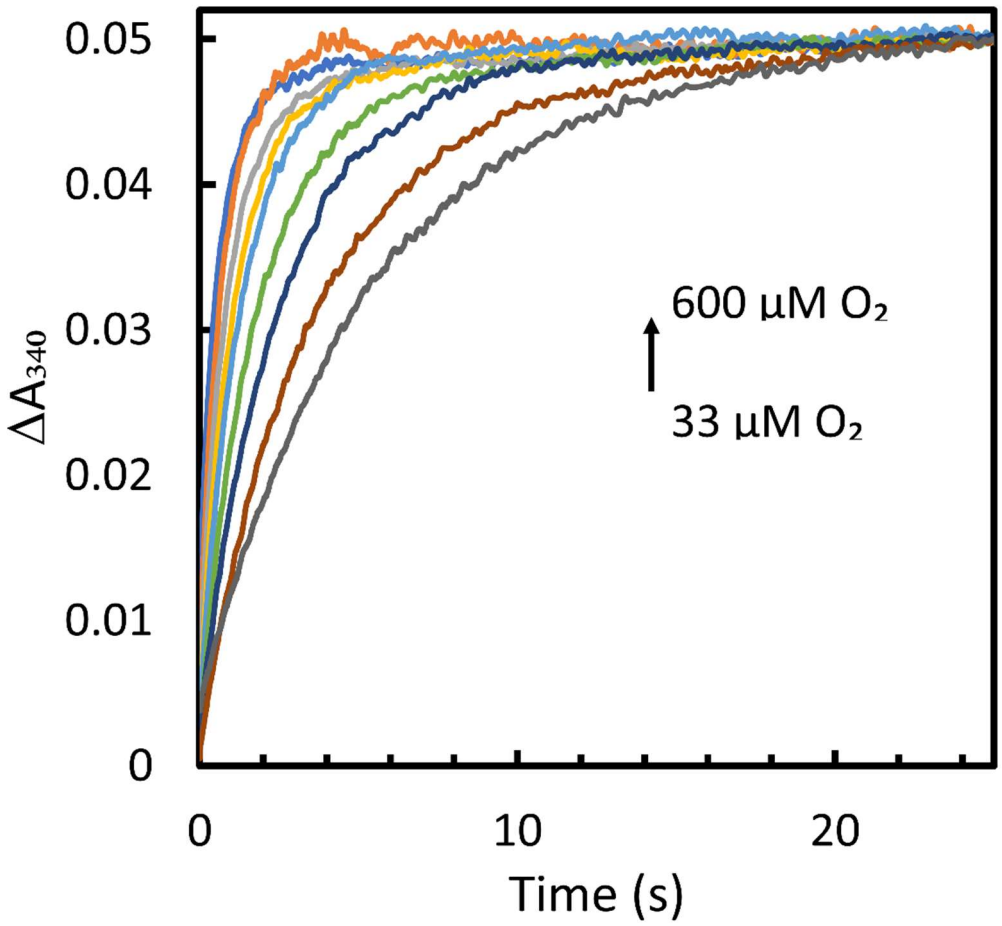


**Fig. 4.4.** The time courses of iron oxidation in the BFR: $Fe^{2+}$ (1 and 48 µM after mixing, respectively) complex by $O_2$ at 25°C at varying [$O_2$]. Each trace represents an average of three mixing experiments. All traces were brought to the same endpoint at 0.05 A.

It is apparent that these time courses are [$O_2$] dependent, becoming faster at higher $O_2$ concentrations. This may also be seen by reference to Fig. 4.5, in which the pseudo-first-order rate constant for the reaction is seen to increase as a function of [$O_2$]. At 25 °C and at 260 µM $O_2$ the value of the rate constant observed is comparable to that reported in the literature for the aerobic reaction (0.42 $s^{-1}$, Wong *et al.*, 2012) when accounting for the negative association between the rate of $Fe^{2+}$ oxidation at the FCs and increasing concentrations of bound heme.

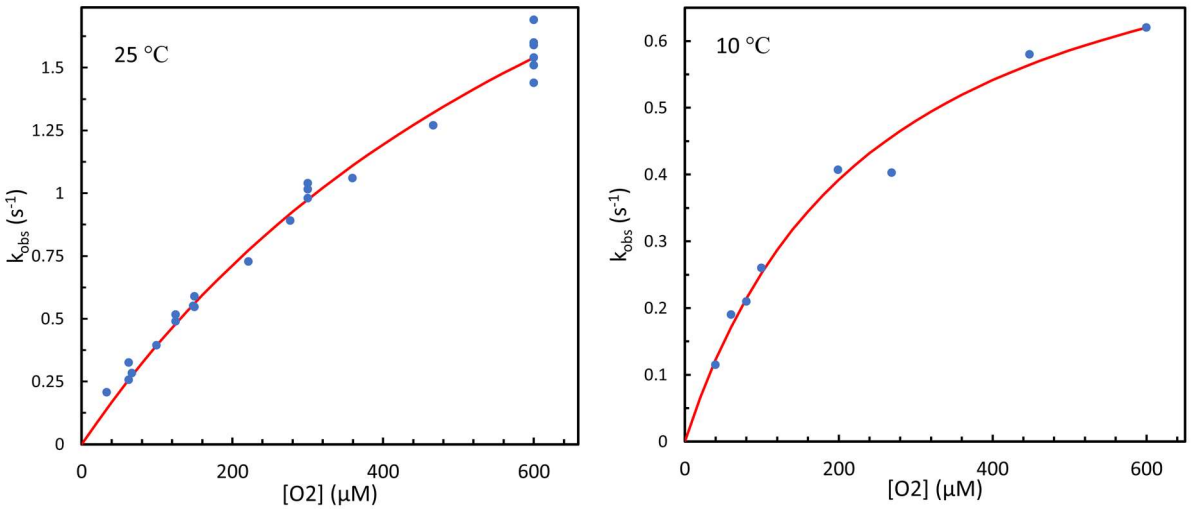


**Fig. 4.5.** The dependence of the observed rate constants for the oxidation of BFR: $Fe^{2+}$ on [$O_2$] are shown at 25 °C and 10 °C. The fits to the data conform to the hyperbolic Eq. 4.3.

Fig. 4.5 suggests that the dependence of the rate constant on [$O_2$] at 25 °C is not linear and may be better fitted by a hyperbolic function. Furthermore, the values of $k_{obs}$ are much lower than those reported for reactions of $O_2$ with other diiron centres that reduce $O_2$, such as methane monooxygenase (Lee, Nesheim and Lipscomb, 1993), toluene/ *o*-xylene monooxygenase hydroxylase (Murray *et al.*, 2007), ribonucleotide reductase (Moënne-Loccoz *et al.*, 1998) or even other ferritins such as human H-chain ferritin (Treffry *et al.*, 1997), *E. coli* FtnA (Treffry *et al.*, 1998), *Pseudo-nitzschia multiseries* ferritin (Pfaffen *et al.*, 2013), or *Syn*Ftn (Bradley *et al.*, 2019). This suggests that a second-order process between $O_2$ and the FC is not being monitored, but rather that the oxidation mechanism is described by a fast but weak binding of $O_2$ to the centre, which is then oxidized at a limiting rate (Eq. 4.3).

$$k_{obs} = \frac{k_{obsmax}[O_2]}{K_D + [O_2]} \quad (4.3)$$

To test this model, we have repeated the experiments at a lower temperature, 10 °C, expecting a higher affinity for $O_2$ which would make the dissociation constant $K_D$ lower, and thus the dependence of $k_{obs}$ on $O_2$ to be a more pronounced hyperbola. Fig. 4.6 illustrates this experiment and shows that indeed, the hyperbolic nature of the dependence is more obvious, supporting the model in Eq. 4.3. The values of $k_{obsmax}$ and $K_D$ at 25 °C and 10 °C were obtained from fits of the data to Eq. 4.3. and are reported in Table 4.1.

**Table 4.1.** Kinetic and equilibrium parameters governing the reaction of BFR: $Fe^{2+}$ oxidation by $O_2$ at 25 °C and 10 °C, obtained by fitting to Eq. 4.3.

| | **25 °C** | **10 °C** | **$\Delta E_a$** | **$\Delta H^0$** |
|---|---|---|---|---|
| ***$k_{obsmax}$*** | 3.68 $s^{-1}$ | 0.87 $s^{-1}$ | 67.3 kJ $mol^{-1}$ | 56.9 kJ $mol^{-1}$ |
| **$K_D$** | 8.23 x $10^{-4}$ M | 2.45 x $10^{-4}$ M | | |

From the data taken at these two temperatures we may estimate the activation energy and the enthalpy of the equilibrium between $O_2$ and the FC. These values are also recorded in Table 4.1 above.

**Is $H_2O_2$ an intermediate in the oxidation of the bacterioferritin: $Fe^{2+}$ complex by $O_2$?**

Fig. 4.2 reports that the stoichiometry of BFR: $Fe^{2+}$ oxidation is $4Fe^{2+}$ :$1O_2$. As it is very unlikely that all four electrons from the iron are donated to the oxygen in a single step it follows

that the reaction should proceed via one, or more, intermediates. One such possible intermediate is $H_2O_2$, the two-electron reduction product of oxygen. To test whether $H_2O_2$ is an intermediate that is released into solution we performed oxidation experiments in the presence of the dye-decolourising peroxidase DtpA which rapidly reacts with $H_2O_2$ to form a stable compound I (CpI) species.

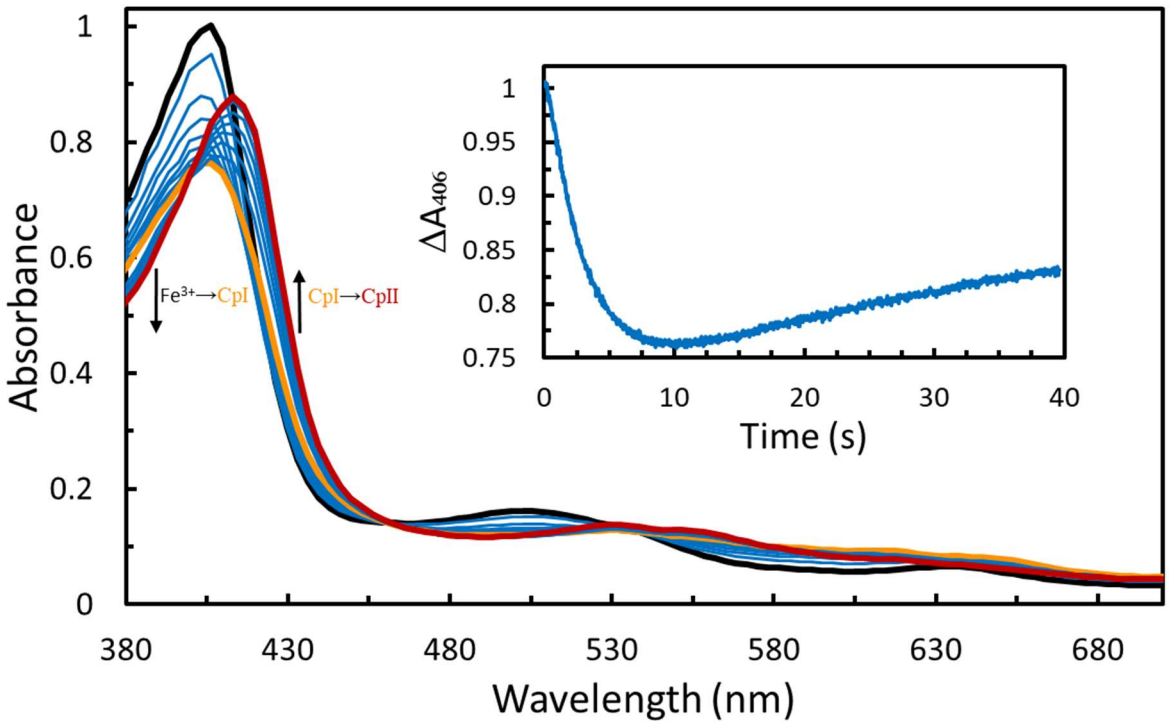


**Fig. 4.6.** The PDA spectrum of 18 µM DtpA in the presence of 0.5 µM WT BFR as it is mixed with 40 µM $Fe^{2+}$ (80 $Fe^{2+}$/24mer) in 263 µM $O_2$. The spectra shown are taken at the following times: t= 0.04, 0.99, 2.1, 3.01, 4.16, 5.15, 6.14, 7.2, 8.24, 9.27, 16.63, 20.79, 24.95, 28.87, 33.07, 37.22 and 39.6 s. The inset figure shows the $\Delta A_{406,}$ associated with formation and decay of the intermediate CpI.

On mixing aerobic solutions of BFR with ferrous ammonium sulfate in the presence of DtpA we observed the time-dependent spectra shown in Fig. 4.6. In this figure the dominant

$Fe^{3+}$DtpA Soret band, centred at 406 nm bleaches over ~5 s, a time that is consistent with the time course of oxidation of the FC by $O_2$ (see Fig. 4.4). The time-dependent spectra collected were subjected to an SVD analysis and then fitted globally to the model:

$$Fe^{3+}DtpA \rightarrow CpI \rightarrow CpII$$

The resulting spectrum shows that a proportion of $Fe^{3+}$DtPA has been converted to CpI (Fig. 4.7, refer back to Fig. 3.3 for comparison to the standard spectra by Chaplin, Wilson and Worrall, 2017). Figs. 4.6 and 4.7 both show the spontaneous decay of CpI to compound II (CpII) over the subsequent 40 s.

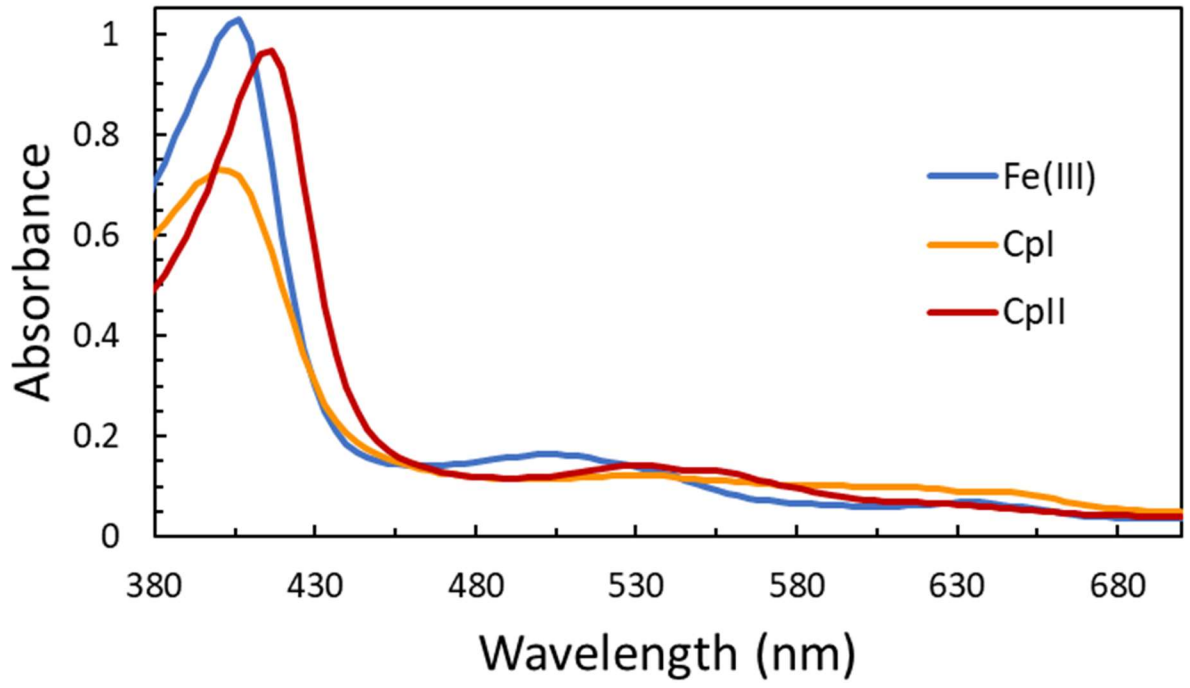


**Fig. 4.7.** A global fit of the data shown in Fig. 4.6, as derived by SVD analysis. This was fitted to a two-phase model, $Fe^{3+}$DtpA → CpI → CpII. The rates for these processes were 0.30 $s^{-1}$ and 0.026 $s^{-1}$ respectively. The $Fe^{2+}$ oxidation in the BFR FCs coincided with the formation of CpI; this is reflected in the global fit.

This experiment unambiguously shows that $H_2O_2$ is formed in the reaction between BFR: $Fe^{2+}$ and $O_2$ and that some or all of this is released into bulk solution where it may react with DtpA. To determine how much $H_2O_2$ is released the experiment was repeated varying the [$Fe^{2+}$] from sub- to supra- stoichiometric concentrations.

The global fits of the spectra collected in experiments where DtpA is mixed with BFR prior to reacting the protein with different [$Fe^{2+}$] loadings show the spectral changes associated with the formation of CpI formed at each [$Fe^{2+}$]. With increased iron loadings more compound I is formed (see Fig. 4.8). Based on the documented differences between the extinction coefficients for $Fe^{3+}$DtpA and for CpI (e.g. 30,000 $M^{-1}cm^{-1}$ at 400 nm, Fig. 3.3) the concentration of CpI formed at each iron loading can be calculated. Fig. 4.9 shows the results of such a calculation. In this figure the concentration of CpI is plotted as a function of the added [$Fe^{2+}$] and indicates that a maximum concentration of compound I is formed at a point where the [$Fe^{2+}$] added is sufficient to fully fill the FCs.

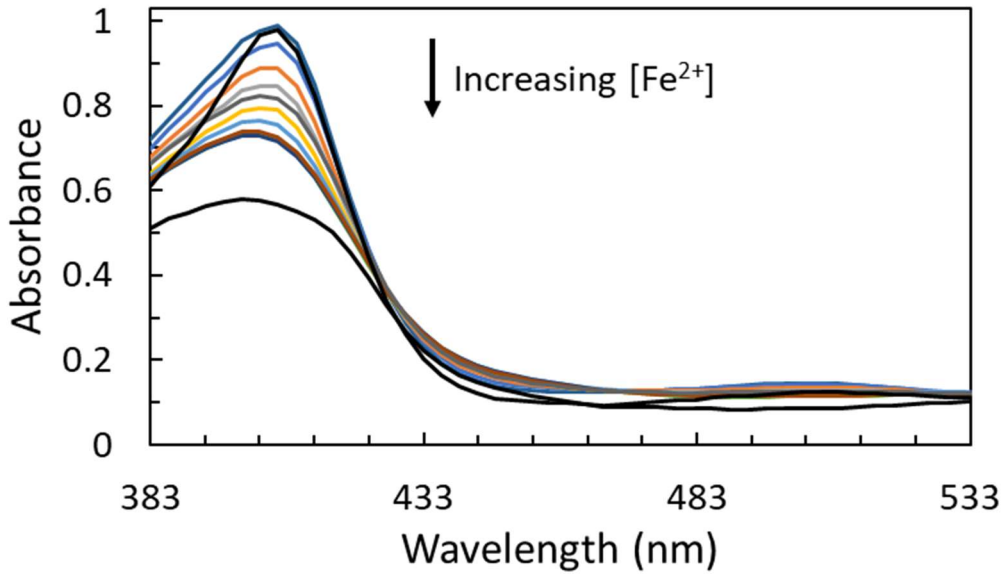

**Fig. 4.8.** Formation of CpI on 18 μM DtpA in the presence of 0.5 μM WT BFR as it is mixed with different [$Fe^{2+}$] in 263 μM $O_2$. The CpI spectra are derived by SVD analysis of the corresponding PDA spectra sets recorded on different [$Fe^{2+}$] additions. The top black line shows the spectrum of the 'resting' ferric DtpA heme group, while the lower black line shows the spectrum of 18 μM DtpA's CpI in the presence of 0.5 μM BFR: 48 $Fe^{2+}$ prior to the decay to CpII.

Given that the second order rate constants of BFR (see below in BFR: $Fe^{2+}$ oxidation by $H_2O_2$) and DtpA for their respective reactions with $H_2O_2$ are 3.8 x $10^6$ $M^{-1}s^{-1}$ and 1.4 x $10^7$ $M^{-1}s^{-1}$, these values can be utilized to work out the proportion of $H_2O_2$ that would react with either protein at any $H_2O_2$ concentration. Knowing the concentration of CpI formed in each reaction, it can be deduced how much of the FCs in BFR have been oxidized using $H_2O_2$ rather than $O_2$. In the absence of DtpA, we would expect 50 % of the FCs to be oxidized by $H_2O_2$ because $H_2O_2$ is generated from the oxidation of $Fe^{2+}$ by $O_2$ and for each $O_2$, one $H_2O_2$ is produced. From examination of Fig. 4.9, one may calculate that some 70 % of the $H_2O_2$ has reacted with DtpA (the details of this calculation are shown in Appendix 5). This proportion is close to the expectation if all the $H_2O_2$ was released from the FC and reacted competitively with either the FC or the DtpA based on their respective rates of oxidation by $H_2O_2$. This is entirely consistent with the idea that DtpA and BFR compete for $H_2O_2$ released into bulk solution.

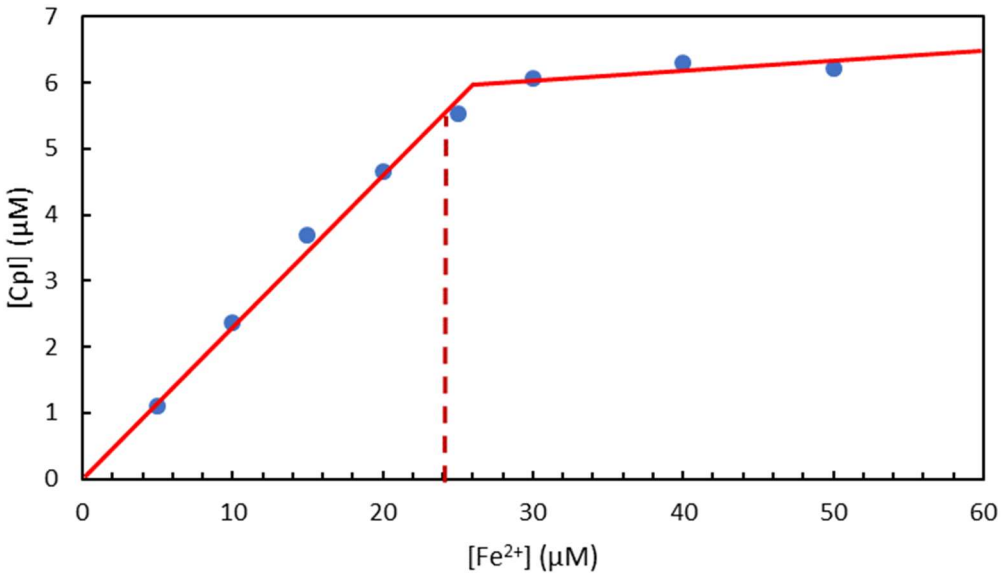


**Fig. 4.9.** A plot showing the concentration of CpI generated in each mixing experiment as a function of [$Fe^{2+}$]. The dashed red line shows the [$Fe^{2+}$] at which all the BFR FCs would be expected to be fully occupied with iron (24 μM).

Fig. 4.9 can be directly compared to the DtpA-coupled $Fe^{2+}$ titration performed with HuHF (Fig. 3.5). In HuHF, the formation of CpI is rate-limited by the decay of the DFP species. However, in BFR the formation of CpI is rate-limited by $Fe^{2+}$ oxidation. This explains why a DFP species has never been observed in *E. coli* BFR; having accounted for all the $H_2O_2$ formed in the $O_2$ reaction, it can be concluded with certainty that the DFP species, if one is present at all, is incredibly short-lived.

**Bacterioferritin: $Fe^{2+}$ oxidation by $H_2O_2$**

Having established that $H_2O_2$ is released from BFR on reaction of the ferrous-loaded protein with $O_2$ and that this $H_2O_2$ must then react with further FCs to complete the reaction in line with the measured stoichiometry (Fig. 4.2), it is now important to establish the details of the latter's reaction mechanism between $H_2O_2$ and the FC.

A similar protocol to that used in the $O_2$ titration was used to titrate anaerobic BFR: $Fe^{2+}$ complex with $H_2O_2$ (Fig. 4.10).

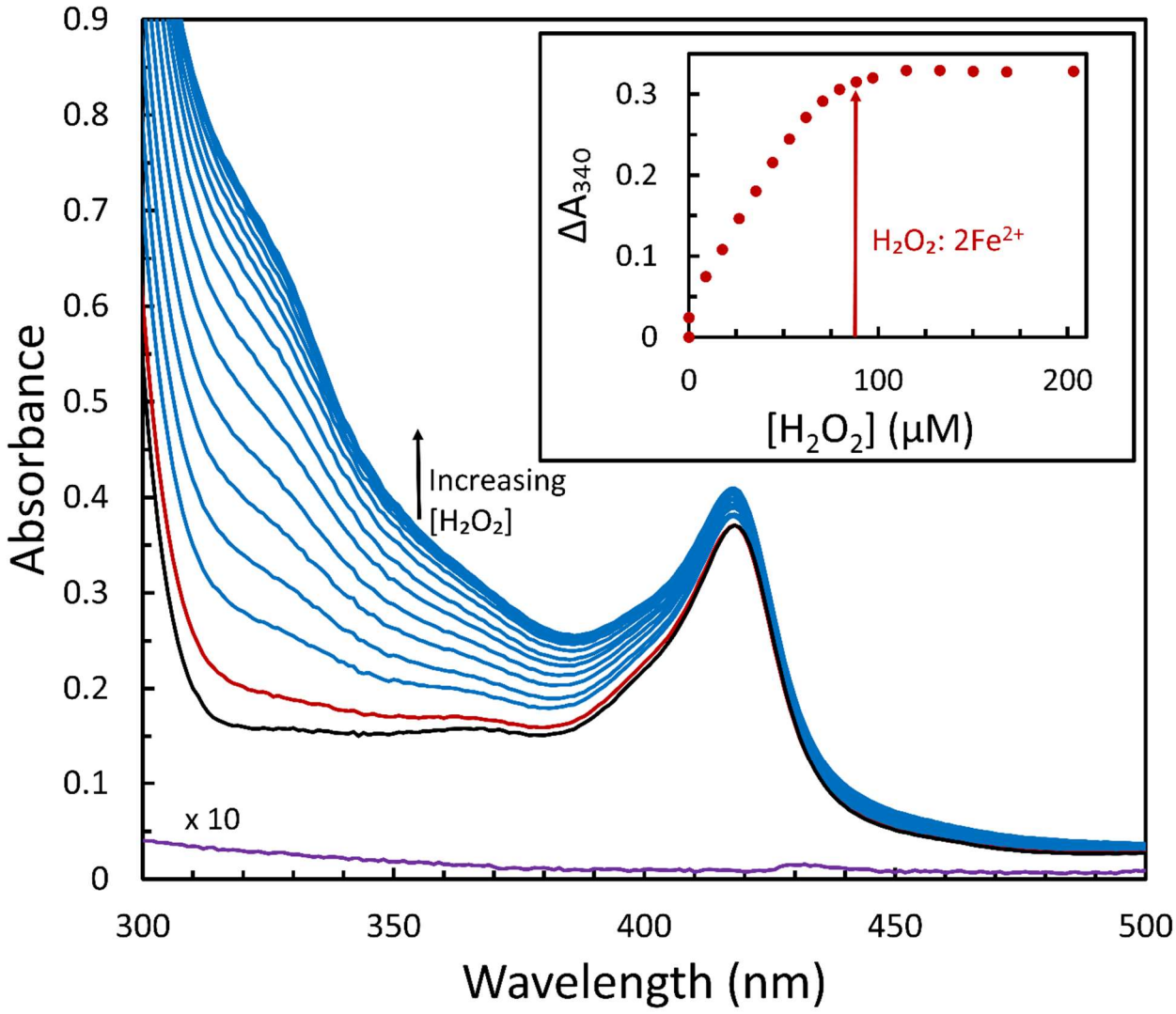


**Fig. 4.10.** Anaerobic apo-BFR (4.23 μM) was incubated with $Fe^{2+}$ (190 μM, which is slightly less than required for complete occupancy of all FCs) and then $H_2O_2$ (1.95 mM) dissolved in MES buffer was titrated into the mixture. The apo-protein is coloured black. After $Fe^{2+}$ was first added, 7 % was oxidized by residual $O_2$; this is shown in the red spectrum. The blue spectra represent subsequent additions of $H_2O_2$ ranging from 6.4 μM to 114.3 μM to the remaining 93% $Fe^{2+}$ (176.7 μM). A 200 μM $Fe^{2+}$ spectrum is shown in purple at the bottom of the figure, multiplied by a factor of 10. The inset figure shows the oxidation of iron as measured by $\Delta A_{340}$, corrected for dilution of the protein. Full oxidation of $Fe^{2+}$ was achieved at around 88.35 μM [$H_2O_2$], consistent with each $H_2O_2$ oxidizing 2 $Fe^{2+}$ ions.

On addition of $Fe^{2+}$ to the anaerobic apo-BFR, some 7 % of the $Fe^{2+}$ was oxidised by residual $O_2$. The titration of the remaining $Fe^{2+}$ with $H_2O_2$ is shown in the figure, and the $\Delta A_{340}$ follows a similar pattern as shown for $O_2$ but with a stoichiometry of two $Fe^{2+}$ per $H_2O_2$ molecule, as predicted in accordance with Eq. 4.4:

$$2Fe^{2+} + H_2O_2 + 2H^+ \rightarrow 2H_2O + 2Fe^{3+} \qquad (4.4)$$

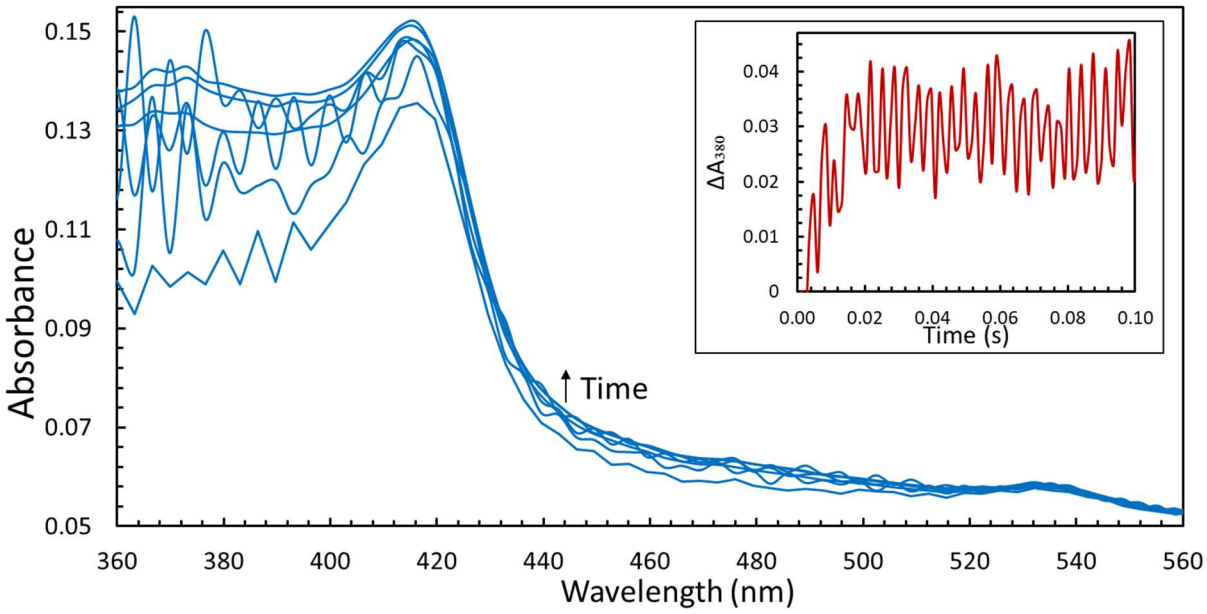


**Fig. 4.11.** The spectral changes associated with oxidation of the BFR: $Fe^{2+}$ complex by $H_2O_2$. The $Fe^{2+}$ (48 µM) was added to apo-BFR (1 µM) anaerobically and subsequently mixed with 40 µM $H_2O_2$ in 100 mM MES (pH 6.5). The spectra shown are taken at the following times: t= 0.0012, 0.05, 0.011, 0.017, 4.09, 8.07 and 20.52 s. The inset figure shows the time course of the reaction monitored at 380nm.

On mixing $H_2O_2$ with an anaerobic BFR: $Fe^{2+}$ complex, in which all the FCs are occupied, spectral changes consistent with spectra given in Fig. 4.2 were observed (Fig. 4.11) indicating

oxidation of the $Fe^{2+}$ in the first 20 ms of the reaction. The spectral features are most clearly seen in the global fit to the overall reaction given in Fig. 4.12.

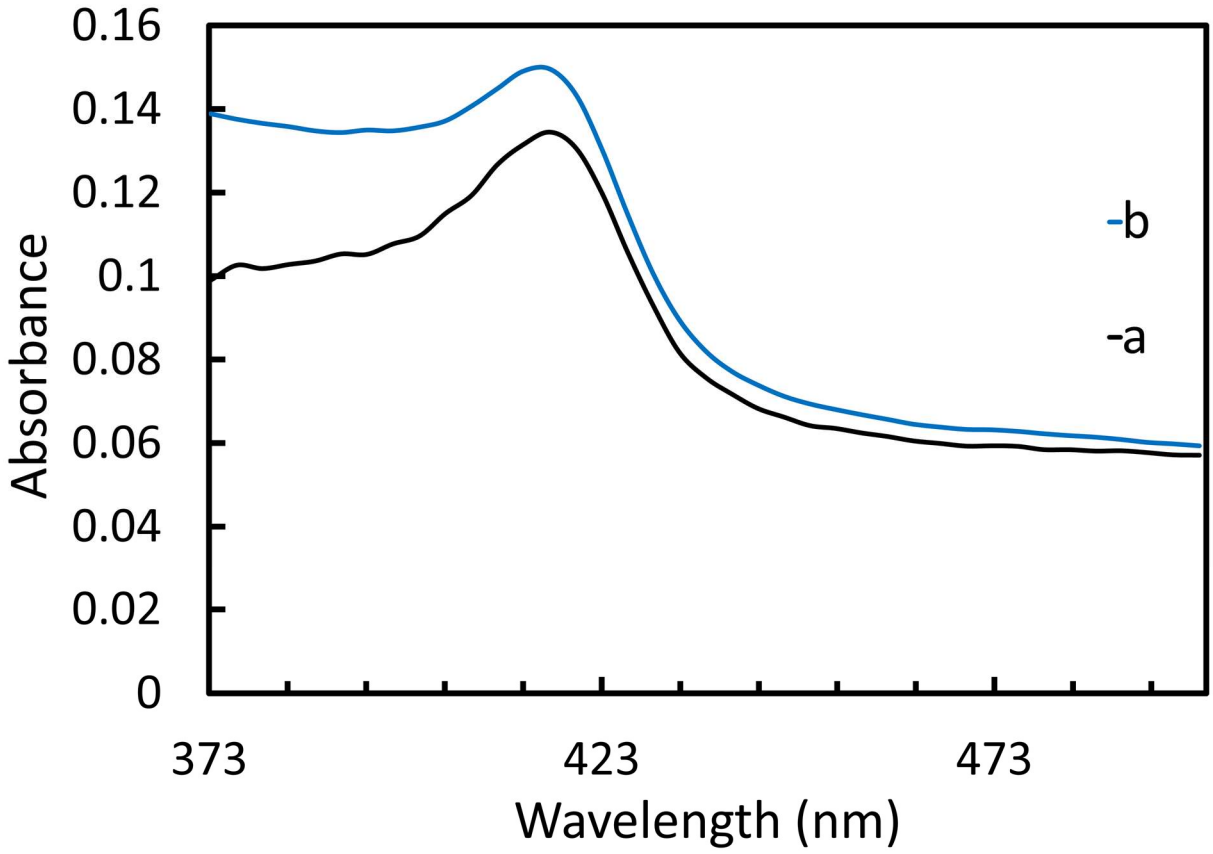


**Fig. 4.12.** The PDA data obtained from the oxidation of BFR: $Fe^{2+}$ by $H_2O_2$ (shown in Fig. 4.11) was fitted globally to a simple model, namely: a → b with a $k_{obs}$ of 3.5 $s^{-1}$.

Fig. 4.11 also indicates that the bulk of the absorbance change occurs very rapidly, but the time resolution of the diode array does not permit determination of the rate constant with sufficient confidence. The experiments have therefore been repeated employing a photomultiplier which has better time resolution and permits monitoring at 340 nm (used in previous studies such as Bradley *et al.*, 2015, Wong *et al.*, 2012). Fig. 4.13 shows the time courses which are seen to comprise fast and slower phases. The fast phases are shown in the inset. Here the fast phase concludes within the first 20 ms, and examination of the time courses reveal that they become

faster at higher [$H_2O_2$] and therefore that at higher concentrations more of the reaction is lost in the dead time of the apparatus, i.e. approximately 2 ms.

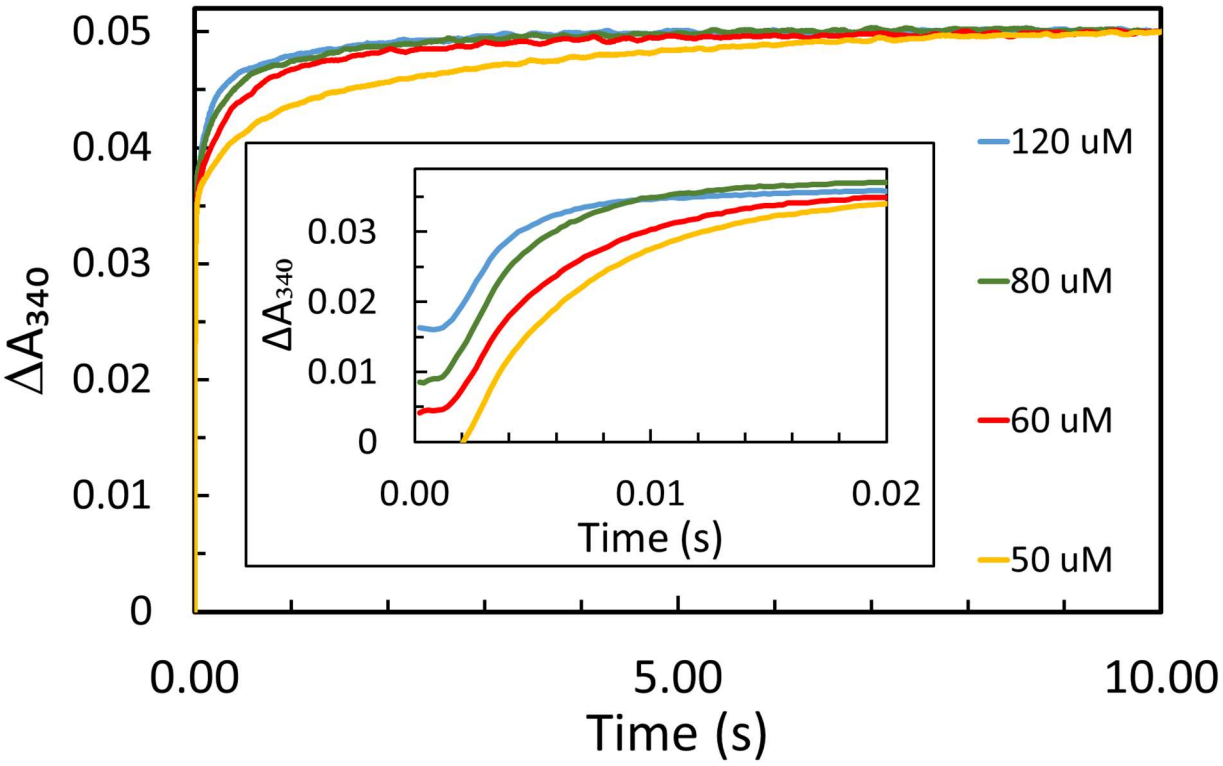


**Fig. 4.13.** Kinetics of BFR: $Fe^{2+}$ oxidation by $H_2O_2$ as a function of [$H_2O_2$]. The concentrations relevant to each time course are given in the colour-coded legend. The inset shows the first 20 ms, during which time the fast phase is observed. Protein and iron concentrations were 1 and 48 μM after mixing, respectively. Each trace was recorded three times and the average is reported here. Data recorded at 340 nm using a photomultiplier. $A_{max}$ was normalized by subtracting a value across each dataset so that each series ended at an absorbance of 0.05.

The rate constants were determined by averaging all time courses at a particular [$H_2O_2$], then fitting kinetic equations to the resultant traces; these are plotted below in Fig. 4.14. At high [$H_2O_2$] the rapid phase of $Fe^{2+}$ oxidation was clearly defined by a single exponential process. At lower concentrations, an exponential equation still fitted the data adequately, albeit the

conditions were not strictly pseudo-first-order. The overall equation for this reaction is shown below (Eq. 4.5). The rate constant for the fast phase, $k_1$, was found to be linearly dependent on [$H_2O_2$] indicating that oxidation is rate limited by the second-order binding of $H_2O_2$ to the FC, and that subsequent oxidation was rapid compared with this.

$$\Delta A_{340} = (A_1 + A_2 + A_3) - A_1 e^{-k_1 t} - A_2 e^{-k_2 t} - A_3 e^{-k_3 t} \quad (4.5)$$

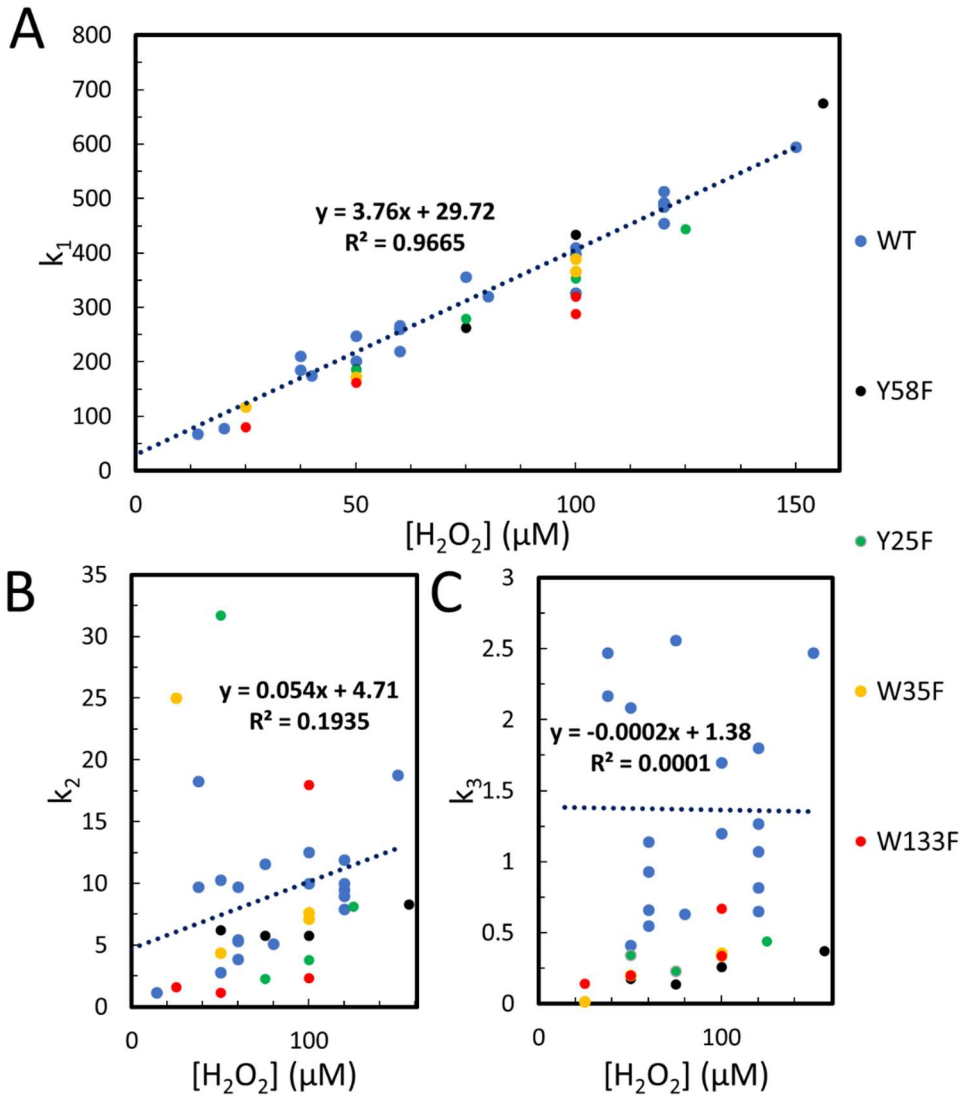


**Fig. 4.14.** Linear plots showing how WT BFR and variants' rate constants vary with $[H_2O_2]$. Trendlines are fitted to WT data. Concentrations of BFR and $Fe^{2+}$ were 1 μM and 48 $Fe^{2+}$/ 24mer respectively. A. A linear plot of the observed first rate constant $k_1$ and its dependence on $[H_2O_2]$. B. A linear plot showing the dependence of the second rate constant $k_2$ on $[H_2O_2]$. C. A linear plot showing the dependence of the third rate constant $k_3$ on $[H_2O_2]$.

A linear fit to the observed rates for the fast phase $k_1$ in Fig. 14A yields a second-order rate constant of 3.76 x $10^6$ $M^{-1}$ $s^{-1}$. The slower phases were fitted to the sum of two exponentials, and the rate constants, $k_2$ and $k_3$ are shown as a function of $[H_2O_2]$ in panels 4.15B and 4.15C.

The data in these panels are scattered and give no indication of a strong dependence of either rate constant on [$H_2O_2$]. This is discussed later.

To investigate sub-stoichiometric [$H_2O_2$] conditions [BFR] and [$Fe^{2+}$] were doubled and the experiment was repeated. The results of experiments conducted at variable sub- to supra-stoichiometric concentrations of $H_2O_2$ are given in Fig. 4.15. At all concentrations the time courses comprised a fast phase followed by slower phases. The amplitudes of the phases are [$H_2O_2$] dependent. This is most clearly seen in the fast phase which gets larger with increasing [$H_2O_2$].

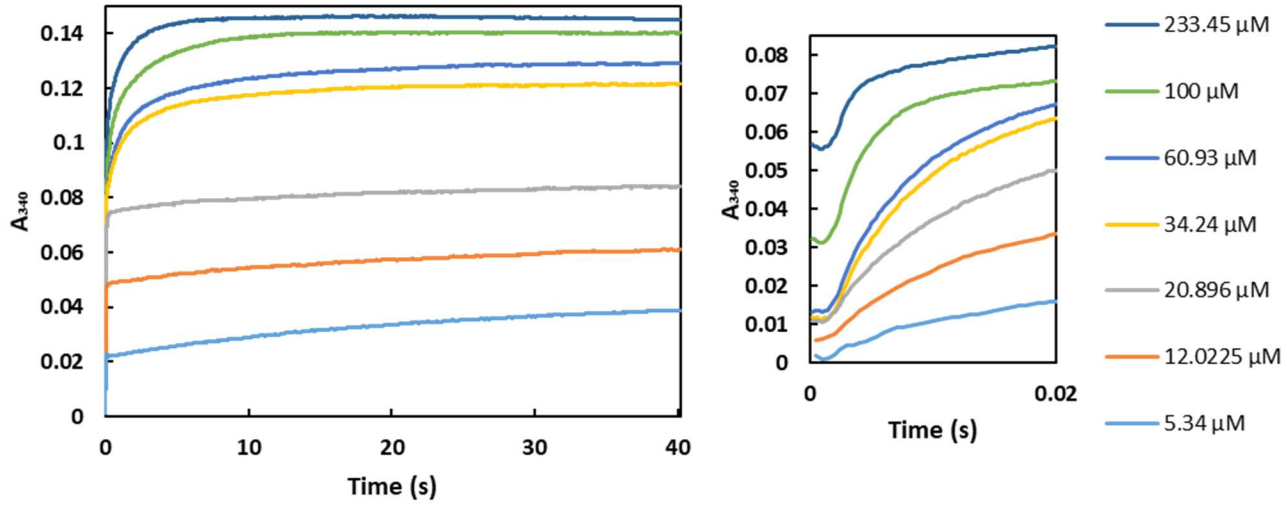


**Fig. 4.15.** Time courses showing $Fe^{2+}$ oxidation by WT BFR in the presence of variable $H_2O_2$ concentrations reported in the legend. Plot on the right shows the first 20 ms of the reaction, showing the fast phase in greater detail. Each trace was recorded three times and the average is reported here. The traces have been shifted upwards on the plots to account for the dead time of the instrument, where some of the reaction proceeds without being observed. Protein and iron concentrations were 2 and 96 µM after mixing, respectively (48 $Fe^{2+}$/ 24mer).

Fig. 4.16 shows a plot of the $\Delta A_{340}$ values at 100 ms, a timepoint where the fast phase of $Fe^{2+}$ oxidation has finished but the slow phase has hardly started. The $\Delta A$ increases as $H_2O_2$ is added to the BFR: $Fe^{2+}$ mixture until it reaches a maximal value where the Fe: $H_2O_2$ stoichiometry is 2:1. After this point, the observed $\Delta A$ decreases because there is no more $Fe^{2+}$ to oxidize, but the reaction's linear dependence on $[H_2O_2]$ means increasingly more of the reaction occurs in the dead time of the instrument. These results demonstrate that it is in the fast phase that $H_2O_2$ receives all the electrons from the FC. It therefore follows that the slow phases either are not associated with oxidation processes or that they reflect electron transfer steps within the protein, i.e. between sites.

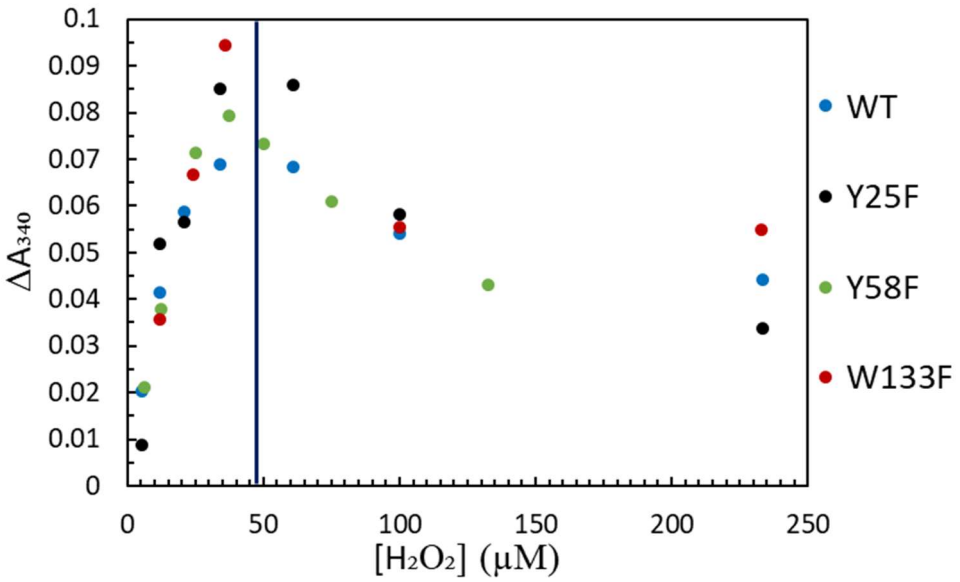


**Fig. 4.16.** A plot of the raw absorbance values at the end of the fast phase $k_1$, for WT BFR and variants as a function of $[H_2O_2]$. The line on the figures shows the stoichiometric amount of $H_2O_2$, where there is enough $H_2O_2$ to oxidize all of the $Fe^{2+}$ in a 2:1 ratio.

Several BFR variants in which redox-active aromatic residues have been substituted for phenylalanine have been examined. Time courses of all these variants are very similar to those of the WT, showing near-identical behaviour of the fast phases (see rate constants in Fig.

4.14A) but showing some differences in the time courses of the slow phases. This is reflected in the differences seen in Fig. 4.14B and 4.15C. In addition, amplitude measurements of the fast phase at sub-stoichiometric [$H_2O_2$] for Y25F, and Y58F and W133F were identical to those collected for the WT protein, as shown in Fig. 4.16. This shows that the BFR: $Fe^{2+}$ complex's rapid reaction rate with $H_2O_2$ is not dependent on the redox-active amino acids surrounding the FC.

To establish that none of the observed phases could not be attributed to Fenton chemistry independent of BFR, anaerobic solutions of $Fe^{2+}$ and $H_2O_2$ were mixed under similar conditions to those pertaining to the experiments in Fig. 4.13. The results of such an experiment are given in Appendix 6 and demonstrate that the reaction of free $Fe^{2+}$ in solution is much slower than we observe in the presence of the protein, supporting the view that the reactions we are following are those of the $Fe^{2+}$ bound to the FC centre of the protein.

**Studying mineralisation in bacterioferritin using $H_2O_2$ as an oxidant**

To study BFR's $H_2O_2$-driven mineralisation reaction, BFR was made anaerobic then incubated with $Fe^{2+}$ at concentrations approximately either double or quadruple that needed to occupy the FCs. $H_2O_2$ was then added and the $Fe^{2+}$ oxidation was monitored at 340 nm (Fig. 4.17).

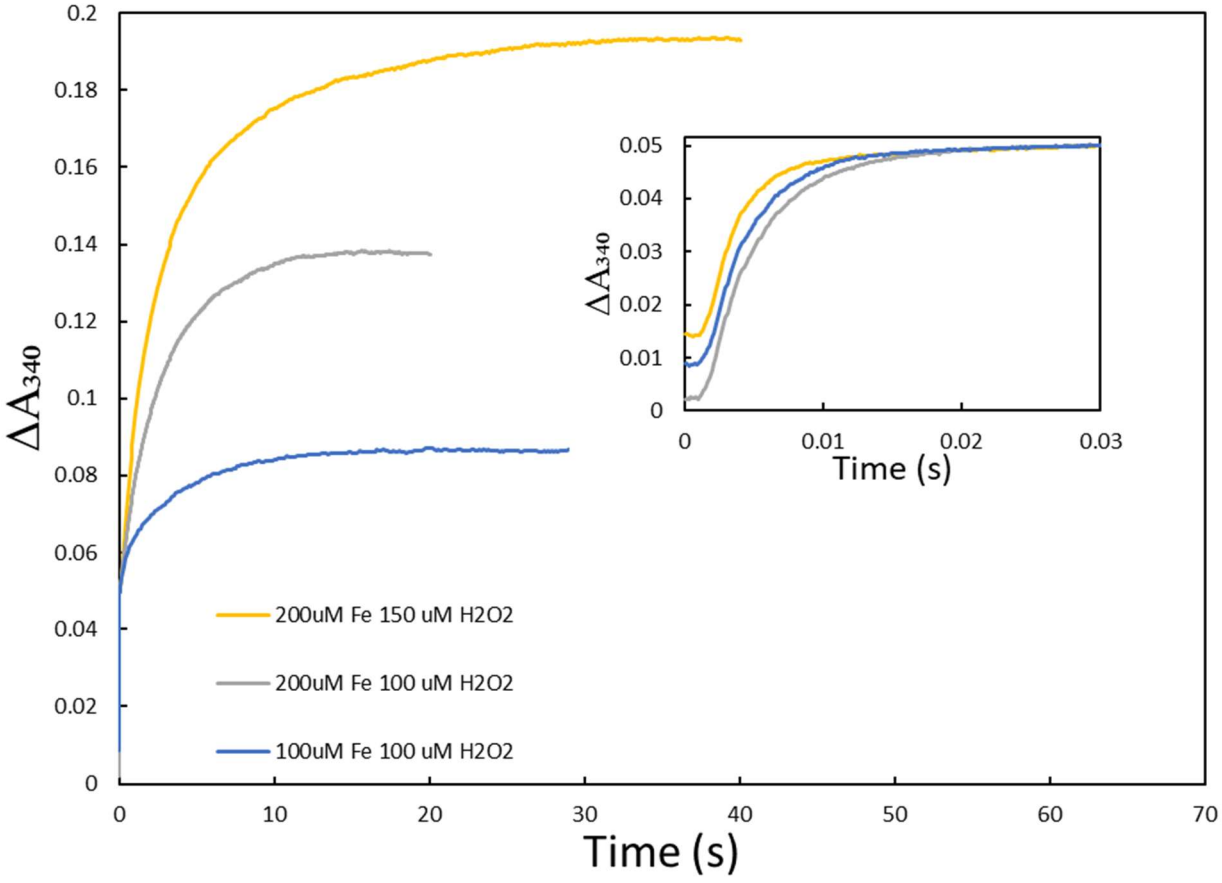


**Fig. 4.17.** Kinetics of $Fe^{2+}$ oxidation by WT BFR in the presence of high [$Fe^{2+}$] and excess $H_2O_2$, to allow the protein to mineralise iron using $H_2O_2$. The protein concentration was 1 µM after mixing. Each trace is an average of three experiments. The data were recorded at 340 nm using a photomultiplier. $A_{max}$ was normalized by subtracting a value across each dataset so that each fast phase of iron oxidation ended at an absorbance of 0.05.

The rates of these reactions are comparable to those observed in the Fenton control experiment in Appendix 6. However, an increase in [$H_2O_2$] resulted in a greater $\Delta A_{340}$, which can be explained by the difference in stoichiometry between mineralisation and Fenton chemistry. In BFR-mediated chemistry, 2 $Fe^{2+}$ reduce $H_2O_2$ to water, but in Fenton chemistry one $H_2O_2$ molecule reacts with a single $Fe^{2+}$ (see Eq. 1.2). Using a 1:1 stoichiometry, [$H_2O_2$] is sub-

stoichiometric in each of the experiments in Fig. 4.17. This conclusively demonstrates that Fenton chemistry dominates in these experiments.

**The transfer of electrons from bacterioferritins's ferroxidase centre to the heme prosthetic group**

In two preparations of the Y25F and Y58F variants, it was observed that the heme was still partially found in the ferrous state, which has not been studied in BFR before (this exception was a result of being quickly buffer-exchanged into sodium dithionite-free buffer during the iron removal process and frozen before the heme could auto-oxidize). Fig. 4.18 shows the optical spectrum of the Y25F mutant before and after being mixed with $Fe^{2+}$.

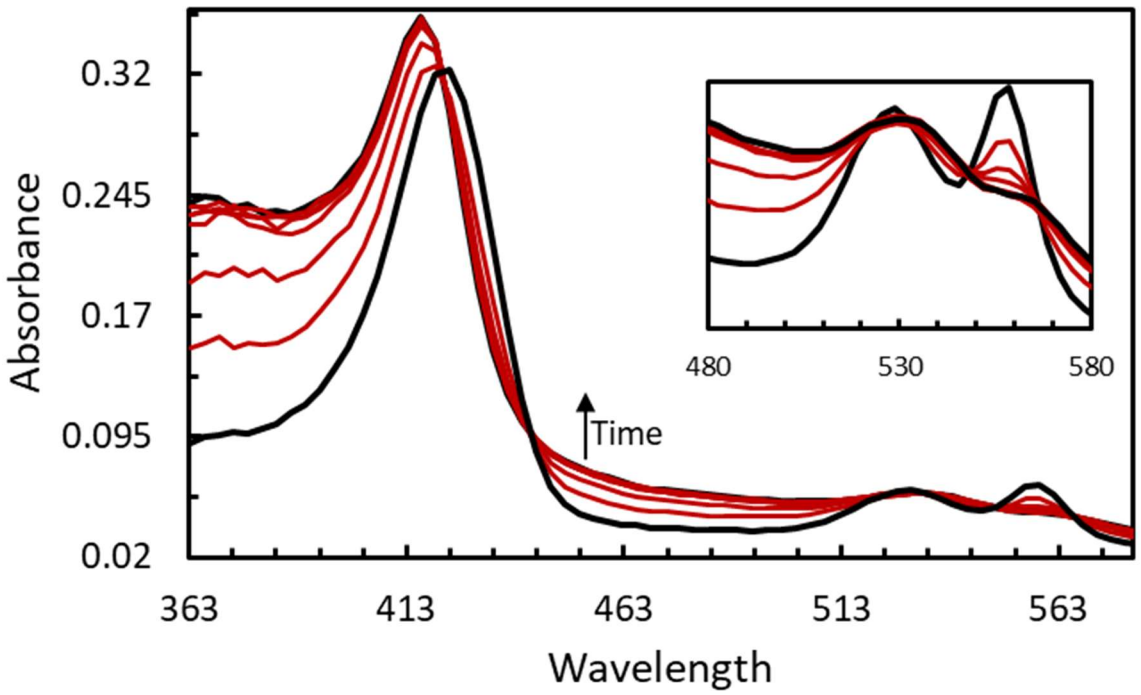


**Fig. 4.18.** PDA spectrum showing 2.09 µM Y25F BFR mixed with 48 $Fe^{2+}$/24mer under aerobic conditions, measured using a photodiode array. The inset shows the transition of the ferrous heme to ferric. The spectra shown are taken at the following times: t= 0.02, 0.05, 0.96, 2.02, 3.07, 4.03, 5.01 and 9.6 s.

While the rate of $Fe^{2+}$ oxidation was found to be the same as has been previously reported when ferric heme is present, what is unprecedented is the observation that the ferrous heme oxidizes on a timescale comparable to the iron bound at the FC. To assess the reactivity of the ferrous heme group in BFR towards potassium ferricyanide, increasing concentrations of the salt were added to oxidize the heme. Little to no spectral changes were observed until a large excess (10 x) of ferricyanide was added and left for approximately 1 hr. Fig. 4.19 shows that there is no notable $Fe^{2+}$ oxidation. The ΔA upon mixing with 100 µM $Fe^{2+}$ is smaller than expected, likely due to the excess ferricyanide in the mixture, which would rapidly oxidize any free $Fe^{2+}$ it encountered. The experiment was repeated using the Y58F variant which also had a ferrous heme group, and similar kinetics were observed.

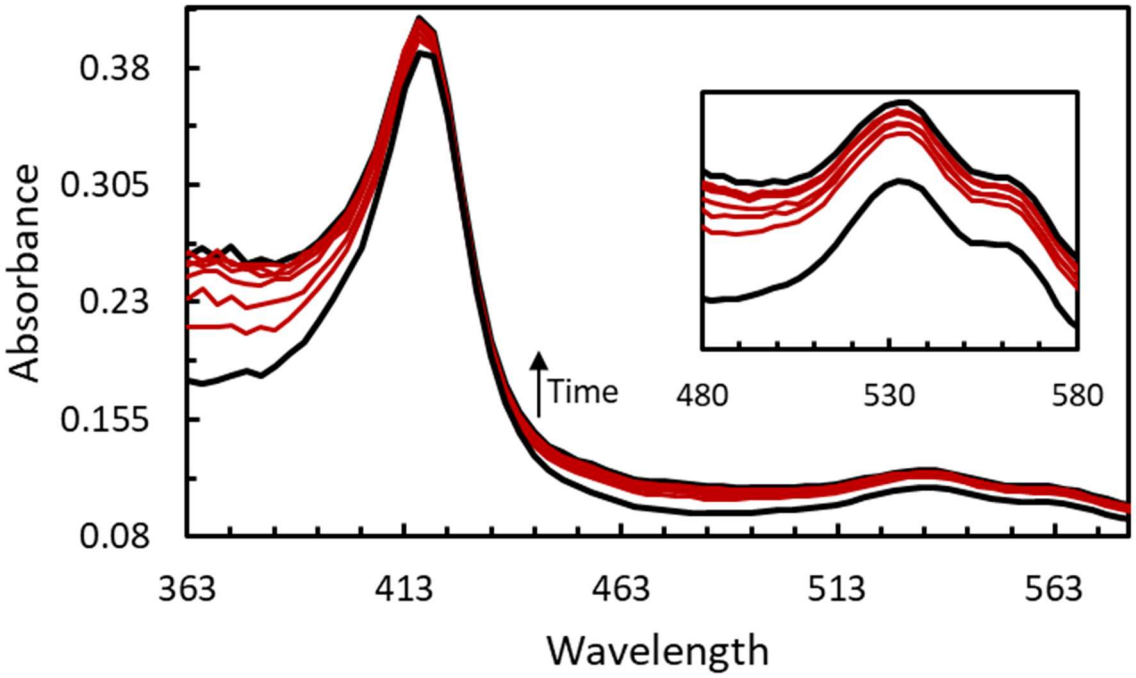


**Fig. 4.19.** Spectrum showing 2.09 μM Y25F BFR (treated with potassium ferricyanide) mixed with 48 $Fe^{2+}$/24mer, measured using a photodiode array. The inset shows where the transition of the ferrous heme to ferric would occur. The traces shown are taken at the following times: t= 0.02, 0.05, 0.96, 2.02, 3.07, 4.03, 5.01 and 9.6 s. The earliest and latest recorded traces are shown in black.

WT BFR was mixed with an excess of sodium dithionite to reduce the heme group, then desalted using a G25 column. Adding $Fe^{2+}$ to this reduced BFR under aerobic conditions yielded similar spectral changes (Fig. 4.20) and rates to the Y25F and Y58F variants.

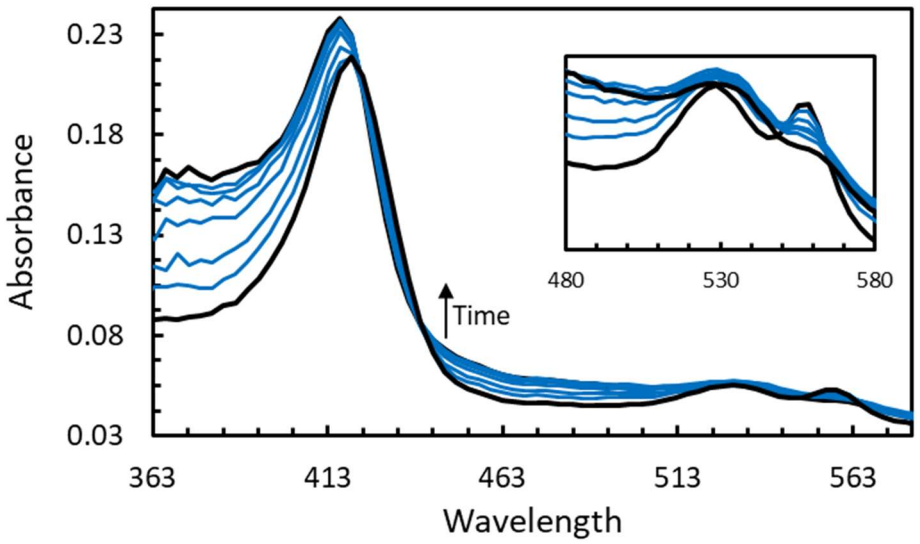


**Fig. 4.20.** Spectrum showing 1 µM WT BFR (where the heme has been reduced with sodium dithionite) mixed with 48 $Fe^{2+}$/24mer in the presence of 263 µM $O_2$, measured using a photodiode array. The inset shows the transition of the ferrous heme to ferric. The spectra shown are taken at the following times: t= 0.012, 0.3, 0.6, 1.26, 1.92, 2.52, 3.13 and 6 s.

SVD analysis was used to prepare a global fit of the data (Fig. 4.21). The spectrum could be interpreted as a sum of four spectral components. The first component *a* is most likely the perturbation of the heme upon iron binding, as observed previously (Le Brun, Wilson, *et al.*, 1993). The second component *b* shows FC iron oxidation without oxidation of the ferrous heme. The third component *c* shows half of the ferrous heme has been oxidized. The final product *d* is indistinguishable from the final spectrum of Fig. 4.3, where the heme was ferric prior to $Fe^{2+}$ addition. This result suggests that the oxidation of the heme requires a ferric FC, and that the heme is oxidized in two phases. It is unclear whether this is because there are two forms of heme in BFR, or if a MVFC is formed after the first heme oxidation step, and a second heme provides the next electron.

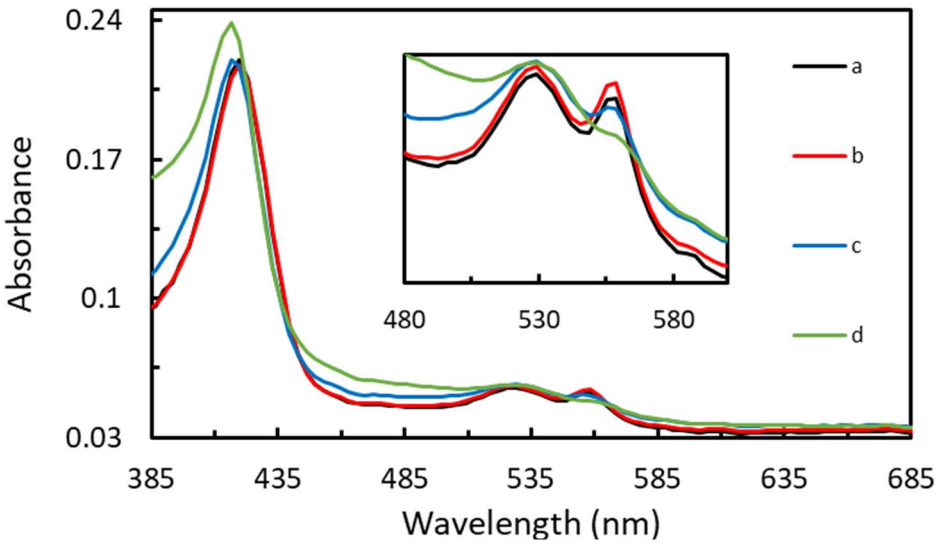


**Fig. 4.21.** An SVD-derived global fit of the data shown in Fig. 4.20, as derived by SVD analysis. This was fitted to a three-phase model, *a* → *b* → *c* → *d*.

Repeating the reaction with higher [$O_2$] (Fig. 4.22) caused *b* and *c* in the global fit to become indistinguishable from each other, and the PDA spectrum could be fitted with just three spectral components (Fig. 4.23).

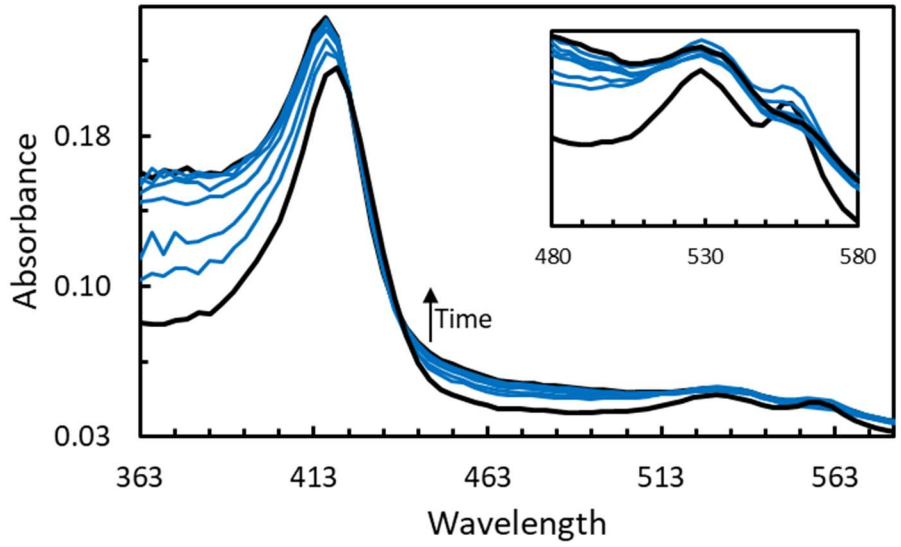


**Fig. 4.22.** Spectrum showing 1 µM WT BFR mixed with 48 $Fe^{2+}$/24mer in the presence of 730 µM $O_2$, measured using a photodiode array. The inset shows the transition of the ferrous heme to ferric. The spectra shown are taken at the following times: t= 0.012, 0.3, 0.6, 1.26, 1.92, 2.52, 3.13 and 6 s.

This may suggest that the second observed phase of heme oxidation is [$O_2$] dependent, but this may be an indirect effect of the dependence of $Fe^{2+}$ oxidation on [$O_2$] discussed above (Fig. 4.5). This could possibly be reminiscent of the HD-domain protein *myo*-inositol oxygenase, where a MVFC is observed under $O_2$ limiting conditions, but not at higher [$O_2$] (Xing, Diao, *et al.*, 2006).

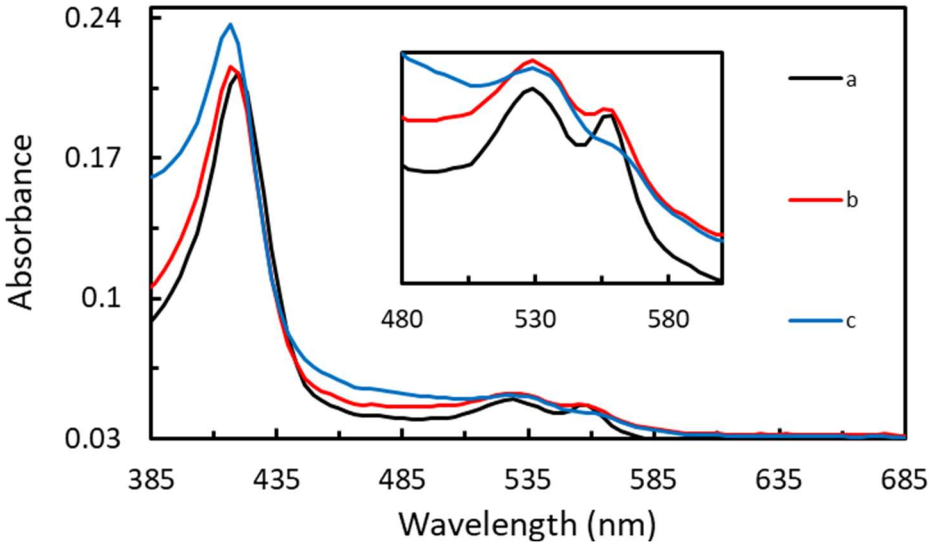


**Fig. 4.23.** A global fit of the spectrum shown in Fig. 4.22. This was fitted to a two-phase model, *a* → *b* → *c* with rates of 7.37 and 1.22 $s^{-1}$ respectively.

Small aliquots of $H_2O_2$ were added to aerobic solutions of WT BFR (again reduced using a stoichiometric amount of sodium dithionite) before being rapidly mixed with $Fe^{2+}$ and monitored using a PDA. An example of these spectra is shown in Fig. 4.24. The $Fe^{2+}$ oxidation is more clearly observed on the PDA here than in Fig. 4.11; this is because the rate of iron binding is much slower than that of $H_2O_2$ oxidizing the FC, and thus the reaction is rate-limited by iron binding at the FCs.

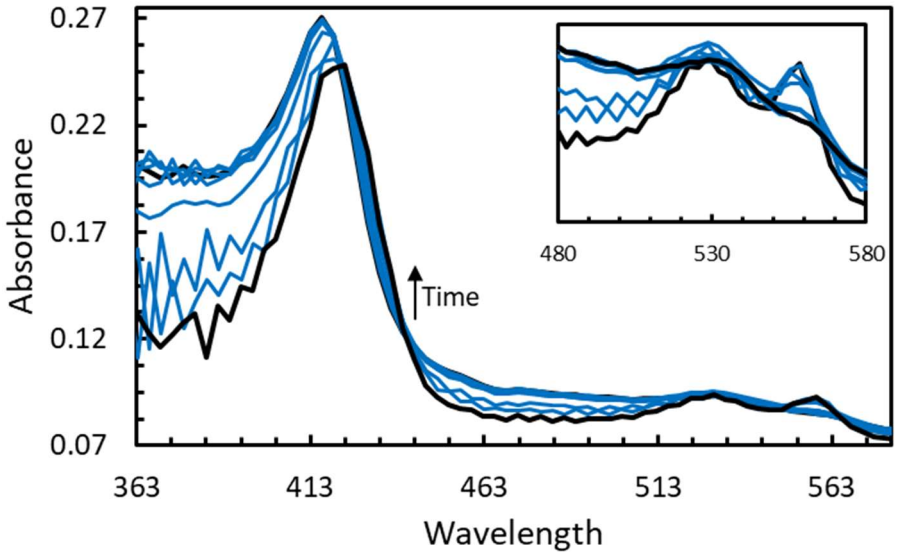


**Fig. 4.24.** Spectrum showing 1 μM sodium dithionite-reduced WT BFR mixed with 48 $Fe^{2+}$/24mer in the presence of 50 μM $H_2O_2$, measured using a photodiode array. The inset shows the transition of the ferrous heme to ferric. The spectra shown are taken at the following times: t= 0.012, 0.03, 0.06, 0.17, 0.70, 1.18, 1.67, 3.96 and 4.92 s.

Fig. 4.25 shows the SVD-derived global fits of the PDA spectra where two different concentrations of $H_2O_2$ (50 and 100 μM) have been aerobically incubated with WT BFR prior to $Fe^{2+}$ addition. These globally fitted spectra also suggest that the oxidation of the heme is dependent, directly or indirectly, on the concentration of the oxidant (this is reflected in the rates; at high [$H_2O_2$] in the experimental setups described in Figs. 4.11 and 4.13, a lower rate constant is observed on the PDA because most of the reaction has already finished during the dead time of the stopped flow instrument, despite the unambiguous evidence provided by photomultiplier experiments that the reaction is second order with respect to [$H_2O_2$]).

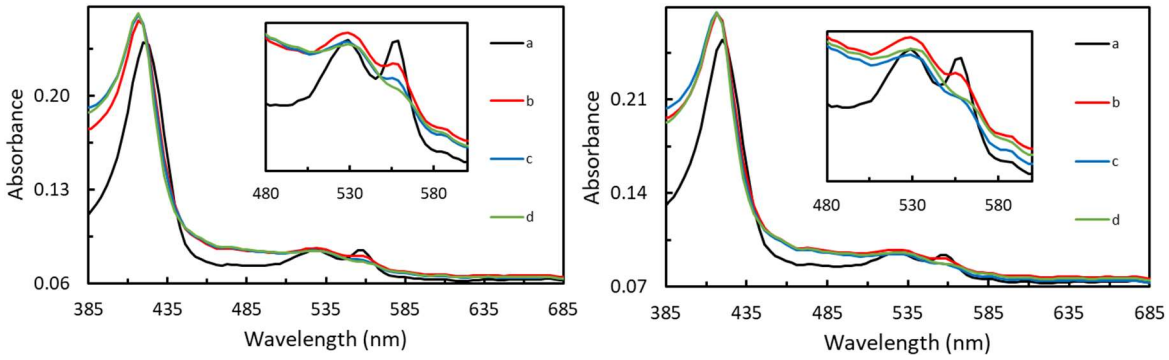


**Fig. 4.25.** Global fits of PDA spectra measured while $Fe^{2+}$ was rapidly mixed with WT BFR incubated with 263 µM $O_2$ and 50 µM (left) or 100 µM $H_2O_2$ (right). These were both fitted to a three-phase model, *a* → *b* → *c* → *d*. The rates for the left fit (50 µM) 14.22, 2.53 and 0.45 $s^{-1}$, while those on the right fit (100 µM) were 11.11, 0.76 and 0.23 $s^{-1}$.

**Mössbauer Spectroscopy of bacterioferritin:$Fe^{2+}$ with $H_2O_2$**

One of the challenges in understanding the fast and slower phases (Fig. 4.14) in the BFR:$Fe^{2+}$ reaction with $H_2O_2$ is that there has been no assignment of the chemical species formed in each of these steps. The products of these phases are too spectroscopically similar to identify using UV/vis absorbance. Anaerobic rapid freeze quench (RFQ) was used to prepare three samples to be measured using both Mössbauer spectroscopy and EPR to identify the oxidation state and ligand environment of the metal centres as well as possible kinetic links to the paramagnetic intermediates.

The following spectra in this section were kindly measured and simulated in Grenoble, France by the Blondin group.

Fig. 4.26 shows the Mössbauer spectra of these samples. The samples were frozen at timepoints which were selected based on the kinetics seen in stopped flow experiments; the first was mixed

with anaerobic water and thus represented 0 s, the next was frozen 45 ms after mixing with $H_2O_2$, which is after the fast phase has completed but before a significant amount of the slow phases has progressed. The final sample (60 s after mixing with $H_2O_2$) is after the reaction is expected (based on UV/vis data) to have finished altogether.

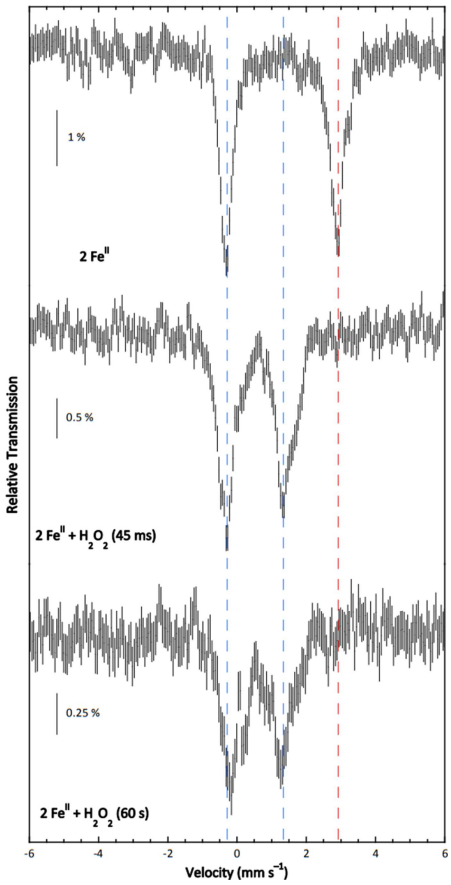


**Fig. 4.26.** Three Mössbauer spectra of BFR:$Fe^{2+}$, mixed with anaerobic water (as a control, top), or $H_2O_2$ in a 1:1 ratio, frozen after 45 ms (middle) and 60 s (bottom) reaction time. The concentrations of BFR, $Fe^{2+}$ and $H_2O_2$ were 83.3 µM, 2 mM and 2 mM respectively. A red dotted line marks the high-velocity line for the di-ferrous control sample. The blue dotted lines show the maxima for the lines in the sample frozen after 45 ms; these are slightly shifted from the maxima in the sample frozen after 60 s.

These spectra show that there was minimal $O_2$ contamination, with the control sample showing only the expected signature of ferrous ions. The high velocity line of these sites (see the red dotted line) is not present after exposure to $H_2O_2$, suggesting that all the $Fe^{2+}$ has been oxidized (this is in agreement with the data shown in Fig. 4.15). The blue dotted lines show that the diferric centres at 45 ms and 60 s are not equivalent, as there is a shift in the lines between the samples. These two diferric samples did not exhibit any signature of magnetic species; this strongly suggests that diamagnetic, dinuclear coupled species are formed. This is in agreement with EPR spectroscopy (see Chapter 5) which showed that the g =4.3 signal associated with $Fe^{3+}$ is never proportional to the amount of iron added.

The spectrum corresponding to the starting sample can be simulated by assuming either a single doublet with non-equal linewidth for the two lines (but in a 1:1 ratio for their relative area) or two doublets with lines of equal linewidth (within each doublet), the relative area of the two doublets being in a 1:1 ratio.

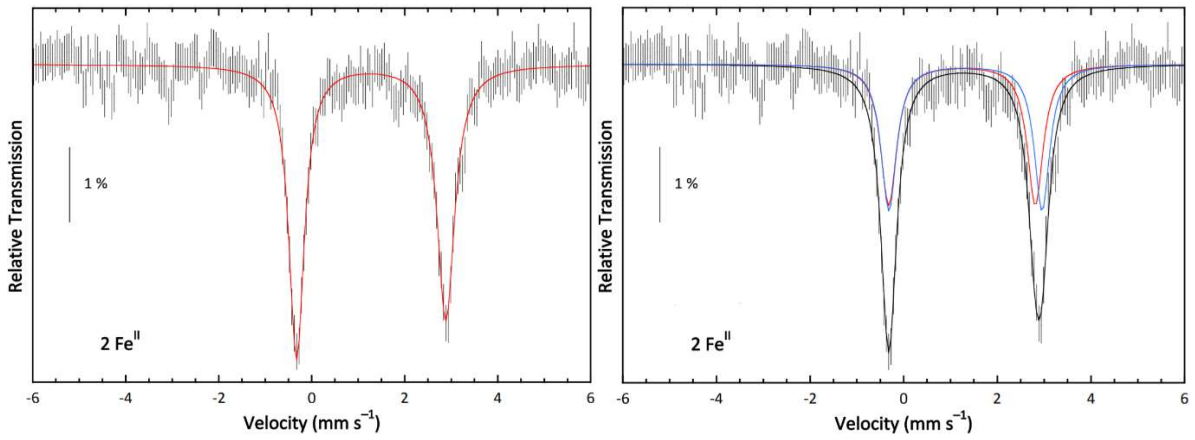


**Fig. 4.27.** Spectrum showing the two means of simulating the Mössbauer spectrum of the diferrous FC, either as a single doublet (left) or as two doublets (right). The parameters for these simulations are shown below in Table 4.2.

The nuclear parameters shown in Table 4.2 are indicative of two high-spin $Fe^{2+}$ in the FC of *E. coli* BFR. These values are close to those reported for the FC of the BFR from *Desulfovibrio vulgaris* ($\delta_1$ = 1.46 mm $s^{-1}$, $\Delta E_{Q,1}$ = 3.24 mm $s^{-1}$, $\delta_2$ = 1.22 mm $s^{-1}$, $\Delta E_{Q,2}$ = 3.20 mm $s^{-1}$, Timóteo *et al.*, 2012) and in reasonable agreement with those previously measured for *E. coli* ribonucleotide reductase (RNR) (average value $\delta$ = 1.26 mm $s^{-1}$, $\Delta E_{Q,}$ = 3.13 mm $s^{-1}$ (Lynch *et al.*, 1989). Two distinct ferrous sites have been identified in soluble methane monooxygenase hydroxylase from *Methylococcus trichosporium* ($\delta_1$ = 1.26 mm $s^{-1}$, $\Delta E_{Q,1}$ = 3.22 mm $s^{-1}$, $\delta_2$ = 1.35 mm $s^{-1}$, $\Delta E_{Q,2}$ = 2.37 mm $s^{-1}$, Banerjee *et al.*, 2013) and in toluene/ *o*-xylene monooxygenase hydroxylase (ToMOH) ($\delta_1$ = 1.32 mm $s^{-1}$, $\Delta E_{Q,1}$ = 3.06 mm $s^{-1}$, $\delta_2$ = 1.39 mm $s^{-1}$, $\Delta E_{Q,2}$ = 2.13 mm $s^{-1}$, Murray *et al.*, 2007).

**Table 4.2.** Simulation parameters for the starting sample (diferrous FC) in BFR:$Fe^{2+}$ mixed with $H_2O_2$.

| | Site | $\delta$ (mm $s^{-1}$) | $\Delta E_Q$ (mm $s^{-1}$) | $\Gamma$ (mm $s^{-1}$) | Area (% vs total area) | $\chi^2$ |
|---|---|---|---|---|---|---|
| **1 doublet** | 1 & 2 | 1.28 | 3.21 | 0.40/0.46 | 100.2 | $4.0\ 10^{-2}$ |
| **2 doublets** | 1 | 1.24 | 3.13 | 0.41 | 49.5 | $4.1\ 10^{-2}$ |
| | 2 | 1.32 | 3.27 | 0.40 | 49.5 | |

Simulation of the sample frozen 45 ms after mixing with $H_2O_2$ was more challenging, as three different doublets were required. These three doublets are sites within the protein where the occupying iron atoms are considered inequivalent; this can be due to the iron binding in a different location on the protein or having a different ligand. A large number of simulations were performed, and the thirteen best simulations were selected based on their $\chi^2$ value which is calculated accorded to Eq. 4.6 below:

$$\chi^2 = \frac{\Sigma_i \left(y_{th} - y_{exp}\right)^2}{\Sigma_i y_{exp}^2} \tag{4.6}$$

Each of these simulations were labelled 1-13 in order of increasing $\chi^2$ value. Figs. 4.28, 4.29 and 4.30 highlight three of these simulations. These three simulations are superimposable and differ only in the nuclear parameters and relative proportions of the doublets.

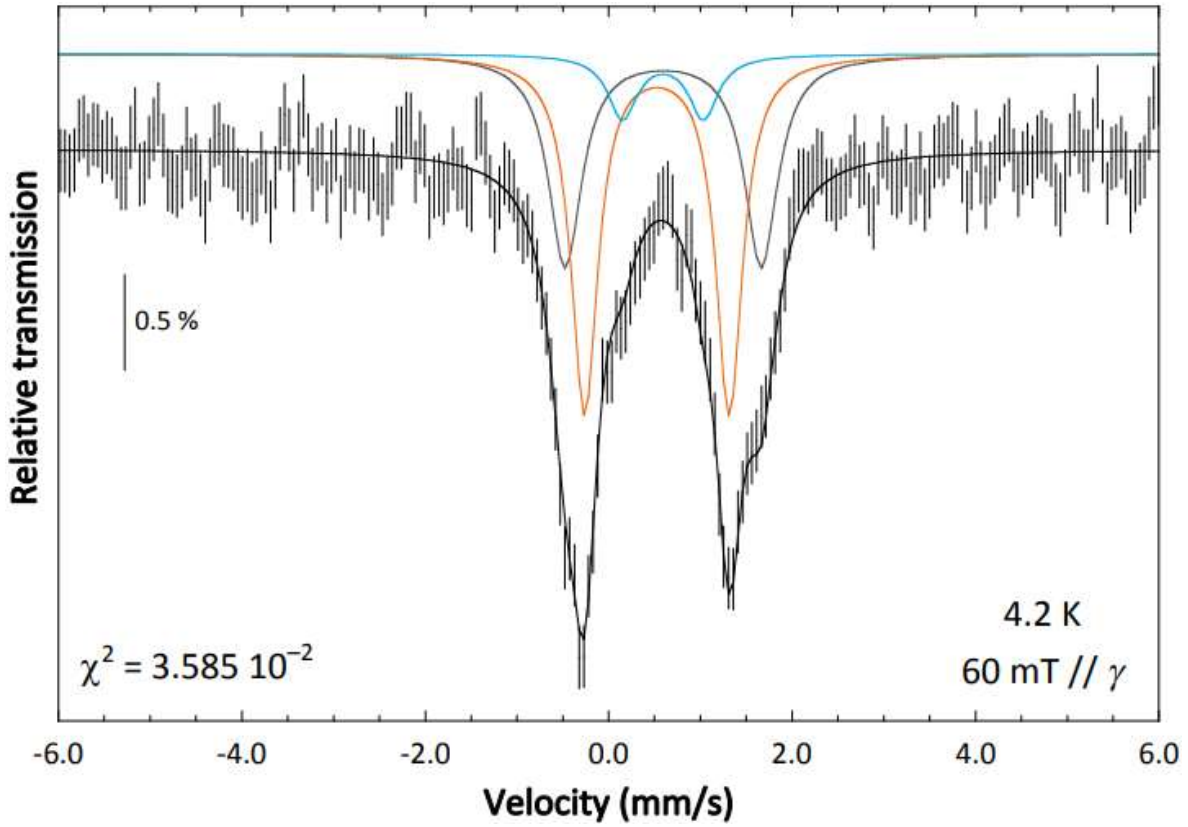


**Fig. 4.28.** Simulation 1 of the Mössbauer spectrum of BFR:$Fe^{2+}$ 45 ms after mixing with $H_2O_2$. This fit has the lowest $\chi^2$ value. The parameters of the doublets in this simulation are reported in Table 4.3.

**Table 4.3.** The nuclear parameters of the three doublets needed to fit Simulation 1 (Fig. 4.28).

| Fit1 | $\delta$ (mm s$^{-1}$) | $\Delta E_Q$ (mm s$^{-1}$) | $\Gamma_{fwhm}$ (mm s$^{-1}$) | % |
|---|---|---|---|---|
| Site 1 | 0.59 | 2.14 | 0.44 | 36 |
| Site 2 | 0.53 | 1.58 | 0.35 | 49 |
| Site 3 | 0.59 | 0.88 | 0.38 | 10 |

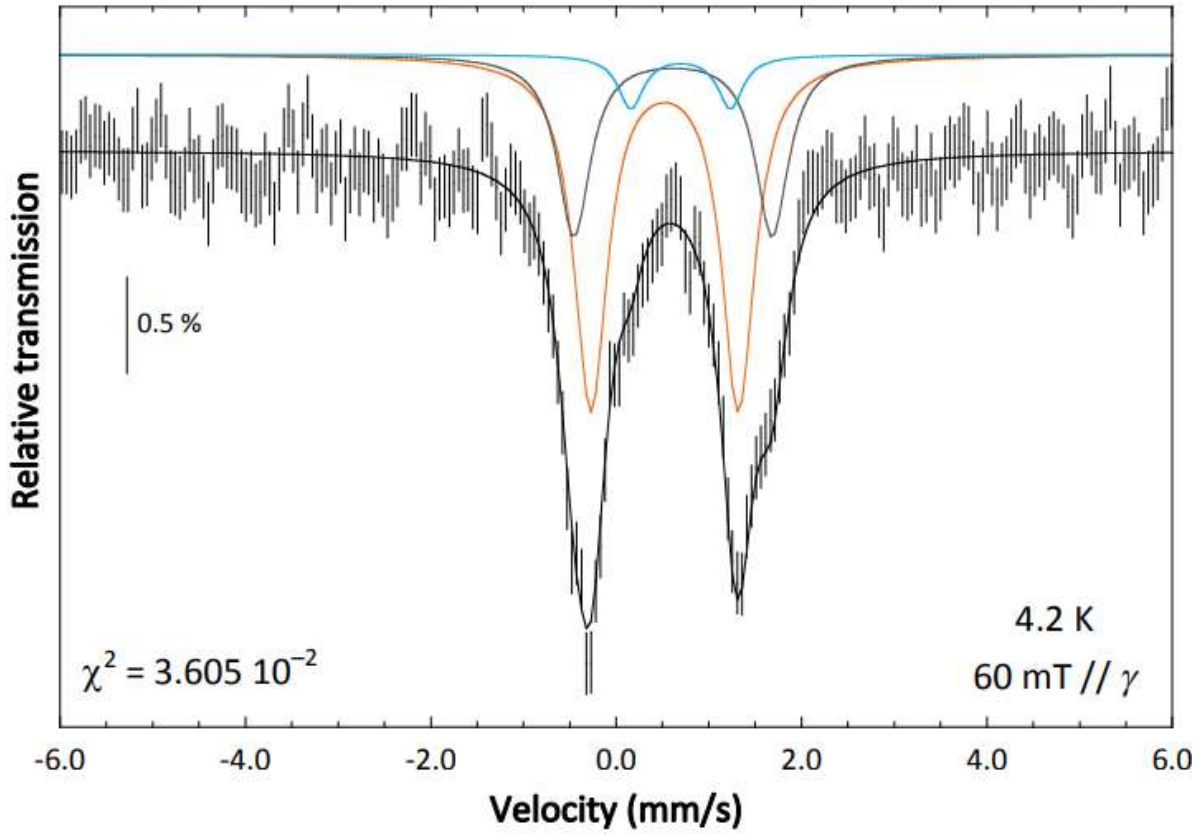


**Fig. 4.29.** Simulation 9 of the Mössbauer spectrum of BFR:$Fe^{2+}$ 45 ms after mixing with $H_2O_2$.

The parameters of the doublets in this simulation are reported in Table 4.4.

**Table 4.4.** The nuclear parameters of the three doublets needed to fit Simulation 9 (Fig. 4.29).

| Fit9 | $\delta$ (mm s$^{-1}$) | $\Delta E_Q$ (mm s$^{-1}$) | $\Gamma_{fwhm}$ (mm s$^{-1}$) | % |
|---|---|---|---|---|
| Site 1 | 0.61 | 2.14 | 0.42 | 30 |
| Site 2 | 0.52 | 1.59 | 0.43 | 59 |
| Site 3 | 0.70 | 1.07 | 0.33 | 7 |

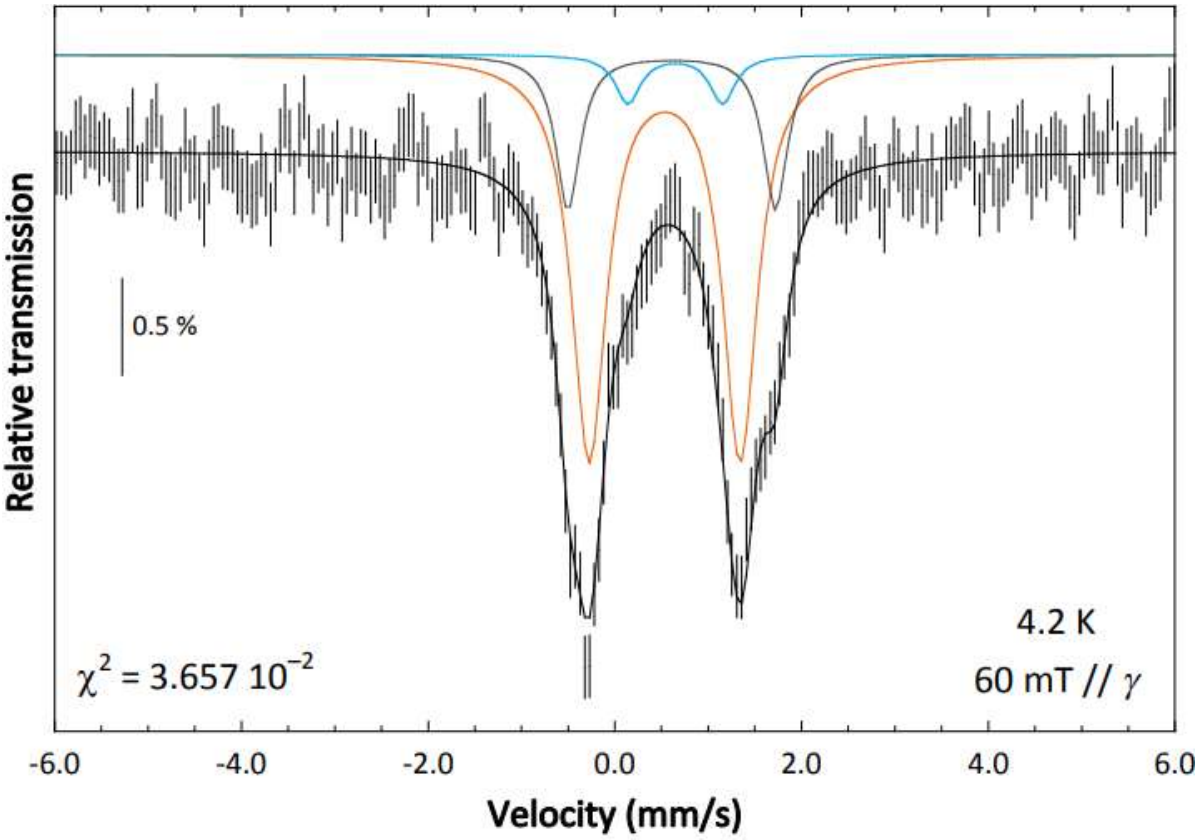


**Fig. 4.30.** Simulation 13 of the Mössbauer spectrum of BFR:$Fe^{2+}$ 45 ms after mixing with $H_2O_2$. This fit has the highest $\chi^2$ value. The parameters of the doublets in this simulation are reported in Table 4.5.

**Table 4.5.** The nuclear parameters of the three doublets needed to fit Simulation 13 (Fig. 4.30).

| Fit13 | $\delta$ (mm s$^{-1}$) | $\Delta E_Q$ (mm s$^{-1}$) | $\Gamma_{fwhm}$ (mm s$^{-1}$) | % |
|---|---|---|---|---|
| Site 1 | 0.61 | 2.22 | 0.31 | 19 |
| Site 2 | 0.53 | 1.62 | 0.45 | 70 |
| Site 3 | 0.65 | 1.01 | 0.33 | 6 |

Fig. 4.31 illustrates the nuclear parameter variation across the best-fitting simulations.

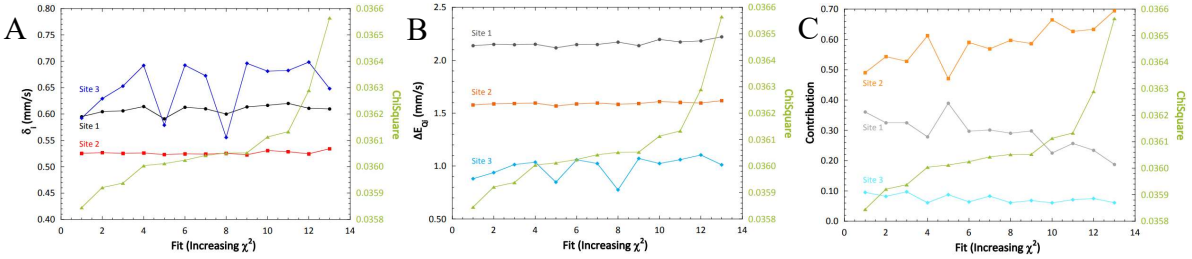


**Fig. 4.31.** The variations in nuclear parameters in multiple simulations of the BFR:$Fe^{2+}$ FC 45 ms after mixing with $H_2O_2$ as a function of the $\chi^2$ value of each simulation. The $\chi^2$ value of each fit is shown as a green trace in each plot. A. Isomer shift ($\delta$, central position of the doublet). B. Quadrupole splitting ($\Delta E_Q$, separation between the low lines). C. Relative contribution of each doublet to the overall spectrum.

These plots suggest that there are correlations between the parameters. In Fig. 4.31A and B, the nuclear parameters of Site 3 can be seen to vary significantly. In 4.31C, the contribution of Sites 1 and 2 appear to be correlated.

The relationship between the isomer shift of Site 3 and the other simulated parameters for each fit are shown in Fig. 4.32. Despite $\delta_3$ appearing to fluctuate randomly in Fig. 4.31A, it can be seen from Fig. 4.32A that the isomer shifts of Sites 1 and 3 are positively associated. The

nuclear parameters of Site 3 are strongly positively associated: $\Delta E_{Q3}$ increases from 0.78 to 1.10 mm $s^{-1}$ upon increasing $\delta_3$ (from 0.56 to 0.70 mm $s^{-1}$).

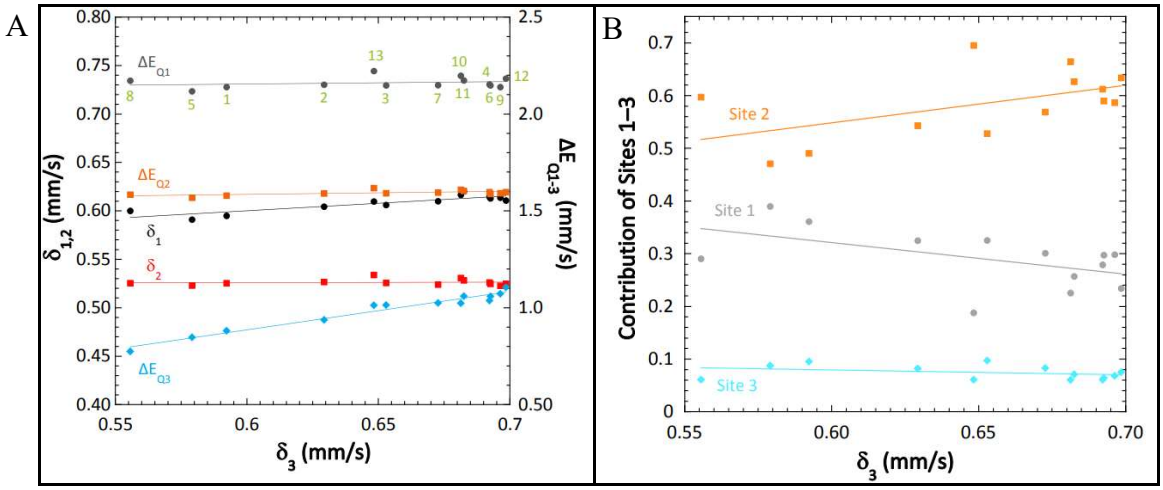


**Fig. 4.32.** A. The correlations between the isomer shift of site 3 ($\delta_3$) and the nuclear parameters of the three doublets. B. The relationship between a simulation's value of $\delta_3$ and the relative contribution of the three different doublets.

Fig. 4.33 shows the dependences, or lack of, the nuclear parameters and contributions of each site on the contribution of Site 1. These show the isomer shifts for Sites 1 and 2 are well defined (0.60(2) and 0.53(1) mm $s^{-1}$ respectively), as is the case for the quadrupole splittings (2.18(4) and 1.60(2) mm $s^{-1}$).

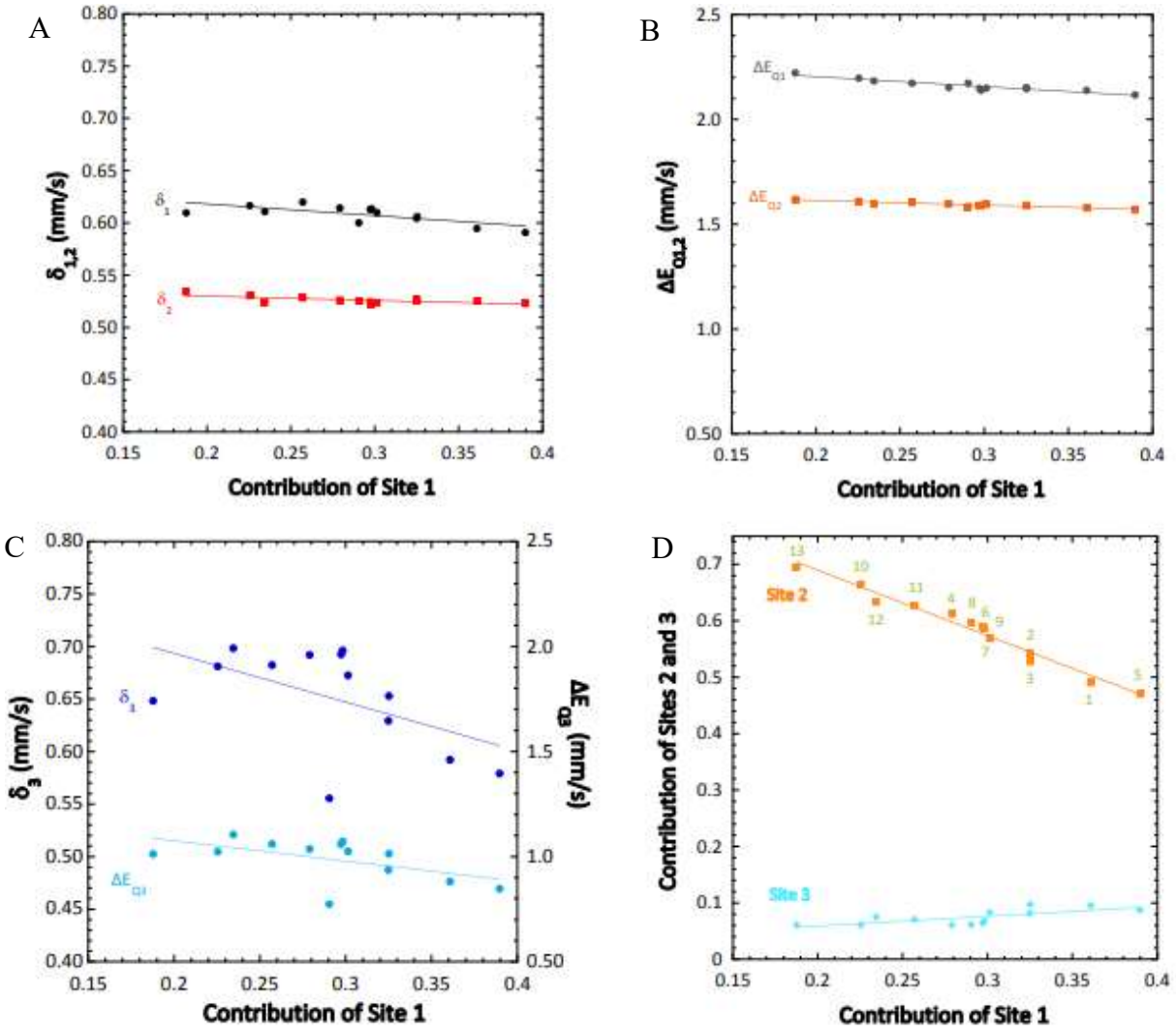


**Fig. 4.33.** The correlations between the relative contribution of Site 1 and various nuclear parameters of the three doublets. A. The contribution of Site 1 and its effect on the isomer shifts of Sites 1 and 2. B. The contribution of Site 1 and its effect on the quadrupole splittings of Sites 1 and 2. C. The dependence of Site 3's nuclear parameters on Site 1's contribution. D. The contributions of Sites 2 and 3 as a function of Site 1's contribution.

In Fig. 4.33D it can be clearly seen that as the contribution of Site 1 increases, that of Site 2 decreases whereas Site 3 increases. The mid-values are 29, 59 and 8 % for Sites 1-3 respectively, with uncertainties of ±10, ±10=1 and ±2.

Sites 1 and 2 may parallel the 1:1 ratio of the peroxo-cycled form of Δ9D (ie, after the peroxo-bridge has decayed): $\delta_1$ = 0.57(2), $\Delta E_{Q1}$ = 1.91(3), $\delta_2$ = 0.52(2), $\Delta E_{Q2}$ = 1.41(3) mm $s^{-1}$ which was assigned as a μ-oxo-bridged diferric centre (Broadwater *et al.*, 1999). It is worth noting that the 1:1 ratio of the doublets is key to the assignment of a μ-oxo-bridge; in the BFR:$Fe^{2+}$ simulations shown, the ratios of Sites 1 and 2 vary from 1.0:1.4 in Simulation 1 to 1.0:3.7 in Simulation 13. Adding the contributions of Site 1 and Site 3 together in Simulation 1 would be close to the 1:1 ratio needed for a bridged species, further supporting the asymmetric binding model proposed above.

A $\mu_{1,1}$-peroxo- form has been proposed for toluene/ *o*-xylene monooxygenase hydroxylase (ToMOH). In this protein the two ferric sites are identical with $\delta$ = 0.55, $\Delta E_Q$ = 0.67-0.70 mm $s^{-1}$ (Song and Lippard, 2011). It is difficult to assign Site 3 definitively to this form due to the large uncertainties in its nuclear parameters. The peroxo-form of frog M ferritin has nuclear parameters ($\delta$ = 0.62, $\Delta E_Q$ = 1.08 mm $s^{-1}$) that closely match the majority of simulations for Site 3.

To improve spectral resolution, and thus simulation of the species, spectra for the samples frozen 45 ms and 60 s after mixing were recorded again within a smaller velocity window (-4 - +4 mm $s^{-1}$). Fig. 4.34 shows the refined simulation of the sample frozen 45 ms after mixing with $H_2O_2$. This shows that the spectrum was simulated as a mixture of three species. The parameters of these species are highlighted in Table 4.6 below.

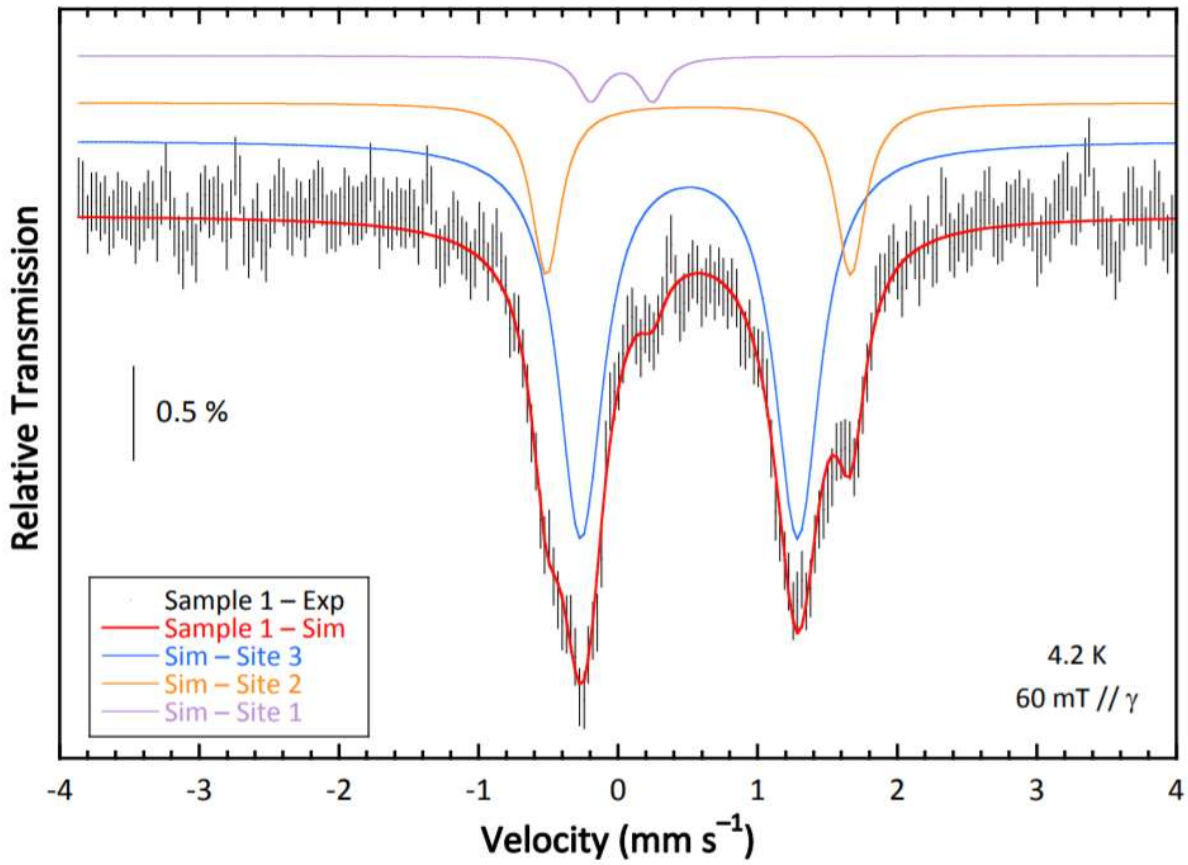


**Fig. 4.34.** Simulation of the Mössbauer spectrum of BFR:$Fe^{2+}$ 45 ms after mixing with $H_2O_2$ on a narrower velocity window. The parameters of the doublets in this simulation are reported in Table 4.6.

**Table 4.6.** The nuclear parameters of the three doublets needed to fit the above simulation (Fig. 4.34).

| | $\delta$ (mm s$^{-1}$) | $\Delta E_Q$ (mm s$^{-1}$) | $\Gamma_{fwhm}$ (mm s$^{-1}$) | % *vs* fixed total area | % (∑ = 100%) |
|---|---|---|---|---|---|
| Site 1 | 0.03 | 0.44 | 0.22 | 5 | 5 |
| Site 2 | 0.58 | 2.18 | 0.26 | 23 | 21 |
| Site 3 | 0.51 | 1.55 | 0.40 | 81 | 74 |

Site 1 in this series is notable for its low δ parameter and relative intensity within the sample. As no other species has comparable parameters within the longer timepoint's sample, it is

assumed that this is a highly transient intermediate. An inorganic $Fe^{4+}$ complex with similar parameters has been described ($\delta$ = 0.02 mm $s^{-1}$, $\Delta E_{Q,}$ = 0.43 mm $s^{-1}$, Lacy *et al.*, 2010). These parameters describe a mononuclear pentacoordinate high spin species which would be highly oxidizing (and thus transient) within the BFR FC. A ferryl intermediate has been described in site C of *Pyrococcus furiosus* ferritin (PfFtn) with different spectral parameters ($\delta$ = 0.25(2) mm $s^{-1}$, $\Delta E_{Q,}$ = 0.46(2) mm $s^{-1}$), but at an equally low percentage of the total $^{57}Fe$ (Honarmand Ebrahimi *et al.*, 2017).

The sample frozen 60 s after mixing also required three different doublets to simulate the spectrum (Fig. 4.35), but with differing parameters for only a single species (Table 4.7).

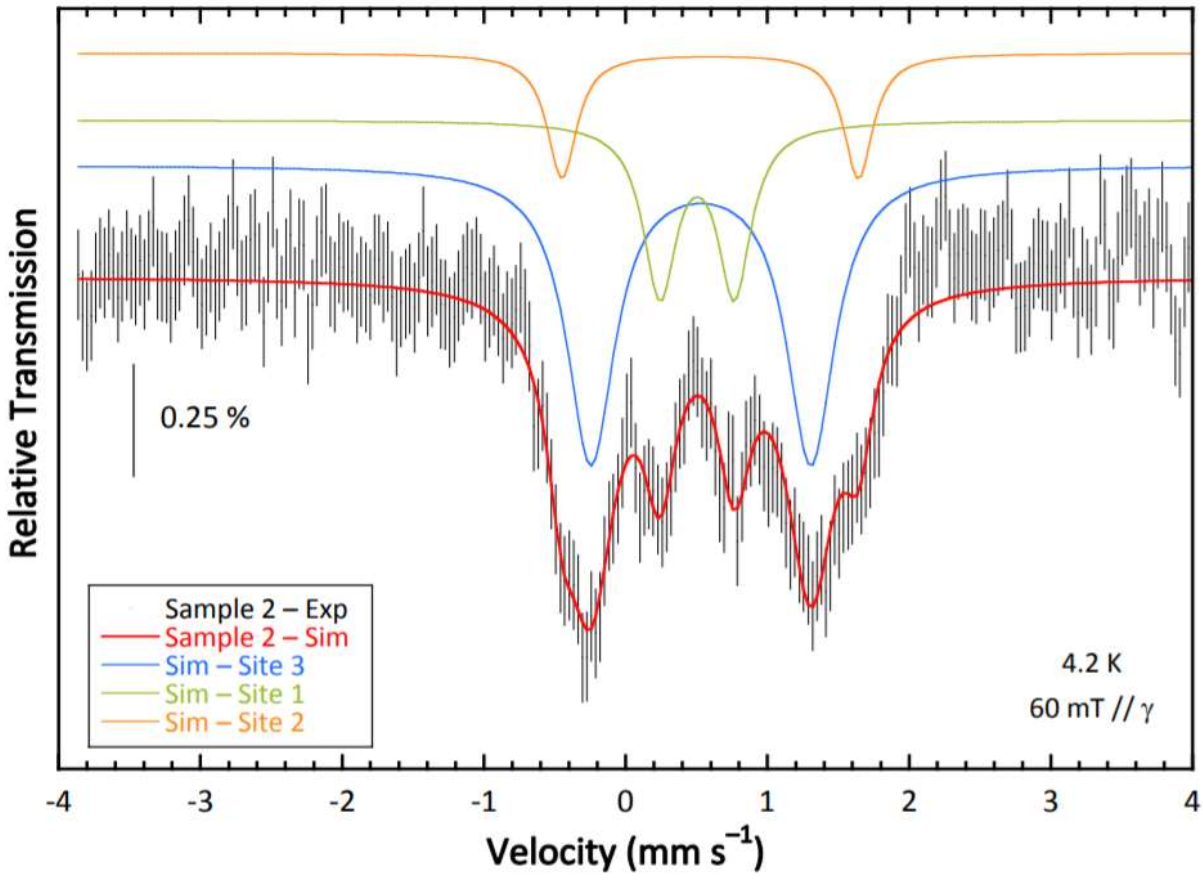


**Fig. 4.35.** Simulation of the Mössbauer spectrum of BFR:$Fe^{2+}$ 60 s after mixing with $H_2O_2$ on a narrower velocity window. The parameters of the doublets in this simulation are reported in Table 4.7.

**Table 4.7.** The nuclear parameters of the three doublets needed to fit the above simulation (Fig. 4.35).

| | $\delta$ (mm $s^{-1}$) | $\Delta E_Q$ (mm $s^{-1}$) | $\Gamma_{fwhm}$ (mm $s^{-1}$) | % *vs* fixed total area | % (∑ = 100%) |
|---|---|---|---|---|---|
| Site 1 | 0.50 | 0.53 | 0.30 | 30 | 25 |
| Site 2 | 0.60 | 2.09 | 0.26 | 20 | 17 |
| Site 3 | 0.53 | 1.54 | 0.39 | 68 | 57 |

From their similar parameters it can be deduced that Sites 2 and 3 are the same species in each sample. They represent different proportions of the iron in each sample, however, and are likely transient species. Site 1 in the early timepoint has drastically different parameters to that in the later sample. Site 1 in the sample frozen 60 s after mixing is likely the final product. Indeed, Site 1 in this sample can be comfortably simulated as a μ-hydroxo-bridged diferric species ($\delta$ = 0.49 mm $s^{-1}$, $\Delta E_Q$ = 0.51 mm $s^{-1}$, Mathevon *et al.*, 2007).

As addressed earlier, Site 2 does not accurately reflect the parameters for any peroxo- species, and has a $\Delta E_Q$ that is more reflecting of a ferrous rather than a ferric species. Site 3 has parameters within the boundaries of peroxo- systems that are already published (Broadwater *et al.*, 1999) but this is a questionable assignment; given that in Fig. 4.6 the release of $H_2O_2$ is seen to occur simultaneously with $Fe^{2+}$ oxidation by $O_2$, it is not feasible to suggest that 74% of the FCs have $H_2O_2$ bound 45 ms after mixing. This is compounded by the fact that 60 s later, when the reaction has finished, Site 3 still accounts for 57 % of the $^{57}Fe$.

One possibility that can be considered has been found in *E. coli* RNR (Wörsdörfer, Conner, *et al.*, 2013). Here, a tyrosyl radical adjacent to a diferric site provided the following parameters: ($\delta_1$ = 0.46 mm $s^{-1}$, $\Delta E_{Q,1}$ = 2.43 mm $s^{-1}$, $\delta_2$ = 0.54 mm $s^{-1}$, $\Delta E_{Q,2}$ = 1.63 mm $s^{-1}$). When the radical was translocated into a different subunit of the protein (with no change in the oxidation state at the diiron site), the parameters changed as follows: ($\delta_1$ = 0.43 mm $s^{-1}$, $\Delta E_{Q,1}$ = 1.89 mm $s^{-1}$, $\delta_2$

= 0.57 mm $s^{-1}$, $\Delta E_{Q,2}$ = 1.76 mm $s^{-1}$). These values indicate a μ-oxo bridged diferric species with a water molecule coordinated to one $Fe^{3+}$ atom. The decrease in $\Delta E_{Q1}$ was attributed to the deprotonation of the coordinated water upon quenching of the tyrosyl radical. A similar effect could be in effect in BFR, where the concentration of free radical is highest in the sample frozen 45 ms after mixing (Fig. 4.36).

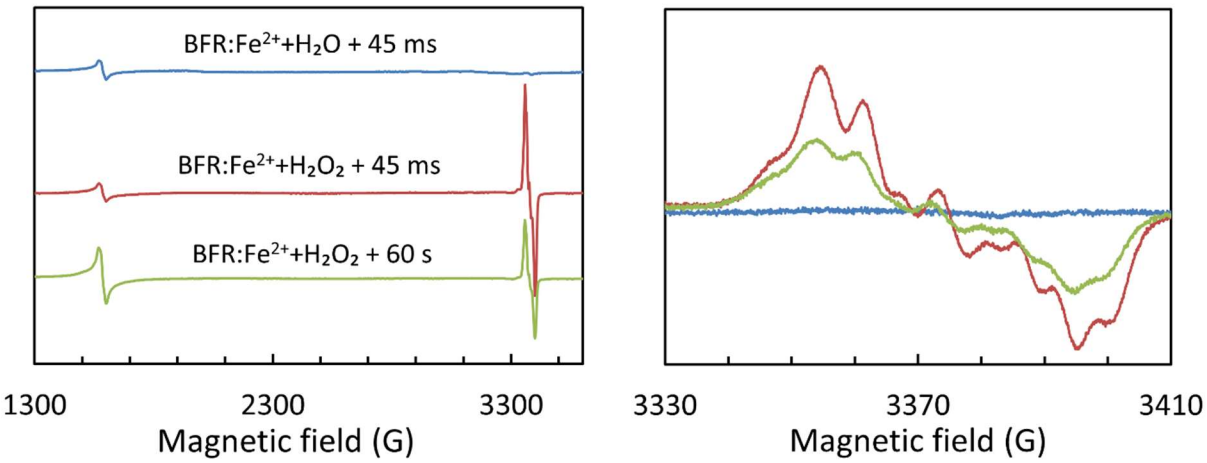


**Fig 4.36.** EPR spectra depicting the g = 4.3 and free radical signals in the Mössbauer samples of BFR: $Fe^{2+}$ when mixed with anaerobic water (blue) or $H_2O_2$ and frozen 45 ms (red) or 60 s (green) after mixing. The free radical spectra are recorded at a lower power in the right hand figure.

There is an increase in visible $Fe^{3+}$ that occurs in the 45 ms- 60 s timespan. As the Mössbauer spectra indicate that all of the iron is oxidized, the spectral differences between the samples must be due to ligand changes occurring within this timescale.

## Discussion

### Binding of $O_2$ to bacterioferritin: A comparison to hemerythrin

The conclusion that BFR: $Fe^{2+}$ binds $O_2$ to form an oxy-complex and that this 'autooxidizes' to release $H_2O_2$ and to yield the di-ferric protein is reminiscent of the behaviour of hemerythrin, the $O_2$-carrying protein in the hemocoel of sipunculid worms and brachinoids (Friesner *et al.*, 2003). This respiratory protein is like BFR in that it has an active centre which contains a μ-hydroxo-bridged pair of ferrous iron atoms (Fig. 4.37). It differs quantitatively from BFR in that it binds $O_2$ with higher affinity ($K_D$ = 1 μM as opposed to 823 μM for BFR, see Table. 4.1) and has a low autooxidation rate as is expected for a functional $O_2$ carrier (Bates *et al.*, 1968).

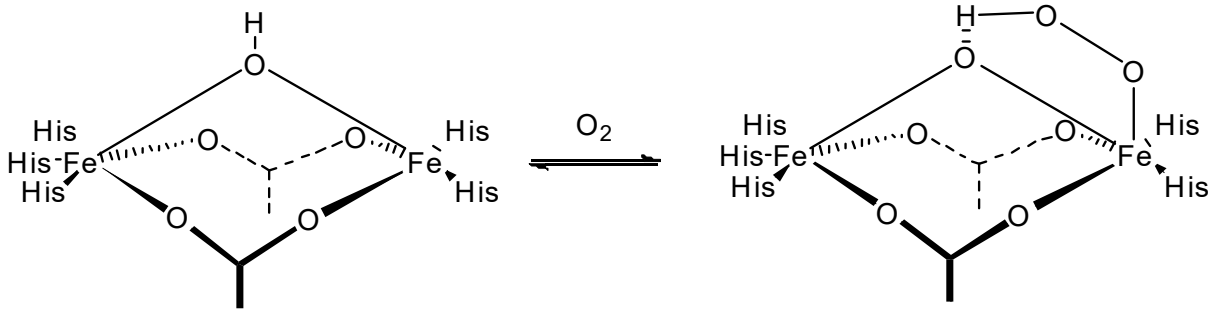


**Fig. 4.37.** Schematic representation of the active site of hemerythrin showing how $O_2$ is stabilised upon binding by proton donation and subsequent hydrogen bonding with the μ-hydroxo-bridging ligand.

Fig. 4.37 depicts in schematic form the structure of the $O_2$-binding site of hemerythrin in its oxy- and deoxy- forms. It may be seen that the two $Fe^{2+}$ ions are bridged by two carboxylate groups and a μ-hydroxo-oxygen atom (Holmes *et al.*, 1991). A further three nitrogen atoms are

supplied to one iron while the other has two, retaining a free coordination site. It is this site that $O_2$ fills. The bound $O_2$ makes a hydrogen bond to the hydroxo-group (Kurtz, 2003). Furthermore, the oxy-complex is further stabilized by partial delocalisation of the electrons available on the $Fe^{2+}$ onto the bound $O_2$ so that the complex may be viewed as having characteristics of a bound ferric-peroxide complex. This configuration stabilizes the oxy-complex, generating a high affinity for $O_2$, but allows for $O_2$ dissociation while resisting full oxidation of the metals. Because the peroxide-like intermediate is also stabilized, peroxide does not readily dissociate to leave the site in the di-ferric state. The X-ray structure of BFR: $Fe^{2+}$ reveals that the two irons are relatively symmetrical in their coordination spheres; they are a distance apart similar to that seen in hemerythrin and are also bridged by two carboxylate groups and a μ-hydroxo group. The bond lengths from the μ-hydroxo group are shown to be significantly longer in $Fe^{2+}$: BFR (2.91 and 2.64 Å) than are found in hemerythrin (2.16 and 1.78 Å) in Fig. 4.38.

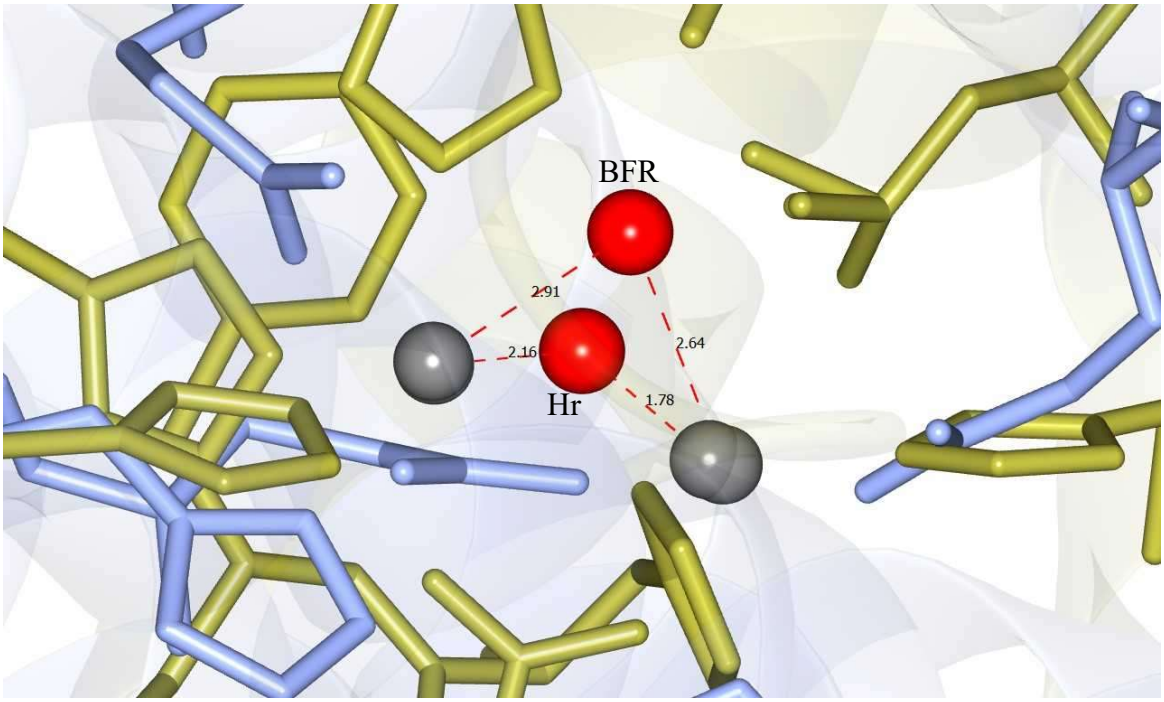


**Fig. 4.38.** The diiron centre of deoxy-hemerythrin (yellow, PDB: 1HMD (Holmes *et al.*, 1991)) overlaid with FC of deoxy-BFR (blue, PDB: 3E1N (Crow *et al.*, 2009)) showing the distance between the μ-hydroxo groups. The grey spheres represent the position of the iron atoms, and the red spheres show the μ-hydroxo bridge, labelled for each protein.

A comparison of the structure of deoxy-hemerythrin with that of the BFR: $Fe^{2+}$ complex is shown in Fig. 4.39. The structure of deoxy-hemerythrin indicates that one iron is pentacoordinate, above which a cavity is lined with non-polar residues.

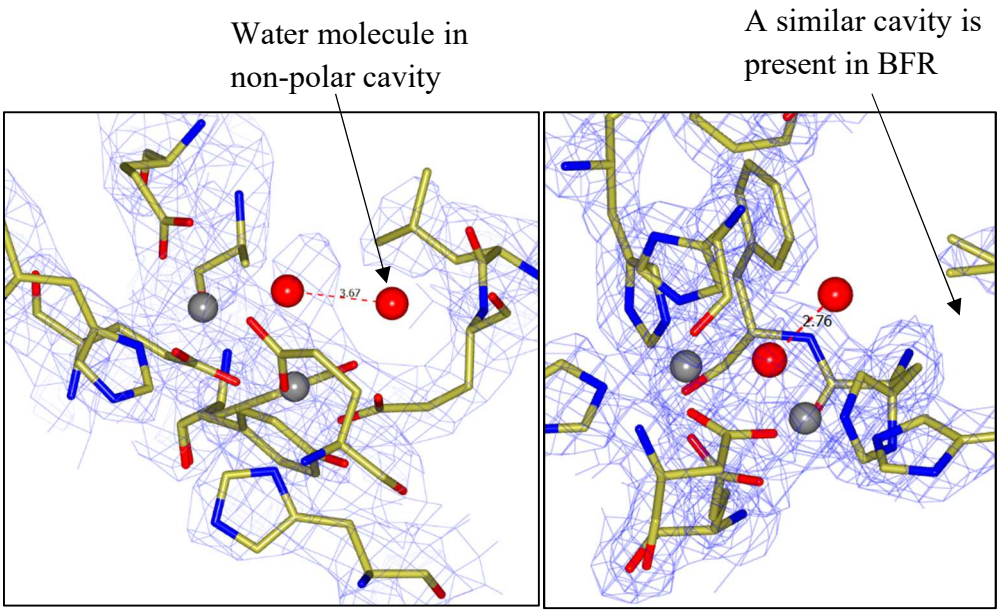


**Fig. 4.39.** The diiron centres of deoxy-hemerythrin (left) and deoxy-BFR (right). The distance between the μ-hydroxo bridge and a water molecule in the pocket are shown.

In BFR, this same cavity exists, but the equivalent iron is hexacoordinate. This suggests that the weak binding (high $K_D$) of $O_2$ to BFR may be ascribed to competitive ligand binding which is not present in hemerythrin. It is not possible to compare the oxy- forms of each protein because BFR autoxidizes so rapidly. However, examination of the oxy-structure of hemerythrin shows the $O_2$ resides over one of the irons within the cavity and that a similar configuration is possible for transient $O_2$-binding in BFR. Given that the hydroxo-iron bond is longer in BFR, it is plausible to suggest that the bonds between these and the bridging $O_2$ will also be longer. This may be a further reason why $O_2$ binding is weaker. In the oxy- form of hemerythrin the $O_2$ is enclosed in a more hydrophobic environment, and there is no easy access for protons necessary for the formation of $H_2O_2$, thus preventing autoxidation. In BFR, the site is less obviously hydrophobic.

**The Mössbauer spectra of bacterioferritin are distinct from other diiron sites**

The isomer shift values for each of the sites after contact with $H_2O_2$ (Fig. 4.31) are all consistent with high-spin $Fe^{3+}$. The nuclear parameters from the simulations can be used to speculate on the nature of the ligands bound to the iron. The lack of magnetic structure means that it is likely that the iron is bound in antiferromagnetically coupled dinuclear structures.

The results of the Mössbauer spectroscopy are interesting because the spectra differ from those reported for other diferric systems. While many comparisons can be made to different diiron protein Mössbauer spectra, none of them have parameters that are close enough to definitively assign the ligands at each step in the mechanism. It is clear, however, that there is a ligand exchange between 45 ms and 1 min reaction time.

Site 1 presents the largest quadrupole splitting among the three sites. This value ($\Delta E_{Q1}$ = 2.18(4) mm $s^{-1}$) is larger than the largest value observed for peroxo- systems in proteins (1.90(2) mm $s^{-1}$ for one of two ferric sites within peroxo- stearoyl-ACP $\Delta^9$-desaturase (Δ9D) (Broadwater *et al.*, 1999). Typically, the values for peroxo- systems lie between 1.0 and 1.6 mm $s^{-1}$ (Tinberg and Lippard, 2011). In addition, the associated isomer shift ($\delta_1$ = 0.60(2) mm $s^{-1}$) lies below the low edge observed for peroxo- systems (at least for the $\mu_{1,2}$-peroxo- coordination mode). However, $\Delta E_{Q1}$ is reminiscent of large quadrupole splitting values observed in μ-oxo-diferric systems. The resting state of RNR-R2 is characterized by $\delta_1$ = 0.46, $\Delta E_{Q1}$ = 2.43, $\delta_2$ = 0.54, $\Delta E_{Q2}$ = 1.63 mm $s^{-1}$, with a 1:1 ratio between the two doublets, one each associated with an individual Fe ion in the diiron centre. The diferric form observed after radical translocation and deprotonation of the coordinated water molecule on Site 1 is characterised by $\delta_1$ = 0.43, $\Delta E_{Q1}$ = 1.89, $\delta_2$ = 0.57, $\Delta E_{Q2}$ = 1.76 mm $s^{-1}$, maintaining the 1:1 ratio (Wörsdörfer, Conner, *et al.*, 2013). The similarity of these parameters to those of BFR make this hypothesis attractive.

Site 2 of RNR is highly similar to Site 2 of BFR simulated above in both isomer shift and quadrupole splitting. Given the resemblance of the coordination spheres in both proteins, and the hypothesis suggested above that only one of the two irons binds the oxidant molecule, this likeness is not surprising. One concern is that in the case of RNR, the two iron sites each account for 50 % of the added $^{57}$Fe. It is much more asymmetric in BFR; this may imply that a small percentage of one of the sites may bind $H_2O_2$ in a η2- peroxo- fashion, or that some sites may form a DFP species analogous to that seen in RNR (Yun *et al.*, 2007). If this is the case, a DFP species would be visible in PDA experiments (concentrations in this Mössbauer study are significantly higher than in the stopped flow experiments).

The possibility of a mixed-valent $Fe^{3+}/Fe^{4+}$ species has been considered in BFR, but was ruled out due to the Mössbauer parameters determined for this species in RNR (Baldwin *et al.*, 2000). The lack of magnetic coupling between the iron atoms when one iron is in the $Fe^{4+}$ state supports the notion that the $Fe^{4+}$ could be pentacoordinate. Iron that is participating in this reaction pathway may form $Fe^{3+}$ products that are not coupled, which may explain the increase in g = 4.3 at the 60 s timepoint (Fig. 4.36).

**The reaction of $H_2O_2$ with bacterioferritin: $Fe^{2+}$ is rate-limited by binding, not oxidation**

While Hr is an adequate protein to describe the binding of $O_2$ to the FC, it is insufficient to explain the kinetic behaviour of the FC. The $Fe^{2+}$: BFR reaction with $H_2O_2$, for instance, is a three-phase process where all the $H_2O_2$ is used in the first, rapid phase of the reaction. As $H_2O_2$ is a two-electron acceptor, the simplest model would be to take one electron from each $Fe^{2+}$ of the FC in a single-phase process. This is compatible with the optical data and consistent with the Mössbauer spectroscopy, which showed no $Fe^{2+}$ remained 45 ms after mixing with $H_2O_2$

(Fig. 4.26, 4.34). This process does not form radicals, as is observed in the RFQ EPR (see Chapter 5).

To explain this data, it is useful to compare the protein to other catalytic diiron centre-containing proteins, such as ribonucleotide reductase, and its B2 subunit. As discussed in Chapter 1, the diiron centre of B2 contains two ferric diiron centres and a tyrosyl radical in its active form. The coordination spheres of these diiron centres closely resemble the FC of BFR, and it has been demonstrated that when the di-ferrous B2 subunit is exposed to $O_2$ the iron atoms are oxidized and the tyrosyl radical forms. Furthermore, when the inactive metB2 form (di-ferric, but containing no free radical) is exposed to $H_2O_2$, the tyrosyl radical is formed, likely proceeding via a ferryl intermediate (Sahlin *et al.*, 1990). The formation of this tyrosyl radical in this instance is not associated with any optically detectable changes in the iron centres (the relevance of this is seen in Fig. 5.4). The similarities between the reactivity of this protein and BFR support the hypothesis that BFR may also go via a ferryl intermediate.

The slow phases seen in the reaction with $H_2O_2$ are not associated with the oxidation of the $Fe^{2+}$ in the FC, but are probably associated with either (or both): a) a relaxation of the newly generated ferric FC site to its resting μ-oxo form; b) the reaction of the newly generated diferric FC with an excess $H_2O_2$ molecule to generate a free radical on BFR as well as a $Fe^{4+}$ state on one of the irons in the FC which subsequently (and rapidly) accepts an electron from the protein to produce a second radical, leaving the FC site in the diferric state (see Chapter 5 for details).

**Ferrous heme oxidation by loading the ferroxidase centre with ferrous ions in an aerobic environment**

The observation that ferrous heme in BFR was oxidized by the diferric FC was accidental; experiments were performed on a Y25F variant sample that happened to contain heme in the ferrous state. Later on, deliberate reduction of the heme in WT BFR was performed to confirm the effect. These preliminary experiments show that while the heme is comparatively inaccessible to the highly oxidizing ferricyanide, the reaction of the FC $Fe^{2+}$ with $O_2$ results in rapid electron transfer from the heme group. This supports the role of the heme as an aide in removing iron from the protein; as the heme is reduced from outside of the ferritin shell, it feeds electrons into the FC which can then lead to $Fe^{2+}$ removal (Yasmin *et al.*, 2011).

One hypothesis for the two-phase heme oxidation in BFR could be that a MVFC forms as iron is oxidized. A clear experiment to test this is to study the reaction using EPR and observe the intermediates formed. Preparation of the samples would likely have to be carried out using anaerobic RFQ to prevent the auto-oxidation of the heme under atmospheric $O_2$, which would become an issue during prolonged experimentation.

**Mechanism of iron oxidation within the ferroxidase centres of bacterioferritin**

A trio of reaction schemes are proposed in Fig. 4.40. Here it is suggested that $O_2$ binds weakly but in a similar way to that seen observed in hemerythrin. The donation of a proton in the second step from an internal residue, e.g. Y25, releases $H_2O_2$ from coordination, leaving the μ-oxo-bridged diferric centre (Fig. 4.40A).

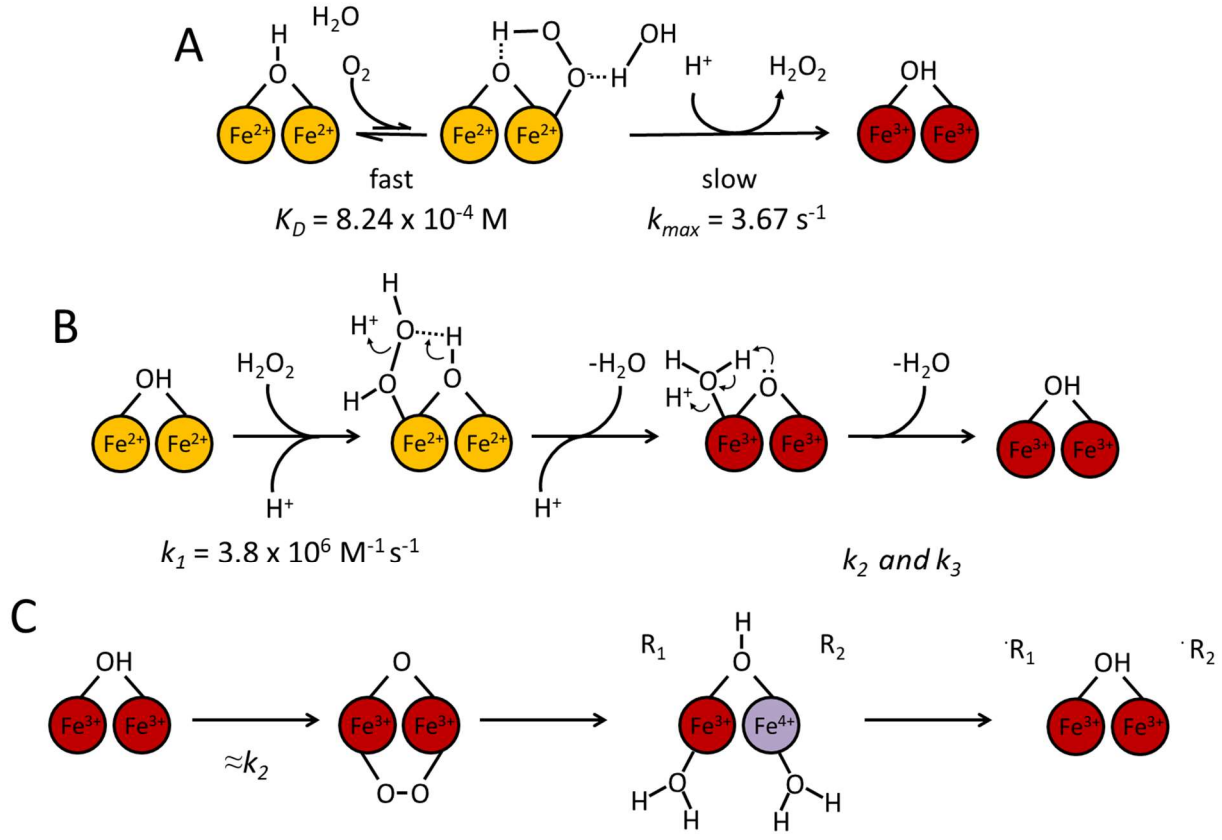


**Fig. 4.40.** Proposed mechanisms through which BFR reacts with both $O_2$ and $H_2O_2$. A. Oxygen binding is fast but weak, with $Fe^{2+}$ oxidation being rate-limited by the protonation of the peroxo- complex. We observe that Tyr25 is well placed to donate this proton. The intermediate is stabilized by hydrogen bonding to a water, which may be situated within a cavity over one of the iron sites. B. Binding of $H_2O_2$ is rate-limiting. Protonation of the complex rapidly releases a water molecule and oxidizes the diferrous FC. A second protonation releases a second water molecule. C. At supra-stoichiometric [$H_2O_2$] the BFR FC is capable of reacting with surplus $H_2O_2$; the mechanism for this is not known but the Mössbauer spectra support the formation of a DFP species and a ferryl intermediate which break down to produce radicals on the protein (the assignment of these radicals is speculated upon in the next chapter).

The Mössbauer spectrum of the BFR:$Fe^{2+}$ complex 45 ms after mixing with $H_2O_2$ (Figs. 4.28 and 4.34) showed that all of the iron was oxidized in this timescale, and that the ligands are different at one minute after mixing.

Hydrogen peroxide binding to the diferrous BFR centre is envisaged to form a complex as depicted in Fig. 4.40B; electron transfer from the two $Fe^{2+}$ to the oxygen atoms and the donation of a proton oxidizes the centre, leaving at least one water coordinated to the ferric atom. This dissociates, and it is the spectral change associated with these dissociation steps that are assigned to the slow phases seen in the $H_2O_2$ reactions (Fig. 4.13).

In the $O_2$ reaction, both schemes 4.40A and 4.40B operate in Fig. 4.4. The fact that we see a strict 4 $Fe^{2+}$ oxidized per $O_2$ atom in our titrations means that all $H_2O_2$ which is generated in scheme 4.35A is all consumed in scheme 4.35B. There is essentially no loss of $H_2O_2$, otherwise the stoichiometry would be less than 4. It is implied in this model that there should be a slow phase arising from water dissociation and site reorganisation as suggested in scheme 4.40B. This phase would be obscured in the $O_2$ reactions because the rate-limiting step in scheme 4.40A is slow and happens on a similar timescale. In addition, $H_2O_2$ is generated from the slow $O_2$ reaction and thus its concentration cannot be higher than that of the oxidised FCs. Hemerythrin-like domains have been reported to react with $H_2O_2$ in a single exponential time course, the rate constant of which is linearly related to [$H_2O_2$], as we observe for BFR. The second order rate constant is however many orders of magnitude lower than it is for BFR. Hydrogen peroxide binding/ reacting with hemerythrin-like domains in MsmHr has been shown to modulate the organism's response to oxidative stress, including $H_2O_2$, in the bacterium *Mycobacterium smegmatis* (Li *et al.*, 2015).

The intricacies of the third scheme (Fig. 4.40C) are less clear, but it is proposed here that this reaction pathway is only observed at supra-stoichiometric [$H_2O_2$]. $H_2O_2$ binds to FCs that have

already been oxidized to form a DFP species. The O-O bond is cleaved to make a single $Fe^{4+}$ species or an uncoupled diferryl species (this intermediate is less likely as it would require both iron centres to be pentacoordinate). The highly oxidizing nature of the $Fe^{4+}$ centres lead to the formation of radicals on the protein.

## Conclusion

These results show that $O_2$ oxidises the BFR FC through a mechanism that involves the rapid formation of a low-affinity complex in which electron transfer from the $Fe^{2+}$ ions to oxygen occurs in a rate-limiting step involving protonation and the subsequent dissociation of $H_2O_2$. In contrast the oxidation of the FC with $H_2O_2$ is very rapid. Given these findings and the likelihood that $O_2$ concentrations are quite low in the bacterium in its natural habitats it is reasonable to suggest that the FC is designed to react not with $O_2$ but specifically with $H_2O_2$. This adds to the increasing evidence that a primary function of BFR is perhaps to act within the cell as an $H_2O_2$ scavenger as a defence against this strongly prooxidant molecule that has been revealed to be a causative agent for oxidative stress.

The function of the heme group in BFR has been the subject of several studies, yet assignment of its function remains inconclusive. This chapter describes a novel new means to study the heme group in BFR, and how its redox properties allow it to interact with the FC.

# Chapter 5

# Free radical formation in bacterioferritin

## Introduction

In bacterioferritin (BFR), Y25 is the site of a universally conserved tyrosine residue that is found adjacent to the FC in all ferritins and is capable of losing an electron to form a free radical (Bradley, Moore and Le Brun, 2014). While not necessary for $Fe^{2+}$ oxidation in all ferritin species (Chen-Barrett *et al.*, 1995), there is clear evidence that this residue, and the resultant radical are necessary for the mineralisation of iron in BFR (Bradley *et al.*, 2015).

Chapter 4 described the reactions of BFR:$Fe^{2+}$ with $O_2$ and $H_2O_2$. Given that these are four and two-electron acceptors respectively, it is still not clear how radicals arise from the oxidation of the FC by these molecules. Now that we have characterised the kinetics of the $H_2O_2$-driven reaction, it is prudent to study the free radicals associated with these kinetic phases. The Tyrosyl Radical Spectra Simulation Algorithm (TRSSA) was developed by Svistunenko and Cooper, 2004 and has been successfully used to simulate the EPR spectra of the radical found in the $O_2$-driven mineralisation reaction by BFR.

Malone *et al.*, 2004 investigated the paramagnetic properties of mineralised iron in bacterioferritin. It was shown to be possible using EPR to identify different isoforms of ferric

iron, but these were never assigned. It may be possible to perform similar experiments on the FC using lower iron loadings.

## Results

### Formation and decay of free radicals on bacterioferritin using $H_2O_2$ as an oxidant

The tyrosyl radicals formed in the $Fe^{2+}$ oxidation by $O_2$ in ferritins have already been well documented (Bradley *et al.*, 2015) (Bradley *et al.*, 2017). In Fig. 5.1, the EPR spectra of the free radicals formed on BFR when $Fe^{2+}$ is oxidized by $O_2$ or $H_2O_2$ are shown.

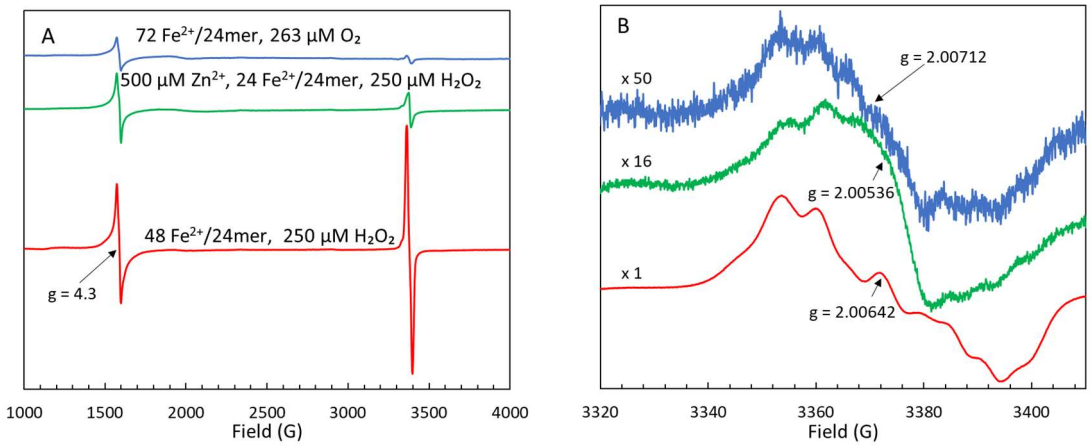


**Fig. 5.1.** Low-temperature EPR spectra of BFR showing how the oxidation of $Fe^{2+}$ in the ferroxidase centres (FCs) by either $O_2$ or $H_2O_2$ affects the resultant intensity and lineshape of the protein-based free radical EPR spectra 10 s after mixing. The blue spectra show 8.3 µM BFR mixed with 600 µM $Fe^{2+}$ (i.e. 72 $Fe^{2+}$/24mer) in the presence of 263 µM $O_2$. The green lines show 8.3 µM BFR where the FCs have been occupied with 500 µM $Zn^{2+}$ (i.e. 60 $Zn^{2+}$/24mer), then incubated anaerobically with 200 µM $Fe^{2+}$ (i.e. 24 $Fe^{2+}$/24mer) before being mixed with 250 µM $H_2O_2$. The red spectra show 8.3 µM BFR incubated anaerobically with 400 µM $Fe^{2+}$ before being mixed with 250 µM $H_2O_2$. The spectra were measured at 10 K at a microwave frequency $\nu_{MW}$ = 9.4673 GHz. A. Samples scanned over a wide magnetic field with showing the relative intensity of the g= 4.3 and FR in each of the spectra. These spectra were recorded using microwave power $P_{MW}$ = 3.16 mW. B. Spectra taken in a narrower field width at $P_{MW}$ = 0.05 mW to show the lineshape features of the free radical signal on the protein. Spectra have been amplified to be more clearly seen, with the multiplication factor shown in the figure.

Fig. 5.1A shows that the g = 4.3 and the free radical signals are larger (with the free radical concentration being 18.7 % of total monomer concentration) when the protein reacts with $H_2O_2$ as opposed to $O_2$. When a small excess of $Zn^{2+}$ (60 $Zn^{2+}$/24mer) is used to fill the FCs before

adding $Fe^{2+}$ or $H_2O_2$, $Fe^{2+}$ is prevented from forming the reactive diiron centre of the protein. This reduced the intensity of the g = 4.3 (mononuclear $Fe^{3+}$) and the free radical (FR) signals observed in the reaction significantly, demonstrating that the FC activity is necessary for free radical formation. While the $Zn^{2+}$ obstruction experiments could be seen as having a greater inhibitive effect on FR formation in the $O_2$-driven reaction (Bradley *et al.*, 2015) as compared to the effect of $Zn^{2+}$ in anaerobic oxidation by $H_2O_2$ reported here, it is important to highlight that these experiments are not equivalent. In the former work, the $O_2$-driven $Fe^{2+}$ oxidation was initiated by the addition of $Fe^{2+}$ and is thus limited by the off-rate of the tightly binding $Zn^{2+}$ ions. Here, BFR is incubated anaerobically with both $Zn^{2+}$ and $Fe^{2+}$, allowing for some $Fe^{2+}$ to displace the $Zn^{2+}$ and thus participate in the FC reaction.

To investigate the free radical formation in the reaction with $H_2O_2$, BFR was incubated with increasing concentrations of $H_2O_2$ then mixed with $Fe^{2+}$ in an aerobic environment (it has been conclusively shown that $H_2O_2$ will always outcompete $O_2$ as an oxidant for the FCs in BFR, compare the rates of reaction of BFR with both oxidants in Figs. 4.5 and 4.14). Fig. 5.2 shows these spectra.

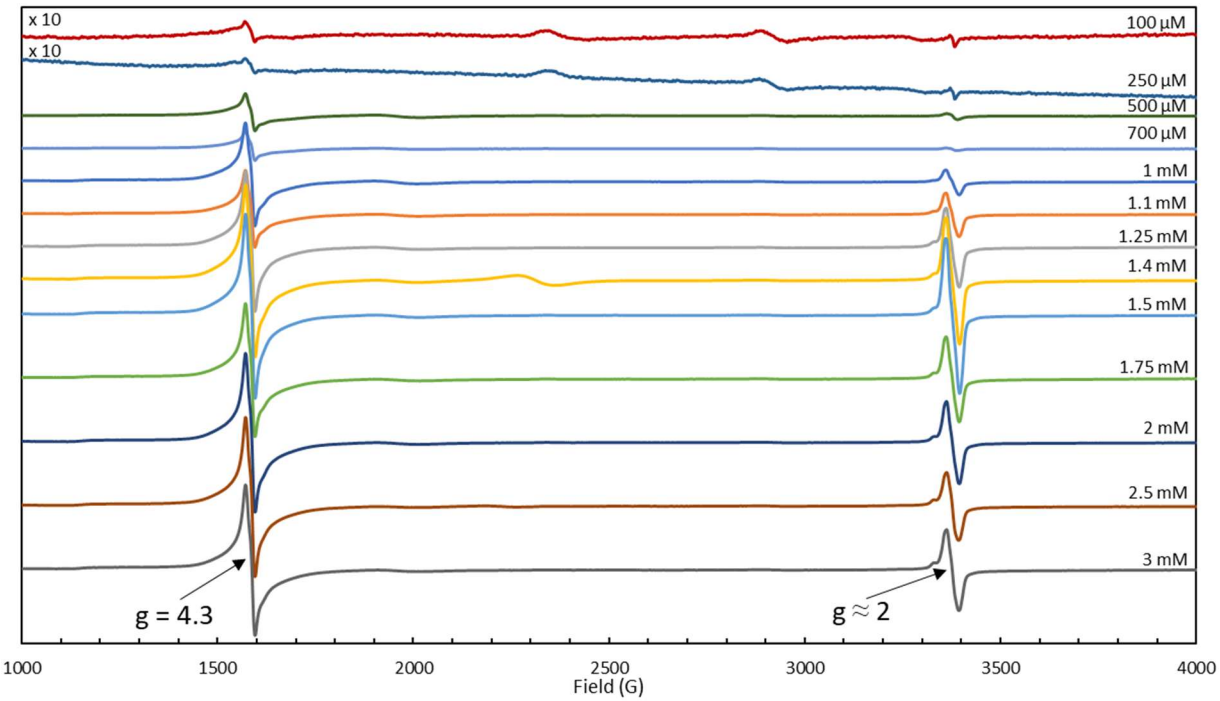


**Fig. 5.2.** Stacked plot showing the effect increasing [$H_2O_2$] has on the observable paramagnetic species in the BFR: $Fe^{2+}$ complex. The BFR (41.65 µM) was incubated with $H_2O_2$ while 2 mM $Fe^{2+}$ was added to start the reaction. Experiment was performed under standard atmospheric conditions (≈ 260 µM $O_2$). Samples were slow-frozen (see Materials and Methods) 13 s after the addition of $Fe^{2+}$. The spectra were measured at 10 K at the following instrumental conditions: microwave frequency $\nu_{MW}$ = 9.4658 GHz; microwave power $P_{MW}$ = 3.16 mW.

Fig. 5.3 shows the corresponding high-resolution free radical spectra. In these, it is clear that both the free radical lineshape and intensity are strongly associated with the stoichiometry of [$H_2O_2$] relative to the concentration of $Fe^{2+}$ in the sample (2 mM). At sub-stoichiometric [$H_2O_2$] (100 µM up to 1 mM, see Eq. 4.4) the intensity of the free radical is very small, with few spectral features. However, at supra-stoichiometric [$H_2O_2$] (>1 mM) the free radical lineshape becomes larger and more complex.

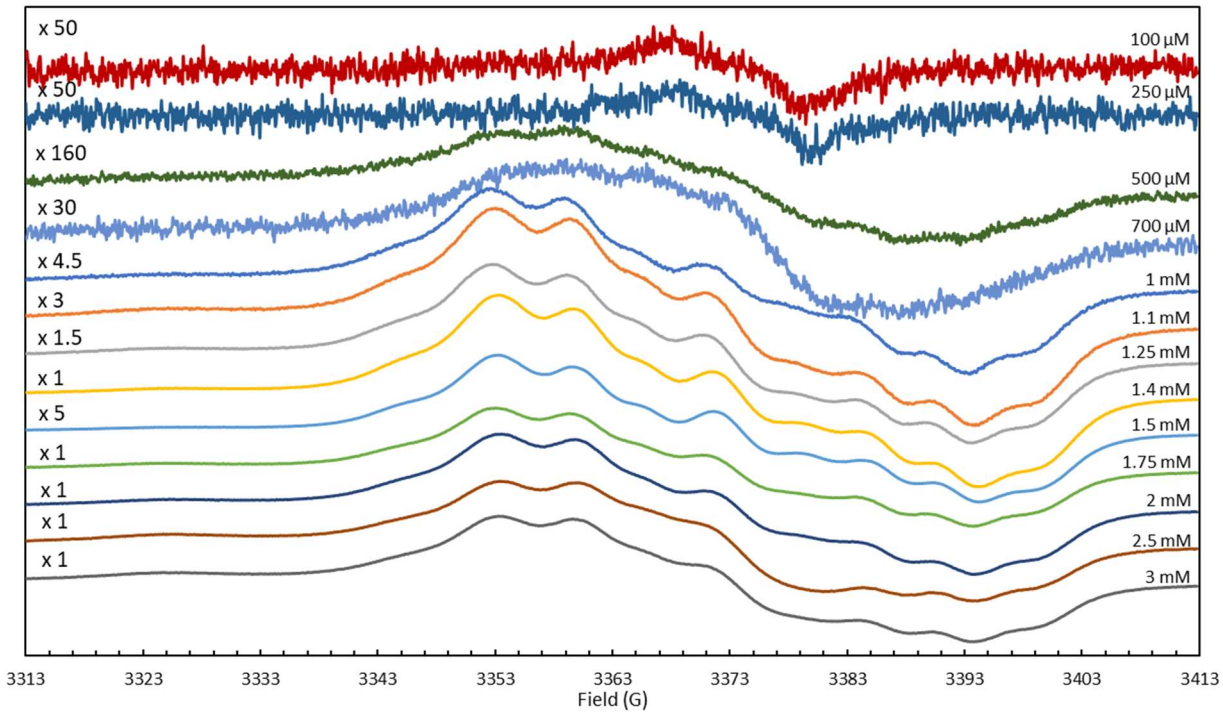


**Fig. 5.3.** A plot showing how the lineshape of the protein-based free radical in the reaction shown in Fig. 5.2 changes with increasing [$H_2O_2$]. The size of each spectrum has been amplified by arbitrarily selected factors shown on the left so that their lineshapes are clearly visible. The BFR (41.65 µM) was incubated with $H_2O_2$ while 2 mM $Fe^{2+}$ was added to start the reaction. Experiment was performed under standard atmospheric conditions (≈ 260 µM $O_2$). Samples were frozen 13 s after the addition of $Fe^{2+}$. The spectra were measured at 10 K at the following instrumental conditions: microwave frequency $\nu_{MW}$ = 9.4658 GHz; microwave power $P_{MW}$ = 0.05 mW.

In Fig. 5.4, the concentration of free radical within each sample has been plotted as a function of [$H_2O_2$]. There are three separate factors that shape this dependence. The first is the stoichiometry; the red line indicates where the combined concentration of $O_2$ (≈260 µM) and $H_2O_2$ in the mixture is sufficient to oxidize all 2 mM of the $Fe^{2+}$ in the FCs (see Eq. 5.1).

$$\frac{2000\ \mu M\ Fe^{2+} - (4 \times 260\ \mu M\ O_2)}{2} = 480\ \mu M\ H_2O_2 \qquad (5.1)$$

Below and close to this value (the 250 and 500 μM spectra, Fig. 5.3), the free radical has an EPR lineshape and intensity comparable to those observed in the $O_2$-driven oxidation reaction (Bradley *et al.*, 2015). Above this value, the free radical intensity increases and the lineshape begins to change. The second factor is the significantly faster rate at which the $H_2O_2$ oxidizes the FCs compared to $O_2$. The blue vertical line in Fig. 5.4 shows where there is a 2:1 $Fe^{2+}$: $H_2O_2$ ratio, and thus where most or all the $Fe^{2+}$ is oxidized by $H_2O_2$. At [$H_2O_2$] greater than this mark, the free radical intensity increases much more quickly while the lineshape does not change much. The final factor is a more complicated relationship between the formation and decay of the free radicals which happens at [$H_2O_2$] > 1.5 mM, where the balance of the free radical formation and decay rate dependences on [$H_2O_2$] changes producing a transient decrease followed by a steady state of observed concentration of the radicals.

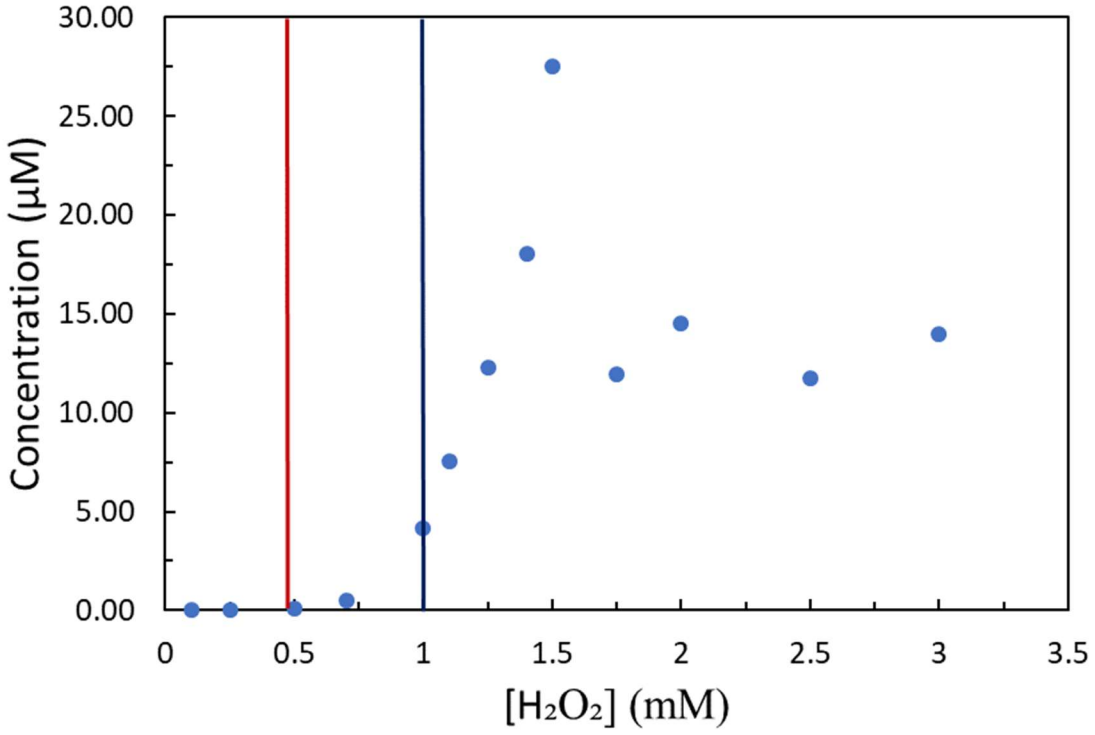


**Fig. 5.4.** The spectra in Fig. 5.3 were double integrated expressed as free radical concentration on [$H_2O_2$] by referring to a double integral of a $Cu^{2+}$ standard spectrum (see Materials and Methods). The red line shows where the combined $H_2O_2$ and $O_2$ concentrations are sufficient to oxidize the entirety of the 2 mM $Fe^{2+}$ present in the sample. The blue line shows where just the [$H_2O_2$] is enough to oxidize all the $Fe^{2+}$ present (NB the much faster reaction of the FC with $H_2O_2$ than with $O_2$). The concentrations of BFR and $Fe^{2+}$ were 41.65 µM and 2 mM respectively.

Given that the large free radical observed in the $H_2O_2$-driven oxidation does not appear at sub-stoichiometric [$H_2O_2$], this free radical cannot be involved in the fast phase of $Fe^{2+}$ oxidation observed in the stopped flow experiments (See Fig. 4.15). This is consistent with the notion that $H_2O_2$ is a two-electron acceptor, and that one $H_2O_2$ oxidizes one site without the need for radicals (see Fig. 4.37).

Fig. 5.5 shows the formation of the free radical at supra-stoichiometric conditions. This shows that at high concentrations, the radical has not decayed in a timescale similar to the slow phase $k_3$ observed in stopped flow experiments (see Fig. 4.16), and that the maximum free radical intensity is reached at approximately 20 s.

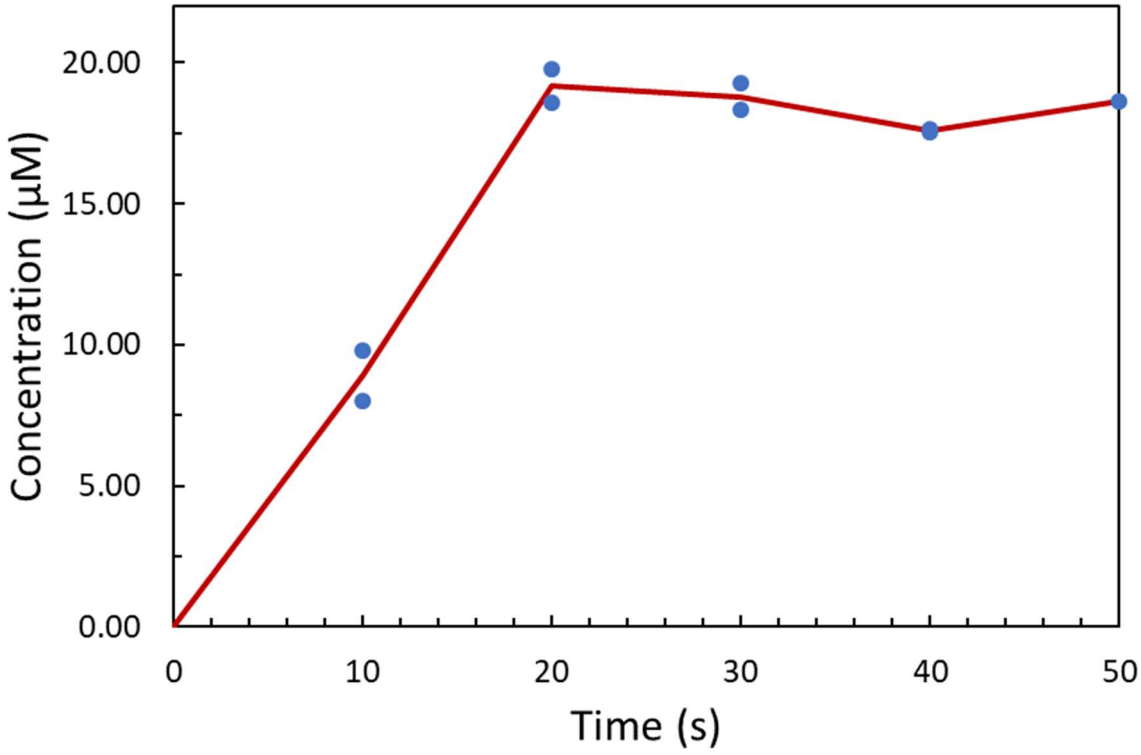


**Fig. 5.5.** The dependence of free radical concentration on time in the reaction of 41.65 μM BFR with 1.25 mM $H_2O_2$. The kinetics were monitored by slow-freezing aerobic BFR/ $H_2O_2$ solutions (see 2.9) after the addition of $Fe^{2+}$. The concentration of free radical was estimated in each sample by comparison to a $Cu^{2+}$ standard spectrum, as stated above in Fig. 5.4. The data for duplicate samples are shown for four of the five time points.

BFR (8.3 μM) was loaded with 48 $Fe^{2+}$/24mer and left for 30 mins to react with $O_2$. When mixed with 250 μM $H_2O_2$ and frozen at 12 s, this did not produce a free radical signal. This

suggests that the ligand change that occurs between 45 ms and 60 s (see Fig. 4.26) prevents the FC from reacting any further with $H_2O_2$.

To complement the stopped flow data in Fig. 4.14, anaerobic RFQ (see Materials and Methods) was performed at concentrations analogous to those used in the $H_2O_2$-driven $Fe^{2+}$ oxidation stopped flow experiments. Fig. 5.6 shows this data.

Since different time points were used in the three data series, to produce averaged time dependences for the two species, the following data processing procedure was used. For each of the series, the experimentally obtained data were complimented with linearly interpolated 'ghost' data points' (open symbols) for the time points used in two other series. Thus, complete sets of three data points for each time point used in the three series were obtained; their averages are represented by the black lines.

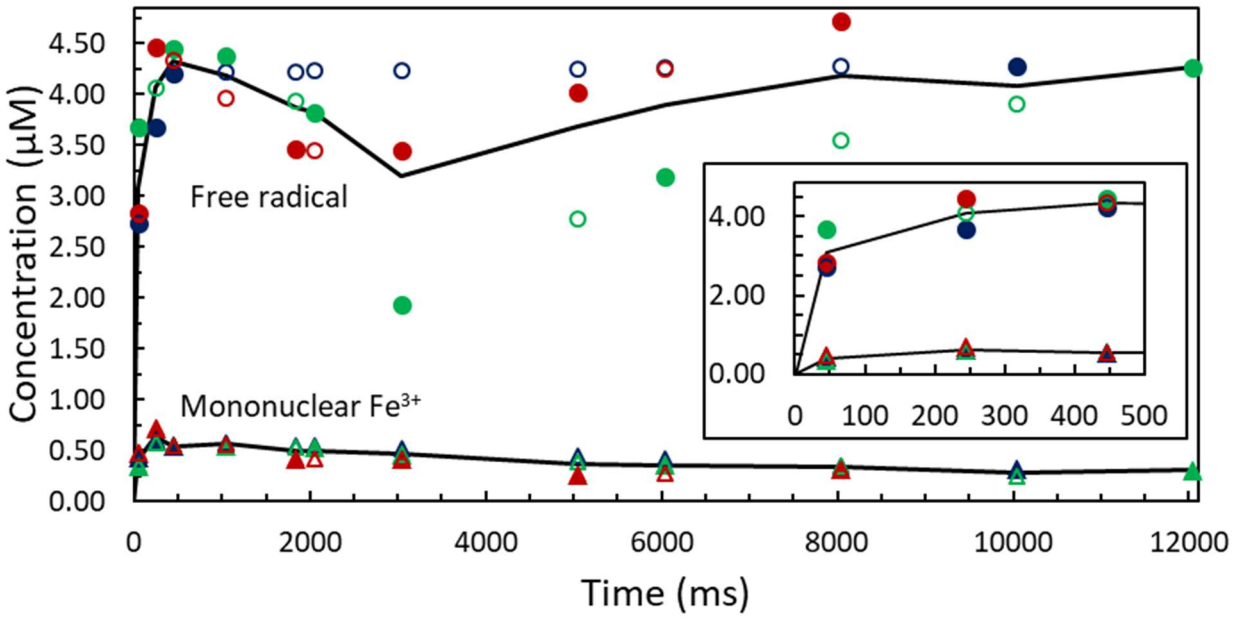


**Fig. 5.6.** Anaerobic RFQ data showing the concentrations of free radical and rhombic ferric iron as functions of time. The BFR and $Fe^{2+}$ mixture pre-incubated anaerobically was mixed with $H_2O_2$ (dissolved in water) in the RFQ machine and frozen at the corresponding time points thereafter. The concentrations of BFR, $Fe^{2+}$ and $H_2O_2$ in the final mixture were 1 μM, 48 μM and 100 μM respectively. Three series of samples were prepared and are represented by red, blue and green filled symbols- circles for the free radical and triangles for the rhombic ferric iron (g = 4.3). 'Ghost' points are represented by the unfilled shapes and are used to generate the average time dependence for each paramagnetic species, shown here by the black lines. The shortest time point on the graph is for 45 ms. The inset shows the timepoints in the first 500 ms in greater detail.

This plot shows that the free radical concentration in this experiment is consistently around 16 % of monomer concentration in the reaction time interval 0.5 – 12 s. Compared to the maximum free radical concentration in Fig. 5.4, where it is only 2.8 % of the total monomer concentration, it is notable that the concentration of free radical observed does not linearly increase with [BFR]. The rate of formation of the free radical in the anaerobic RFQ experiments (approx. 16

$s^{-1}$), however, is of a similar magnitude as the rate observed for $k_2$ in the stopped flow experiments (approx. 10 $s^{-1}$, see Fig. 4.14).

An example of the spectra that are attained from the anaerobic RFQ setup are shown in Fig. 5.7 below. As shown previously when discussing FtMt RFQ spectra in Chapter 3, RFQ samples are often contaminated with large oxygen lines. This may seem counterintuitive to anaerobic RFQ, but it must be emphasised that the $O_2$ is dissolved in the liquid nitrogen that is mixed with the frozen protein when transferring the sample to the EPR tube and is not able to react with the protein at this point.

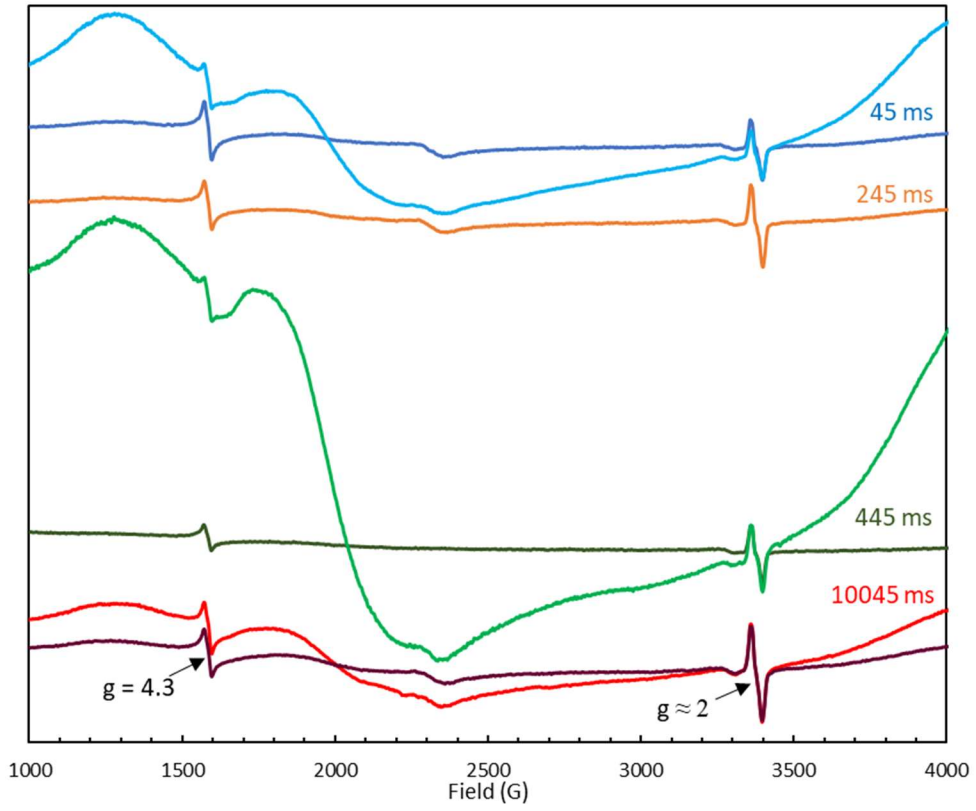


**Fig. 5.7.** The spectra of one of the three data series plotted in Fig. 5.6 (the blue dataset) above. Matching timepoints are colour-coordinated and overlaid.

**Free radical electron paramagnetic resonance signal lineshapes in bacterioferritin variants**

Variant BFRs where redox-active aromatic residues near the FC were replaced with Phe were expressed. These were then degassed, incubated with $Fe^{2+}$ and mixed with $H_2O_2$ under identical conditions to those shown in Fig. 1. The resultant free radical lineshapes are plotted below in Fig. 5.8.

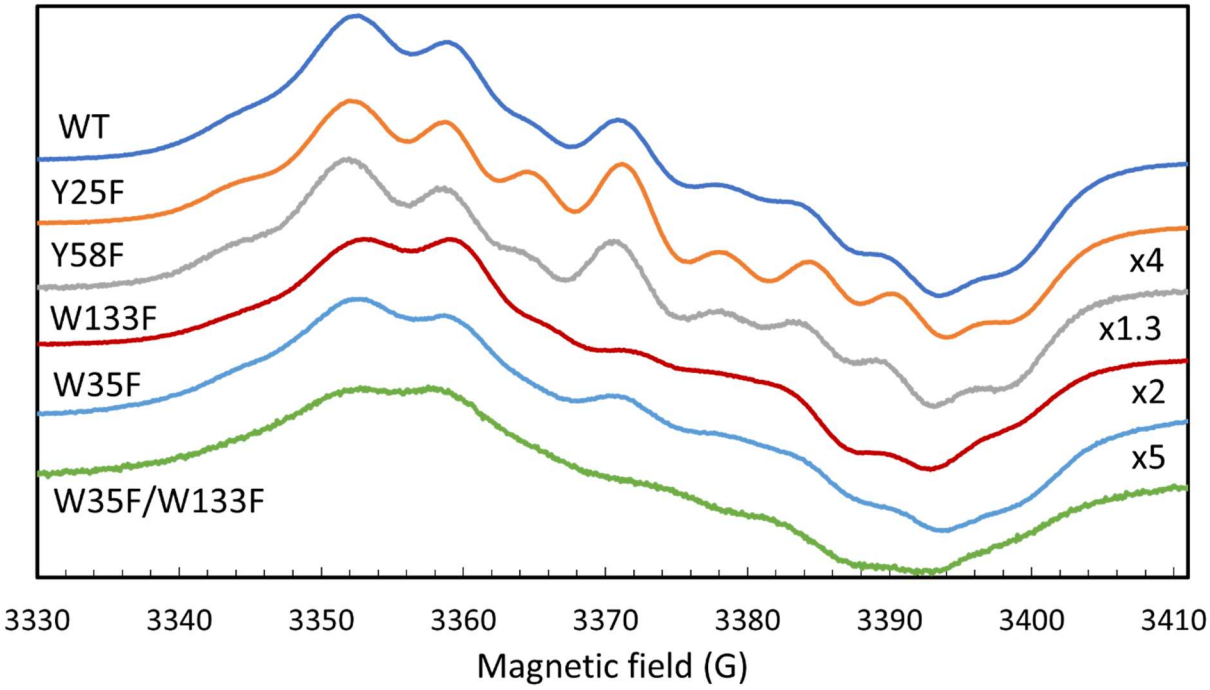


**Fig. 5.8.** Different lineshapes of the EPR spectra of BFR variants in which the redox-active amino acids near the FC have been substituted with phenylalanine. The instrumental conditions used to record the spectra are the same as in Fig. 5.1B. Some of the spectra have been multiplied by the factors reported on the right to make them all of similar amplitudes. Final protein, $Fe^{2+}$ and $H_2O_2$ concentrations in the samples are 8.3 μM, 400 μM and 250 μM respectively, slow frozen 15 s after peroxide addition to the anaerobic BFR + $Fe^{2+}$ mixture.

This figure shows that the lineshape is dependent on these redox-active amino acids. These mutations also caused differences in intensity, especially in the Y58F, W35F and W35F/ W133F variants. As such, a working hypothesis is that two tyrosines and two tryptophan residues are the localised sites for several free radicals. Several means of deconvoluting these spectra have been tested. For instance, subtracting the lineshape of a protein variant from that of the WT is one means of attempting to identify pure radical EPR lineshapes which can be simulated (Fig. 5.9).

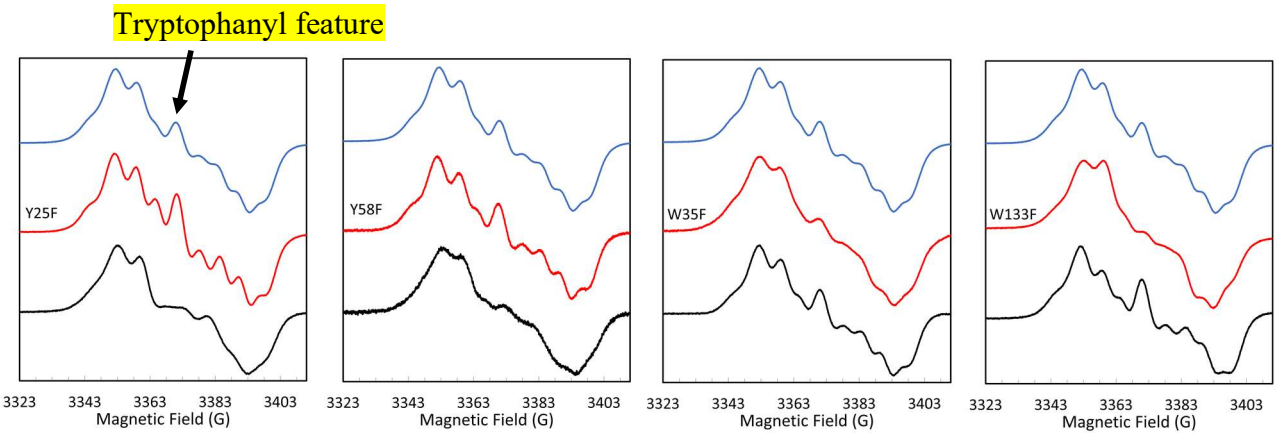


**Fig. 5.9.** Subtractions with a variable coefficient (see Materials and Methods) of the spectra presented in Fig. 5.8. The blue spectrum in each panel is that of the WT. The black spectrum is the result of subtracting the variant from the WT.

In each of the variants, some of the spectral features of the radical are weaker than in the WT protein's spectrum. Subtracting the variant from the WT spectrum causes these spectral features to have a higher contribution. It is immediately clear that the two tyrosine residues that are on opposing sides of the FC (see Fig. 5.10) are associated with one particular form of lineshape, while the two tryptophan residues in the protein are associated with a more complex lineshape. This allows us to suggest, for instance, that the feature in the spectrum at 3370 G

originates from either W35F or W133F, or both. The observation of tryptophanyl radicals in ferritins is unprecedented.

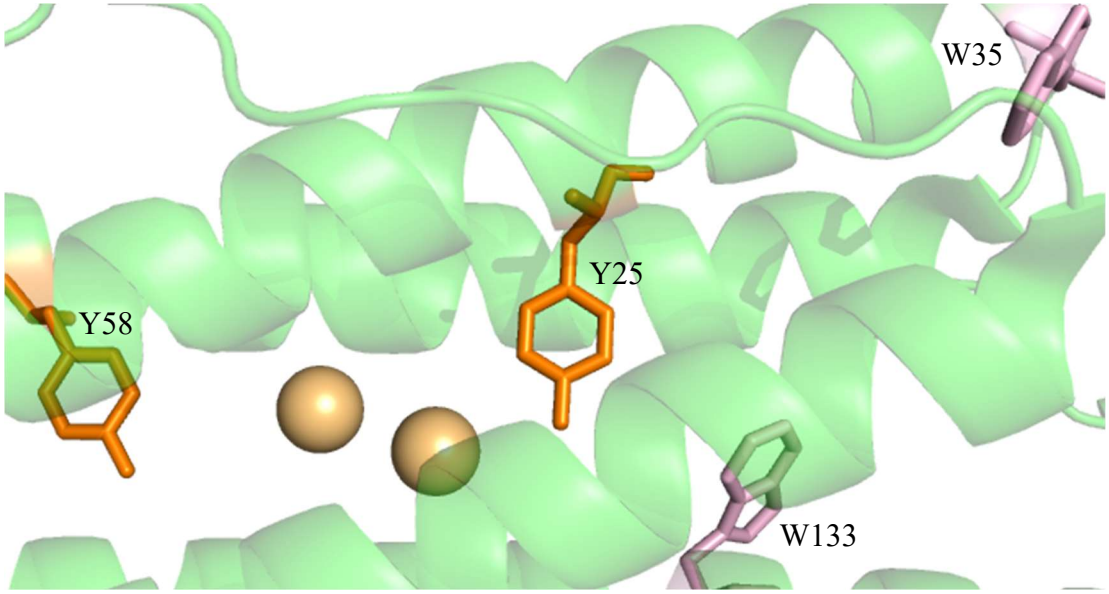


**Fig. 5.10.** Aromatic residues in the proximity of the FC that were substituted with phenylalanine are labelled. Image adapted from PDB 2VXI (Willies *et al.*, 2009).

**Microwave power and temperature dependences of the $H_2O_2$-induced free radical signal in bacterioferritin**

The hypothesis about the disperse (multi-centred) nature of the free radical in BFR oxidized with $H_2O_2$ can also be investigated by altering the microwave power and the temperature of the EPR measurements. Fig. 5.11 shows the result of using subtraction by variable coefficient to derive two different lineshapes from two EPR spectra of a sample recorded at two different microwave power values. The green spectrum shown below is the resultant difference spectrum acquired by subtracting a spectrum recorded at high microwave power from a spectrum recorded at a low microwave power. As this appears to be a combination of a doublet and a

triplet of lines (this is discussed and shown in Fig. 5.23) this lineshape is henceforth referred to as the Multiplet component. Subtracting this lineshape from the low power spectrum gives a difference spectrum that is identical to the EPR spectrum of the BFR free radical recorded at 50 K (purple line) so this was called the Residual component.

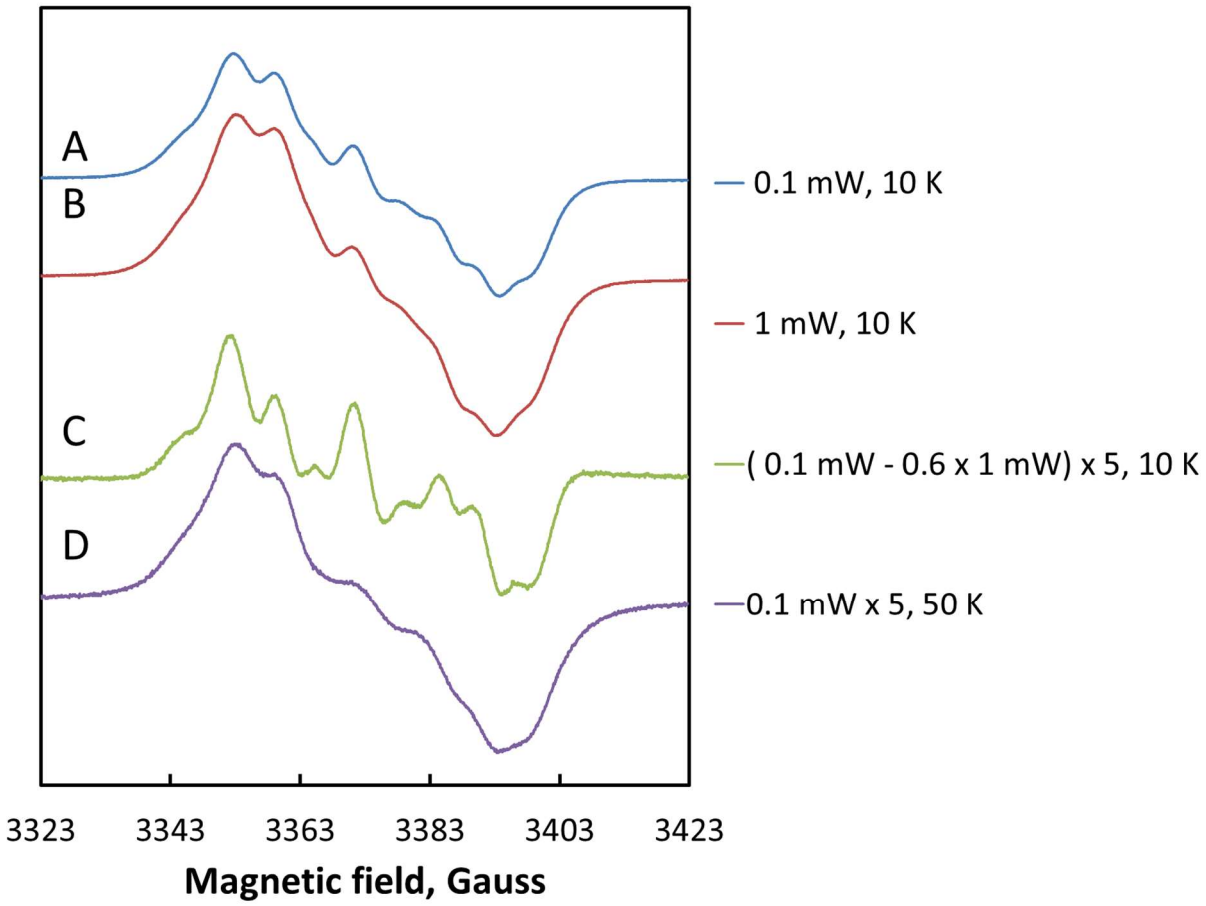


**Fig. 5.11.** The experimental spectra A and B of a sample (8.3 µM BFR incubated with 400 µM $Fe^{2+}$ mixed with 250 µM $H_2O_2$, frozen at 10 s) recorded at two different microwave power values (indicated) have been used to obtain a difference lineshape C named *Multiplet* (the formula of the subtraction is indicated). The features of the Multiplet were not observed when the EPR measurement temperature was raised to 50 K, therefore the spectrum at this temperature (D) was considered as the other lineshape and named *Residual*, i.e. referring to the signal that remains after the Multiplet's signal has been subtracted.

Thus it appears that the Multiplet and Residual are two contributors to the free radical EPR spectrum of BFR anaerobically treated with $H_2O_2$ that are characterised by different microwave power and temperature dependences. Fig. 5.12 shows a comprehensive map of the FR EPR signal lineshape at different MW power values and different temperatures of measurements.

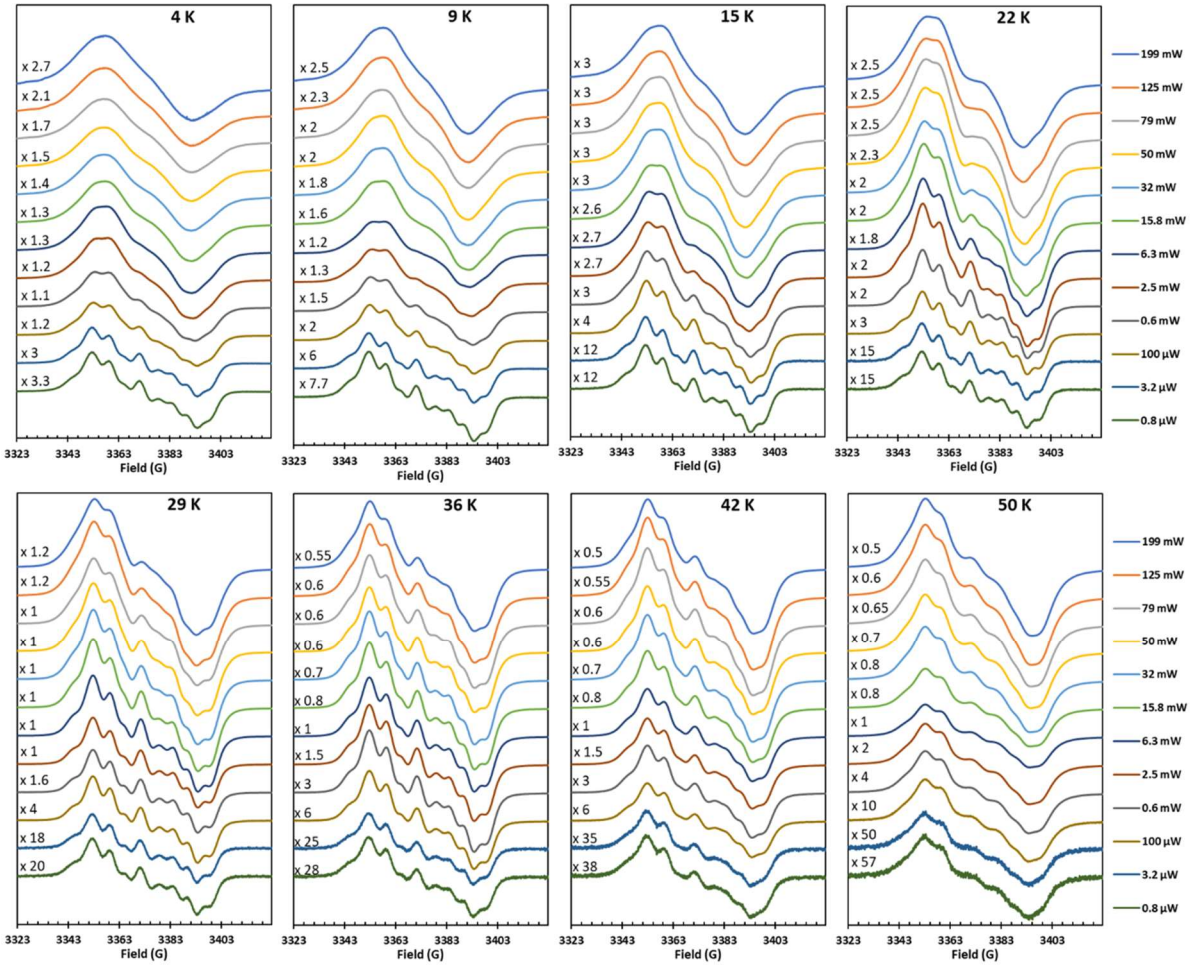


**Fig. 5.12.** The EPR signal of WT BFR free radical measured at eight values of temperature (4 K-50 K) and twelve values of microwave power (0.8 µW – 199 mW). Protein, $Fe^{2+}$ and $H_2O_2$ concentrations are 8.3 µM, 400 µM and 250 µM respectively. The sample was slow frozen after 15 s.

This saturation map shows the dramatic change of the lineshape and intensity of the free radical EPR signal with both temperature and microwave power. In the absence of saturation, EPR signal intensity will have a linear relationship with the square root of microwave power *P* until the microwave power is enough to saturate the sample. Fig. 5.13 shows the relationship between microwave power and signal intensities at eight different temperatures. These were obtained by subtracting the low-power spectrum at each temperature where the multiplet was clearly visible and subtracting it from each spectrum measured at that temperature. Double integration was used to plot the residual and the multiplet in common units.

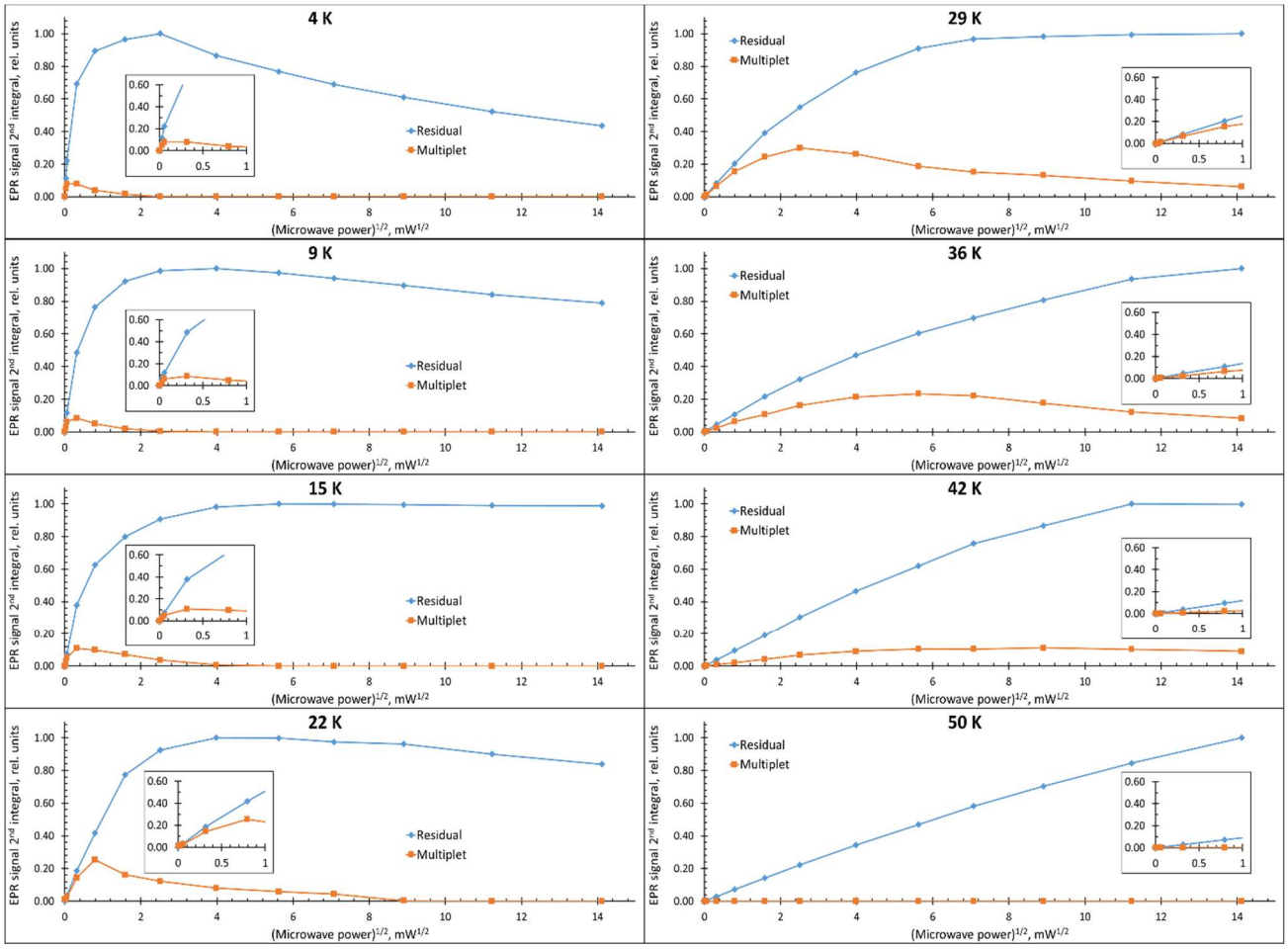


**Fig. 5.13.** The relative intensities of the Multiplet (orange) and the Residual (blue) lineshapes at each temperature in the WT BFR spectra shown in Fig. 5.12. The inset graphs show the lower microwave powers in more detail. The two signals' intensities are expressed in common

units of second integral in each panel, these units are different, however, in different panels normalised to 1.00 of the Residual maximal intensity.

This data shows that the Multiplet saturates with microwave power much sooner than the Residual signal, with its power dependence profile suggesting a homogenously broadened line (Marrale *et al.*, 2006). The Residual signal starts to saturate at higher microwave power values, with its line broadening non-homogenously. This is reminiscent of the behaviour of the tyrosyl radical in *Syn*Ftn (Fig. 3.12). In Fig. 5.13, the 50 K panel shows that it seems to be the lowest temperature at which the Residual signal does not saturate and the Multiplet cannot be observed at all, possibly due to broadening.

Interestingly, it seems that initial slopes of the two signal dependences are rather close or might be identical, at each temperature. Considering the two signals' intensities are expressed in common units of second integral, this observation might indicate that the species responsible for Residual and the Multiplet are present at close or even equal concentrations and thus could have mechanistic implications.

Curie's Law (Eq. 5.2) states that the magnetization ($M$) of a paramagnetic material is directly proportional to the applied magnetic field ($B$) and inversely proportional to absolute temperature:

$$M = \approx \frac{B}{T} \tag{5.2}$$

Curie's Law only applies at relatively high temperatures or low magnetic fields. At low temperatures, the Boltzmann distribution is already heavily favouring the lower energy population, and thus the applied magnetic field $B$ has little effect. This is referred to as

magnetization saturation. At higher temperatures, hyperfine coupling constants tend to get larger, which is referred to as line broadening.

Fig. 5.14 shows the temperature dependences of the Multiplet EPR signal in WT BFR and deviations from this relationship. The Multiplet is already beginning to deviate significantly from Curie's Law at just 0.1 mW.

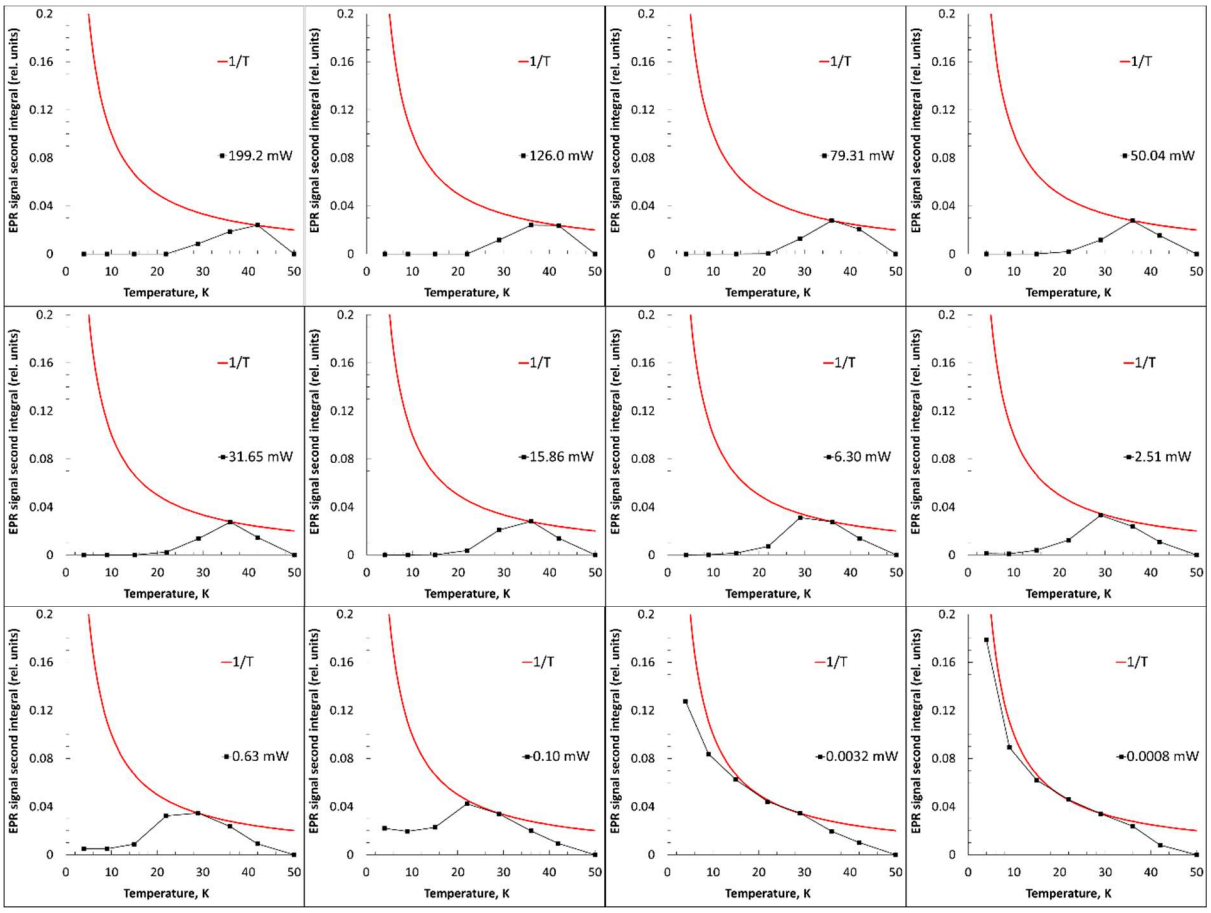


**Fig. 5.14.** Temperature dependences of the Multiplet EPR signal reported in the WT BFR spectra (Fig. 5.13) at twelve values of microwave power. The red line in each panel is the 1/T dependence. The Multiplet EPR signal intensities are those reported in Fig. 5.13 multiplied by a factor, individual for each panel, to make the curve touch the 1/T line from beneath.

The Residual lineshape appears to follow Curie Law more closely, as seen in Fig. 5.15. This suggests that the Residual does not saturate or broaden at low microwave power (or at least within the specific microwave powers used in this study). At the lowest microwave power used (0.0008 mW), the Residual signal was too small to accurately observe.

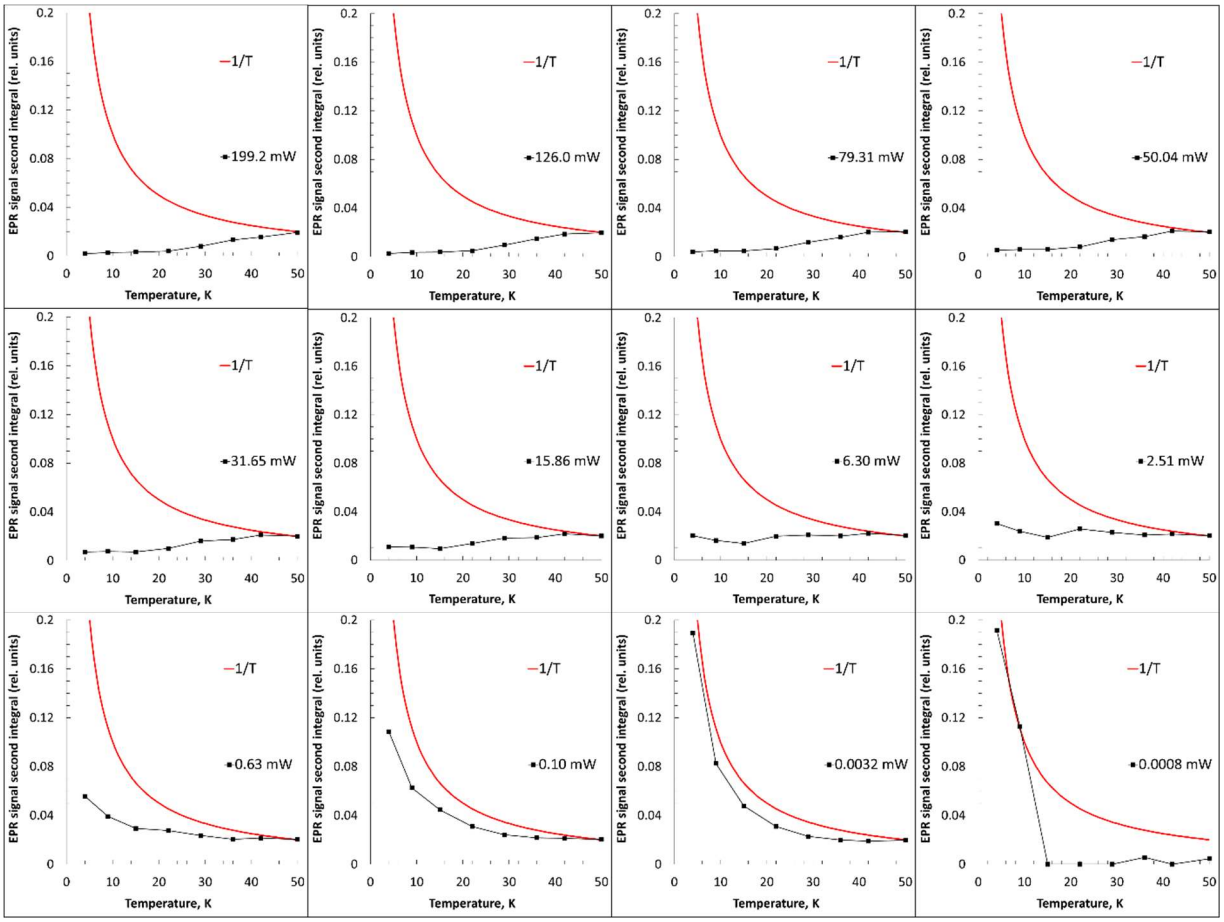


**Fig. 5.15.** Like Fig. 5.14 above, showing deviation from Curie law of the Residual signal in the WT BFR spectra (Fig. 5.13), at different MW power values. The red line in each panel is the 1/T dependence. The Residual EPR signal intensities are those reported in Fig. 11 multiplied by a factor, individual for each panel, to make the curve touch the 1/T line from beneath.

At 50 K, the Multiplet is not visible at any microwave power, but the residual remains. This is useful information for allowing us to identify the lineshapes, (see the simulation of the

lineshapes below) but it also indicates how close the radical site might be to the FCs: the closer residues are to a metal centre, the faster they relax. This physical effect is known as relaxation enhancement. The lack of saturation in the Residual signal suggests that the associated free radicals are based on residues in close proximity to the diiron centre, while those of the Multiplet might be further away.

Fig. 5.16 shows the power/ temperature dependence maps of the W133F BFR variant's EPR signal. While many spectral features of the Multiplet that appeared to be associated with tryptophanyl radicals are diminished in this variant (see Fig. 5.9) they are not absent. This suggests that the WT protein's Multiplet is not comprised of a single free radical species.

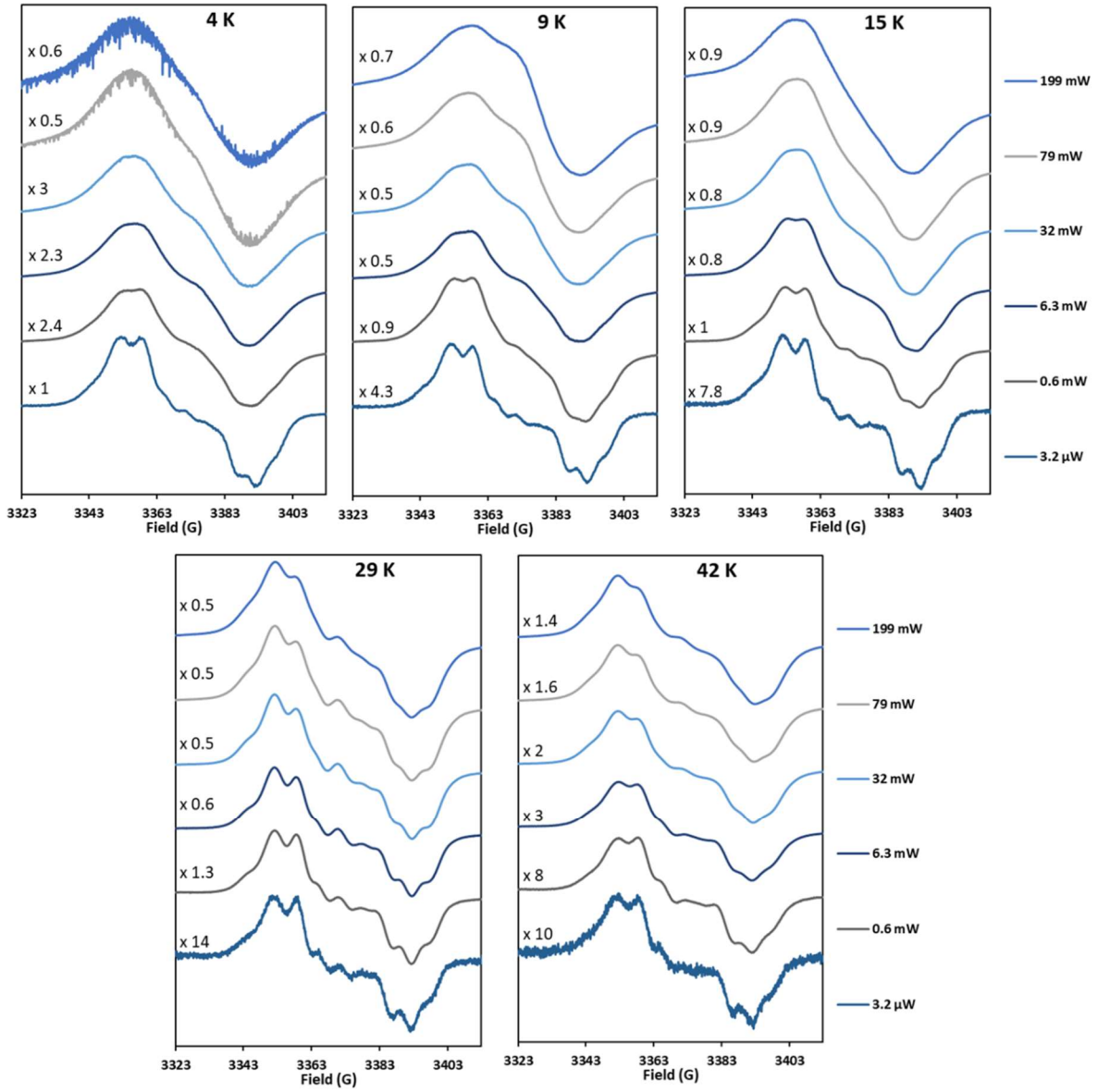


**Fig. 5.16.** The EPR signal of W133F BFR free radical measured at five values of temperature (4 K- 42 K) and six values of microwave power (0.8 µW – 199 mW). Protein, $Fe^{2+}$ and $H_2O_2$ concentrations are 8.3 µM, 400 µM and 250 µM respectively, slow frozen after 11 s. The spectra were measured at the following instrumental conditions: microwave frequency $\nu_{MW}$ = 9.4651 GHz; microwave power $P_{MW}$ = 0.05 mW.

The power saturation behaviour of the W133F Residual and Multiplet can be compared to the EPR signals in the WT protein. Fig. 5.17 shows the power dependence of the two signals in the

W133F variant. The general trends of the variants show similar saturation behaviour, which implies that the Residual and the Multiplet are similar radical species in each protein, as expected. At 29 and 42 K, the Multiplet appears to have a larger relative proportion in comparison to the WT protein. In Fig. 5.8, it is clear that the free radical observed is much smaller in the W133F variant than the WT protein; the relative proportions shown in Fig. 5.17 imply that the W133F substitution causes a reduction in both the Residual and the Multiplet lineshapes, but also affects the lineshape of the Multiplet, which is not equivalent to that of the WT.

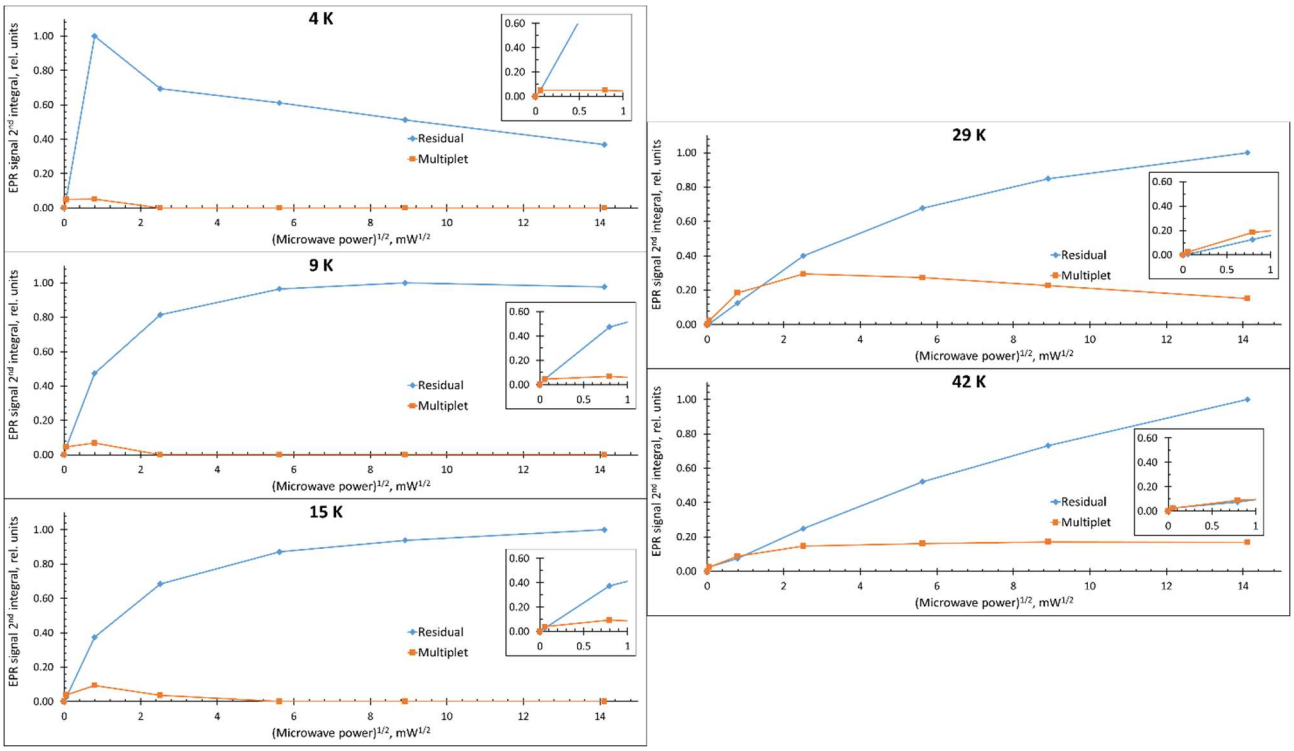


**Fig. 5.17.** The relative intensities of the Multiplet (orange) and the Residual (blue) lineshapes at each temperature in the W133F BFR spectra shown in Fig. 5.16. The Multiplet's signal was determined in a similar fashion to that described for the WT (Fig. 5.13). The inset graphs show the lower microwave powers in more detail. The two signals' intensities are expressed in common units of second integral in each panel, these units are different, however, in different panels.

The temperature dependence of the W133F Multiplet is plotted below (Fig. 5.18), showing similar behaviour to that of the WT. Differences could be attributed to the missing W133 tryptophanyl radical.

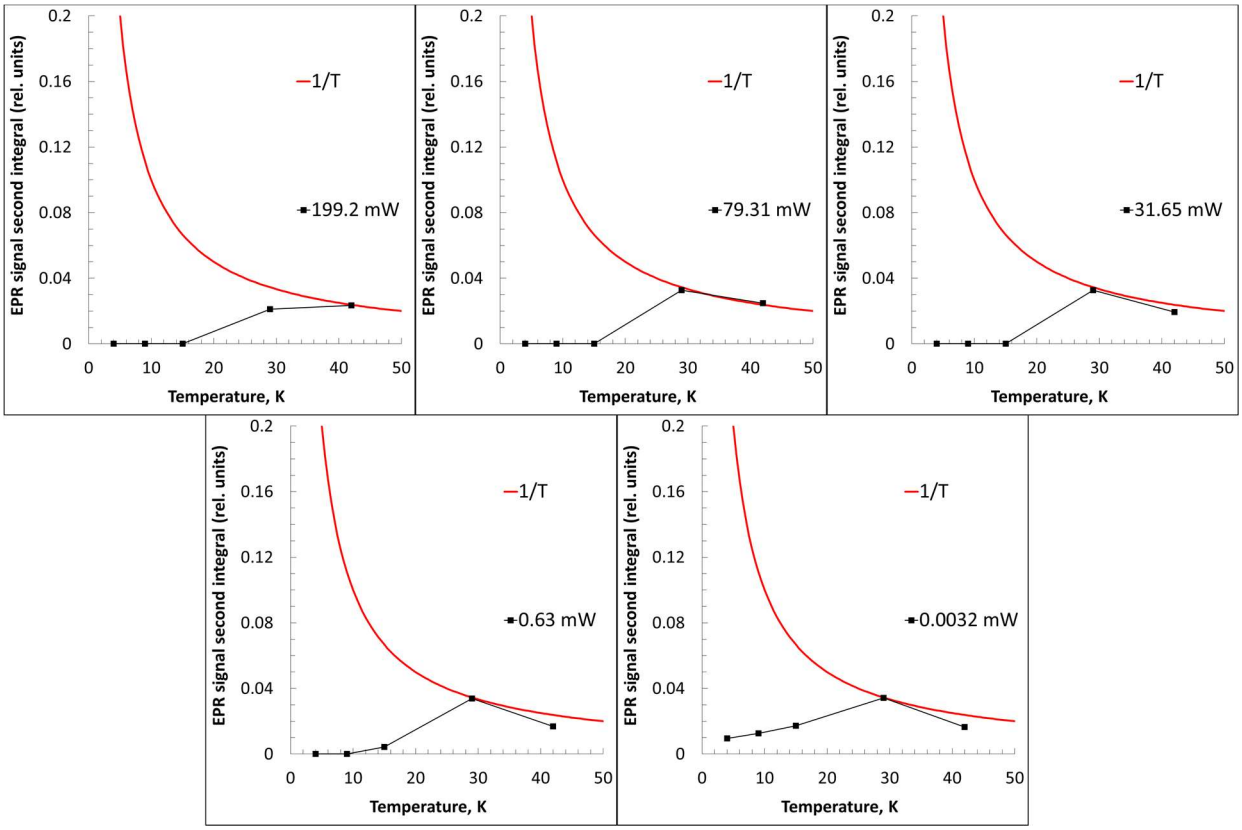


**Fig. 5.18.** Temperature dependences of the Multiplet EPR signal in the W133F BFR spectra (Fig. 5.16) at five values of microwave power. The red line in each panel is the 1/T dependence. The Multiplet EPR signal intensities are those reported in Fig. 5.17 multiplied by a factor, individual for each panel, to make the curve touch the 1/T line from beneath.

The Residual signal in the W133F variant has notably different temperature dependence (Fig. 5.19) to the WT protein. The W133F appears to more closely follow Curie's Law at higher powers, with less saturation of the EPR signal at 199.2- 0.63 mW than the WT protein, yet at 0.0032 mW the WT protein appears to have a closer fit to the 1/T dependence of Curie's Law.

This could suggest that the W133F variant has a different conformation which results in the Residual free radical being located closer the iron in the FC (thus saturating more slowly) or that the Residual free radical in the W133F variant may simply be a different radical species to that observed in the WT protein.

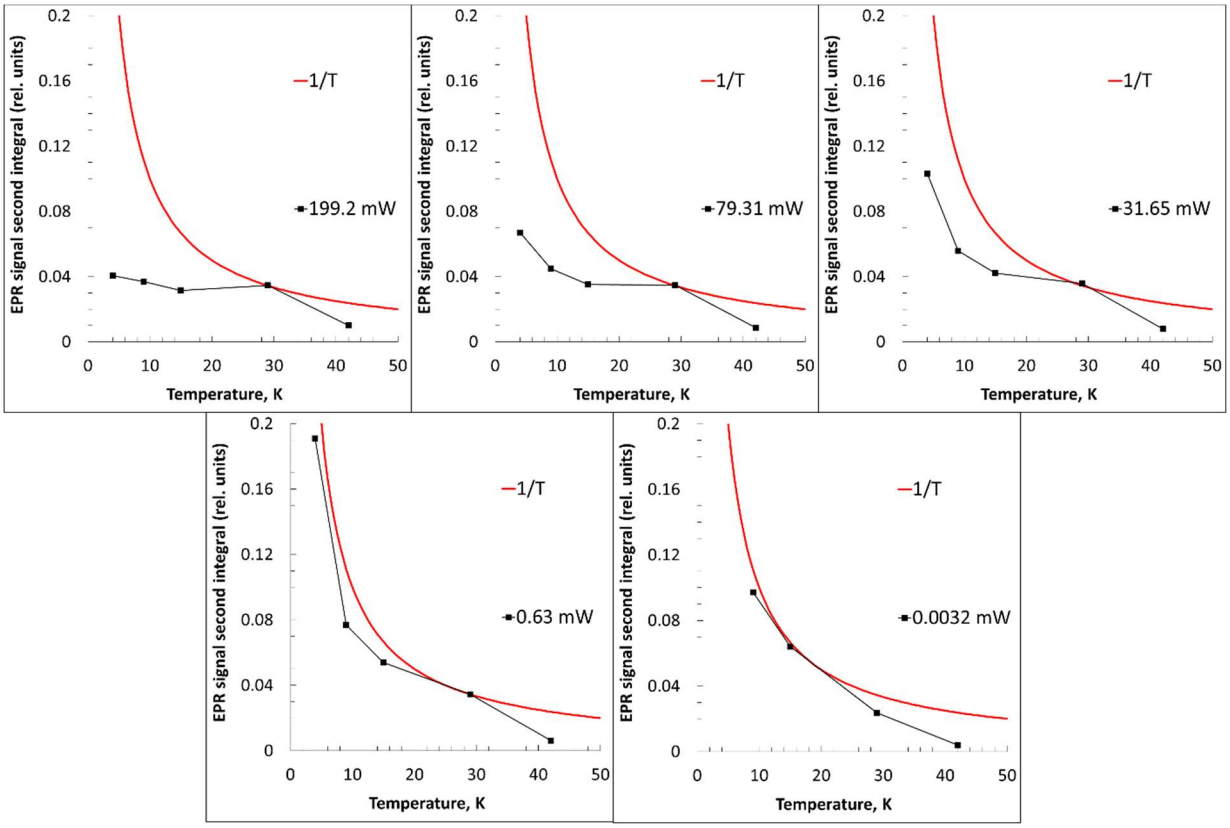


**Fig. 5.19.** Temperature dependences of the Residual EPR signal in the W133F BFR spectra (Fig. 14) at five values of microwave power. The red line in each panel is the 1/T dependence. The Residual EPR signal intensities are those reported in Fig. 5.17 multiplied by a factor, individual for each panel, to make the curve touch the 1/T line from beneath.

The W35F/W133F BFR variant has a lineshape (Fig. 5.20) that closely resembles that of the Residual spectrum. This does not change significantly with power or temperature, suggesting that this variant is comprised entirely of the Residual component. The loss of 'structure' that

can be seen at higher powers between 4- 22 K should not be mistaken for a lineshape change; this is a well-established broadening effect seen at high microwave power (Fajer, 2006).

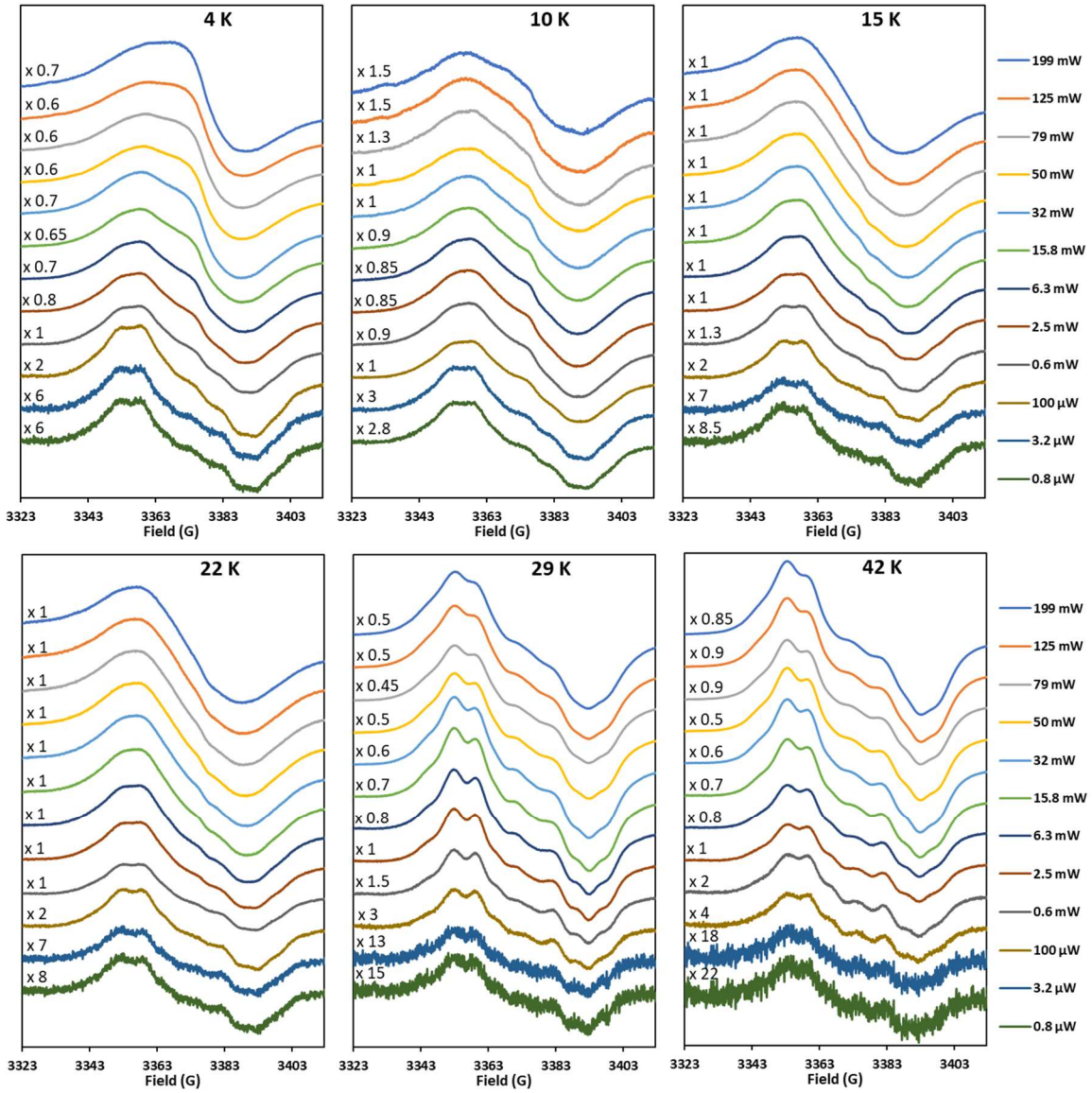


**Fig. 5.20.** The EPR signal of W35F/ W133F BFR free radical measured at six values of temperature (4 K- 42 K) and twelve values of microwave power (0.8 µW – 199 mW). Protein, $Fe^{2+}$ and $H_2O_2$ concentrations are 8.3 µM, 400 µM and 250 µM respectively, slow frozen after 15 s. The spectra were measured at 10 K at the following instrumental conditions: microwave frequency $\nu_{MW}$ = 9.4663 GHz; microwave power $P_{MW}$ = 0.05 mW modulation frequency $\nu_M$ = 100 kHz; modulation amplitude $A_M$ = 3 G; scan rate v = 0. 60 G/s; time constant $\tau$ = 81.92 ms; conversion time, at a 2048 data point scan range, $t_{conv}$ = 81.92 ms.

The Residual signal has a similar saturation profile (Figs. 5.19 and 5.20) to the WT protein.

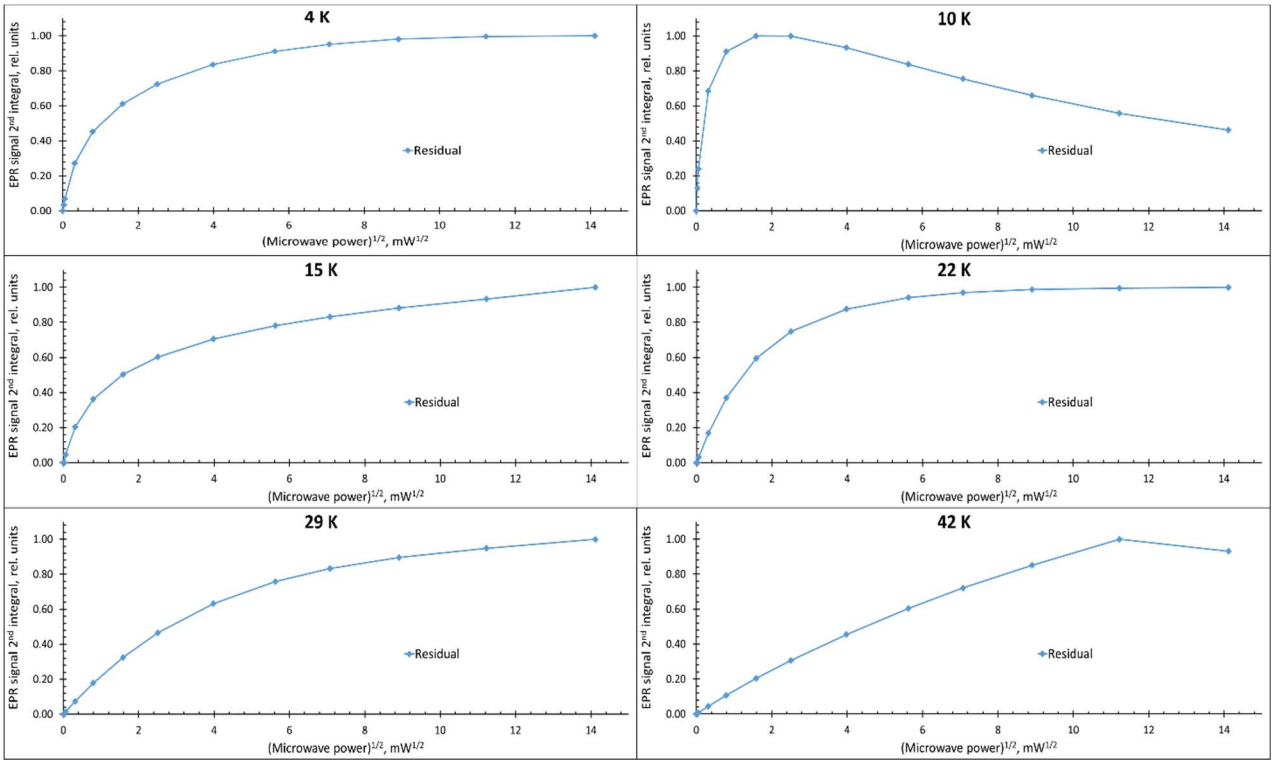


**Fig. 5.21.** The relative intensities of the EPR free radical at each temperature in the W35F/W133F BFR spectra shown in Fig. 5.20.

The temperature dependence of the W35F/W133F variant (Fig. 5.22) is also highly comparable to the Residual signal in the WT protein (Fig. 5.15). These suggest that the Residual EPR signal is based on the same amino acids in both the WT and the W35F/W133F variant proteins.

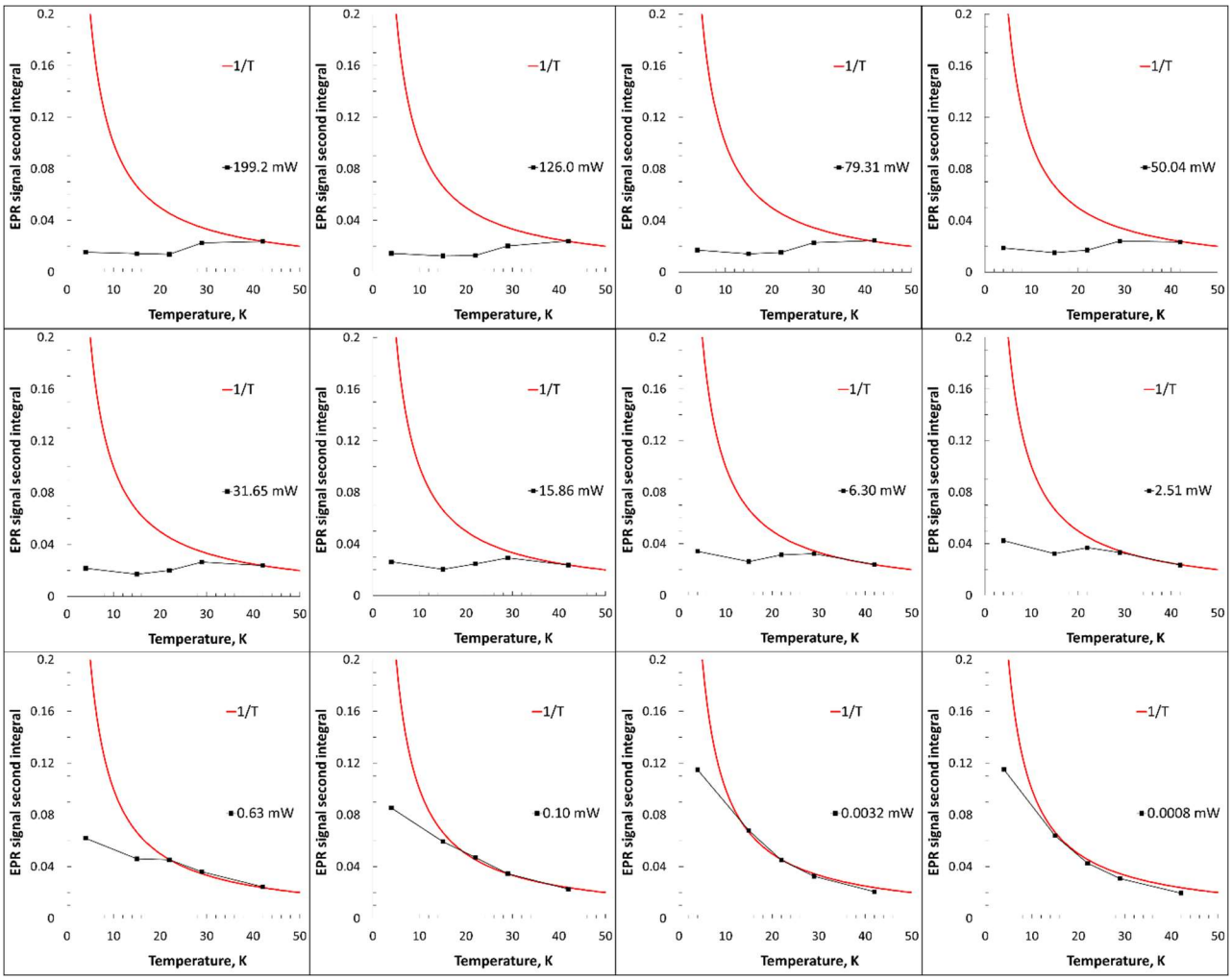


**Fig. 5.22.** Temperature dependences of the EPR signal in the W35F/ W133F BFR spectra (Fig. 5.20) at six values of microwave power. The red line in each panel is the 1/T dependence. The Residual EPR signal intensities are those reported in Fig. 5.21 multiplied by a factor, individual for each panel, to make the curve touch the 1/T line from beneath.

These power and temperature dependence maps (Figs. 5.12-5.22) suggest that the Multiplet could be a mixture of radicals, with a significant proportion of this mixture being tryptophanyl in nature.

**Simulation of the free radicals in BFR**

TRSSA-W (Chaplin *et al.*, 2017) was used to simulate the Multiplet which was hypothesised to be a Trp radical (Fig. 5.23). Neither TRSSA-Y or TRSSA-W were able to simulate the Multiplet as a single lineshape. Simulation of the Multiplet can be achieved by considering the signal to be a sum of two Trp radical spectra.

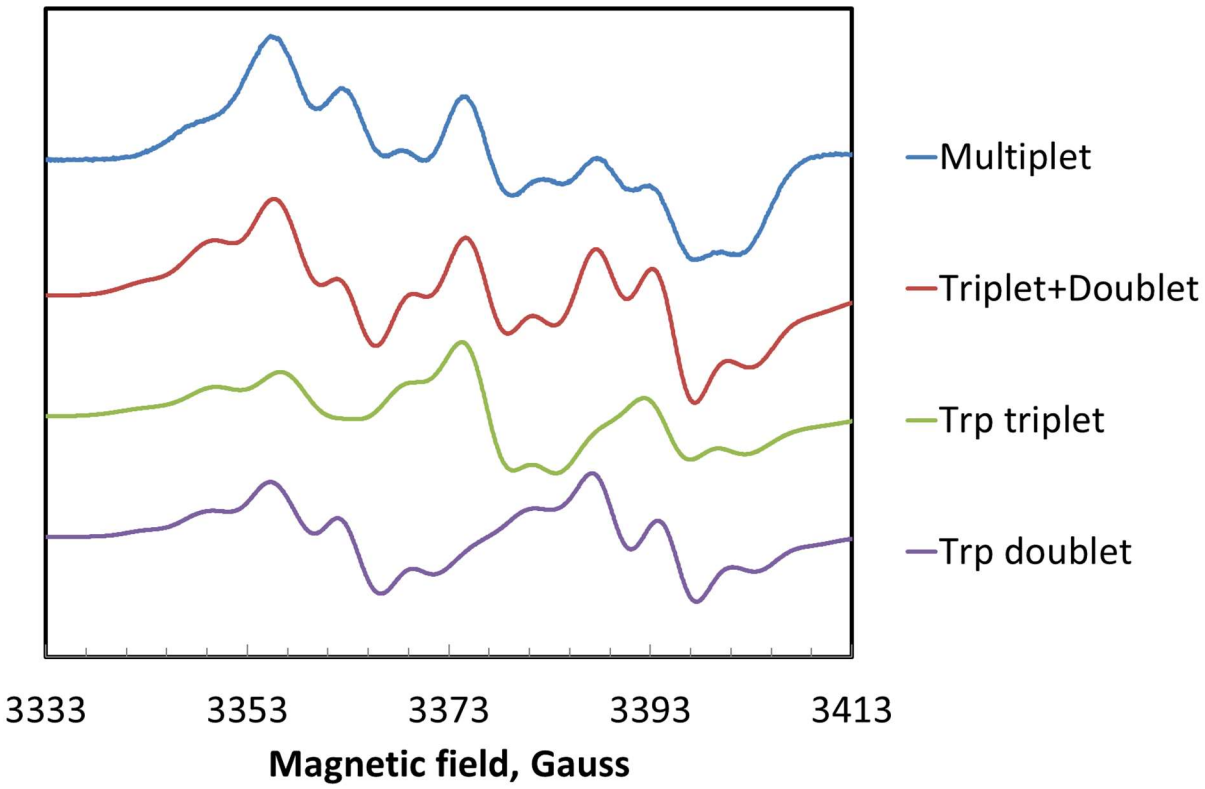


**Fig. 5.23.** The Multiplet (Fig. 5.11C) identified in the free radical EPR signal of BFR during iron oxidation driven by $H_2O_2$ can be simulated as a sum of two Trp radical spectra (red). The two Trp lineshapes resembled a triplet (green simulation) and a doublet (purple simulation). The TRSSA-W parameters for these simulations are reported in Tables 5.1 and 5.2.

It could thus be expected that W35 or W133 could be assigned to either the doublet or triplet lineshape, and that substituting one of these residues with phenylalanine in variant proteins would isolate these lineshapes. This was not the case as shown in Fig. 5.8. However, replacing either of these residues with phenylalanine significantly reduces the input of the observed multiplet, with the W35F/W133F removing it entirely. Looking at the BFR 3D structure, it could be suggested that W35 and W133 each assume a free radical state. Fig. 5.24 shows that W35 and W133 in a different monomer are aligned to form a circle around the four-fold channel and may be involved in an electron transport mechanism.

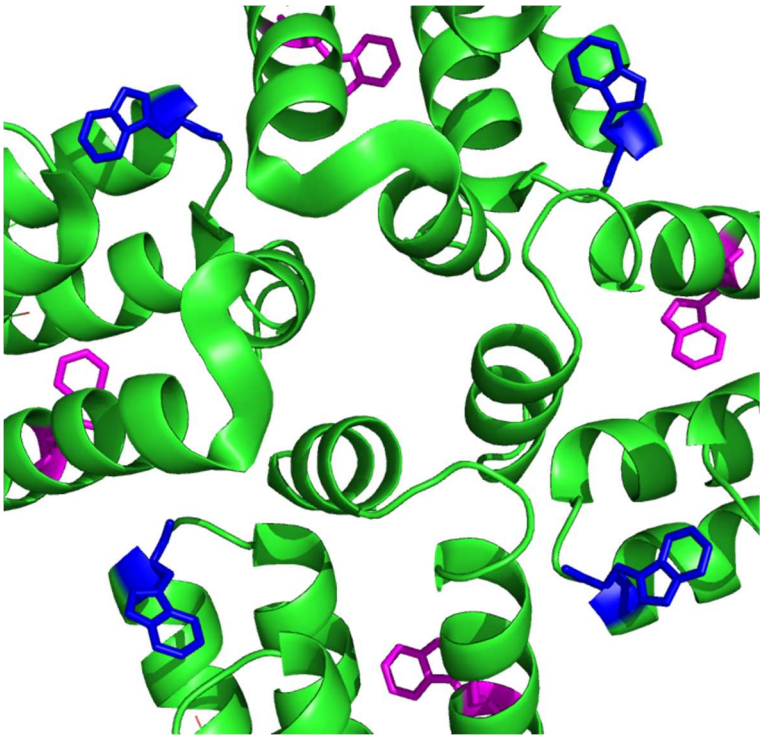

**Fig. 5.24.** A view of the four fold channel from outside the ferritin shell, taken from a crystal structure of BFR (PDB 2VXI, Willies *et al.*, 2009). W35 is shown in blue, facing towards the outside of the ferritin shell, while W133 is in pink and is facing towards the mineral core.

Tables 5.1 and 5.2 below describe the parameters used to simulate the free radicals. It is important to emphasise that neither of these simulations have been assigned to an individual tryptophan in BFR's structure.

**Table 5.1.** TRSSA-W generated parameters used to simulate the hydrophobic Trp radical doublet signal.

| Microwave frequency, GHz |
|---|
| 9.46577 |

Colour code:
- Instrumental parameters
- Radical parameters generated by the algorithm
- Conserved parameters (the same for all Trp radicals)
- Values are allowed to be varied

| $H_1$, G | $H_2$, G |
|---|---|
| 3313.2 | 3413.1 |

| Data points |
|---|
| 2048 |

| gx | gy | gz |
|---|---|---|
| 2.00568 | 2.00466 | 2.00406 |

| Hyperfine coupling matrix principal values | | | Euler angle α | Euler angle β | Euler angle γ | Scaling factor 1 | Scaling factor 2 |
|---|---|---|---|---|---|---|---|
| $A^{\beta1}cc$, MHz | $A^{\beta1}bb$, MHz | $A^{\beta1}aa$, MHz | $-\Phi_1^{\beta1}$, degree | $-\Phi_2^{\beta1}$, degree | $-\Phi_3^{\beta1}$, degree | | |
| 93.68 | 83.72 | 83.72 | 0.0 | 0.0 | 0.0 | | |
| $A^{\beta2}cc$, MHz | $A^{\beta2}bb$, MHz | $A^{\beta2}aa$, MHz | $-\Phi_1^{\beta2}$, degree | $-\Phi_2^{\beta2}$, degree | $-\Phi_3^{\beta2}$, degree | | |
| 23.04 | 17.29 | 17.29 | 0.0 | 0.0 | 0.0 | | |
| $A^{C5}cc$, MHz | $A^{C5}bb$, MHz | $A^{C5}aa$, MHz | $-\Phi_1^{C5}$, degree | $-\Phi_2^{C5}$, degree | $-\Phi_3^{C5}$, degree | | |
| -26.04 | -21.42 | -8.50 | 6.6 | 0.0 | -90.0 | 1.27 | 0.9 |
| $A^{C7}cc$, MHz | $A^{C7}bb$, MHz | $A^{C7}aa$, MHz | $-\Phi_1^{C7}$, degree | $-\Phi_2^{C7}$, degree | $-\Phi_3^{C7}$, degree | | |
| -24.46 | -17.36 | -5.54 | 77.0 | 0.0 | -90.0 | 1.27 | 0.9 |
| $A^{N1}cc$, MHz | $A^{N1}bb$, MHz | $A^{N1}aa$, MHz | $-\Phi_1^{N1}$, degree | $-\Phi_2^{N1}$, degree | $-\Phi_3^{N1}$, degree | | |
| 0.43 | 0.49 | 12.16 | 61.3 | -85.0 | -16.3 | 0.34 | 1.0 |
| $A^{C6}cc$, MHz | $A^{C6}bb$, MHz | $A^{C6}aa$, MHz | $-\Phi_1^{C6}$, degree | $-\Phi_2^{C6}$, degree | $-\Phi_3^{C6}$, degree | | |
| 0.72 | 2.04 | 4.36 | 82.0 | 0.0 | 0.0 | 1.00 | 1.0 |

| $\Delta H_x$, G | $\Delta H_y$, G | $\Delta H_z$, G |
|---|---|---|
| 3.36 | 5.76 | 3.32 |

**Table 5.2.** TRSSA-W generated parameters used to simulate the hydrophilic Trp radical triplet signal.

| Microwave frequency, GHz |
|---|
| 9.46577 |

Colour code:
- Instrumental parameters
- Radical parameters generated by the algorithm
- Conserved parameters (the same for all Trp radicals)
- Values are allowed to be varied

| $H_1$, G | $H_2$, G |
|---|---|
| 3313.2 | 3413.1 |

| Data points |
|---|
| 2048 |

| gx | gy | gz |
|---|---|---|
| 2.00561 | 2.00466 | 2.00406 |

| Hyperfine coupling matrix principal values | | | Euler angle α | Euler angle β | Euler angle γ | Scaling factor 1 | Scaling factor 2 |
|---|---|---|---|---|---|---|---|
| $A^{\beta1}cc$, MHz | $A^{\beta1}bb$, MHz | $A^{\beta1}aa$, MHz | $-\Phi_1^{\beta1}$, degree | $-\Phi_2^{\beta1}$, degree | $-\Phi_3^{\beta1}$, degree | | |
| 53.84 | 48.07 | 48.07 | 0.0 | 0.0 | 0.0 | | |
| $A^{\beta2}cc$, MHz | $A^{\beta2}bb$, MHz | $A^{\beta2}aa$, MHz | $-\Phi_1^{\beta2}$, degree | $-\Phi_2^{\beta2}$, degree | $-\Phi_3^{\beta2}$, degree | | |
| 51.73 | 46.17 | 46.17 | 0.0 | 0.0 | 0.0 | | |
| $A^{C5}cc$, MHz | $A^{C5}bb$, MHz | $A^{C5}aa$, MHz | $-\Phi_1^{C5}$, degree | $-\Phi_2^{C5}$, degree | $-\Phi_3^{C5}$, degree | | |
| -21.28 | -17.51 | -6.95 | 6.6 | 0.0 | -90.0 | 1.04 | 0.9 |
| $A^{C7}cc$, MHz | $A^{C7}bb$, MHz | $A^{C7}aa$, MHz | $-\Phi_1^{C7}$, degree | $-\Phi_2^{C7}$, degree | $-\Phi_3^{C7}$, degree | | |
| -19.99 | -14.19 | -4.53 | 77.0 | 0.0 | -90.0 | 1.04 | 0.9 |
| $A^{N1}cc$, MHz | $A^{N1}bb$, MHz | $A^{N1}aa$, MHz | $-\Phi_1^{N1}$, degree | $-\Phi_2^{N1}$, degree | $-\Phi_3^{N1}$, degree | | |
| 1.02 | 1.15 | 28.91 | 61.3 | -85.0 | -16.3 | 0.81 | 1.0 |
| $A^{C6}cc$, MHz | $A^{C6}bb$, MHz | $A^{C6}aa$, MHz | $-\Phi_1^{C6}$, degree | $-\Phi_2^{C6}$, degree | $-\Phi_3^{C6}$, degree | | |
| 0.72 | 2.04 | 4.36 | 82.0 | 0.0 | 0.0 | 1.00 | 1.0 |

| $\Delta H_x$, G | $\Delta H_y$, G | $\Delta H_z$, G |
|---|---|---|
| 3.84 | 6.33 | 3.75 |

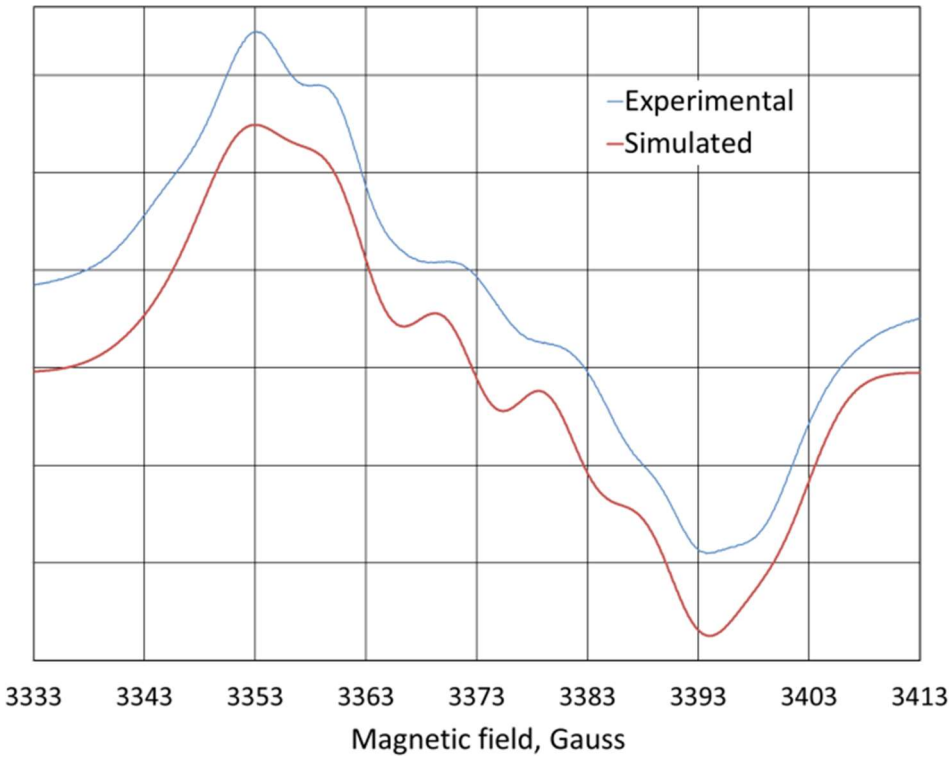


**Fig. 5.25.** TRSSA-Y simulation of the Residual EPR signal as a single Tyr radical. Parameters are shown in Table 5.3 below.

Subtracting Y25F and Y58F mutant spectra from the WT EPR spectrum both resulted in lineshapes that were similar to each other and to the Residual signal (Fig. 5.9), so attempts were made to simulate the Residual as a single lineshape. The best result is reported in Fig. 5.25, with the corresponding parameters shown in Table 5.3.

**Table 5.3.** TRSSA-Y generated parameters used to simulate the Residual signal.

| Microwave frequency, GHz |
|---|
| 9.46609 |

| $H_1$, G | $H_2$, G |
|---|---|
| 3322.9 | 3422.7 |

| Data points |
|---|
| 2048.0 |

| $g_x$ | $g_y$ | $g_z$ |
|---|---|---|
| 2.00725 | 2.00424 | 2.00220 |

| Hyperfine coupling matrix principal values | | | Euler angle α | Euler angle β | Euler angle γ |
|---|---|---|---|---|---|
| $A^{\beta 1}_{cc}$, MHz | $A^{\beta 1}_{bb}$, MHz | $A^{\beta 1}_{aa}$, MHz | $-\Phi_1^{\beta 1}$, degree | $-\Phi_2^{\beta 1}$, degree | $-\Phi_3^{\beta 1}$, degree |
| 58.68 | 52.44 | 52.44 | 9 | -26 | -78 |
| $A^{\beta 2}_{cc}$, MHz | $A^{\beta 2}_{bb}$, MHz | $A^{\beta 2}_{aa}$, MHz | $-\Phi_1^{\beta 2}$, degree | $-\Phi_2^{\beta 2}$, degree | $-\Phi_3^{\beta 1}$, degree |
| 32.33 | 28.55 | 28.55 | 22 | 11 | -43 |
| $A^{C3}_{cc}$, MHz | $A^{C3}_{bb}$, MHz | $A^{C3}_{aa}$, MHz | $-\Phi_1^{C3}$, degree | $-\Phi_2^{C3}$, degree | $-\Phi_3^{C3}$, degree |
| -25.9 | -8.1 | -20.5 | 23.0 | 0.0 | 0.0 |
| $A^{C5}_{cc}$, MHz | $A^{C5}_{bb}$, MHz | $A^{C5}_{aa}$, MHz | $-\Phi_1^{C5}$, degree | $-\Phi_2^{C5}$, degree | $-\Phi_3^{C5}$, degree |
| -25.9 | -8.1 | -20.5 | -23.0 | 0.0 | 0.0 |
| $A^{C2}_{cc}$, MHz | $A^{C2}_{bb}$, MHz | $A^{C2}_{aa}$, MHz | $-\Phi_1^{C2}$, degree | $-\Phi_2^{C2}$, degree | $-\Phi_3^{C2}$, degree |
| 7.5 | 5.0 | 1.5 | 40.0 | 0.0 | 0.0 |
| $A^{C6}_{cc}$, MHz | $A^{C6}_{bb}$, MHz | $A^{C6}_{aa}$, MHz | $-\Phi_1^{C6}$, degree | $-\Phi_2^{C6}$, degree | $-\Phi_3^{C6}$, degree |
| 7.5 | 5.0 | 1.5 | -40.0 | 0.0 | 0.0 |

| $\Delta H_x$, G | $\Delta H_y$, G | $\Delta H_z$, G |
|---|---|---|
| 8.67 | 7.03 | 6.83 |

**$Fe^{2+}$ oxidation by bacterioferritin in the presence of ABTS**

In an attempt to 'trap' the ferryl intermediate hypothesised to arise as a result of the diferric FC's reaction with $H_2O_2$, BFR was mixed with 2,2'-azino-bis(3-ethylbenzothiazoline-6-sulfonic acid (ABTS) This is a dye compound commonly used in conjunction with $H_2O_2$ as a substrate for peroxidases to indirectly follow their reaction kinetics. ABTS is selected for this

role because it readily reacts with $Fe^{4+}$ species due to their low redox potentials to form a coloured, paramagnetic species. Fig. 5.26 reports the attempt to capture this species.

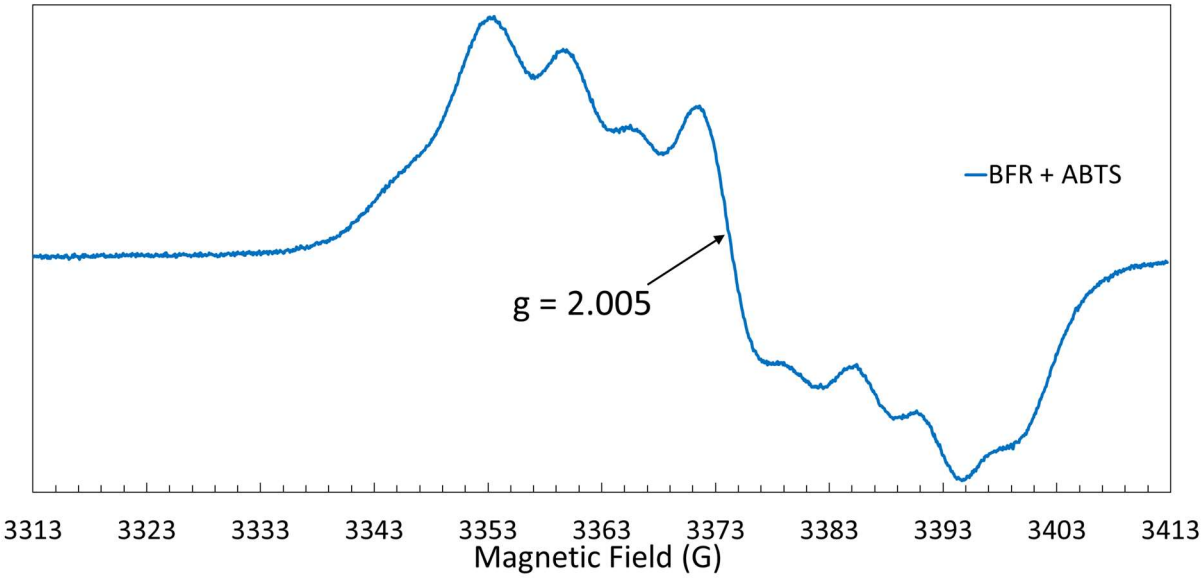


**Fig. 5.26.** An EPR spectrum showing the free radical generated when $Fe^{2+}$ oxidation by $H_2O_2$ is driven by BFR in the presence of ABTS. The concentration of BFR, $Fe^{2+}$, ABTS and $H_2O_2$ was 8.3 µM, 200 µM, 5 mM and 250 µM respectively, slow frozen after 11 s. The spectra were measured at 10 K at the following instrumental conditions: microwave frequency $\nu_{MW}$ = 9.4686 GHz; microwave power $P_{MW}$ = 0.05 mW.

Despite the lineshape of the free radical observed containing all the same spectral features as the radical formed in the absence of ABTS, the central component observed at approx. 3373 G is much more prominent. It was not possible to conclude that this was due to the presence of oxidized ABTS. In peroxidases, several cycles of the enzyme's reaction scheme allow for a build-up of oxidized ABTS. In BFR, this is not the case, and the reactive centre only reacts once. Given the rapid speed of the $H_2O_2$ reaction (and the low concentration of $Fe^{4+}$ observed

in the Mössbauer spectra), it is unlikely that a large amount of ABTS˙ would be observed, even if a ferryl species was oxidizing the dye.

## Discussion

### Free radical formation in the $H_2O_2$-driven oxidation of bacterioferritin:$Fe^{2+}$

At sub-stoichiometric concentrations of $H_2O_2$, a low concentration of free radical can be detected as a result of the reaction with BFR:$Fe^{2+}$ (Fig. 5.3). This free radical is of a similar lineshape and concentration to that seen in the $O_2$ reaction. It can therefore be suggested that $O_2$ does not form a free radical when reacting with BFR:$Fe^{2+}$; all observed free radicals are due to the successive reaction of the protein with the newly released $H_2O_2$. It is important to highlight that the 'resting' diferric FC in BFR (in the protein which has been left for 30 mins after addition of $Fe^{2+}$) yields no free radical when mixed with $H_2O_2$. As such, the diferric FC formed in the fast phase (≈20 ms after mixing with $H_2O_2$) is likely able to react with additional $H_2O_2$, but that further ligand changes prevent this reaction. As of the current date, there is no Mössbauer data available to support this suggestion.

The freshly formed diferric FC in BFR reacting with another $H_2O_2$ molecule may produce a ferryl iron centre and a radical, likely remaining near the FC on Y25. This ferryl rapidly decays to form another radical, which at sub-stoichiometric quantities of $H_2O_2$ is most likely to sit at Y58. Our data suggests that Y25 and Y58 have similar lineshapes, and their comparable proximity to the FCs means their relaxation behaviour should be similar. At supra-stoichiometric amounts of $H_2O_2$, a FC may undergo this cycle several times, which leads to W35 and W133 also oxidizing to a radical state. According to the simulations (Fig. 5.23) these tryptophanyl radicals appear to found in two stable conformations which are comparable between both residues, and line the four-fold channel of the 24meric shell. This may contribute to the function of this non-polar channel, which remains unclear. As BFR relies on its FC for

electron transfer (i.e. the core does not drive mineralisation at high iron loadings like it has been seen to do in some ferritins, like HuHF) there is no need for reagents like $O_2$ to enter through this pore.

**A ferryl intermediate in bacterioferritin**

Mössbauer spectroscopy suggested that a small yet nonetheless detectable concentration of mononuclear $Fe^{4+}$ formed when $H_2O_2$ reacts with BFR. This is useful when explaining how free radicals are generated from the diferric FC without the formation of a transient radical intermediate. Fig. 5.26 shows the result of an attempt to oxidize the BFR:$Fe^{2+}$ complex with $H_2O_2$ in the presence of ABTS, but unlike other systems where ABTS is used to detect the formation of ferryl species (Linde *et al.*, 2014), the BFR FC only turns over once, so it is not possible to generate a large concentration of $ABTS^{\cdot}$ radicals (this process competes with the seemingly rapid reduction of the $Fe^{4+}$ by an aromatic residue). As such, the lineshape change is too subtle to conclusively suggest the formation of $ABTS^{\cdot}$, and thus the presence of a ferryl intermediate on BFR.

**Conclusion**

The importance of redox-active aromatic residues to the mineralisation process in BFR (Bradley *et al.*, 2015) suggests that a free radical mechanism could likely be of great significance to the protein when handling large quantities of iron, but there is no evidence that they are necessary for the oxidation of iron at the FC.

When supra-stoichiometric concentrations of $H_2O_2$ are added to BFR:$Fe^{2+}$, several free radicals form. Simulation and studying variant BFR proteins have suggested the working hypothesis that there are two tyrosyl radicals and two tryptophanyl radicals, located on Y25, Y58, W35 and W133 respectively. While the tyrosyl radicals have different spectra that can be isolated, the tryptophanyl radicals appear to be conformationally flexible and give similar EPR spectra. Their function is not clear, but it is possible that they could be involved in electron transport mechanisms to distribute electrons to and from the FC, iron ion channels or across the protein shell (to diffuse radical damage and preserve the integrity of the protein shell).

# Chapter 6

## Summary

The work in this thesis has provided further insight into how ferritins can prevent oxidative stress; three of the five ferritins described here (*Syn*Ftn, human mitochondrial ferritin (FtMt) and *E. coli* bacterioferritin (BFR)) have been indicated to protect against oxidative stress. Several techniques were developed or refined in this study which can be applied to other ferritins in future, particularly the anaerobic rapid freeze quench (RFQ) technique that allows for protein kinetics to be monitored by EPR at time points as early as 45 ms after mixing. Unlike more expensive setups for anaerobic RFQ, this methodology does not require the use of a glove box.

*Syn*Ftn is upregulated in response to high copper levels and clearly provides an advantage to the coastal cyanobacterial species that express it. A mechanism has been proposed for *Syn*Ftn that requires the formation of a mixed valence ferroxidase centre (MVFC) which may add as a single electron donor/acceptor for the elimination of reactive oxygen species (ROS). The *n* ferr protein should be studied alongside *Syn*Ftn, and further work must be carried out to ensure that the MVFC in HuHF is a reproducible event.

For BFR, a mechanism has been proposed that establishes how $H_2O_2$ is reduced to water and is thus detoxified. Progress has been made on the assignment of radicals when under supra-stoichiometric [$H_2O_2$] conditions, but the assignment in this work is far from unambiguous.

The reaction schemes shown in Fig. 4.40 still do not make it clear why a free radical is needed in the oxidation of the FC when there is no iron to mineralise.

The controlled generation of BFR-based free radicals through $H_2O_2$ reduction at the BFR site is likely to be an adaptive advantage as it increases the stoichiometry of the FC when reacting with $H_2O_2$ so that each BFR molecule is as efficient as possible *in vivo*. It has not yet been determined how BFR is regulated, or whether it can itself serve as a signalling molecule to the cell indicating oxidative damage.

**Unity vs diversity theory of ferritin mechanism**

It has been suggested that all ferritins oxidize iron through a universal mechanism: "what is true for iron-storage mechanism of *P. furiosus* ferritin (PfFtn) is also true for that of human H-chain ferritin (HuHF) (and for that matter for any catalytically active ferritin on this planet be it eukaryotic, bacterial, or archaeal)… Although in the course of evolution the amino acid sequence of (bacterio)-ferritins has changed or modifications have emerged to satisfy a special need of an organism, the basic principles of $Fe^{2+}$ oxidation and storage mechanism in (bacterio)ferritin have remained the same" (Honarmand Ebrahimi, Hagedoorn and Hagen, 2015).

With respect to HuHF, the finding of a MVFC may support the $Fe^{2+}Fe^{3+}$ displacement mechanism (two alternative versions of this are shown in Appendix 1) if the protein already contained a moderate amount of $Fe^{3+}$. The proponents argue that the breakdown of a μ-1,2 peroxo-diferric species to a diferric iron cluster that moves into the core is implausible. They also note that nuclear magnetic resonance (NMR) data supporting the existence of these clusters (Ha *et al.*, 1999) and their movement into the core from across the long axis of the monomeric subunit (Turano *et al.*, 2010), in actuality, supports the finding that iron does not leave the FC (Hagen, Hagedoorn and Honarmand Ebrahimi, 2017). This alternative

interpretation was acknowledged by the authors of the work themselves (Piccioli and Turano, 2015).

The use of transferrin to selectively remove the iron from the FC and not the central cavity is a creative experiment (Honarmand Ebrahimi *et al.*, 2012), but with the low iron loadings, it is not possible to assume with absolute certainty that the iron is bound within the central cavity, and is not within a channel of the protein where it remains close to the surface. Indeed, there has been evidence of gated pores in ferritins which open or close based on biological need (Theil, Liu and Tosha, 2008). It is important to stipulate that the only pore gate discovered at this point in time controls $Fe^{2+}$ egress from the protein, and $Fe^{2+}$ entry to the FC, neither of which would strictly prevent $Fe^{3+}$ from reaching the central cavity.

The argument for the existence of a site C in mammalian ferritins has been addressed in the introduction already (below Fig. 1.5) and is far from unambiguous. However, its refutation (that most crystal structures show no third iron binding site, and the 'site C' that has been identified is most likely transient transport site, Bradley, Moore and Le Brun, 2017) is equally circumstantial, and does not close the matter.

The reaction scheme is not without more substantial flaws, as the mechanism does not account for the regeneration of the FC's fast phase within 10 mins of iron addition (Yang *et al.*, 1998). This finding does not appear to have been acknowledged by the proponents of the $Fe^{2+}Fe^{3+}$ displacement hypothesis, who then proceed to generate 'loaded' HuHF by incubating the protein with 48 $Fe^{2+}$/24mer for at least 5 hours (Ebrahimi, Hagedoorn and Hagen, 2013). Many (but notably, not all) of the results that they find can be corroborated with those found by scientists who claim the effect is due to $Fe^{3+}$ found within the central cavity.

*Syn*Ftn also poses challenges for the $Fe^{2+}Fe^{3+}$ displacement mechanism, where it is unclear how a stoichiometry of two is achieved while achieving the same spectral intermediate (a diferric

peroxo- (DFP) species) as other ferritins. Furthermore, a relatively stable MVFC forms upon the aerobic addition of 48 $Fe^{2+}$/24mer to apoprotein, which is not explained by either of the current displacement models. However, it is acknowledged that this concern could be addressed with minor changes to the mechanism without rejecting the 'unified' approach to ferritin mechanisms.

While it cannot be conclusively proven in this thesis that a single unified mechanism accounts for all ferritin mechanisms, the differences in the reactivity between the ferritins discussed in Chapter 3 and *E. coli* BFR make this unlikely. The authors explicitly state that it is unclear that $H_2O_2$ is a product of BFR mechanism, that $H_2O_2$ is a favoured over $O_2$ as an oxidant for BFR and claim that the $Fe^{2+}Fe^{3+}$ displacement mechanism is a better fit to the model than the current, convoluted model proposed for BFRs (Honarmand Ebrahimi, Hagedoorn and Hagen, 2015). First, it can be determined unambiguously that $H_2O_2$ is released stoichiometrically from the protein at a rate which explains the absence of a spectroscopically observable DFP species. Second, the difference in oxidation rates between the $O_2$ and the $H_2O_2$-driven should eliminate all doubt that it is not a preferred substrate. This point alone should raise concerns about the plausibility of a similar model to mammalian ferritins, where the FC shows very low, if any, activity towards $H_2O_2$. No MVFC has ever been measured in BFR under any of the circumstances measured. The experiments where a MVFC were observed in HuHF were not repeated exactly (most experiments described with BFR in this thesis only add 48 $Fe^{2+}$/24mer to apo-protein before the addition of an oxidant, not 24 $Fe^{2+}$/24mer to 'loaded' ferritin as in Honarmand Ebrahimi *et al.*, 2012). However, it is impossible to remove all $Fe^{3+}$ from BFR in the iron removal procedure, and some inevitably remains. As such, control experiments where no oxidant was added should have revealed at least some MVFC. It is straightforward to design experiments to directly test this hypothesis.

Overall the data presented in this work cannot emphatically reject the hypothesis of a unified reaction scheme that operates in all ferritins, but at the very least the work does suggest that the $Fe^{2+}Fe^{3+}$ displacement mechanism proposed as the unifying mechanism cannot address all the data across all ferritin families.

# References


Abdul-Tehrani, H. *et al.* (1999) 'Ferritin mutants of Escherichia coli are iron deficient and growth impaired, and fur mutants are iron deficient', *Journal of Bacteriology*, 181(5), pp. 1415–1428. doi: 10.1126/science.287.5458.1655.

Adamec, J. *et al.* (2000) 'Iron-dependent self-assembly of recombinant yeast frataxin: Implications for Friedreich ataxia', *American Journal of Human Genetics*, 67(3), pp. 549–562. doi: 10.1086/303056.

Ahmad, S., Kitchin, K. T. and Cullen, W. R. (2000) 'Arsenic Species That Cause Release of Iron from Ferritin and Generation of Activated Oxygen', *Archives of Biochemistry and Biophysics*, 382(2), pp. 195–202. doi: 10.1006/abbi.2000.2023.

Aitken-Rogers, H. *et al.* (2004) 'Effect of phosphate on bacterioferritin-catalysed iron(II) oxidation', *JBIC Journal of Biological Inorganic Chemistry*, 9(2), pp. 161–170. doi: 10.1007/s00775-003-0504-1.

Albretsen, J. (2006) 'The toxicity of iron, an essential element', *Veterinary Medicine Toxicology Brief*, (February), pp. 82–90.

Almiron, M. *et al.* (1992) 'A novel DNA-binding protein with regulatory and protective roles in starved Escherichia coli.', *Genes & Development*, 6(12b), pp. 2646–2654. doi: 10.1101/gad.6.12b.2646.

Andrews, S. C. *et al.* (1995) 'Site-directed replacement of the coaxial heme ligands of bacterioferritin generates heme-free variants', *Journal of Biological Chemistry*, 270(40), pp. 23268–23274. doi: 10.1074/jbc.270.40.23268.

Andrews, S. C. (2010) 'The Ferritin-like superfamily: Evolution of the biological iron storeman from a rubrerythrin-like ancestor', *Biochimica et Biophysica Acta - General Subjects*. Elsevier B.V., 1800(8), pp. 691–705. doi: 10.1016/j.bbagen.2010.05.010.

Atkin, C. L. *et al.* (1973) 'Iron and free radical in ribonucleotide reductase. Exchange of iron and Mössbauer spectroscopy of the protein B2 subunit of the Escherichia coli enzyme.', *The Journal of biological chemistry*, 248(21), pp. 7464–72. Available at: http://www.ncbi.nlm.nih.gov/pubmed/4355582.

Baaghil, S. *et al.* (2003) 'Core Formation in Escherichia coli Bacterioferritin Requires a Functional Ferroxidase Center †', *Biochemistry*, 42(47), pp. 14047–14056. doi: 10.1021/bi035253u.

Babcock, M. (1997) 'Regulation of Mitochondrial Iron Accumulation by Yfh1p, a Putative Homolog of Frataxin', *Science*, 276(5319), pp. 1709–1712. doi: 10.1126/science.276.5319.1709.

Baldwin, J. *et al.* (2000) 'Mechanism of Rapid Electron Transfer during Oxygen Activation in the R2 Subunit of Escherichia c oli Ribonucleotide Reductase. 1. Evidence for a Transient Tryptophan Radical', *Journal of the American Chemical Society*, 122(49), pp. 12195–12206. doi: 10.1021/ja001278u.

Balla, G. *et al.* (1992) 'Ferritin: A cytoprotective antioxidant strategem of endothelium', *Journal of Biological Chemistry*, 267(25), pp. 18148–18153.

Banerjee, R. *et al.* (2013) 'Intermediate P* from Soluble Methane Monooxygenase Contains a Diferrous Cluster', *Biochemistry*, 52(25), pp. 4331–4342. doi: 10.1021/bi400182y.

Baraibar, M. A. *et al.* (2012) 'A mutant light-chain ferritin that causes neurodegeneration has enhanced propensity toward oxidative damage', *Free Radical Biology and Medicine*, 52(9), pp. 1692–1697. doi: 10.1016/j.freeradbiomed.2012.02.015.

Bartnikas, T. B. *et al.* (2010) 'Characterization of mitochondrial ferritin-deficient mice', *American Journal of Hematology*, 85(12), pp. 958–960. doi: 10.1002/ajh.21872.

Bates, G. *et al.* (1968) 'Hemerythrin. I. Thermodynamic and kinetic aspects of oxygen binding', *Biochemistry*, 7(8), pp. 3016–3020. doi: 10.1021/bi00848a044.

Bauminger, E. R. *et al.* (1991) 'Mössbauer spectroscopic investigation of structure-function relations in ferritins', *Biochimica et Biophysica Acta (BBA) - Protein Structure and Molecular Enzymology*, 1118(1), pp. 48–58. doi: 10.1016/0167-4838(91)90440-B.

Bauminger, E. R. *et al.* (1994) 'Iron incorporation into ferritins: evidence for the transfer of monomeric Fe(III) between ferritin molecules and for the formation of an unusual mineral in the ferritin of Escherichia coli.', *The Biochemical journal*, 302 ( Pt 3, pp. 813–20. Available at: http://www.pubmedcentral.nih.gov/articlerender.fcgi?artid=1137303&tool=pmcentrez&rendertype=abstract.

Biemond, P. *et al.* (1984) 'Iron mobilization from ferritin by superoxide derived from stimulated polymorphonuclear leukocytes. Possible mechanism in inflammation diseases.', *Journal of Clinical Investigation*, 73(6), pp. 1576–1579. doi: 10.1172/JCI111364.

Biemond, P. *et al.* (1988) 'Superoxide dependent iron release from ferritin in inflammatory diseases', *Free Radical Biology and Medicine*, 4(3), pp. 185–198. doi: 10.1016/0891-5849(88)90026-3.

Bonkovsky, H. *et al.* (1996) 'An update on iron metabolism: Summary of the Fifth International Conference on Disorders of Iron Metabolism', *Hepatology*, 24(3), pp. 718–729. doi: 10.1053/jhep.1996.v24.ajhep0240718.

Bottero, J. Y. *et al.* (1994) 'Structure and mechanisms of formation of iron oxide hydroxide (chloride) polymers', *Langmuir*, 10(1), pp. 316–319. doi: 10.1021/la00013a046.

Bou-Abdallah, F. *et al.* (2002) 'Iron detoxification properties of Escherichia coli bacterioferritin.', *The Journal of biological chemistry*, 277(40), pp. 37064–9. doi: 10.1074/jbc.M205712200.

Bou-Abdallah, F. *et al.* (2005) 'Unique iron binding and oxidation properties of human mitochondrial ferritin: A comparative analysis with human H-chain ferritin', *Journal of Molecular Biology*, 347(3), pp. 543–554. doi: 10.1016/j.jmb.2005.01.007.

Bou-Abdallah, F. (2010) 'The iron redox and hydrolysis chemistry of the ferritins', *Biochimica et Biophysica Acta (BBA) - General Subjects*. Elsevier B.V., 1800(8), pp. 719–731. doi: 10.1016/j.bbagen.2010.03.021.

Bou-Abdallah, F. *et al.* (2014) 'Functionality of the three-site ferroxidase center of Escherichia coli bacterial ferritin (EcFtnA)', *Biochemistry*, 53(3), pp. 483–495. doi: 10.1021/bi401517f.

Boyer, R. F., Clark, H. M. and LaRoche, A. P. (1988) 'Reduction and Release of Ferritin Iron By Plant Phenolics', *Journal of Inorganic Biochemistry*, 32(3), pp. 171–181. doi: 10.1016/0162-0134(88)80025-4.

Bradley, J. M. *et al.* (2015) 'Three Aromatic Residues are Required for Electron Transfer during Iron Mineralization in Bacterioferritin', *Angewandte Chemie International Edition*, 54(49), pp. 14763–14767. doi: 10.1002/anie.201507486.

Bradley, J. M. *et al.* (2017) 'Tyr25, Tyr58 and Trp133 of Escherichia coli bacterioferritin transfer electrons between iron in the central cavity and the ferroxidase centre', *Metallomics*. Royal Society of Chemistry, 9(10), pp. 1421–1428. doi: 10.1039/C7MT00187H.

Bradley, J. M. *et al.* (2019) 'Reaction of O2 with a diiron protein generates a mixed-valent Fe2+/Fe3+ center and peroxide', *Proceedings of the National Academy of Sciences*, 116(6), pp. 2058–2067. doi: 10.1073/pnas.1809913116.

Bradley, J. M., Moore, G. R. and Le Brun, N. E. (2014) 'Mechanisms of iron mineralization in ferritins: One size does not fit all', *Journal of Biological Inorganic Chemistry*, 19(6), pp. 775–785. doi: 10.1007/s00775-014-1136-3.

Bradley, J. M., Moore, G. R. and Le Brun, N. E. (2017) 'Diversity of Fe 2+ entry and oxidation in ferritins', *Current Opinion in Chemical Biology*. Elsevier Ltd, 37, pp. 122–128. doi: 10.1016/j.cbpa.2017.02.027.

Briat, J. F. (1992) 'Iron assimilation and storage in prokaryotes.', *Journal of general microbiology*, 138(12), pp. 2475–2483. doi: 10.1099/00221287-138-12-2475.

Broadwater, J. A. *et al.* (1999) 'Mossbauer studies of the formation and reactivity of a quasi-stable peroxo intermediate of stearoyl-acyl carrier protein Δ9-desaturase', *Biochemistry*, 38(38), pp. 12197–12204. doi: 10.1021/bi9914199.

Le Brun, N. E., Cheesman, M. R., *et al.* (1993) 'An EPR investigation of non-haem iron sites in Escherichia coli bacterioferritin and their interaction with phosphate. A study using nitric oxide as a spin probe', *FEBS Letters*, 323(3), pp. 261–266. doi: 10.1016/0014-5793(93)81353-2.

Le Brun, N. E., Wilson, M. T., *et al.* (1993) 'Kinetic and structural characterization of an intermediate in the biomineralization of bacterioferritin', *FEBS Letters*, 333(1–2), pp. 197–202. doi: 10.1016/0014-5793(93)80404-I.

Le Brun, N. E. *et al.* (2010) 'Iron core mineralisation in prokaryotic ferritins', *Biochimica et Biophysica Acta - General Subjects*. Elsevier B.V., 1800(8), pp. 732–744. doi: 10.1016/j.bbagen.2010.04.002.

Bulteau, A. L. *et al.* (2004) 'Frataxin acts as an iron chaperone protein to modulate mitochondrial aconitase activity', *Science*, 305(5681), pp. 242–245. doi: 10.1126/science.1098991.

Campanella, A. *et al.* (2004) 'The expression of human mitochondrial ferritin rescues respiratory function infrataxin-deficient yeast', *Human Molecular Genetics*, 13(19), pp. 2279–2288. doi: 10.1093/hmg/ddh232.

Campanella, A. *et al.* (2009) 'Mitochondrial ferritin limits oxidative damage regulating mitochondrial iron availability: Hypothesis for a protective role in Friedreich ataxia', *Human Molecular Genetics*, 18(1), pp. 1–11. doi: 10.1093/hmg/ddn308.

Carmona, F. *et al.* (2013) 'Ferritin iron uptake and release in the presence of metals and metalloproteins: Chemical implications in the brain', *Coordination Chemistry Reviews*. Elsevier B.V., 257(19–20), pp. 2752–2764. doi: 10.1016/j.ccr.2013.03.034.

Chaplin, A. K. *et al.* (2017) 'Tyrosine or Tryptophan? Modifying a Metalloradical Catalytic Site by Removal of the Cys–Tyr Cross-Link in the Galactose 6-Oxidase Homologue GlxA', *Angewandte Chemie - International Edition*, 56(23), pp. 6502–6506. doi: 10.1002/anie.201701270.

Chaplin, A. K., Wilson, M. T. and Worrall, J. A. R. (2017) 'Kinetic characterisation of a dye decolourising peroxidase from Streptomyces lividans: New insight into the mechanism of anthraquinone dye decolourisation', *Dalton Transactions*. Royal Society of Chemistry, 46(29), pp. 9420–9429. doi: 10.1039/c7dt01144j.

Cheesman, M. R. *et al.* (1993) 'Haem and non-haem iron sites in Escherichia coli bacterioferritin: spectroscopic and model building studies.', *The Biochemical journal*, 292 ( Pt 1(June 1992), pp. 47–56. Available at: http://www.biochemj.org/bj/292/bj2920047.htm.

Chen-Barrett, Y. *et al.* (1995) 'Tyrosyl radical formation during the oxidative deposition of iron in human apoferritin.', *Biochemistry*, 34(24), pp. 7847–53. Available at: http://www.ncbi.nlm.nih.gov/pubmed/7794895.

Chen, C. and Paw, B. H. (2012) 'Cellular and mitochondrial iron homeostasis in vertebrates', *Biochimica et Biophysica Acta - Molecular Cell Research*. Elsevier B.V., 1823(9), pp. 1459–1467. doi: 10.1016/j.bbamcr.2012.01.003.

Chiancone, E. *et al.* (2004) 'Iron and proteins for iron storage and detoxification', *BioMetals*, 17(3), pp. 197–202. doi: 10.1023/B:BIOM.0000027692.24395.76.

Cornell, T. A. *et al.* (2017) 'The Crystal Structure of a Maxi/Mini-Ferritin Chimera Reveals Guiding Principles for the Assembly of Protein Cages', *Biochemistry*, 56(30), pp. 3894–3899. doi: 10.1021/acs.biochem.7b00312.

Corsi, B. *et al.* (2002) 'Human mitochondrial ferritin expressed in HeLa cells incorporates iron and affects cellular iron metabolism.', *The Journal of biological chemistry*, 277(25), pp. 22430–7. doi: 10.1074/jbc.M105372200.

Crow, A. *et al.* (2009) 'Structural basis for iron mineralization by bacterioferritin', *Journal of the American Chemical Society*, 131(19), pp. 6808–6813. doi: 10.1021/ja8093444.

Davydov, R. *et al.* (1999) 'An EPR study of the dinuclear iron site in the soluble methane monooxygenase from Methylococcus capsulatus (Bath) reduced by one electron at 77 K: The effects of component interactions and the binding of small molecules to the diiron(III) center', *Biochemistry*, 38(13), pp. 4188–4197. doi: 10.1021/bi982391o.

Davydov, R. M. *et al.* (1997) 'EPR study of the mixed-valent diiron sites in mouse and herpes simplex virus ribonucleotide reductases. Effect of the tyrosyl radical on structure and reactivity of the diferric center', *Biochemistry*, 36(30), pp. 9093–9100. doi: 10.1021/bi9700375.

Dexter, D. T. T. *et al.* (1991) 'Alterations in the Levels of Iron , Ferritin and Other Trace Metals in Parkinson ' S Disease and Other Neurodegenerative', *Brain.*, 114(Pt 4), pp. 1953–1975. doi: 10.1093/brain/114.4.1953.

Dhungana, S. *et al.* (2005) 'Kinetics of Iron Release from Ferric Binding Protein (FbpA): Mechanistic Implications in Bacterial Periplasm-to-Cytosol Fe 3+ Transport †', *Biochemistry*, 44(28), pp. 9606–9618. doi: 10.1021/bi0505518.

De Domenico, I., McVey Ward, D. and Kaplan, J. (2008) 'Regulation of iron acquisition and storage: consequences for iron-linked disorders', *Nature Reviews Molecular Cell Biology*, 9(1), pp. 72–81. doi: 10.1038/nrm2295.

Dudits, D. *et al.* (1999) 'Plants ectopically expressing the iron- binding protein, ferritin, are tolerant to oxidative damage and pathogens', *Nature Biotechnology*, 17(2), pp. 192–196. doi: 10.1038/6198.

Dufresne, A., Garczarek, L. and Partensky, F. (2005) 'Accelerated evolution associated with genome reduction in a free-living prokaryote', *Genome Biology*, 6(2), p. R14. doi: 10.1186/gb-2005-6-2-r14.

Ebrahimi, K. H. *et al.* (2016) 'Spectroscopic evidence for the role of a site of the di-iron catalytic center of ferritins in tuning the kinetics of Fe(II) oxidation', *Molecular BioSystems*. Royal Society of Chemistry, 12(12), pp. 3576–3588. doi: 10.1039/C6MB00235H.

Ebrahimi, K. H., Hagedoorn, P. L. and Hagen, W. R. (2013) 'A conserved tyrosine in ferritin is a molecular capacitor', *ChemBioChem*, 14(9), pp. 1123–1133. doi: 10.1002/cbic.201300149.

Fajer, P. G. (2006) 'Electron Spin Resonance Spectroscopy Labeling in Peptide and Protein Analysis', in *Encyclopedia of Analytical Chemistry*. Chichester, UK: John Wiley & Sons, Ltd. doi: 10.1002/9780470027318.a1609.

Falvo, E. *et al.* (2013) 'Antibody–drug conjugates: targeting melanoma with cisplatin encapsulated in protein-cage nanoparticles based on human ferritin', *Nanoscale*, 5(24), p. 12278. doi: 10.1039/c3nr04268e.

Finazzi, D. and Arosio, P. (2014) 'Biology of ferritin in mammals: an update on iron storage, oxidative damage and neurodegeneration', *Archives of Toxicology*, 88(10), pp. 1787–1802. doi: 10.1007/s00204-014-1329-0.

Finkelstein, E., Rosen, G. M. and Rauckman, E. J. (1982) 'Production of hydroxyl radical by decomposition of superoxide spin-trapped adducts.', *Molecular pharmacology*, 21(2), pp. 262–5. Available at: http://www.ncbi.nlm.nih.gov/pubmed/6285165.

Friesner, R. A. *et al.* (2003) 'How iron-containing proteins control dioxygen chemistry: A detailed atomic level description via accurate quantum chemical and mixed quantum mechanics/molecular mechanics calculations', *Coordination Chemistry Reviews*, 238–239, pp. 267–290. doi: 10.1016/S0010-8545(02)00284-9.

Galvez, N. *et al.* (2008) 'Comparative Structural and Chemical Studies of Ferritin', *J. Ann. Chem. Society*, 130(5), pp. 8062–8068.

Greene, B. L. *et al.* (2017) 'Conformationally Dynamic Radical Transfer within Ribonucleotide Reductase', *Journal of the American Chemical Society*, 139(46), pp. 16657–16665. doi: 10.1021/jacs.7b08192.

Guaraldo, M. *et al.* (2016) 'Characterization of human mitochondrial ferritin promoter: Identification of transcription factors and evidences of epigenetic control', *Scientific Reports*, 6(September), pp. 1–11. doi: 10.1038/srep33432.

Gundersen, J. K., Ramsing, N. B. and Glud, R. N. (1998) 'Predicting the signal of O 2 microsensors from physical dimensions, temperature, salinity, and O 2 concentration', *Limnology and Oceanography*, 43(8), pp. 1932–1937. doi: 10.4319/lo.1998.43.8.1932.

Ha, Y. *et al.* (1999) 'Crystal structure of bullfrog M ferritin at 2.8 Å resolution: analysis of

subunit interactions and the binuclear metal center', *JBIC Journal of Biological Inorganic Chemistry*, 4(3), pp. 243–256. doi: 10.1007/s007750050310.

Hagen, W. R., Hagedoorn, P. L. and Honarmand Ebrahimi, K. (2017) 'The workings of ferritin: A crossroad of opinions', *Metallomics*. Royal Society of Chemistry, 9(6), pp. 595–605. doi: 10.1039/c7mt00124j.

Hanna, P. M., Chen, Y. and Chasteen, N. D. (1991) 'Initial iron oxidation in horse spleen apoferritin. Characterization of a mixed-valence iron(II)-iron(III) complex', *Journal of Biological Chemistry*, 266(2), pp. 886–893.

Harrison, P. M. *et al.* (1974) 'Ferritin iron uptake and release. Structure–function relationships', *Biochemical Journal*, 143(2), pp. 445–451. doi: 10.1042/bj1430445.

Harrison, P. M. (1979) 'Iron storage in bacteria', *Nature*, 279(5708), pp. 15–16. doi: 10.1038/279015a0.

Harrison, P. M. and Arosio, P. (1996) 'The ferritins: Molecular properties, iron storage function and cellular regulation', *Biochimica et Biophysica Acta - Bioenergetics*, 1275(3), pp. 161–203. doi: 10.1016/0005-2728(96)00022-9.

Hempstead, P. D. *et al.* (1994) 'Direct observation of the iron binding sites in a ferritin', *FEBS Letters*, 350(2–3), pp. 258–262. doi: 10.1016/0014-5793(94)00781-0.

Holmes, M. A. *et al.* (1991) 'Structures of deoxy and oxy hemerythrin at 2.0 Å resolution', *Journal of Molecular Biology*, 218(3), pp. 583–593. doi: 10.1016/0022-2836(91)90703-9.

Honarmand Ebrahimi, K. *et al.* (2009) 'Catalysis of iron core formation in Pyrococcus furiosus ferritin', *Journal of Biological Inorganic Chemistry*, 14(8), pp. 1265–1274. doi: 10.1007/s00775-009-0571-z.

Honarmand Ebrahimi, K. *et al.* (2012) 'The catalytic center of ferritin regulates iron storage via Fe(II)-Fe(III) displacement', *Nature Chemical Biology*. Nature Publishing Group, 8(11), pp. 941–948. doi: 10.1038/nchembio.1071.

Honarmand Ebrahimi, K. *et al.* (2017) 'Spectroscopic evidence for the presence of a high-valent Fe(IV) species in the ferroxidase reaction of an archaeal ferritin', *FEBS Letters*, 591(12), pp. 1712–1719. doi: 10.1002/1873-3468.12697.

Honarmand Ebrahimi, K., Hagedoorn, P.-L. and Hagen, W. R. (2015) 'Unity in the Biochemistry of the Iron-Storage Proteins Ferritin and Bacterioferritin', *Chemical Reviews*, 115(1), pp. 295–326. doi: 10.1021/cr5004908.

Horowitz, M. P. and Greenamyre, J. T. (2010) 'Mitochondrial Iron Metabolism and Its Role in Neurodegeneration', *Journal of Alzheimer's Disease*. Edited by X. Zhu et al., 20(s2), pp. S551–S568. doi: 10.3233/JAD-2010-100354.

Ichikawa, Y. *et al.* (2014) 'Cardiotoxicity of doxorubicin is mediated through mitochondrial iron accumulation', *Journal of Clinical Investigation*, 124(2), pp. 617–630. doi: 10.1172/JCI72931.

Jameson, G. N. L. *et al.* (2002) 'Stoichiometric production of hydrogen peroxide and parallel formation of ferric multimers through decay of the diferric-peroxo complex, the first detectable intermediate in ferritin mineralization', *Biochemistry*, 41(45), pp. 13435–13443. doi: 10.1021/bi026478s.

Jasniewski, A. J. and Que, L. (2018) 'Dioxygen Activation by Nonheme Diiron Enzymes: Diverse Dioxygen Adducts, High-Valent Intermediates, and Related Model Complexes', *Chemical Reviews*, 118(5), pp. 2554–2592. doi: 10.1021/acs.chemrev.7b00457.

Keech, A. M. *et al.* (1997) 'Spectroscopic Studies of Cobalt (II) Binding to Escherichia coli Bacterioferritin *', 272(1), pp. 422–429.

Kilic, M. A., Spiro, S. and Moore, G. R. (2003) 'Stability of a 24-meric homopolymer: Comparative studies of assembly-defective mutants of Rhodobacter capsulatus bacterioferritin and the native protein', *Protein Science*, 12(8), pp. 1663–1674. doi: 10.1110/ps.0301903.

Küberl, A., Polen, T. and Bott, M. (2016) 'The pupylation machinery is involved in iron homeostasis by targeting the iron storage protein ferritin', *Proceedings of the National Academy of Sciences of the United States of America*, 113(17), pp. 4806–4811. doi: 10.1073/pnas.1514529113.

Kuppusamy, P. and Zweier, J. L. (1989) 'Characterization of free radical generation by xanthine oxidase. Evidence for hydroxyl radical generation', *Journal of Biological Chemistry*, 264(17), pp. 9880–9884.

Kurtz, D. M. (2003) 'Dioxygen-binding Proteins', in *Comprehensive Coordination Chemistry II*. Elsevier, pp. 229–260. doi: 10.1016/B0-08-043748-6/08171-8.

Lacy, D. C. *et al.* (2010) 'Formation, structure, and EPR detection of a high spin FeIV-Oxo Species Derived from Either an FeIII-Oxo or FeIII-OH Complex', *Journal of the American Chemical Society*, 132(35), pp. 12188–12190. doi: 10.1021/ja1047818.

Langlois d'Estaintot, B. *et al.* (2004) 'Crystal Structure and Biochemical Properties of the Human Mitochondrial Ferritin and its Mutant Ser144Ala', *Journal of Molecular Biology*, 340(2), pp. 277–293. doi: 10.1016/j.jmb.2004.04.036.

Lauffer, R. B. *et al.* (1983) '1H-NMR studies of porcine uteroferrin', *Journal of Biological Chemistry*, 258(23), pp. 14212–14218.

Lawson, D. M. *et al.* (1991) 'Solving the structure of human H ferritin by genetically engineering intermolecular crystal contacts', *Nature*, 349(6309), pp. 541–544. doi: 10.1038/349541a0.

Lawson, T. L. *et al.* (2009) 'Monitoring the Iron Status of the Ferroxidase Center of Escherichia coli Bacterioferritin Using Fluorescence Spectroscopy', *Biochemistry*, 48(38), pp. 9031–9039. doi: 10.1021/bi900869x.

Lee, M. *et al.* (1994) 'Identification of the EPR-active iron-nitrosyl complexes in mammalian ferritins.', *Biochemistry*, 33(12), pp. 3679–87. Available at: http://www.ncbi.nlm.nih.gov/pubmed/8142366.

Lee, S. K., Nesheim, J. C. and Lipscomb, J. D. (1993) 'Transient intermediates of the methane monooxygenase catalytic cycle', *Journal of Biological Chemistry*, 268(29), pp. 21569–21577.

Levi, S. *et al.* (1992) 'Evidence of H- and L-chains have co-operative roles in the iron-uptake mechanism of human ferritin.', *The Biochemical journal*, 288 ( Pt 2(Pt 2), pp. 591–6. Available at: http://www.ncbi.nlm.nih.gov/pubmed/1463463.

Levi, S. *et al.* (1994) 'The role of the L-chain in ferritin iron incorporation. Studies of homo and heteropolymers.', *Journal of molecular biology*, pp. 649–654. doi: 10.1006/jmbi.1994.1325.

Levi, S. *et al.* (1996) 'Evidence that residues exposed on the three-fold channels have active roles in the mechanism of ferritin iron incorporation.', *The Biochemical journal*, 317(Pt 2), pp. 467–473. doi: 10.1042/bj3170467.

Levi, S. *et al.* (2001) 'A Human Mitochondrial Ferritin Encoded by an Intronless Gene', *Journal of Biological Chemistry*, 276(27), pp. 24437–24440. doi: 10.1074/jbc.C100141200.

Li, C., Hu, X. and Zhao, G. (2009) 'Two different H-type subunits from pea seed (Pisum sativum) ferritin that are responsible for fast Fe(II) oxidation', *Biochimie*. Elsevier Masson SAS, 91(2), pp. 230–239. doi: 10.1016/j.biochi.2008.09.008.

Li, X. *et al.* (2015) 'A bacterial hemerythrin-like protein MsmHr inhibits the SigF-dependent hydrogen peroxide response in mycobacteria', *Frontiers in Microbiology*, 5(January), p. 800. doi: 10.3389/fmicb.2014.00800.

Linde, D. *et al.* (2014) 'Catalytic surface radical in dye-decolorizing peroxidase: a computational, spectroscopic and site-directed mutagenesis study', *Biochemical Journal*, 466(2), pp. 253–262. doi: 10.1042/bj20141211.

Liu, X. and Theil, E. C. (2005) 'Ferritins: Dynamic management of biological iron and oxygen chemistry', *Accounts of Chemical Research*, 38(3), pp. 167–175. doi: 10.1021/ar0302336.

Lynch, J. B. *et al.* (1989) 'Mossbauer and EPR studies of the binuclear iron center in ribonucleotide reductase from Escherichia coli. A new iron-to-protein stoichiometry', *Journal of Biological Chemistry*, 264(14), pp. 8091–8096.

Maccarinelli, F. *et al.* (2014) 'Mice lacking mitochondrial ferritin are more sensitive to doxorubicin-mediated cardiotoxicity', *Journal of Molecular Medicine*, 92(8), pp. 859–869. doi: 10.1007/s00109-014-1147-0.

Macedo, S. *et al.* (2003) 'The nature of the di-iron site in the bacterioferritin from Desulfovibrio desulfuricans.', *Nature structural biology*, 10(4), pp. 285–90. doi: 10.1038/nsb909.

Macomber, L. and Imlay, J. A. (2009) 'The iron-sulfur clusters of dehydratases are primary intracellular targets of copper toxicity', *Proceedings of the National Academy of Sciences of the United States of America*, 106(20), pp. 8344–8349. doi: 10.1073/pnas.0812808106.

Malone, S. A. *et al.* (2004) 'Protein-Template-Driven Formation of Polynuclear Iron Species', *Journal of the American Chemical Society*, 126(2), pp. 496–504. doi: 10.1021/ja036483z.

Marchetti, A. *et al.* (2009) 'Ferritin is used for iron storage in bloom-forming marine pennate diatoms', *Nature*. Nature Publishing Group, 457(7228), pp. 467–470. doi: 10.1038/nature07539.

Marrale, M. *et al.* (2006) 'Power Saturation of ESR Signal in Ammonium Tartrate Exposed to 60 Co γ-Ray Photons, Electrons and Protons', *Radiation Research*, 166(5), pp. 802–809. doi: 10.1667/RR0600.1.

Mathevon, C. *et al.* (2007) 'tRNA-modifying MiaE protein from Salmonella typhimurium is a nonheme diiron monooxygenase', *Proceedings of the National Academy of Sciences*, 104(33), pp. 13295–13300. doi: 10.1073/pnas.0704338104.

Mazur, A. *et al.* (1958) 'Mechanism of Release of Ferritin Iron In Vivo by Xanthine Oxidase', *Journal of Clinical Investigation*, 37(12), pp. 1809–1817. doi: 10.1172/JCI103774.

Mena, N. P. *et al.* (2015) 'Mitochondrial iron homeostasis and its dysfunctions in

neurodegenerative disorders', *Mitochondrion*. Elsevier B.V., 21, pp. 92–105. doi: 10.1016/j.mito.2015.02.001.

Minnihan, E. C., Nocera, D. G. and Stubbe, J. (2013) 'Reversible, Long-Range Radical Transfer in E. coli Class Ia Ribonucleotide Reductase', *Accounts of Chemical Research*, 46(11), pp. 2524–2535. doi: 10.1021/ar4000407.

Minotti, G. *et al.* (2004) 'Anthracyclines: Molecular advances and pharmacologie developments in antitumor activity and cardiotoxicity', *Pharmacological Reviews*, 56(2), pp. 185–229. doi: 10.1124/pr.56.2.6.

Moënne-Loccoz, P. *et al.* (1998) 'O2 activation by non-heme diiron proteins: Identification of a symmetric μ-1,2-peroxide in a mutant of ribonucleotide reductase', *Biochemistry*, 37(42), pp. 14659–14663. doi: 10.1021/bi981838q.

Monteiro, H. P. and Winterbourn, C. C. (1989) '6-Hydroxydopamine releases iron from ferritin and promotes ferritin-dependent lipid peroxidation', *Biochemical Pharmacology*, 38(23), pp. 4177–4182. doi: 10.1016/0006-2952(89)90512-1.

Mottley, C., Connor, H. D. and Mason, R. P. (1986) '[ 17 O]oxygen hyperfine structure for the hydroxyl and superoxide radical adducts of the spin traps DMPO, PBN and 4-POBN', *Biochemical and Biophysical Research Communications*, 141(2), pp. 622–628. doi: 10.1016/S0006-291X(86)80218-2.

Muckenthaler, M. U., Galy, B. and Hentze, M. W. (2008) 'Systemic Iron Homeostasis and the Iron-Responsive Element/Iron-Regulatory Protein (IRE/IRP) Regulatory Network', *Annual Review of Nutrition*, 28(1), pp. 197–213. doi: 10.1146/annurev.nutr.28.061807.155521.

Murray, L. J. *et al.* (2007) 'Characterization of the Arene-Oxidizing Intermediate in ToMOH as a Diiron(III) Species', *Journal of the American Chemical Society*, 129(46), pp. 14500–14510. doi: 10.1021/ja076121h.

Nandal, A. *et al.* (2010) 'Induction of the ferritin gene ( ftnA ) of Escherichia coli by Fe 2+ - Fur is mediated by reversal of H-NS silencing and is RyhB independent', *Molecular Microbiology*, 75(3), pp. 637–657. doi: 10.1111/j.1365-2958.2009.06977.x.

Nie, G. (2005) 'Overexpression of mitochondrial ferritin causes cytosolic iron depletion and changes cellular iron homeostasis', *Blood*, 105(5), pp. 2161–2167. doi: 10.1182/blood-2004-07-2722.

Ormö, M. *et al.* (1995) 'Residues Important for Radical Stability in Ribonucleotide Reductase from Escherichia coli', *Journal of Biological Chemistry*, 270(12), pp. 6570–6576. doi: 10.1074/jbc.270.12.6570.

Palenik, B. *et al.* (2006) 'Genome sequence of Synechococcus CC9311: Insights into adaptation to a coastal environment', *Proceedings of the National Academy of Sciences*, 103(36), pp. 13555–13559. doi: 10.1073/pnas.0602963103.

Parker Siburt, C. J., Mietzner, T. A. and Crumbliss, A. L. (2012) 'FbpA - A bacterial transferrin with more to offer', *Biochimica et Biophysica Acta - General Subjects*. Elsevier B.V., 1820(3), pp. 379–392. doi: 10.1016/j.bbagen.2011.09.001.

Pearce, L. L. *et al.* (1987) 'Reduction of the Binuclear Iron Site in Octameric Methemerythrins. Characterizations of Intermediates and a Unifying Reaction Scheme', *Journal of the American Chemical Society*, 109(24), pp. 7286–7293. doi: 10.1021/ja00258a007.

Pearce, M. J. *et al.* (2008) 'Ubiquitin-Like Protein Involved in the Proteasome Pathway of Mycobacterium tuberculosis', *Science*, 322(5904), pp. 1104–1107. doi: 10.1126/science.1163885.

Pereira, A. S. *et al.* (1998) 'Direct Spectroscopic and Kinetic Evidence for the Involvement of a Peroxodiferric Intermediate during the Ferroxidase Reaction in Fast Ferritin Mineralization', *Biochemistry*, 37(28), pp. 9871–9876. doi: 10.1021/bi980847w.

Pfaffen, S. *et al.* (2013) 'Mechanism of ferrous iron binding and oxidation by ferritin from a pennate diatom', *Journal of Biological Chemistry*, 288(21), pp. 14917–14925. doi: 10.1074/jbc.M113.454496.

Pfaffen, S. *et al.* (2015) 'A Diatom Ferritin Optimized for Iron Oxidation but Not Iron Storage', *Journal of Biological Chemistry*, 290(47), pp. 28416–28427. doi: 10.1074/jbc.M115.669713.

Piccioli, M. and Turano, P. (2015) 'Transient iron coordination sites in proteins: Exploiting the dual nature of paramagnetic NMR', *Coordination Chemistry Reviews*. Elsevier B.V., 284, pp. 313–328. doi: 10.1016/j.ccr.2014.05.007.

Ponka, P. (1997) 'Tissue-specific regulation of iron metabolism and heme synthesis: Distinct control mechanisms in erythroid cells', *Blood*, 89, pp. 1–25. Available at: http://www.pnas.org/cgi/doi/10.1073/pnas.0912925107.

Poulsen, C. *et al.* (2010) 'Proteome-wide identification of mycobacterial pupylation targets', *Molecular Systems Biology*, 6(1), p. 386. doi: 10.1038/msb.2010.39.

Pozzi, C. *et al.* (2015) 'Iron binding to human heavy-chain ferritin', *Acta Crystallographica Section D Biological Crystallography*. International Union of Crystallography, 71(9), pp. 1909–1920. doi: 10.1107/S1399004715013073.

Quintana, C., Cowley, J. M. and Marhic, C. (2004) 'Electron nanodiffraction and high-resolution electron microscopy studies of the structure and composition of physiological and pathological ferritin', *Journal of Structural Biology*, 147(2), pp. 166–178. doi: 10.1016/j.jsb.2004.03.001.

Reif, D. W. (1992) 'Ferritin as a source of iron for oxidative damage', *Free Radical Biology and Medicine*, 12(5), pp. 417–427. doi: 10.1016/0891-5849(92)90091-T.

Reif, D. W. and Simmons, R. D. (1990) 'Nitric oxide mediates iron release from ferritin', *Archives of Biochemistry and Biophysics*, 283(2), pp. 537–541. doi: 10.1016/0003-9861(90)90680-W.

Rivera, M. (2017) 'Bacterioferritin: Structure, Dynamics, and Protein–Protein Interactions at Play in Iron Storage and Mobilization', *Accounts of Chemical Research*, 50(2), pp. 331–340. doi: 10.1021/acs.accounts.6b00514.

Sahlin, M. *et al.* (1990) 'Activation of the iron-containing B2 protein of ribonucleotide reductase by hydrogen peroxide.', *Biochemical and biophysical research communications*, 167(2), pp. 813–8. Available at: http://www.ncbi.nlm.nih.gov/pubmed/2182022.

Santambrogio, P. *et al.* (2011) 'Over-expression of mitochondrial ferritin affects the JAK2/STAT5 pathway in K562 cells and causes mitochondrial iron accumulation', *Haematologica*, 96(10), pp. 1424–1432. doi: 10.3324/haematol.2011.042952.

Sazinsky, M. H. and Lippard, S. J. (2006) 'Correlating structure with function in bacterial multicomponent monooxygenases and related diiron proteins', *Accounts of Chemical*

*Research*, 39(8), pp. 558–566. doi: 10.1021/ar030204v.

Smirnova, E. *et al.* (1998) 'A Human Dynamin-related Protein Controls the Distribution of Mitochondria', *The Journal of Cell Biology*, 143(2), pp. 351–358. doi: 10.1083/jcb.143.2.351.

Smith, J. L. (2004) 'The physiological role of ferritin-like compounds in bacteria.', *Critical reviews in microbiology*, 30(3), pp. 173–85. doi: 10.1080/10408410490435151.

Smoukov, S. K. *et al.* (2003) 'EPR and ENDOR evidence for a 1-His, hydroxo-bridged mixed-valent diiron site in Desulfovibrio vulgaris rubrerythrin', *Biochemistry*, 42(20), pp. 6201–6208. doi: 10.1021/bi0300027.

Song, W. J. and Lippard, S. J. (2011) 'Mechanistic Studies of Reactions of Peroxodiiron(III) Intermediates in T201 Variants of Toluene/ o -Xylene Monooxygenase Hydroxylase', *Biochemistry*, 50(23), pp. 5391–5399. doi: 10.1021/bi200340f.

Stefanini, S. *et al.* (1996) 'Thermal stability of horse spleen apoferritin and human recombinant H apoferritin.', *Archives of biochemistry and biophysics*, 325(1), pp. 58–64. doi: 10.1006/abbi.1996.0007.

Stuart, R. K. *et al.* (2009) 'Coastal Strains of Marine Synechococcus Species Exhibit Increased Tolerance to Copper Shock and a Distinctive Transcriptional Response Relative to Those of Open-Ocean Strains', *Applied and Environmental Microbiology*, 75(15), pp. 5047–5057. doi: 10.1128/AEM.00271-09.

Stuart, R. K. *et al.* (2013) 'Genomic island genes in a coastal marine Synechococcus strain confer enhanced tolerance to copper and oxidative stress', *The ISME Journal*. Nature Publishing Group, 7(6), pp. 1139–1149. doi: 10.1038/ismej.2012.175.

Sun, S. and Chasteen, N. D. (1994) 'Rapid Kinetics of the EPR-Active Species Formed during Initial Iron Uptake in Horse Spleen Apoferritin', *Biochemistry*, 33(50), pp. 15095–15102. doi: 10.1021/bi00254a019.

Svistunenko, D. A. *et al.* (2000) 'A New Method for Quantitation of Spin Concentration by EPR Spectroscopy: Application to Methemoglobin and Metmyoglobin', *Journal of Magnetic Resonance*, 142(2), pp. 266–275. doi: 10.1006/jmre.1999.1935.

Svistunenko, D. A. (2001) 'An EPR study of the peroxyl radicals induced by hydrogen peroxide in the haem proteins', *Biochimica et Biophysica Acta (BBA) - Protein Structure and Molecular Enzymology*, 1546(2), pp. 365–378. doi: 10.1016/S0167-4838(01)00157-1.

Svistunenko, D. A. and Cooper, C. E. (2004) 'A New Method of Identifying the Site of Tyrosyl Radicals in Proteins', *Biophysical Journal*. Elsevier, 87(1), pp. 582–595. doi: 10.1529/biophysj.104.041046.

Swartz, L. *et al.* (2006) 'Redox-dependent structural changes in the Azotobacter vinelandii bacterioferritin: New insights into the ferroxidase and iron transport mechanism', *Biochemistry*, 45(14), pp. 4421–4428. doi: 10.1021/bi060146w.

Tan, G. (2001) 'Frataxin expression rescues mitochondrial dysfunctions in FRDA cells', *Human Molecular Genetics*, 10(19), pp. 2099–2107. doi: 10.1093/hmg/10.19.2099.

Tatur, J. *et al.* (2006) 'A highly thermostable ferritin from the hyperthermophilic archaeal anaerobe Pyrococcus furiosus', *Extremophiles*, 10(2), pp. 139–148. doi: 10.1007/s00792-005-0484-x.

Tatur, J. and Hagen, W. R. (2005) 'The dinuclear iron-oxo ferroxidase center of Pyrococcus furiosus ferritin is a stable prosthetic group with unexpectedly high reduction potentials', *FEBS Letters*, 579(21), pp. 4729–4732. doi: 10.1016/j.febslet.2005.07.045.

Tatur, J., Hagen, W. R. and Matias, P. M. (2007) 'Crystal structure of the ferritin from the hyperthermophilic archaeal anaerobe Pyrococcus furiosus', *Journal of Biological Inorganic Chemistry*, 12(5), pp. 615–630. doi: 10.1007/s00775-007-0212-3.

Theil, E. C. (1987) 'Ferritin: Structure, gene regulation, and cellular function in animals, plants, and microorganisms', *Annual Reviews of Biochemistry*, 56(1), pp. 289–315.

Theil, E. C., Liu, X. S. and Tosha, T. (2008) 'Gated pores in the ferritin protein nanocage', *Inorganica Chimica Acta*, 361(4), pp. 868–874. doi: 10.1016/j.ica.2007.08.025.

Thomson, A. M., Rogers, J. T. and Leedman, P. J. (1999) 'Iron-regulatory proteins, iron-responsive elements and ferritin mRNA translation', *International Journal of Biochemistry and Cell Biology*, 31(10), pp. 1139–1152. doi: 10.1016/S1357-2725(99)00080-1.

Timóteo, C. G. *et al.* (2012) 'Desulfovibrio vulgaris bacterioferritin uses H 2 O 2 as a co-substrate for iron oxidation and reveals DPS-like DNA protection and binding activities', *Biochemical Journal*, 446(1), pp. 125–133. doi: 10.1042/BJ20111439.

Tinberg, C. E. and Lippard, S. J. (2011) 'Dioxygen Activation in Soluble Methane Monooxygenase', *Accounts of Chemical Research*, 44(4), pp. 280–288. doi: 10.1021/ar1001473.

Torti, F. M. and Torti, S. V. (2002) 'Regulation of ferritin genes and protein', *Blood*, 99(10), pp. 3505–3516. doi: 10.1182/blood.V99.10.3505.

Tosha, T. *et al.* (2010) 'Moving Metal Ions through Ferritin−Protein Nanocages from Three-Fold Pores to Catalytic Sites', *Journal of the American Chemical Society*, 132(41), pp. 14562–14569. doi: 10.1021/ja105583d.

Touati, D. *et al.* (1995) 'Lethal oxidative damage and mutagenesis are generated by iron in delta fur mutants of Escherichia coli: protective role of superoxide dismutase.', *Journal of Bacteriology*, 177(9), pp. 2305–2314. doi: 10.1128/jb.177.9.2305-2314.1995.

Treffry, A. *et al.* (1995) 'Iron(II) oxidation by H chain ferritin: evidence from site-directed mutagenesis that a transient blue species is formed at the dinuclear iron center', *Biochemistry.*, 34(46), pp. 15204–15213.

Treffry, A. *et al.* (1997) 'Dinuclear center of ferritin: Studies of iron binding and oxidation show differences in the two iron sites', *Biochemistry*, 36(2), pp. 432–441. doi: 10.1021/bi961830l.

Treffry, A. *et al.* (1998) 'How the presence of three iron binding sites affects the iron storage function of the ferritin (EcFtnA) of Escherichia coli', *FEBS Letters*, 432(3), pp. 213–218. doi: 10.1016/S0014-5793(98)00867-9.

Trehoux, A., Mahy, J. P. and Avenier, F. (2016) 'A growing family of O2 activating dinuclear iron enzymes with key catalytic diiron(III)-peroxo intermediates: Biological systems and chemical models', *Coordination Chemistry Reviews*. Elsevier B.V., 322, pp. 142–158. doi: 10.1016/j.ccr.2016.05.014.

Turano, P. *et al.* (2010) 'NMR reveals pathway for ferric mineral precursors to the central cavity of ferritin', *Proceedings of the National Academy of Sciences*, 107(2), pp. 545–550. doi:

10.1073/pnas.0908082106.

Velayudhan, J. *et al.* (2007) 'The role of ferritins in the physiology of Salmonella enterica sv. Typhimurium: a unique role for ferritin B in iron-sulphur cluster repair and virulence', *Molecular Microbiology*, 63(5), pp. 1495–1507. doi: 10.1111/j.1365-2958.2007.05600.x.

Wajnberg, E. *et al.* (2001) 'Ferromagnetic Resonance of Horse Spleen Ferritin: Core Blocking and Surface Ordering Temperatures', *Journal of Magnetic Resonance*, 153(1), pp. 69–74. doi: 10.1006/jmre.2001.2430.

Waldo, G. S. and Theil, E. C. (1993) 'Formation of iron(III)-tyrosinate is the fastest reaction observed in ferritin', *Biochemistry*, 32(48), pp. 13262–13269. doi: 10.1021/bi00211a039.

Wang, W. *et al.* (2010) 'Serum ferritin: Past, present and future', *Biochimica et Biophysica Acta - General Subjects*. Elsevier B.V., 1800(8), pp. 760–769. doi: 10.1016/j.bbagen.2010.03.011.

Watt, G. D. *et al.* (1986) 'Redox properties and Moessbauer spectroscopy of Azotobacter vinelandii bacterioferritin', *Biochemistry*, 25(15), pp. 4330–4336. doi: 10.1021/bi00363a023.

Weeratunga, S. K. *et al.* (2009) 'Binding of Pseudomonas aeruginosa Apobacterioferritin-Associated Ferredoxin to Bacterioferritin B Promotes Heme Mediation of Electron Delivery and Mobilization of Core Mineral Iron', *Biochemistry*, 48(31), pp. 7420–7431. doi: 10.1021/bi900561a.

Weinberg, E. D. and Miklossy, J. (2008) 'Iron withholding: a defense against disease.', *Journal of Alzheimer's disease : JAD*, 13(4), pp. 451–63. doi: 10.1007/BF00140609.

Wencka, M. *et al.* (2009) 'Magnetic and EPR study of ferric green rust- and ferrihydrite-coated sand prepared by different synthesis routes', *Journal of Physics D: Applied Physics*, 42(24). doi: 10.1088/0022-3727/42/24/245301.

Willies, S. C. *et al.* (2009) 'The binding of haem and zinc in the 1.9 Å X-ray structure of Escherichia coli bacterioferritin', *JBIC Journal of Biological Inorganic Chemistry*, 14(2), pp. 201–207. doi: 10.1007/s00775-008-0438-8.

Wong, S. G. *et al.* (2012) 'Fe-haem bound to Escherichia coli bacterioferritin accelerates iron core formation by an electron transfer mechanism.', *The Biochemical journal*, 444(3), pp. 553–60. doi: 10.1042/BJ20112200.

Wörsdörfer, B., Conner, D. A., *et al.* (2013) 'Function of the diiron cluster of Escherichia coli class Ia ribonucleotide reductase in proton-coupled electron transfer', *Journal of the American Chemical Society*, 135(23), pp. 8585–8593. doi: 10.1021/ja401342s.

Wörsdörfer, B., Lingaraju, M., *et al.* (2013) 'Organophosphonate-degrading PhnZ reveals an emerging family of HD domain mixed-valent diiron oxygenases', *Proceedings of the National Academy of Sciences of the United States of America*, 110(47), pp. 18874–18879. doi: 10.1073/pnas.1315927110.

Xing, G., Hoffart, L. M., *et al.* (2006) 'A coupled dinuclear iron cluster that is perturbed by substrate binding in myo-inositol oxygenase', *Biochemistry*, 45(17), pp. 5393–5401. doi: 10.1021/bi0519607.

Xing, G., Diao, Y., *et al.* (2006) 'Evidence for C-H cleavage by an iron-superoxide complex in the glycol cleavage reaction catalyzed by myo-inositol oxygenase', *Proceedings of the National Academy of Sciences*, 103(16), pp. 6130–6135. doi: 10.1073/pnas.0508473103.

Xu, B. and Chasteen, N. D. (1991) 'Iron oxidation chemistry in ferritin. Increasing Fe/O2 stoichiometry during core formation.', *The Journal of biological chemistry*, 266(30), pp. 19965–70. Available at: http://www.ncbi.nlm.nih.gov/pubmed/1939058.

Xu, X., Persson, H. L. and Richardson, D. R. (2005) 'Molecular pharmacology of the interaction of anthracyclines with iron', *Molecular Pharmacology*, 68(2), pp. 261–271. doi: 10.1124/mol.105.013383.

Yang, X. *et al.* (1998) 'Reaction Paths of Iron Oxidation and Hydrolysis in Horse Spleen and Recombinant Human Ferritins †', *Biochemistry*, 37(27), pp. 9743–9750. doi: 10.1021/bi973128a.

Yang, X., Chiancone, E., *et al.* (2000) 'Iron oxidation and hydrolysis reactions of a novel ferritin from Listeria innocua.', *The Biochemical journal*, 349 Pt 3, pp. 783–6. Available at: http://www.ncbi.nlm.nih.gov/pubmed/10903139.

Yang, X., Le Brun, N. E., *et al.* (2000) 'The Iron Oxidation and Hydrolysis Chemistry of Escherichia coli Bacterioferritin †', *Biochemistry*, 39(16), pp. 4915–4923. doi: 10.1021/bi992631f.

Yasmin, S. *et al.* (2011) 'A New Role for Heme, Facilitating Release of Iron from the Bacterioferritin Iron Biomineral', *Journal of Biological Chemistry*, 286(5), pp. 3473–3483. doi: 10.1074/jbc.M110.175034.

Yun, D. *et al.* (2007) 'Intermediate X in the Assembly of the Iron-Radical Cofactor of Ribonucleotide Reductase from Mouse', 1925, pp. 1925–1932. doi: 10.1021/bi061717n.

Zamora, P. L. and Villamena, F. A. (2012) 'Theoretical and Experimental Studies of the Spin Trapping of Inorganic Radicals by 5,5-Dimethyl-1-pyrroline N -Oxide (DMPO). 3. Sulfur Dioxide, Sulfite, and Sulfate Radical Anions', *The Journal of Physical Chemistry A*, 116(26), pp. 7210–7218. doi: 10.1021/jp3039169.

Zanella, I. *et al.* (2008) 'The effects of frataxin silencing in HeLa cells are rescued by the expression of human mitochondrial ferritin', *Biochimica et Biophysica Acta (BBA) - Molecular Basis of Disease*, 1782(2), pp. 90–98. doi: 10.1016/j.bbadis.2007.11.006.

Zhao, G. *et al.* (2001) 'Is Hydrogen Peroxide Produced during Iron(II) Oxidation in Mammalian Apoferritins? †', *Biochemistry*, 40(36), pp. 10832–10838. doi: 10.1021/bi011052j.

Zhao, G. *et al.* (2002) 'Iron and hydrogen peroxide detoxification properties of DNA-binding protein from starved cells. A ferritin-like DNA-binding protein of Escherichia coli', *Journal of Biological Chemistry*, 277(31), pp. 27689–27696. doi: 10.1074/jbc.M202094200.

Zhao, G. *et al.* (2003) 'Multiple Pathways for Mineral Core Formation in Mammalian Apoferritin. The Role of Hydrogen Peroxide †', *Biochemistry*, 42(10), pp. 3142–3150. doi: 10.1021/bi027357v.

Zhao, Z. *et al.* (1997) 'Catalytic iron(II) oxidation in the non-haem ferritin of Escherichia coli: the early intermediate is not an iron tyrosinate *', *Journal of the Chemical Society, Dalton Transactions*, (21), pp. 3977–3978. doi: 10.1039/a703675b.

# Appendices

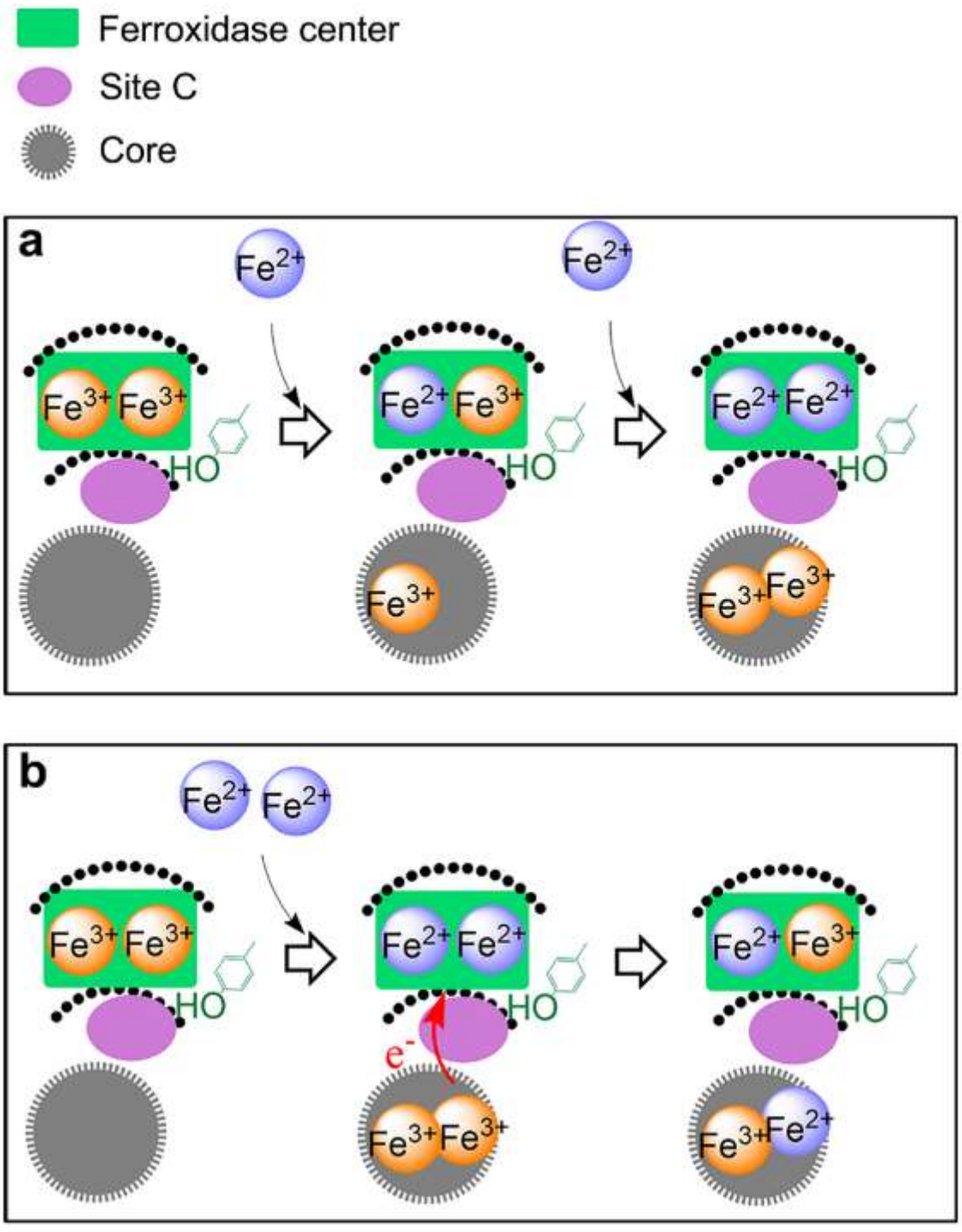


**Appendix 1.** Two alternative versions of the 'displacement' model of iron oxidation of ferritins. $Fe^{3+}$ is stable in the FC until displaced by $Fe^{2+}$. This displacement can be sequential

(model a) or simultaneous (model b). This figure is displayed as published in (Honarmand Ebrahimi, Hagedoorn and Hagen, 2015).

**Appendix 2.** An in-depth explanation of the methodology used to calculate the concentration of $H_2O_2$ formed in the DtpA-coupled oxidation of $Fe^{2+}$ by HuHF using $O_2$ as an oxidant is described below.

$$\frac{[Fe^{2+}]}{2}$$

The amount of $H_2O_2$ (and thus CpI) that is predicted to form as a result of a certain concentration of iron being oxidized with a 2:1 stoichiometry. The concentration of CpI was calculated from the documented differences between the extinction coefficients for $Fe^{3+}$DtpA and for CpI (30,000 $M^{-1}cm^{-1}$ at 400 nm). These numbers were used to plot the blue points in Fig. 3.5. As HuHF oxidizes iron using $O_2$ in a 2:1 stoichiometry it was assumed that 100 % of the $H_2O_2$ would be released.

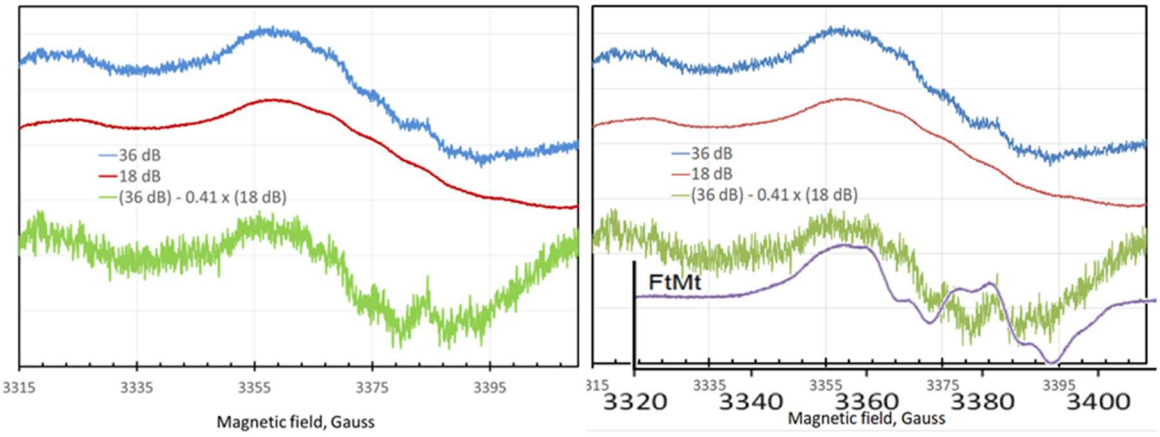


**Appendix 3.** The free radical on the Δ9 FtMt variant was unlike that found in previous batches; by averaging the RFQ EPR free radical spectra shown in Fig. 3.21 (blue) and subtracting an averaged series of spectra recorded at $P_{MW}$ = 3.16 mW (red) the green difference spectrum was attained. This had similar structural features to the tyrosyl-like spectrum submitted as a grant proposal in 2017 (purple).

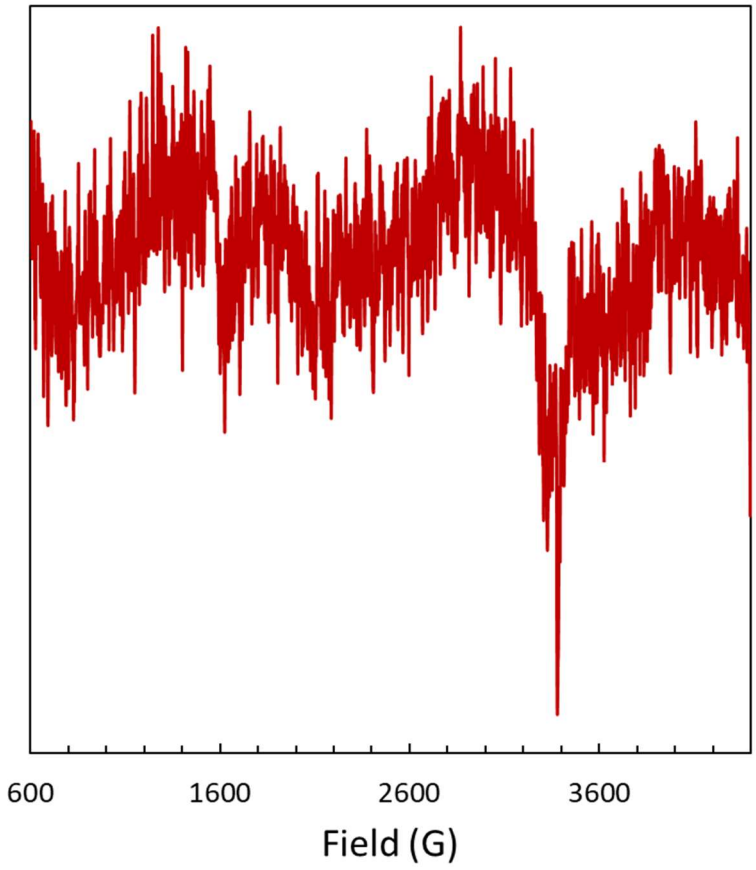


**Appendix 4.** An EPR spectrum of the apo-HuHF protein at a concentration of 8.3 μM.

**Appendix 5.** An in-depth explanation of the methodology used to calculate the concentration of $H_2O_2$ formed in the DtpA-coupled oxidation of $Fe^{2+}$ by BFR using $O_2$ as an oxidant is described below.

As in Appendix 2 where HuHF was measured, $O_2$ was expected to form one molecule of $H_2O_2$ for every two iron atoms, and the concentration of CpI was determined by the difference in extinction coefficients between $Fe^{3+}$DtpA and CpI at 400 nm. However, this reaction was complicated by BFR's ability to also utilise $H_2O_2$ as an oxidant. This was accounted for by

determining the proportion of $H_2O_2$ which would react with each protein based on their second order rate constants:

$$\frac{k_{BFR}}{k_{DtpA}} = \frac{3.76 \times 10^6\ M^{-1}s^{-1}}{1.40 \times 10^7\ M^{-1}s^{-1}} = 0.27$$

Thus the ratio of $H_2O_2$ that would be expected to react with BFR based on its rate is calculated as shown below:

$$1 - 0.27 = 0.73$$

As such, the total amount of $H_2O_2$ released could be calculated by dividing [CpI] by 0.73. In this manner it could be calculated how much $Fe^{2+}$ was oxidized by $H_2O_2$, and thus what percentage was oxidized by $O_2$.

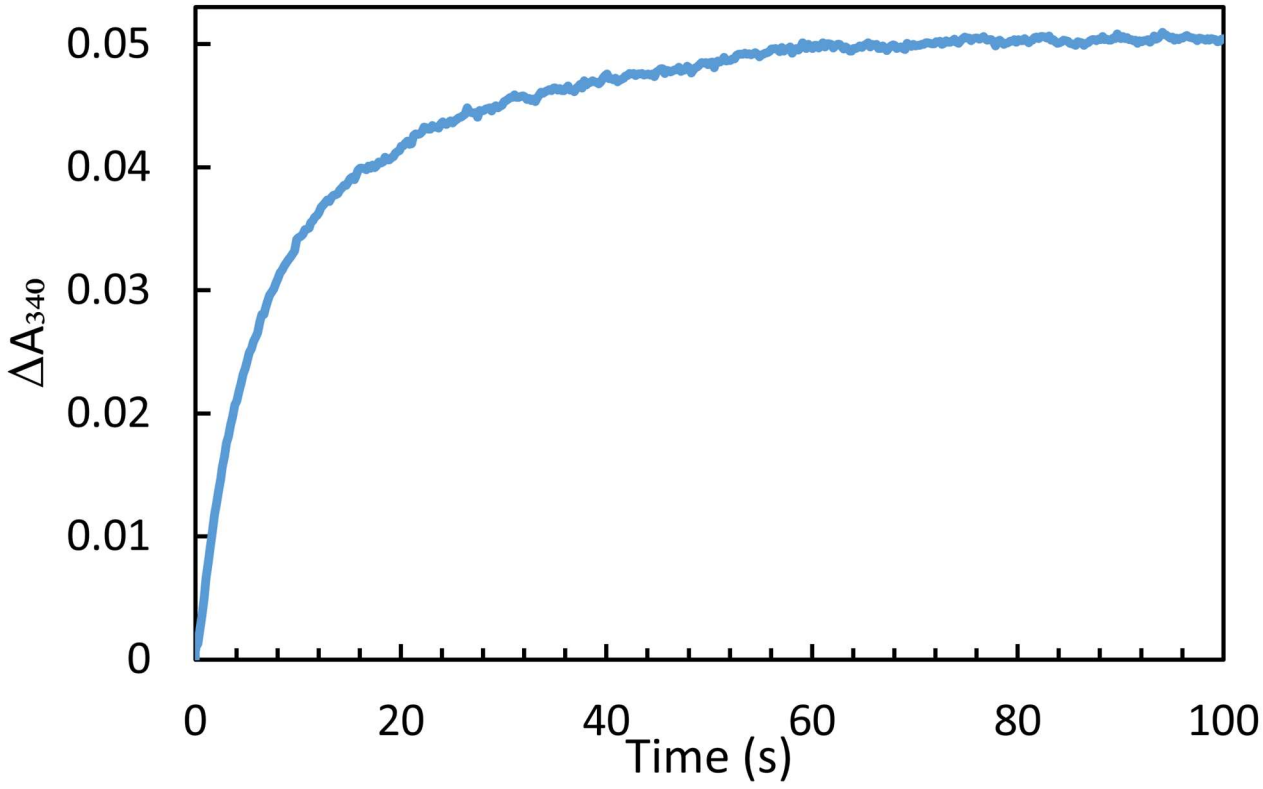


**Appendix 6.** Kinetics of 48 µM $Fe^{2+}$ oxidation in MES (100 mM, pH 6.5) by $H_2O_2$ (120 µM). Trace shown is an average of three repeats.